

Development and investigation of conducting polymer electrodes for microbial fuel cells

Submitted in partial fulfillment of the requirements

of the degree of

Doctor of Philosophy

of the

Indian Institute of Technology Bombay, India

and

Monash University, Australia

by

Jayesh Manohar Sonawane

Supervisors:

Prof. Prakash Chandra Ghosh (IIT Bombay)

Prof. Samuel Adeloju (Monash University)



The course of study for this award was developed jointly by Monash University, Australia and the Indian Institute of Technology, Bombay and was given academic recognition by each of them. The programme was administrated by The IITB-Monash Research Academy

(2018)

This page intentionally left blank

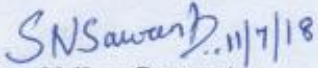
विद्या शस्त्रस्य शास्त्रस्य द्वे विद्ये प्रतिपत्तये ।
आद्या हास्याय वृद्धत्वे द्वितीयाद्रियते सदा ॥

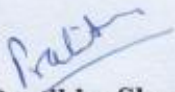
Dedicated to the memories of my Grandfather late. Chintaman Sonawane (Aanna), my Grandmother late. Vastala Sonawane (Aaji).

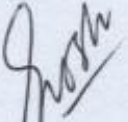
My mother Malti Sonawane (Aai) and Father Manohar Sonawane (Nana) who always supported me, whatever path I took.

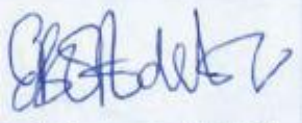
Approval Sheet

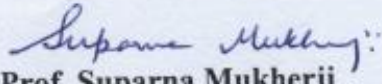
The thesis entitled "*Development and investigation of conducting polymer electrodes for microbial fuel cells*" by *Jayesh Manohar Sonawane* is approved for the degree of **Doctor of Philosophy**


Dr. Shilpa Sawant
External Examiner


Prof. Pratibha Sharma
Internal Examiner


Prof. Prakash Ghosh
IITB Supervisor


Prof. Samuel Adeloju
Monash Supervisor


Prof. Suparna Mukherji
Chairman

Date: July 11, 2018

Place: IITB-Monash Research Academy, Mumbai.

Declaration

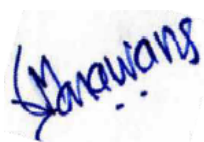
I declare that this written submission represents my ideas in my own words and where others' ideas or words have been included, I have adequately cited and referenced the original sources. I also declare that I have adhered to all principles of academic honesty and integrity and have not misrepresented or fabricated or falsified any idea/data/fact/source in my submission. I understand that any violation of the above will be cause for disciplinary action by the Institute and can also evoke penal action from the sources which have thus not been properly cited or from whom proper permission has not been taken when needed.

Notice 1

Under the Copyright Act 1968, this thesis must be used only under the normal conditions of scholarly fair dealing. In particular, no results or conclusions should be extracted from it, nor should it be copied or closely paraphrased in whole or in part without the written consent of the author. Properly written acknowledgement should be made for any assistance obtained from this thesis.

Notice 2

I certify that I have made all reasonable efforts to secure copyright permissions for third-party content included in this thesis and have not knowingly added copyright content to my work without the owner's permission.



Student Name: Jayesh Manohar Sonawane

IITB ID: 124174002

Monash ID: 25203029

Publications outcomes

Journal Publications -

1. **JM Sonawane**, A Yadav, PC Ghosh, SB Adeloju. Recent advances in the development and utilization of modern anode materials for high performance microbial fuel cells, Biosensors and Bioelectronics 90, 558-576, 2017. **IF- 8.173.**
2. **JM Sonawane**, S Al-Saadi, RKS Raman, PC Ghosh, SB Adeloju, Exploring the use of polyaniline-modified stainless-steel plates as low-cost, high-performance anodes for microbial fuel cells, Electrochimica Acta 268, 484-493, 2018. **IF- 5.116.**
3. **JM Sonawane**, RKS Raman, PC Ghosh, SB Adeloju, Synthesis and utilisation of polypyrrole coated stainless steel as a low-cost anode for high-performance microbial fuel cells ChemElectroChem (To be submitted)
4. **JM Sonawane**, PC Ghosh, SB Adeloju, Electrokinetic behavior of conducting polymer modified stainless steel anodes during the enrichment phase in microbial fuel cells, Electrochimica Acta (Accepted). **IF- 5.116.**
5. **JM Sonawane**, SA Patil, PC Ghosh, SB Adeloju Low-cost stainless-steel wool anodes modified with polyaniline and polypyrrole for high-performance microbial fuel cells, Journal of Power Sources 379, 103-114. 2018. **IF- 6.945.**
6. **JM Sonawane**, D Pant, PC Ghosh, SB Adeloju. Fabrication of a carbon paper/polyaniline-copper composite cathode as a replacement for platinum cathode in low-temperature fuel cells, Journal of Material Chemistry A, Elsevier. (Under review).
7. **JM Sonawane**, D Pant, PC Ghosh, SB Adeloju. Exploration of a carbon paper/polyaniline-copper hybrid as an air cathode for microbial fuel cells, Applied Materials and Interfaces, ACS. (To be submitted)
8. **JM Sonawane**, R Goenka, PC Ghosh, SB Adeloju. A highly efficient microbial fuel cell stack for enhanced power generation and treatment of a landfill leachate, Materials Today, Elsevier. (To be submitted)
9. **JM Sonawane**, SB Adeloju, PC Ghosh. Landfill leachate: A promising substrate for microbial fuel cells, International Journal of Hydrogen Energy 42 (37), 23794-23798, 2017. **IF- 4.229.**
10. **JM Sonawane**, E Marsili, PC Ghosh, Treatment of domestic and distillery wastewater in high surface microbial fuel cells. International journal of hydrogen energy 39 (36), 21819-21827, 2014. **IF- 4.229.**

11. **JM Sonawane**, A Gupta, PC Ghosh, Multi-electrode microbial fuel cell (MEMFC): a close analysis towards large scale system architecture International journal of hydrogen energy 38 (12), 5106-5114, 2013. **IF- 4.229**.

Conference Publications -

1. **JM Sonawane**, Rajam, SB Adeloju, PC Ghosh, Graphene: a promising electrode for microbial fuel cells, 2nd International Conference on Green Energy & Expo, Atlanta, USA

Content (Brief)

<i>Abstract</i>	xxii
Chapter 1	1
Recent advances in the development and utilisation of modern anode materials for high-performance microbial fuel cells	1
Aims of study	53
Chapter 2	55
Exploring the use of polyaniline-modified stainless-steel plates as low-cost, high performance anodes for microbial fuel cells	55
Chapter 3	87
Synthesis and utilisation of polypyrrole coated stainless steel as a low-cost anode for high-performance microbial fuel cells	87
Chapter 4	107
Electrokinetic behaviour of conducting polymer modified stainless steel anodes during the enrichment phase in microbial fuel cells	107
Chapter 5	139
Low-cost stainless-steel wool anodes modified with polyaniline and polypyrrole for high-performance microbial fuel cells	139
Chapter 6	173
Fabrication of a carbon paper/polyaniline-copper composite cathode as a replacement for platinum cathode in low-temperature fuel cells	173
Chapter 7	205
Exploration of a carbon paper/polyaniline-copper hybrid as an air cathode for microbial fuel cells	205
Chapter 8	233
A highly efficient microbial fuel cell stack for enhanced power generation and treatment of a landfill leachate	233
Chapter 9	259
Conclusions and Future Directions	259

Content (Extended)

<i>Abstract</i>	xxii
Chapter 1	1
Recent advances in the development and utilisation of modern anode materials for high-performance microbial fuel cells.....	1
1.1 Introduction.....	5
1.2 Anode materials for MFCs.....	9
1.2.1 Modern carbon-based anodes	10
1.2.1.1 Natural anode materials	13
1.2.1.2 Synthetic anode materials	16
1.2.2 Composite anodes	18
1.2.2.1 Graphite-polymer composites	18
1.2.2.2 Carbon nanotubes composite	25
1.2.2.3 Multi-walled carbon nanotubes composite	26
1.2.2.4 Graphene-based anode	27
1.2.3 Surface modified anodes.....	30
1.2.3.1 Conductive polymer coatings	34
1.2.3.2 Graphite/carbon surface treatment.....	36
1.2.4 Metal-based anode	38
1.3 Challenges and future directions.....	42
1.4 Conclusion	42
References	44
Aims of study	53
Chapter 2	55
Exploring the use of polyaniline-modified stainless-steel plates as low-cost, high performance anodes for microbial fuel cells.....	55
2.1 Introduction.....	59
2.2 Materials and methods.....	61
2.2.1 Electrochemical cell setup and electrode preparation.....	61
2.2.2 Cathode fabrication.....	61
2.2.3 Electropolymerisation of Polyaniline (PANi).....	61

2.2.4	Contact angle measurement and Scanning electron microscopy	62
2.2.5	Fourier Transform Infrared Spectroscopy (FTIR)	62
2.2.6	Time-dependent electrochemical impedance spectroscopy	63
2.2.7	Setup and operation of MFCs	63
2.3	Results and discussion	64
2.3.1	PANi film formation	65
2.3.1.1	PANi film formation with sulphuric acid	65
2.3.1.2	PANi film formation using sulfamic acid	66
2.3.1.3	PANi film formation with oxalic acid	67
2.3.1.4	PANi film formation with nitric acid	69
2.3.2	Characterisation of PANi coatings	71
2.3.2.1	Cyclic voltammetry	71
2.3.2.2	Fourier-transform infrared spectroscopy (FTIR)	72
2.3.2.3	Contact angle measurement	74
2.3.2.4	Scanning Electron Microscope	74
2.3.3	Evaluation of coating durability	74
2.3.4	Microbial fuel cells with SS-P/PANi anode	77
2.3.4.1	Comparison with previous studies	80
2.4	Conclusion	81
	References	82
	Chapter 3	87
	Synthesis and utilisation of polypyrrole coated stainless steel as a low-cost anode for high-performance microbial fuel cells	87
3.1	Introduction	91
3.2	Materials and Methods	92
3.2.1	Electrochemical cell setup and sample preparation	92
3.2.2	Electropolymerisation of Polypyrrole (PPy)	93
3.2.3	Surface profilometry and contact angle measurement	93
3.2.4	Fourier Transform Infrared Spectroscopy (FTIR)	93
3.2.5	Cathode fabrication	93
3.2.6	Experimental setup and operation of MFCs	94
3.2.7	Operation of MFCs	94
3.3	Results and discussion	95

3.3.1	PPy film formation with L-(+)-Tartaric acid	95
3.3.2	PPy coating characterisation	96
3.3.2.1	Fourier Transform Infrared Spectroscopic Studies of PPy Films	96
3.3.2.2	Contact angle measurement	97
3.3.2.3	Scanning Electron Microscope	98
3.3.3	Evaluation of coating durability by time-dependent electrochemical spectroscopy ..	98
3.4	Performance of microbial fuel cells	100
3.5	Conclusion	102
Chapter 4		107
Electrokinetic behaviour of conducting polymer modified stainless steel anodes during the enrichment phase in microbial fuel cells		107
4.1.	Introduction	112
4.2	Experimental	114
4.2.1	Synthesis of PANi and PPy on SS	114
4.2.2	MFC configuration	115
4.2.3	Operation	115
4.2.4	MFC performance evaluation	116
4.2.4.1	Maximum current generation from the different SS anodes	116
4.2.4.2	Electrochemical characterisation	116
4.2.4.3	Tafel Plot	117
4.2.4.4	Polarisation behaviour of the anodes	118
4.2.4.5	Fourier transform infrared spectroscopy (FTIR)	119
4.3	Result and discussion	119
4.3.1	Maximum current generation	119
4.3.2.	Bioelectroperformance of anode materials during incubation	120
4.3.2.1	Exchange current densities of anode materials	120
4.3.2.2	Charge transfer resistance of anode materials	125
4.4	Fourier Transform Infrared (FTIR) Spectroscopic Studies	129
4.5	Conclusion	132
References		133
Chapter 5		139
Low-cost stainless-steel wool anodes modified with polyaniline and polypyrrole for high-performance microbial fuel cells		139

5.1	Introduction.....	144
5.2	Materials and methods.....	146
5.2.1	Electrode materials.....	146
5.2.2	Polyaniline (PANi) and polypyrrole (PPy) anode modification	147
5.2.3	Cathode fabrication.....	147
5.2.4	Characterisation of anode materials.....	147
5.2.5	MFC reactor configuration	148
5.2.6	Operation of MFCs	148
5.2.7	Analytics and calculations	149
5.3.	Results and discussion.....	151
5.3.1	Morphological features, surface area and hydrophilicity of polymer coated SS-P anodes	151
5.3.2	Bioelectrocatalytic performances of SS-W and SS-P anodes.....	153
5.3.3	Charge transfer resistance of SS-W and SS-P anodes	155
5.3.4	Electrokinetic behaviour of PANi coated SS-W based anodes	158
5.3.5	Polarisation behaviour of all SS based anodes	160
5.3.6	Comparison with previous work.....	162
5.4	Conclusions.....	165
Chapter 6.....		173
Fabrication of a carbon paper/polyaniline-copper composite cathode as a replacement for platinum cathode in low-temperature fuel cells.....		173
6.1	Introduction.....	177
6.2	Materials and methods.....	179
6.2.1	Electrochemical cell setup and PANi synthesis.....	179
6.2.2	Electropolymerisation of polyaniline (PANi).....	180
6.2.3	Platinum coating on carbon paper.....	181
6.2.4	Electrochemical Characterisation	181
6.2.4.1	Linear Sweep Voltammetry	181
6.2.4.2	Tafel Plot.....	181
6.2.5	Morphological study of the cathodes	182
6.2.6	X-ray Photoelectron Spectroscopy (XPS)	182
6.2.7	Fourier Transform Infrared Spectroscopy (FTIR)	183
6.3	Results	183

6.3.1	Electrochemical deposition of PANi-Cu on CP.....	183
6.3.2	Electrochemical characterisation	184
6.3.2.1	Electrochemical activity of CP/PANi-Cu and CP/PANi	186
6.3.2.2	Influence of Pt loading on electrochemical performance	187
6.3.2.3	Electrochemical performance of CP/PANi-Cu coating	189
6.3.3	X-ray Photoelectron Spectroscopy (XPS)	190
6.3.4	Fourier Transform Infrared Spectroscopy (FTIR)	192
6.3.4.1	FTIR of CP/Pt cathode.....	192
6.3.4.2	FTIR of CP/PANi-Cu cathode	193
6.3.5	3D Profilometry and 4D X-ray microscopy.....	194
6.4.	Conclusion	195
	References	197
	Chapter 7	205
	Exploration of a carbon paper/polyaniline-copper hybrid as an air cathode for microbial fuel cells	205
7.1.	Introduction.....	208
7.2	Materials and method	210
7.2.1	Electrode preparation	210
7.2.1.1	Anode fabrication.....	210
7.2.1.2	Preparation of CP/PANi-Cu cathode	210
7.2.1.3	Fabrication of Pt cathode	211
7.2.1.4	Hotpressing of Pt and PANi-Cu electrodes	211
7.2.2	Configuration of MFC reactor	211
7.2.3	Characterisation of Pt and PANi-Cu cathodes.....	212
7.2.3.1	Microscopy	212
7.2.3.2	Time-of-Flight Secondary Ion Mass Spectrometry (ToF-SIMS)	212
7.2.3.3	Attenuated Total Reflectance -Fourier Transform Infrared Spectroscopy	212
7.2.4	Operation of the MFCs	213
7.2.5	Analytics and calculations	213
7.3	Results and discussion.....	214
7.3.1	Morphology of Pt and CP/PANi-Cu cathodes	214
7.3.2	Time-of-Flight Secondary Ion Mass Spectrometry (ToF-SIMS)	215
7.3.3	Bioelectrocatalytic performance of Pt and CP/PANi-Cu cathodes.....	216

7.3.4	Current-voltage characteristics	217
7.3.5	Longevity of cathodic activity	218
7.3.6	Biofouling of Nafion membrane	221
7.3.7	Four-dimensional X-ray microscopy	223
7.3.8	Attenuated Total Reflectance Fourier Transformed Infrared Spectroscopy	223
7.4	Conclusion	226
	References	227
	Chapter 8	233
	A highly efficient microbial fuel cell stack for enhanced power generation and treatment of a landfill leachate.....	233
8.1	Introduction.....	237
8.2	Materials and Methods	239
8.2.1	Construction of MFC stack.....	239
8.2.2	Polyaniline (PANi) anode preparation.....	240
8.2.3	Cathode fabrication.....	240
8.2.4	Operation.....	240
8.2.5	Analytics and Calculations	241
8.2.6	Physicochemical characterisation of leachate.....	242
8.2.6.1	Chemical Oxygen Demand & Coulombic Efficiency	242
8.3	Results and Discussions	243
8.3.1	Bioelectrocatalytic performance	243
8.3.1.1	Individual cell operation	243
8.3.1.2	Stacked cell operation	245
8.3.1.3	Polarisation behaviour	245
8.3.2	Physicochemical analysis.....	246
8.3.2.1	Chemical oxygen demand and Coulombic Efficiency.....	246
8.3.2.2	pH, conductivity and elemental composition.....	248
8.3.3	Comparison with previous work.....	250
8.4	Conclusion	253
	Chapter 9	259
	Conclusions and Future Directions	259
9.1	Conclusions.....	260
9.2	Future prospective.....	266

List of the figures

Chapter 1

- Fig. 1.2** Working principle and basic construction of MFC6
- Fig. 1.3** Timeline of recent developments of anode materials for microbial fuel cells8
- Fig. 1.4** Classification of anode materials used for MFCs9
- Fig. 1.5** [a] Photographic image of a single recyclable layered corrugated carbon electrode and [b] scanning electron micrographs of bamboo charcoal tube surface. Reproduced [a] from [22] and [b] from [50].13
- Fig. 1.6** Some Natural materials that have been considered as anode materials in MFC systems [a, b] king mushroom, [c, d] wild mushroom and [e, f] corn stem. FE-SEM micrographs after carbonization [b,d,f]. Reproduced from [41].14
- Fig. 1.7** SEM images of artificial 3D anode [a] electrospun and solution blown three-dimensional carbon fiber nonwovens, [b] polycrystalline carbon rod, [c] carbon fiber veil pictorial presentation of artificial 3D anode structures, [d] graphite fiber brush anode, [e] interlaced carbon yarn with stainless steel, and [f] rotating spiral carbon bush anode. Reproduced [a] from [53], [b] and [c] from [15], [d] from [14], [e] from [40] and [f] from [42].17
- Fig. 1.8** [a] Loofah sponge carbon (LSC) -TiO₂ and [b] photographic image of LSC-TiO₂. Reproduced from [57].19
- Fig. 1.9** SEM images of composite anodes [a, b] 3D carbon scaffold anodes from polyacrylonitrile, [c, d] carbon nanofibers modified graphite felt, ESEM images of [e] PAN precursor, [f] stabilized PAN, [g] carbon nanofibers (CNF), [h] activated carbon nanofibers nonwoven (ACNFN). Reproduced [a and b] from [58], [c and d] from [26], and [e, f, g and h] from [60].20
- Fig. 1.10** SEM images of some composite anode material. [a] carbon nanotube-textile (CNT-textile) composite, [b] and [c] a 3D-ordered macroporous carbon derived from a natural resource as anode carbon nanotubes (CNT)-sponge electrode, [d] image of the CNT-spong and [e] picture of a CNT-sponge electrode. Reproduced [a] from [70], [b and c] from [50] and [d and e] from [70].26

- Fig. 1.11** SEM and FESEM images of MWCNTs-based nanocomposite electrodes. [a] MWCNTs on Poreflon membrane and [b] MWCNTs spray-coated on carbon cloth. Reproduced from [5].27
- Fig. 1.12** SEM images of [a] graphene-based anodes and [b] graphene–sponge (G–S) composite electrode, [c] bare carbon cloth, [d] RGO-SnO₂/carbon cloth electrode, [e] plain nickel foam, [f] rGO–2–Ni (2 = the number of loading cycles) foams. Scale bars are 200 mm, [g] plain nickel foam, [h] digital pictures (insets) of plain nickel foam and rGO–Ni foam. Scale bars are 200 mm, and (i) digital picture of a curved rGO–Ni foam. Inset: rGO–Ni foam rolled up into a cylindrical shape. Reproduced [a, b] from [70], [c, d] from [76], and [e, f, g, h, i] from [36].29
- Fig. 1.13** SEM [a] micrographs of m-WO₃ and [b] 20%w PANI/m-WO₃ composite. Reproduced from [65].34
- Fig. 1.14** SEM images of the stainless-steel fiber felts (SSFFs) before and after polyaniline modification. [a, b] PANI/SSFF, [c] CP, [d] CP/GNS, and [e] CP/IL-GNS, and [f] CNT/PANI carbon paper electrode. Reproduced [a, b] from [28], [c, d, e] from [82] and [f] CNT/PANI carbon paper electrode. Reproduced [a, b] from [28], [c, d, e] from [82] and [f] from [24].35
- Fig. 1.15** [a] Micrographs of TiO₂–C/C dual nanofiber calcined at 1000°C for 3 h at N₂ atmosphere, [b] MCM-41, [c] NaX, FESEM images of the bare CP electrode, [d] TiO₂-NSs/CP electrode, [e] TiO₂-NSs/CP electrode obtained under optimal conditions, SEM images of electrodes, [f] CV20 (20 layered carbon veil), [g] CV30 (30 layered carbon veil), [h] CC, [i] CV20-MPL, [j] CC-MPL, and [k] MPL structure on CC-MPL. Reproduced [a] from [17], [b, c] reproduced from [77], [d, e] from [80], and [f, g, h, i, j, k] from [79].....37
- Fig. 1.16** Macroscopic and fluorescence images of anodes with and without biofilms on [a] carbon cloth, [b] smooth stainless steel, [c] macrostructured smooth stainless steel and [d] microstructured smooth stainless steel. Images from left to right are: macroscopic view of the clean electrode, epifluorescence image and treated image for assessment of biofilm surface coverage ratio. Reproduced from [21].39

Chapter 2

- Scheme 2.1** Schematic for surface modification of SS-Ps with PANi by galvanostatic polymerisation of ANi, characterisation, and exploration of PANi modified SS-P as an anode in a microbial fuel cell.....64
- Fig. 2.1** Chronopotentiograms obtained for formation of PANi layer on SS plate with (a) varying sulfuric acid concentration in presence of 0.1 M ANi and (b) varying ANi concentration in presence of 0.3 sulphuric acid. Concentrations of sulphuric acid in (a) are: (i) 0.1, (ii) 0.2, (iii) 0.3, (iv) 0.4, (v) 0.5, (vi) 0.6 and (vii) 0.7 M. ANi concentration in (b) are: (i) 0.1, (ii) 0.2, (iii) 0.3, (iv) 0.4 and (v) 0.5 M.66
- Fig. 2.2** Chronopotentiograms obtained for the formation of PANi layer on SS plate with (a) varying sulfamic acid concentration in the presence of 0.1 M ANi and (b) varying ANi concentration in the presence of 0.7 M sulphamic acid. Sulphamic acid concentrations (a): (i) 0.1, (ii) 0.2, (iii) 0.3, (iv) 0.4, (v) 0.5, (vi) 0.6, and (vii) 0.7 M. ANi concentrations in (b): (i) 0.1, (ii) 0.2, (iii) 0.3, (iv) 0.4, and (v) 0.5 M.67
- Fig. 2.3** Chronopotentiograms obtained for the formation of PANi layer on SS plate with (a) varying oxalic acid concentration in the presence of 0.1 M ANi and (b) varying ANi concentration in the presence of 0.3 M oxalic acid. Oxalic acid concentrations in (a): (i) 0.1, (ii) 0.2, (iii) 0.3, (iv) 0.4, (v) 0.5, (vi) 0.6, and (vii) 0.7 M. ANi concentration in (b): (i) 0.1, (ii) 0.2, (iii) 0.3, (iv) 0.4, and (v) 0.5 M.....68
- Fig. 2.4** Chronopotentiograms obtained for formation of PANi layer on SS plate with (a) varying nitric acid concentration in the presence of 0.1 M Ani and (b) varying ANi concentration in the presence of 0.7 M nitric acid. Nitric acid concentrations in (a): (i) 0.1, (ii) 0.2, (iii) 0.3, (iv) 0.4, (v) 0.5, (vi) 0.6, and (vii) 0.7 M. ANi concentrations in (b): (i) 0.1, (ii) 0.2, (iii) 0.3, (iv) 0.4, and (v) 0.5 M.....71
- Fig. 2.5** Cyclic voltammograms obtained for PANi-coated SS in 0.7 nitric acid. (a) cyclic voltammogram obtained at 5 mV/s scan rate, and (b) cyclic voltammograms obtained at: (i) 5, (ii) 10, (iii) 25, (iv) 50, (v) 75, (vi) 100, and (vii) 200 mV/s.....72
- Fig. 2.6** Characterisation of PANi modified SS-P. (a) FTIR spectrum, (b) contact angle measurement for pristine SS-P (i, i') and PANi modified SS-P (ii, ii') and (c) SEM images of PANi modified SS-P.....73

- Fig. 2.7** Electrochemical characterisation of PANi coating on SS. (a) Equivalent circuit used for impedance measurement, (b) change in PANi coating resistance as a function of time, (c) frequency dependences of the impedance and (d) phase shift in the Bode plots of PANi film synthesised in nitric acid.77
- Fig. 2.8** Performance of the MFCs with the SS-P and SS-P/PANi anodes. (a) Open circuit voltage output during the start-up phase of the MFCs system, (b) current generation from MFCs system with 100 Ω resistance connected across the cell, (c) polarisation curves of the MFCs with SS-P anode, and (d) polarisation curves of the MFCs with SS-P/PANi anode.79

Chapter 3

- Fig. 3.1** Chronopotentiograms obtained for the formation of a PPy layer on SS plate with (a) varying L-(+)-Tartaric acid concentration in the presence of 0.1 M Py and (b) varying Py concentration in the presence of 0.7 M L- (+)-Tartaric acid. L-(+)-Tartaric acid concentrations in (a): (i) 0.1, (ii) 0.2, (iii) 0.3, (iv) 0.4, (v) 0.5, (vi) 0.6, and (vii) 0.7 M. Py concentrations in (b): (i) 0.1, (ii) 0.2, (iii) 0.3, (iv) 0.4, and (v) 0.5 M.....96
- Fig. 3.2** Characterisation of PPy film on SS plate (a) FTIR spectra of PPy film on SS plate, and (b) Contact angle measurement of (i, i`) SS plate and (ii, ii`) PPy plate (c) SEM images of PPy on SS plate.....98
- Fig. 3.3** Electrochemical analysis of PPy coating by time dependant electrochemical spectroscopy; a) The equivalent circuit utilised for impedance; b) Change in PPy charge transfer resistance as a function of time in 0.1 M NaCl; c) measurement Frequency dependences of the impedance and d) phase shift in the Bode plots of PPy film synthesised from 0.4 M pyrrole in 0.7 M L-(+)-Tartaric acid.....99
- Fig. 3.4** Performance of the MFCs fortified with SS-P anode and SS/PPy-P anodes. a) Open circuit voltage output during the start-up phase of the MFCs system. b) current generation from MFCs system by connecting 100 Ω across the cell. c) Polarisation curves of the MFCs with SS-P anode. d) Polarisation curves of the MFCs with SS/PPy-P anode.....101

Chapter 4

- Fig. 4.1** Characterisation of anode materials by SEM. (a) Pristine SS, (b) SS-PANi, and (c) SS-PPy.....114
- Fig. 4.2** Operating points employed for MFC performance evaluation: 1. All sets of MECs enriched in the activation region (without external resistance) 2. All sets of MECs enriched in the Ohmic region, where $R_{ext}=R_{int}$ 3. All sets of MFCs enriched with the application of very low resistance in the mass transfer region.....116
- Fig. 4.3** I-V curves obtained with SS-P, SS-W, SS/PANi-P, SS/PANi-W, SS/PPy-P and SS/PPy-W anodes used to determine maximum current.120
- Fig. 4.4** Variation of j_0 values obtained for all SS based MFC systems with time. (a) MFCs with SS-P anodes, and (b) MFCs with SS-W anodes.....121
- Fig. 4.5** Variation of j_0 values obtained for all PANi anodes with time. (a) MFCs with SS/PANi-P anodes, and (b) MFCs with SS/PANi-W anodes.122
- Fig. 4.6** Variation of j_0 values obtained for all PPy anodes with time. (a) MFCs with SS/PPy-P anodes, and (b) MFCs with SS/PPy-W anodes.....123
- Fig. 4.7** EIS plots for stainless steel-based anodes. (a) the system operated under OCV mode, (b) system operated under $R_{ext}=R_{int}$, and (c) system operated under very low R_{ext}125
- Fig. 4.8** EIS plots of SS wool-based anode system. (a) the system operated under OCV mode, (b) system operated under 100 Ω , and (c) system operated under 10 Ω125
- Fig. 4.9** EIS plots of PANi based anode system. (a) the system operated under OCV mode, (b) system operated under 60 Ω , and (c) system operated under 10 Ω127
- Fig. 4.10** EIS plots of SS-PANi-W based anode system. (a) the system operated under OCV mode, (b) system operated under 10 Ω , and (c) system operated under 5 Ω127
- Fig. 4.11** EIS plots of PPy based anode system. (a) system operated under OCV mode, (b) system operated under 200 Ω , and (c) system operated under 20 Ω128
- Fig. 4.12** EIS plots of SS/PPy-W based anode system. (a) system operated under OCV mode, (b) system operated under 20 Ω , and (c) system operated under 10 Ω129
- Fig. 4.13** ATR-FTIR spectra obtained for SS anodes enriched under three different conditions. An electrode harvested at the end of the 7th day of the experiment; (a) SS-P anode, (b) SS/PANi-P anode, and (c) SS/PPy-P anode.131

Chapter 5

- Fig. 5.1** Anode materials and MFC systems used in this study. Stainless steel wool (SS-W) anodes: (a) pristine SS-W, (b) SS-W coated with polyaniline, (c) SS-W coated with polypyrrole, (d) the system architecture of the MFC, and (e) the experimental setup for MFCs along with a data logger.....149
- Fig. 5.2** The electrical equivalent circuit used to analyse the EIS data: a) for uncoated SS electrodes, and b) for PANi and PPy coated SS electrodes.....151
- Fig. 5.3** Scanning electron microscopy images of (a) SS-P, (b) SS/PANi-P, and (c) SS/PPy-P anode materials.....152
- Fig. 5.4** (A) Contact angles, and (B) Profilometer images of (a) SS-P, (b) SS/PANi-P, and (c) SS/PPy-P anode materials.153
- Fig. 5.5** Variation of open circuit voltages of (a) SS-P and (b) SS-W anode based MFCs monitored for two cycles. Bioelectrocatalytic performances presented in terms of current densities for (c) SS-P and (d) SS-W anode-based air-cathode MFCs operated under constant resistance mode (100 Ω).155
- Fig. 5.6** Nyquist plots of EIS spectra for all SS based anodes: (a) SS-P, (b) SS-W, (c) SS/PANi-P, (d) SS/PANi-W, (e) SS/PPy-P, and (f) SS/PPy-W.157
- Fig. 5.7** Electrokinetics behaviour of SS-P based and SS-W based anodes. Tafel plots of SS-P based (a) and SS-W based (b) anodes. The $j_{0(\text{apparent})}$ values of SS-P based (c) and SS-W based (d) anodes. All figures include data for anodes without and with biofilm (suffixed by '+').159
- Fig. 5.8** Polarisation curves for the SS-P (a), SS/PANi-P (b), SS/PPy-P (c), SS-W (d), SS/PANi-W (e), and SS/PPy-W (f) anode based systems. The maximum power outputs expressed in terms of mW cm^{-2} are 0.036 ± 0.004 , 0.180 ± 0.019 , 0.071 ± 0.012 , 0.127 ± 0.011 , 0.288 ± 0.036 and 0.187 ± 0.017 for the respective anode systems.161

Chapter 6

- Scheme 6.1** Electropolymerisation of CP/PANi-Cu on carbon paper, preparation of membrane electrode assembly (MEA) and electrochemical testing of the cathodes in an aqueous proton conductor with a three- electrode assembly.....180

- Fig. 6.1** Chronopotentiogram of (a) electrodeposition of CP/PANi-Cu on carbon paper as a function of time and (b) (the representative figure for PANi-Cu deposition) 5 min PANi coating using chronopotentiometry followed by Cu deposition for 1 min using chronoamperometry.....184
- Fig. 6.2** SEM images of (a) Pristine carbon paper, (b) carbon coated with 0.5 mg cm^{-2} Pt, (c) CP/PANi-Cu (20 mins) electrodeposited on carbon paper and (d) measured CP/PANi-Cu nanofibers from SEM image.....185
- Fig. 6.3** Electrochemical characterisation of the cathodes and effect of PANi electrosynthesis using Cu and SS counter electrode. (a) Tafel plots of pristine CP, CP/PANi-Cu, CP/PANi and CP/Pt cathode, (b) Exchange current densities_(apparent) of the CP, CP/PANi-Cu, CP/PANi and CP/Pt cathode, (c) Cathodic linear sweep polarisation of CP, CP/PANi-Cu, CP/PANi and CP/Pt cathode, (d) Maximum reduction current of CP, CP/PANi-Cu, CP/PANi and CP/Pt cathode.187
- Fig. 6.4** Dependence of electrochemical performance of cathode on Pt loading. (a) Tafel plots, (b) LSVs, (c) exchange current densities and reduction current densities as a function of platinum loading on carbon paper, and (d) Pt on carbon paper and its associated charge transfer resistance (R_{ct}) as a function of loading. Pt loadings: (i) pristine, (ii) 0.25, (iii) 0.5, (iv) 0.75, (v) 1.0, (vii) 1.25 and (vii) 1.5 mg.188
- Fig. 6.5** Dependence of electrochemical performance of CP/PANi-Cu cathode with polymerisation time. (a) Tafel plots, (b) LSVs, and (c) exchange current densities and reduction current densities as a function of CP/PANi-Cu. Polymerisation time: (i) - pristine, (ii) 5, (iii) 10, (iv) 15, (v) 20, (vii) 25 and (vii) 30 min. (d) CP/PANi-Cu polymerisation on carbon paper and its associated charge transfer resistance (R_{ct}) as a function of polymerisation time.190
- Fig. 6.6** XPS pattern of CP/Cu-PANi cathode and CP/Pt cathode, a, b, c survey, Cu2p presence and various states of the presence of Cu respectively. a', b' and c,' survey, Pt presence and different states of Pt presence respectively.....192
- Fig. 6.7** Fourier transform infrared (FTIR) spectra of (a) CP/Pt cathode with 0.5 Pt loading on carbon paper and (b) CP/PANi-Cu cathode electrodeposited for 20 min.193
- Fig. 6.8** 3D profilometry of (a) pristine carbon paper, (b) carbon paper coated with 0.5 mg cm^{-2} CP/Pt/C, and (c) CP/PANi-Cu. CP/PANi-Cu coating was obtained by electrodeposition for 20 mins.195

Fig. 6.9	4D X-ray microscopy of (a) carbon coated with 0.5 mg cm^{-2} and (b) CP/PANi-Cu (20 mins) electrodeposited on carbon paper.	195
-----------------	--	-----

Chapter 7

Fig. 7.1	Micrographs of the different cathodes explored in the study. Profilometer image of (a) pristine CP, (b) CP/ PANi-Cu cathode and (c) CP/Pt cathode; and (d) scanning electron micrograph of the CP/ PANi-Cu cathode (magnification 100,000X).	215
Fig. 7.2	2D image of ion counts obtained by ToF SIMS. (a) CP/Pt cathode and (b) CP/PANi-Cu cathode.	216
Fig. 7.3	Performance of CP/Pt and CP/PANi-Cu cathodes in MFCs. (a) Open circuit voltage as a function of time, and (b) current generation as a function of time.	217
Fig. 7.4	Polarisation curves of the MFCs operated with CP/Pt and CP/PANi-Cu. (a) CP/Pt cathode, and (b) CP/PANi-Cu cathode.	218
Fig. 7.5	Evidence of the formation of Al_2O_3 on current collectors used with the CP/Pt and CP/PANi-Cu cathodes after exposure to the M9 media.	219
Fig. 7.6	Electrochemical analysis of the longevity of the cathodes. (a) Tafel plots of CP/Pt cathode, (b) Tafel plots of CP/PANi-Cu cathode. (c) $j_{0_apparent}$ of CP/Pt cathode after every successive cycle. (i) is for the initial cycle, (ii) for cycle 2, (iii) for cycle 3, and so on to cycle 6 (vi) for cycle 6 and (d) $j_{0_apparent}$ of CP/PANi-Cu cathode after every successive cycle. (i) is for the initial cycle, (ii) for cycle 2, (iii) for cycle 3, and so on to cycle 6.	220
Fig. 7.7	Observed changes in Nafion membranes before and after exposure to M9 media. (a) membrane attached to the CP/Pt cathode before and after the experiment, and (b) membrane attached to the CP/PANi-Cu cathode before and after the experiments. 3D-profilogram of the used Nafion membrane attached to (c) CP/Pt and (d) CP/PANi-Cu cathodes (50X).	222
Fig. 7.8	4D X-Ray micrograph of Nafion membrane attached to CP/Pt and CP/Cu-PANi cathodes.	223
Fig. 7.9	ATR-FTIR spectra of Nafion membrane attached to CP/Pt and CP/PANi-Cu cathodes.	225

Chapter 8

- Fig. 8.1** Experimental setup of the 18 unit MFC stack. (a) top view of air cathode, (b) air cathode sandwiched in PANi-coated wool, (c) top view of anode wool in each cell, and (d) complete assembly of MFC stack.239
- Fig. 8.2** Variation in the bioelectrocatalytic performance of the cells in a) the first stage with two open circuit voltage cycles, b) the second stage with three constant resistance cycles, c) the third stage with one open circuit voltage cycle of the stack, and d) the fourth stage with two constant resistance cycles of the stack.244
- Fig. 8.3** Polarisation behaviour of the individual cell in a stack a) current density b) power density.246
- Fig. 8.4** COD removal from landfill leachate a) COD removal from individual cells b) COD of initial landfill leachate, treated from the landfill leachate treatment plant, COD removal from OCV cycle, current cycle one and current cycle two.247
- Fig. 8.5** Coulombic efficiency of the MFC stack a) individual cells for cycle 1, 2, and 3 for each cells b) all the cells operated as a stack after the various cycles of operation.248
- Fig. 8.6** Variation in pH and conductivity of individual cells after (a) OCV(1) cycle, (b) OCV(2) cycle, (c) CR(1) cycle, (d) CR(2) cycle, Σ CR(3) cycle, and (f) various cycles of operation as a stack [UL-Untreated leachate, ATL-Commercial aerobic treated leachate].....249
- Fig. 8.7** Elemental composition of leachate; UL-untreated leachate, ATL-aerobic treated leachate, OCV-leachate from open circuit voltage, CR (1) – leachate from constant resistor cycle1 and CR (2) – leachate from constant resistor cycle 2.....249

List of Tables

Chapter 1

Table 1.1 A brief account of carbon-based anode materials explored in MFC research.11

Table 1.2 Comparison of some reported composite anode materials used for construction of in MFC research22

Table 1.3 Comparison of the performance of some surface modified anodes in MFC31

Table 1.4 Comparisons of the performance of some metal-based anodes used for MFCs41

Chapter 2

Table 2.1 Optimum activation and stabilisation potentials obtained for PANi formation on SS plate from different acids and ANi concentrations.71

Table 2.2 Changes in charge transfer resistance [R_{ct} (Ohm.cm²)] for PANi formed in different acids.....76

Table 2.3 Comparison of the performances of PANi modified anodes in MFCs.81

Chapter 3

Table 3.1 Optimum activation and stabilisation potentials obtained for PPy formation on SS plate from L-(+)-Tartaric acid with different Py concentrations.....96

Table 3.2 Change in charge transfer resistance [R_{ct} (Ohm.cm²)] for PPy formed in L-(+)-Tartaric acid.....100

Chapter 4

Table 4.1 Applied resistance to the MFCs for evaluation of kinetics under various conditions120

Table 4.2 Changes in exchange current densities after incubation of MFCs with applied external resistance124

Table 4.3 Variation of charge transfer resistance (R_{ct}) in plate based anode system126

Table 4.4 Variation of charge transfer resistance (R_{ct}) in SS-wool based anode system128

Table 4.5 Changes in charge transfer resistance after incubation of MFCs with applied external resistance	129
--	-----

Chapter 5

Table 5.1 Charge transfer resistance (R_{ct}) obtained for the bare anodes (without biofilm) and bioanodes (with biofilms).....	157
--	-----

Table 5.2 Comparison of bioelectrocatalytic performance of different SS based and some other metallic anodes used for MFCs	163
---	-----

Table 5.3 Comparison of bioelectrocatalytic performance of PANi modified anodes in MFCs.	163
--	-----

Table 5.4 Comparison of bioelectrocatalytic performance of PPy modified anodes in MFCs.	164
---	-----

Chapter 6

Table 6.1 Elemental ID and quantification of CP/PANi-Cu	192
--	-----

Table 6.2 Elemental ID and quantification of CP-Pt	192
---	-----

Chapter 7

Table 7.1 Surface profile of CP/Pt and CP/PANi-Cu cathodes	222
---	-----

Chapter 8

Table 8.1 Comparison with previous works.....	251
--	-----

Acknowledgements

First and foremost, I express my gratitude towards my supervisors **Prof. Prakash C. Ghosh**, (IIT Bombay, India) and **Prof. Samuel Adeloju** (Monash University, Australia) for giving me an opportunity to work on an interesting theme in their groups, and for their invaluable suggestions, support and encouragement throughout my PhD candidature.

I would like to sincerely acknowledge Prof. Raman Singh, Department of Mechanical Engineering and Aerospace Engineering, Monash University, Clayton Campus, Australia for providing me research facilities during my Monash stay.

I would like to express my gratitude towards research progress committee members Prof. Pratibha Sharma, Prof. Sanjeeva Srivastava and Prof. Xiwang Zhang for their valuable feedback during annual progress seminars.

Also, I am very grateful to our collaborators, Dr. Deepak Pant from Flemish Institute for Technological Research, VITO, Belgium and Dr. Sunil Patil from Technical University Braunschweig, Germany.

I appreciate and owe much to Chinmay, Yogita, Abhishek, Rahulraj, Isha, Ratikanta, Ajay, Reeshab, Amit, Saad, Anis, and all members of the fuel cell research facility, IIT Bombay, India also all members of the Corrosion group, Monash University, Australia for their readily help and the excellent friendly atmosphere in the laboratory.

Last but not the least; I extend my gratitude to all my IITB-Monash Research Academy friends and most important, my mother (Aai), my father (Nana), my wife Vrushali and relatives for their moral support and encouragement.

-Jayesh M. Sonawane

Abstract

With the increasing global demand for resources and energy, there is a growing need to look beyond the conventional sources and search for new clean, renewable energy sources. Microbial fuel cells (MFCs) are novel bioelectrochemical devices for single-step conversion of biomass into electricity, based on the use of metabolic activity of bacteria.

The literature review in chapter 1 describes the recent advances in the development of anode materials and configurations over the past five years. The key limitations of anode materials which have hindered the development of large-scale MFCs are identified, and the potential solutions to these are discussed.

Chapters 2 and 3 describe the synthesis of polyaniline and polypyrrole on stainless steel (SS), and their use to evaluate startup time of MFCs. We explored the use of polyaniline (PANi) and polypyrrole (PPy) modified stainless steel plates (SS-Ps) as potential low-cost anodes for MFCs, with capability for effective promotion of microbial growth and retention of long-term stability. Careful and selective choice of acid and aniline concentrations for galvanostatic polymerisation produced highly uniform and adherent conductive PANi coating on SS-P which are desirable for use as anodes in MFC. The optimum PANi coating on SS formed by galvanostatic polymerisation was obtained with 0.4 M aniline in 0.7 M nitric acid. On the other hand, the optimum Ppy coating was obtained with 0.4 pyrrole in 0.7 M L-(+)-Tartaric acid with an applied current density of 2.5 mA cm⁻² for 15 mins.

Chapter 4 investigates the influence of the application of an external resistance on the SS coated PANi and PPy electrodes during MFC start-up phase. The half-cell reactors were enriched under different conditions including without R_{ext} (Open circuit mode), with $R_{ext}=R_{int}$ (Ohmic region), and with very low R_{ext} (mass transfer region). The MFC anodes enriched under $R_{ext}=R_{int}$ gave maximum exchange current density (j_{0max}) on the 4th day of operation. The calculated j_{0max} for SS wool (SS-W), SS/PANi-W and SS/PPy-W anodes were 0.03 ± 0.02 mA cm⁻², 1.05 ± 0.04 mA cm⁻² and 0.50 ± 0.04 mA cm⁻², respectively. The lowest charge transfer resistance (R_{ct}) of 0.23Ω cm⁻² was obtained with SS/PANi-W anode which exhibited the highest electron transfer kinetics and better biocompatibility than SS/PPy-W. The high current drawn from the system during the biofilm establishment phase did not support electroactive biofilm formation because it prevented the growing anode-respiring bacteria (ABR) from providing sufficient electron flow to the counter electrode.

In Chapter 5, the use of PANi and PPy coatings on stainless-steel wool (SS-W) is proposed as a low-cost anode for MFCs. When coated with PANi and PPy, the pristine SS-W, SS/PANi-W and SS/PPy-W anodes produced maximum current densities of 0.30 ± 0.04 , 0.67 ± 0.05 , 0.56 ± 0.07 mA cm⁻², respectively, in air-cathode MFCs. Also, based on achieved power density, both SS/PANi-W and SS/PPy-W achieved 0.288 ± 0.036 mW cm⁻² and 0.187 ± 0.017 mW cm⁻², respectively, which were superior to 0.127 ± 0.011 mW cm⁻² obtained with the pristine SS-W. Further, in comparison with SS plate-based anodes, all SS-W based anodes gave improved power densities under similar experimental conditions by at least 70%.

Chapter 6 investigates the use of a carbon paper/polyaniline-Cu composite (CP/PANi-Cu) as a potential low-cost replacement for the conventional Pt cathode. The incorporation of copper, through the addition of CuSO₄ to the monomer and deposition of the metal from this solution, enhanced the catalytic activity of CP/PANi-Cu cathode for oxygen reduction reaction, yielding a 170% higher $j_{0\text{apparent}}$ of 0.088 ± 0.003 mA cm⁻² than with a conventional Pt cathode (0.0325 ± 0.0031 mA cm⁻²) made up with 0.5 mg cm⁻² Pt loading. Even with a Pt loading of 1.5 mg cm⁻², the $j_{0\text{apparent}}$ of the Pt cathode (0.086 ± 0.004 mA cm⁻²) was still slightly lower. Also, the optimum CP/PANi-Cu cathode gave a much lower R_{ct} of 1.456Ω cm⁻² compared to the R_{ct} of 3.95Ω cm⁻² obtained with the conventional Pt cathode, but the Pt cathode with the higher Pt loading gave a closer R_{ct} of 1.485Ω cm⁻². The results of this study demonstrate that the proposed CP/PANi-Cu cathode can be adopted as a suitable low-cost replacement for Pt cathode.

Chapter 7 describes the use of a carbon paper/copper-polyaniline (CP/PANi-Cu) hybrid as a cheap and efficient air cathode. The resulting CP/PANi-Cu cathode is characterised by a uniform layer and relatively strong adhesion of PANi-Cu which enabled a significant oxygen reduction reaction (ORR). The maximum current generated by the CP/PANi-Cu cathode was 0.50 ± 0.02 mW cm⁻² which was significantly higher than 0.35 ± 0.03 mA cm⁻² obtained with a traditional Pt cathode. The power densities obtained for MFCs with these cathodes were 2.44 ± 0.14 mW cm⁻² under a current density of 0.85 ± 0.08 mA cm⁻² for Pt cathode, and 1.01 ± 0.01 mW cm⁻² at 0.37 ± 0.04 mA cm⁻² for CP/PANi-Cu cathode. Despite showing a loss of cathodic activity of 33%, the CP/PANi-Cu cathode experienced much less biofouling of the associated Nafion membrane than with the membrane used with the Pt cathode, and, thus, indicated that on the basis of overall performance, usage and stability, the CP/PANi-Cu cathode was better than the Pt cathode.

In Chapter 8, the fabrication of an 18 cell MFC stack containing PANi coated SS-W is undertaken and then explored as an anode for power generation with a landfill leachate. A maximum OCV of 12.8 V was achieved with the stack, and the total current generated were 78 and 83 mA for first and second parallel current cycles, respectively. The chemical oxygen demand (COD) removal in the OCV mode was 79.7 %. In the current generation mode, COD removals of 87.0 % and 86.3 % from first and second cycle were achieved, respectively. Average coulombic efficiencies (η) of 28.86 ± 1.82 , 23.38 ± 0.88 and 22.71 ± 0.42 were achieved from first, second and third cycles, respectively. Moreover, 35.3 and 36.9 % operated in series connection from the first and second cycle, respectively.

Chapter 9 concludes that the successful development of SS/PANi-W anode and CP/PANi-Cu cathode in this study has resulted in the achievement of significant increment in power generation when compared to the traditional 2D carbon-based electrodes. However, there is still a considerable possibility for using conductive polymers with a non-precious metal catalyst for the development of new cathodes. On the other hand, the use of engineered bacterial strain may provide new opportunities for the development of high-performance MFCs. The use of computational fluid dynamics can also be employed to further investigate the developed MFC stack to gain an understanding of the charge transfer and mixing phenomena. This investigation may subsequently enable the deployment of the MFC stack in real wastewater process train as a pilot plant for wastewater treatment and power generation.

Chapter 1

Recent advances in the development and utilisation of modern anode materials for high-performance microbial fuel cells

[Published as, J.M. Sonawane, A. Yadav, P.C. Ghosh, S.B. Adeloju, Recent advances in the development and utilization of modern anode materials for high-performance microbial fuel cells, Biosensors and Bioelectronics. 90 (2017) 558–576, Elsevier]

Abstract

Microbial fuel cells (MFCs) are a novel bio-electrochemical device for spontaneous or single-step conversion of biomass into electricity, based on the use of metabolic activity of bacteria. The design and use of MFCs have attracted considerable interests because of the potential new opportunities they offer for sustainable production of energy from biodegradable and reused waste materials. However, the associated slow microbial kinetics and costly construction materials have limited a much broader commercial use of the technology. In the past ten years, there have been significant new developments in MFCs which has resulted in a several-fold increase in achievable power density. There is still a considerable possibility for further improvement in performance and development of new cost-effective materials. This Chapter comprehensively reviews recent advances in the construction and utilisation of novel anodes for MFCs. In particular, it highlights some of the critical roles and functions of anodes in MFCs, strategies available for improving surface areas of anodes, dominant performance of stainless-steel based anode materials, and the emerging benefits of inclusion of nanomaterials. The Chapter also demonstrates that some of the materials are very promising for large-scale MFC applications and are likely to replace conventional anodes for the development of next-generation MFC systems. The hurdles to the development of commercial MFC technology are also discussed. Furthermore, the future directions in the design and selection of materials for construction and utilisation of anodes used for MFCs are highlighted.

Abbreviations

3D	Three-dimensional
2D	Two-dimensional
ACNFN	Activated carbon nanofiber nonwoven
ARB	Anode respiring bacteria
BMFCs	Benthic microbial fuel cells
CC	Carbon cloth
CC-A	Concentrated nitric acid
CNF	Carbon nanofiber
CNFs/GF	Carbon nanofibers modified graphite fibers
CNT	Carbon nanotube
CNT-textile	Carbon nanotube-textile
COD	Chemical oxygen demand
CP	Carbon paper
CS–CS–GR	Open-celled carbon scaffold
CV	Carbon veil
EET	Extracellular electron transfer
EWP	Egg white protein
FBMF	Flow fixed-bed microbial fuel cell
GAC	Granular activated carbon
GF	Graphite felt
GMS	Graphene modified stainless steel mesh
GNRs	Graphene nanoribbons
GPM	Gold/poly (ε-caprolactone) microfiber
GPM	Gold/poly (ε-caprolactone) microfiber
GPN	Gold/poly(ε-caprolactone) nanofiber
IL-GNS	Ionic liquid functionalized graphene nanosheets
G–S	Graphene–sponge
LCC	Layered corrugated carbon
LSC	Loofah sponge carbon
MCM 41	Mobil catalytic materials number 41
MFC	Microbial fuel cell
MFC-GFB	Graphite fiber brush

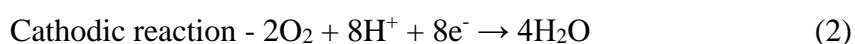
MFC-GG	Graphite granules
MPL	Micro-porous layer
MWCNTs	Multi-walled carbon nanotubes
m-WO ₃	Mesoporous tungsten trioxide
PAN	Polyacrylonitrile
PAN-GR	PAN/graphite composites,
PANI	Polyaniline
PG	Planar gold
PTFE	Polytetrafluoroethylene
RACNT	Randomly aligned CNT
rGO/SnO ₂	Reduced graphene oxide
rGO-CNT	Reduced graphene oxide/carbon nanotube
SS	Stainless-steel
SSFFs	Stainless steel fiber felt
SSLbL	Spin-spray layer-by-layer
SSM	Stainless steel mesh
VACNT	Vertically aligned CNT
WW	Wastewater

1.1 Introduction

The growth in the use of energy has a direct link with the well-being, quality of life and prosperity of society. There is an increasing need for not only generating sufficient energy but also to find energy from new sources that are safe, sustainable and environmentally friendly. As the availability of coal, oil and gas are being exhausted [1], there is a growing need to consider alternative energy sources. Reliance on the current renewable energy sources alone will not sufficiently meet the required needs in the future. It would be increasingly necessary to rely on the discovery of new energy sources to continue to meet future energy needs [2].

One of the promising solutions for addressing this energy problem is to develop and deploy specific energy sources for different utilities. This will involve developing strategies that enable the derivation of energy from waste materials. For example, across the world, huge volumes of wastewater are continuously pumped directly into rivers, streams and the oceans. The impact of this huge wastewater disposal is severe, ranging from damage to the marine environment and fisheries. Such disposal of wastewater does little to preserve water at a time when we are facing serious global water shortage, and the problem is likely to be exacerbated by the impact of climate change. In many cases, the effluent contains a significant amount of organic substances which are a potentially vital source of energy. One way of achieving this is by using microbial fuel cell (MFC) which is capable of directly converting chemical energy present in the organic materials to electricity by using microorganisms as catalysts [3–5]. The power generated can be used for maintenance and operation of the wastewater treatment facility, and, thus, creating a self-sustaining energy supply for the water treatment facility and, hence, to reduce operational costs [6].

A typical microbial fuel cell consists of an anode and cathode compartments separated by proton exchange membrane, as illustrated in Figure 1.1. The anode is the site where biocatalyst grows in the form of biofilm which promotes the decomposition of organic materials to produce electrons and protons. The electrons are transferred to the cathode compartment through an external circuit, while the protons are transferred to the cathode compartment through the proton exchange membrane (PEM). The electrons and protons are consumed in the cathode compartment with the protons combining with oxygen to form water [7,8], as shown in Figure 1.1. The chemical reactions which occur in the anodic and cathodic chambers, respectively, are given by equations (1) and (2) below [9]:



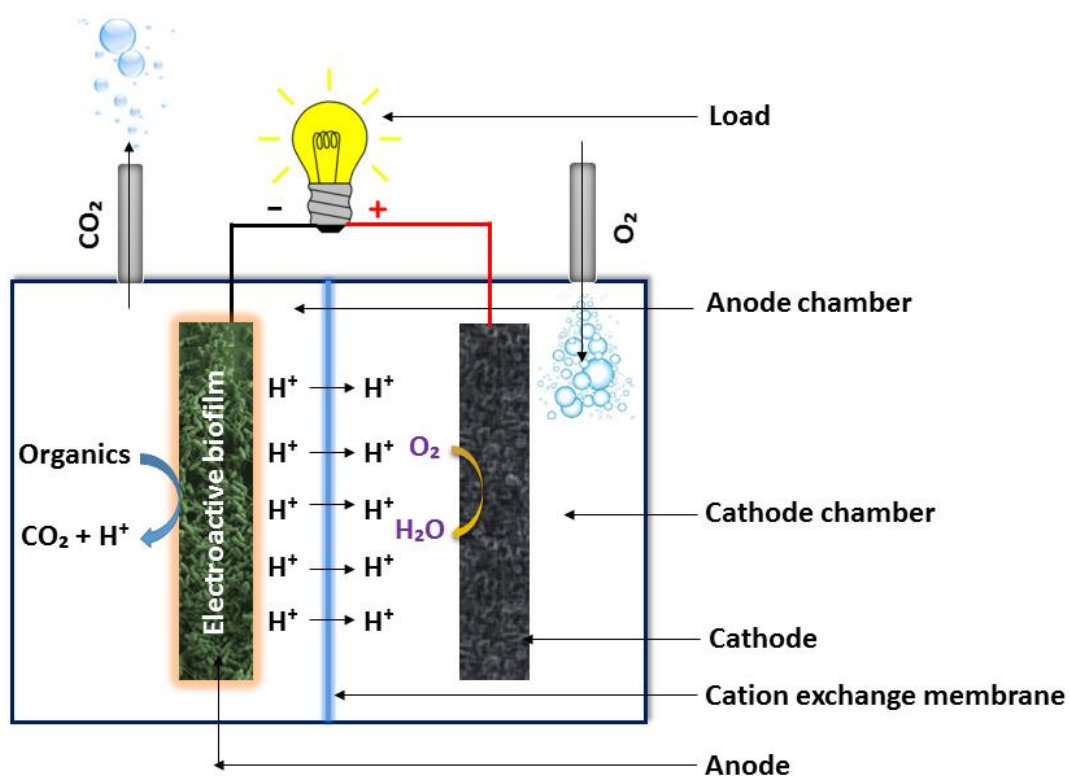


Fig. 1.1 Working principle and basic construction of MFC

The chosen electrode materials play a significant role in the performance of the MFC, and it is critically important for the successful utilisation of this technology for efficient energy generation. In the past two decades, many different materials have been explored as anodes for MFCs. While most of the earlier studies focused on the use of carbon-based material, such as graphite rod, graphite felt, carbon cloth, flexible graphite sheets, graphite granules and activated carbon [10–13], recent studies have found that these two dimensional electrodes have many limitations, such as low surface area, high internal resistance, high activation and mass transfer overpotential which hinders their ability to achieve high performance with MFCs. With recent advances in materials science and nanotechnology, the use of second-generation three-dimensional (3D) electrode material has attracted considerable interest for the development of MFCs. In 2007, Logon et al. developed a graphite fibre brush anode electrode with a 3D structure. They achieved a maximum power density of 2400 mW m^{-2} with a single chamber air cathode [14]. 3D surface anodes offer high surface areas for efficient colonisation of bacterial communities and, hence, for increasing substrate access to the anode respiring bacteria (ARB) and, consequently, minimising mass transfer limitation [15]. In addition to this

surface characteristics, 3D surface anodes are very quintessential in adhesion of bacterial colonies, have high volume to surface ratio, and excellent biocompatibility [16,17].

The anode surface also plays a significant role in promoting and maintaining bio-catalytic activity. Surfaces can be modified to become favourable habitats for biofilms which are capable of enhancing electron transfer from bacteria to the anode surface. The achievement of more bacterial adhesion enables the generation of more power with minimum loss [18]. It has been demonstrated in a recent study that surface modification not only increases MFC system performance but also decreases the MFC start-up time [19].

Many studies have also recently developed and extensively studied the use of graphene-based anodes, composite anodes, and surface modified anodes [20]. Each electrode material has its own merits and demerits. Metal-based or metal composite anodes have not been thoroughly studied or explored for MFCs. Most of the metals failed to pass the set criteria for best anode electrodes for MFC because of their tendency to corrode [13]. Pocaznoi et al. claimed recently that, of most metals, stainless steel is the most promising material for MFC anodes. However, there is still much scope for further improvement in the use of stainless steel for MFC anode development, as well as other new low-cost, efficient materials [21]. The achievement of large-scale development and economic viability of MFCs systems requires the availability of cost-effective anodes capable of achieving higher performance for long-term operation, while also involving easy maintenance or, where possible, to be completely free of maintenance [22].

This chapter reviews the recent advances in the development of anode materials and configurations over the past five years. The significant developments in anode materials for microbial fuel cells within this period are illustrated in Figure 1.2, and this demonstrates that the achievement of high-performance MFCs is closer to becoming a reality than it is widely realised.

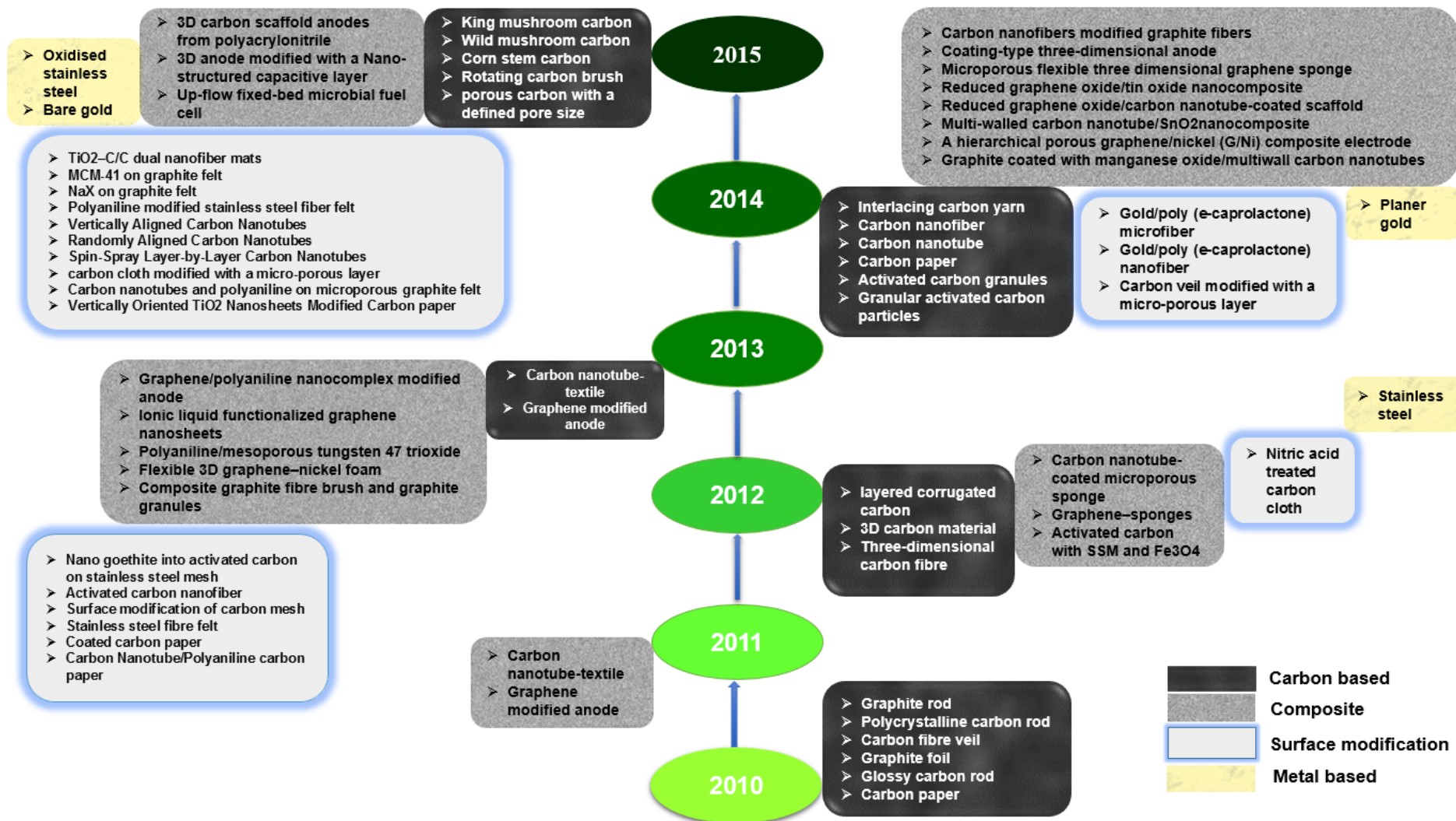


Fig. 1.2 Timeline of recent developments of anode materials for microbial fuel cells

To simplify the discussion in this literature survey, we have classified the anode materials into four broad categories and sub-categories according to the source of the materials, fabrication and modification strategies with one or more materials. The different categories are outlined in Figure 1.3 with specific examples listed under each category. The advantages and disadvantages of the anodes are compared regarding their characteristics and performances. Also, the key limitations of anode materials which have hindered the development of large-scale MFCs are identified, and the potential solutions to these are discussed.

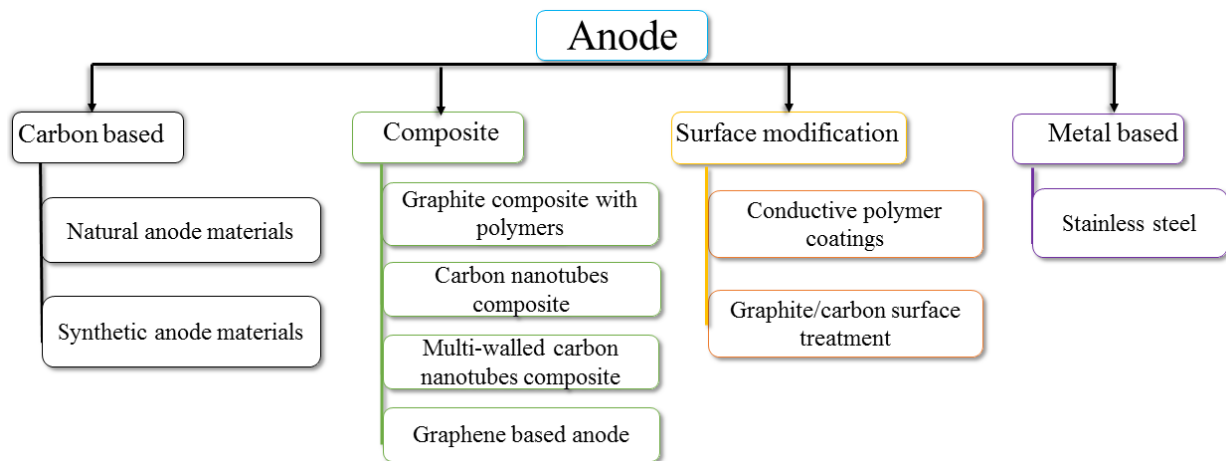


Fig. 1.3 Classification of anode materials used for MFCs

1.2 Anode materials for MFCs

The choice of an anode material and its architecture can directly affect key performance parameters, such as microbial adhesion, electron transfer, and fuel oxidation. The achievable power density of a MFC system is dependent on the choice of an anode which defines the power density limit and can significantly affect the performance of a MFC system [23]. Consequently, the achievement of a higher power density requires a capacity to promote better electron transfer from the bacterial community to the external circuit, and the anode is central to achieving this goal [8]. The mechanism of the electron transfer process necessitates the donation of an electron from the anode respiring bacteria (ARB) to the anode surface via extracellular electron transfer (EET) and, consequently, resulting in the passage of a current in the external circuit. This current generation mechanism has been elucidated to be similar to direct electron transfer from cell to anode surface, diffusion of soluble electron shuttles and electron transfer through solid component (Pili) from biofilm [8]. Key properties for anode materials to achieve a high performance include biocompatibility [9,23,24], corrosion resistant [9,21], low electrical resistance [9,25] and, high electrical conductivity [9]. The anode must

also be made of a chemically stable material which is capable of working in an environment which contains varied and diverse biodegradable wastewaters containing various organic and inorganic constituents capable of reacting with the anode material to cause deterioration and performance reduction [26].

In the last five years, many anode materials have been used for the construction of anodes for MFC systems. In particular, the material of choice for anode construction is influenced significantly by advances in various system architectures of MFCs. Notably, the use of different non-conventional carbonaceous anode materials is on the rise. This new class of carbonaceous anodes includes stainless steel [21], surface modified stainless steel [27–31] and graphene-based anodes [23,32–34]. The graphene-based anodes are very promising and have been reported in several recent studies. The use of composite graphene anodes has also been reported to produce high power density [35–39]. Similarly, the use of single-walled carbon nanotubes [16,23], multi-walled carbon nanotubes [5], and carbon nanofibers anodes has also been reported [26] for high-performance MFCs. Some of the recent advances in anode materials and configurations have been categorised in this chapter into four broad types, namely modern carbon-based anodes, metal based-anodes, carbon-based composite anodes, and surface modified metal-based anodes. Each of this category is discussed separately in the proceeding sections.

1.2.1 Modern carbon-based anodes

In the past decade, several carbon-based materials have been proposed and demonstrated for use as an anode in MFC systems. These include carbon paper, graphite plates or sheets, graphite rod, and carbon cloth [13]. The advantages of using carbon-based anode materials include low cost, biocompatibility, excellent electrical conductivity and chemical stability [13]. This group of materials has been acknowledged as being very useful for construction of MFCs because of their potentially high-performance improvement and excellent properties. One of the critical factors that influence the performance of these anode materials is the accessible surface area. The data provided in Table 1.1 demonstrate that several carbon-based anodes offer very high accessible surface areas, up to 1018 cm² [40]. The various types of modern carbon-based anodes that have been used for MFCs are described in more details in the subsequent sub-sections.

Table 1.1 A brief account of carbon-based anode materials explored in MFC research.

Carbon-based anode					Performance				
Anode	Cathode	System Architecture	Source of inoculation	Substrate	Anode surface area (cm ²)	I max (A/m ²)	Pmax (mW/m ²)	Reference	
layered carbon	corrugated	NA	Three-electrode cell	Primary wastewater	Artificial wastewater	26.52	390†	NA	[22]
3D carbon material	NA	Electrochemical cell	Domestic wastewater	Acetate substrate	Artificial wastewater	5.11	25.3	NA	[22]
Three-dimensional carbon fibre	NA	Electrochemical cell	Wastewater	Artificial wastewater	Artificial wastewater	NA	30	NA	[22]
Graphite rod	NA	Three-electrode half-cell	Domestic wastewater	Artificial wastewater	Artificial wastewater	11.5	5.17	NA	[15]
Polycrystalline carbon rod	NA	Three-electrode half-cell	Domestic wastewater	Artificial wastewater	Artificial wastewater	15	4.96	NA	[15]
Carbon fibre veil	NA	Three-electrode half-cell	Domestic wastewater	Artificial wastewater	Artificial wastewater	12	7.05	NA	[15]
Graphite foil	NA	Three-electrode half cell	Domestic wastewater	Artificial wastewater	Artificial wastewater	15	0.07	NA	[15]
Polycrystalline carbon rod	NA	Three-electrode half-cell	Domestic wastewater	Artificial wastewater	Artificial wastewater	15	9.21	NA	[15]
Glassy carbon rod	NA	Three-electrode half-cell	Domestic wastewater	Artificial wastewater	Artificial wastewater	3.18	2.5	NA	[15]
Carbon paper	NA	Three-electrode half-cell	Domestic wastewater	Artificial wastewater	Artificial wastewater	7	12.58	NA	[15]
Interlacing carbon yarn	Air cathode	Single chamber dual cathode	Distillery wastewater	Distillery wastewater	Distillery wastewater	1018	18.15	364	[40]

Interlacing carbon yarn	Air cathode	Single dual cathode	chamber	Domestic WW	Domestic WW	1018	22.04	621	[40]
King mushroom carbon	NA	Mini bioreactors	glassy	sewage treatment plant	Acetate media	0.25	20.9	NA	[41]
Wild mushroom carbon	NA	Mini bioreactors	glassy	sewage treatment plant	Acetate media	0.25	30.2	NA	[41]
Corn stem carbon	NA	Mini bioreactors	glassy	sewage treatment plant	Acetate media	0.25	31.2	NA	[41]
Rotating carbon brush	Carbon cloth	Tubular MFC		Wastewater effluent	Acetate media	60**	945***	210****	[42]
Carbon nanofiber	Gold foil	Micro-litre MFC	size	primary clarifier influent	Acetate mineral media	0.28	0.083	22000	[43]
Carbon nanotube	Gold foil	Micro-litre MFC	size	primary clarifier influent	Acetate mineral media	0.28	0.0234	49000	[43]
Carbon paper	Gold foil	Micro-litre MFC	size	primary clarifier influent	Acetate mineral media	0.28	0.096	10000	[43]
Activated carbon granules	graphite plates	fluidized capacitive system		Influent from enriched MFC	Acetate buffer phosphate	11	1.3	NA	[44]
carbon mesh anodes	Activated carbon	Single chamber		Domestic wastewater	Acetate buffer phosphate	7	NA	1330	[45]
multi-brush anode	Air cathode	Single chamber		Effluent from MFC	Acetate media	8	4.2	1200	[46]
porous carbon with a defined pore size	Air cathode	Single chamber		<i>Escherichia coli</i>	Glucose phosphate-buffered basal medium	9	13.4	1606	[47]
Granular activated carbon particles	Air cathode	Dual chamber		Effluent from MFC	Acetate media	10	2.6	951	[48]
Tubular charcoal bamboo	Carbon cloth	Tubular chamber MFC	two	Effluent from enriched MFC	Synthetic media	NA	NA	1652	[49]

† Six corrugated layered anode **Cathode surface ***A/m³ ****W/m³

1.2.1.1 Natural anode materials

The synthesis of high-performance anode materials involving the use of natural and recyclable materials provides an excellent green approach for deriving useful energy from nature and also for ensuring sustainability [22]. Developed layered corrugated carbon (LCC) anode developed from inexpensive packaging material by carbonisation is an exciting example. Figure 1.4a shows a LCC anode. It is important to note that the 3D surface of the LCC can usually be tuned by varying the layers and flute height. Increasing the number of layers from one to six resulted in a linear increment in current density due to the provision of increased surface area for biofilm. It has been demonstrated that LCC gives up to four-fold increase in current density when compared to conventional graphite felt [22].

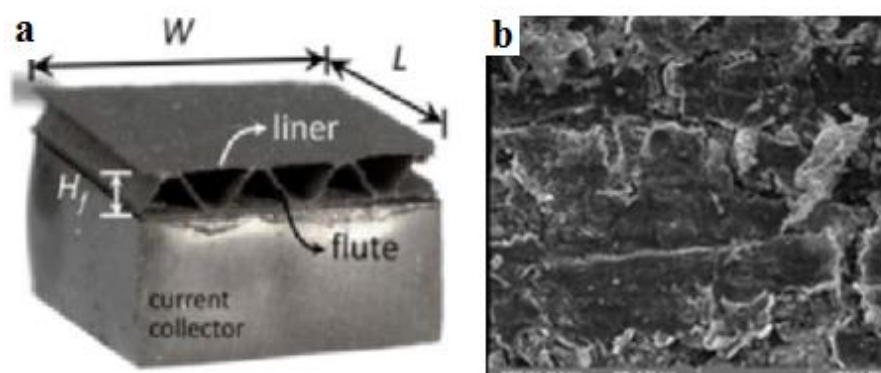


Fig. 1.4 [a] Photographic image of a single recyclable layered corrugated carbon electrode and [b] scanning electron micrographs of bamboo charcoal tube surface. Reproduced [a] from [22] and [b] from [50].

Natural-material carbon anodes are suitable low-cost alternatives for MFCs because of their meso/microporous 3D structures, high electron transfer rate and the achievable high kinetics of electroactive bacterial community [41]. Majority of the recently developed highly porous 3D anode materials utilised natural material LCC as an inexpensive and high-performance anode material, usually prepared from recycled paper by carbonisation [22,41,50,51].

High performances have also been achieved with 3D anodes based on the three-dimensional growth of exoelectrogens. Better anode kinetics can be accomplished by increasing the anode surface area, but the performance only improves when a reaction occurs at the triple phase boundary, i.e., anode, cathode and electrolyte with lower internal resistance. To minimise the internal resistance of the system [52], Chen et al. [53] developed an anode from Kenaf

(*Hibiscus cannabinus*) stem by using heat dry carbonisation at 1000°C under N₂ environment. The resulting material was connected to a stainless steel wire to make a complete anode electrode. Kenaf contains a natural 3D structure in its stem, so it offers a mesoporous ordered structure for the growth of biofilm, and also the electrical conductivity is sufficient to consider it as a suitable electrode material. A piece of Kenaf of 10 mm diameter and 15 cm in length had only 10 Ω resistance. It also exhibits a power density three times higher than that of graphite under the same experimental conditions [22,52]. It has also been reported that carbonised king mushroom, wild mushroom and corn stem exhibited good electrode properties [50]. Interestingly, carbonised corn stem exhibits 8 times better performance than plane graphite electrode. Figure 1.5 shows some of the natural materials such as (a, b) king mushroom, (c, d) wild mushroom and (e, f) corn stem that has been used as anode materials for MFCs. The scanning electron micrographs of these materials indicate that they have high porosities and large surface areas/roughness [41].

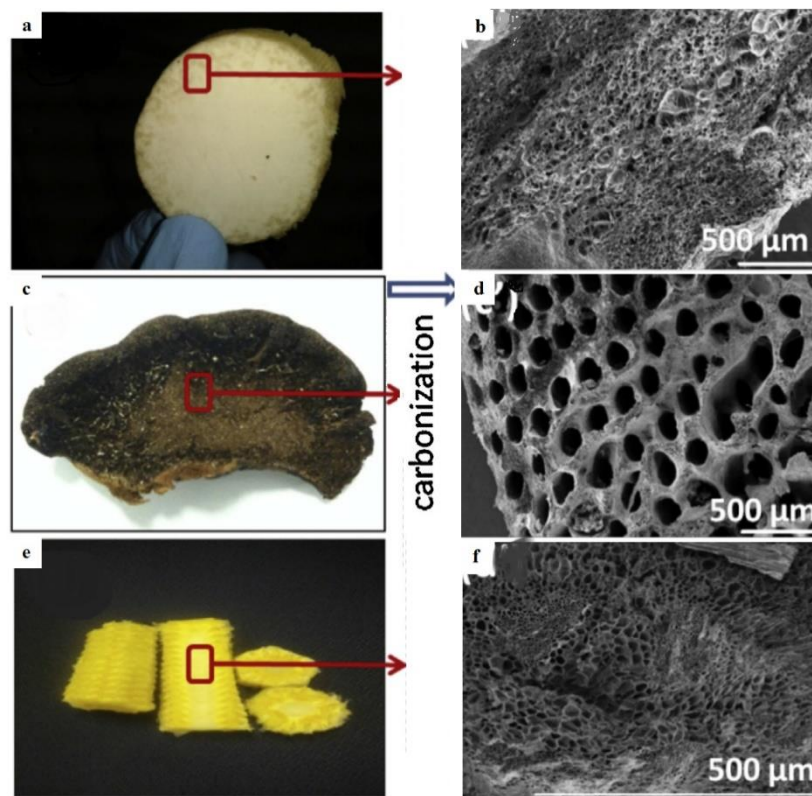


Fig. 1.5 Some Natural materials that have been considered as anode materials in MFC systems [a, b] king mushroom, [c, d] wild mushroom and [e, f] corn stem. FE-SEM micrographs after carbonization [b,d,f]. Reproduced from [41].

Similarly, prepared bamboo charcoal has also been found to exhibit excellent electrode properties compared to a conventional graphite rod. Figure 1.4b shows the SEM image of a

bamboo charcoal tube surface which was very rough with many visible cracks [51]. Nevertheless, some of the observed advantages of this electrode material include low internal resistance, better biocompatibility and a rougher surface which promoted biofilm adhesion. It was evident from the results obtained in a recent study [51] that the introduction of C=N bonds facilitates electron transfer from bacteria to the anode. Consequently, the bamboo charcoal gave 50% better performance than a graphite tube [51]. Apparently, the kinetics and performance are improved substantially with the accessibility of high anode surface area to microbes.

The use of granular electrodes for MFCs provides a cost-effective approach for creating high surface areas that are beneficial for achieving high current and power densities [44]. Activated carbon (AC) granules attached with exoelectrogens are capable of extracting electrons from acetate and storing the electrons in the granules [44]. This behaves like a capacitor where AC granules are charged in a charging column, and the stored charge is harvested from the AC granules in an external discharge cell. During charging of AC granules, cations surround the granules along with charge, making this charging mode form a double-layered capacitor. Consequently, during discharge of AC granules, cations are also released along with the charge, resulting in a local high conductivity which leads to minimal ohmic losses. Also, mass transfer loss is minimised because of the well-mixed system architecture. In general, wastewater with low conductivity does not pose major limitations for use with charging AC granules [44].

Granular activated carbon (GAC) fluidised (with stirring) in an anode chamber results in intermittent contact with GAC and the current collector. It has been demonstrated in a recent study that the maximum power densities produced with and without stirring are 951 mW/m^2 and 813 mW m^{-2} , respectively [48]. Evidently, stirring has a beneficial effect in increasing the power density by 17%, and the results confirmed that the biofilm produced on GAC behaves like a capacitor. The charge stored in the bacterial biofilm and GAC granules is discharged when in contact with the current collector [48].

A recent study [54] has also demonstrated that the capacitance behaviour of the anode is significantly increased with the addition of Fe_3O_4 [54]. Chen et al. proposed a new approach for making an anode for MFC, based on the use of porous carbon with defined pore size. It was demonstrated that the achieved performance of the MFCs was four times better than obtained with the use of a pristine carbon felt anode [47].

Layered corrugated electrode, produced from the carbonisation of one of the most abundant packing materials, was found to be the best performing anode among all carbon-based anodes. The achieved current densities were 200 A m^{-2} and 390 A m^{-2} from three and six corrugated

layers, respectively [22]. This is the least expensive and high-performance material for MFC construction.

1.2.1.2 Synthetic anode materials

It has been demonstrated that three-dimensional nonwoven carbon fibre prepared by electrospinning and solution blowing (Fig. 1.6a) can achieve a maximum current density up to 30 A m^{-2} [53]. The occurrence of inter-fibre junctions as crosslinking points are evident in Figure 1.6 a, and these are important for providing an additional improvement of performance. Figure 1.6 (b-d) shows the images/pictures of a graphite rod, carbon fibre veil, and graphite fibre brush anode before biofilm formation. A 3D interlaced carbon yarn anode in a stainless steel frame with double sided air cathode developed by Sonawane et al. is shown in Figure 1.6e. The performance of MFCs based on these 3D materials also depends on the system architecture [40]. Double-sided air cathode helps to reduce mass transfer limitations. With this design, a stainless steel frame has been used as a current collector and as a support for the carbon fibre in the 3D matrix [40]. In a recent study [46], it was demonstrated that a Logan Carbon brush anode with an improved version of the multi-brush carbon anode (Fig. 1.6f) achieved an excellent power generation [46]. However, the power generated is similar to that achieved with a single brush carbon anode (Fig. 1.6d) MFC system because of cathodic limitations [42].

Liu et al. gave a comparative account for carbon-based anode materials, such as graphite, polycrystalline carbon rod (Fig. 1.6b), carbon fibre veil (Fig. 1.6c), graphite foil, glossy carbon rod and carbon paper. The maximum achievable current density was estimated by using a well-established biofilm enriched with domestic wastewater. Both graphite and polycrystalline carbon rods achieved catalytic currents of about $500 \mu\text{A cm}^{-2}$ at 30°C . In contrast, carbon fibre veil or carbon paper-based material gave $\sim 40\%$ higher current than achieved with graphite rod due to their large accessible surface for microbes [15]. The rotation of carbon brush anodes used in tubular MFC achieved 2.7 times improvement in performance than achieved with a steady state reactor [42]. The rotation was effective for achieving adequate nutrient mixing and for minimising mass transport limitation [42].

In general, several studies have indicated that the kinetics of biocatalyst was influenced by nature and electrode material [43]. It has also been demonstrated that the internal resistance is one of the important factors which affect the overall performance [55].

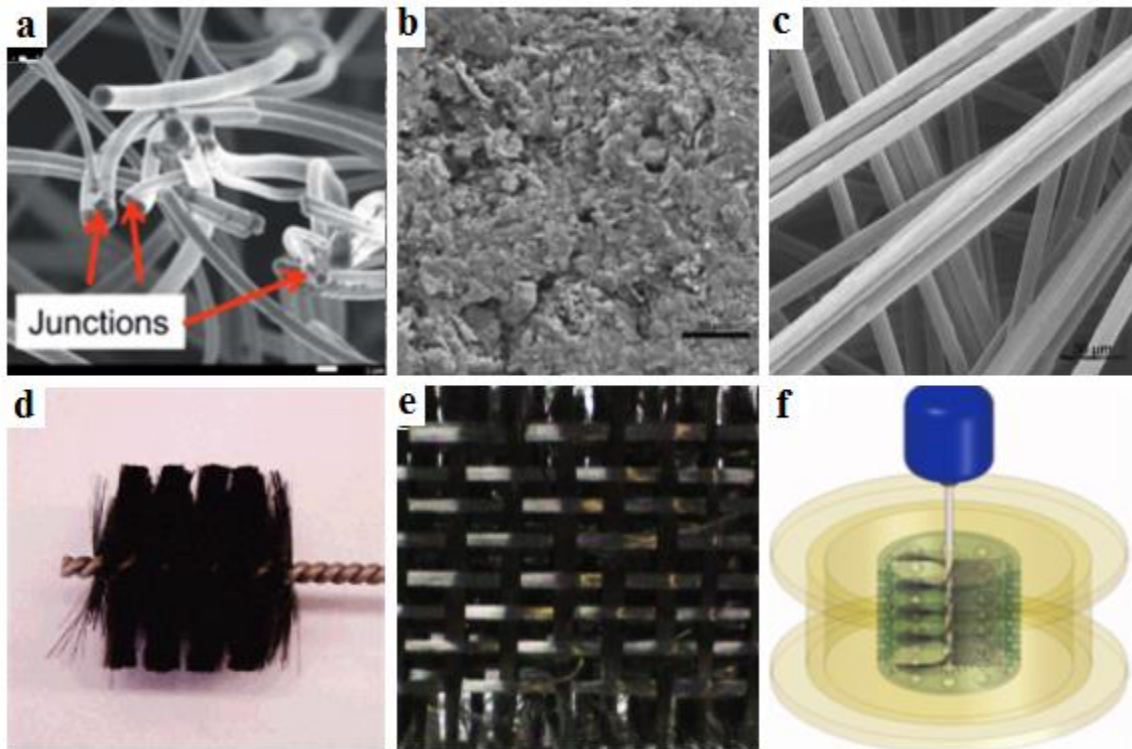


Fig. 1.6 SEM images of artificial 3D anode [a] electrospun and solution blown three-dimensional carbon fiber nonwovens, [b] polycrystalline carbon rod, [c] carbon fiber veil pictorial presentation of artificial 3D anode structures, [d] graphite fiber brush anode, [e] interlaced carbon yarn with stainless steel, and [f] rotating spiral carbon bush anode. Reproduced [a] from [53], [b] and [c] from [15], [d] from [14], [e] from [40] and [f] from [42].

There has been an increasing preference for using three-dimensional anode structures, such as carbon nanotubes (CNTs), carbon nanofibers (CNF), gold/poly (ε-caprolactone) microfiber (GPM), and gold/poly(ε-caprolactone), for reducing the internal resistance of MFCs. 3D anode material exhibit lower internal resistance than macroscopic and two-dimensional anodes [43]. Such anode materials are beneficial in increasing the nutrient/proton/oxygen transfer efficiency through the biofilm than with macroscopic carbon paper and planer gold anodes. It has been demonstrated that the chemical surface modification of CNT- and CNF-based anodes lower kinetic losses and cellular toxicity [43]. Ren et al. [56] investigated three different CNT-based electrode materials, namely: vertically aligned CNT (VACNT), randomly aligned CNT (RACNT), and spin-spray layer-by-layer (SSLbL)-CNT. The chosen nanotube-materials have very high surface areas to volume ratio of 4000 m^{-1} . The results revealed that CNT-based materials attracted more exoelectrogens, *Geobacter sp.*, than the bare gold and, consequently, resulted in a thicker biofilm formation. A maximum power generation density of 3320 W m^{-3}

was achieved by using CNTs in a miniature MFC system. This was 8.5 times more than achieved with the 2D-electrode systems [56].

1.2.2 Composite anodes

Composite anodes have attracted considerable interest in recent years. These materials have been used to achieve synergistic effects with two or more materials or by modification of original material, leading to improved anodic kinetics performance. Table 1.2 summarises the high performances achieved for MFC construction with composite anodes. As can be observed from these data, a current density as high as 35.7 A m^{-2} and a power density as high as 3903 mW m^{-2} can be achieved with some of the reported composite anodes. The different classes of composite anodes are discussed in the following sub-sections.

1.2.2.1 Graphite-polymer composites

Tang et al. prepared a 3D anode modified with a nano-structured capacitive layer, which composed of titanium dioxide (TiO_2) and egg white protein (EWP)-derived carbon assembled core-shell nanoparticles. This was integrated into a loofah sponge carbon (LSC) to obtain a high-capacitive 3D electrode, as illustrated in Figure 1.7. The coating of the LSC with TiO_2 and heat treatment resulted in the decoration of its surface with small particles (Fig. 1.7b). The resulting anode produced 201% more power than a graphite anode. The enhanced power output was attributed to the boosted electrochemical capacitance of 3D anodes, and the synergistic effects of TiO_2 and EMP derived carbon, which has good properties, such as high surface area, good biocompatibility, and favourable surface functionalization for extracellular electron transfer [57].

Open-celled carbon scaffold (CS) and carbon scaffold – graphite (CS–GR) anodes have been prepared by carbonising microcellular polyacrylonitrile (PAN) and PAN/graphite composites (PAN–GR) [58]. The PAN-GR were obtained by foaming with supercritical carbon dioxide (Sc-CO_2) as a physical foaming agent. It was demonstrated that the maximum current density obtained with a CS anode was 101 % more than obtained with carbon felt [58]. The improved performance was attributed to the enhanced hydrophilicity and biocompatibility resulting from carbonisation.

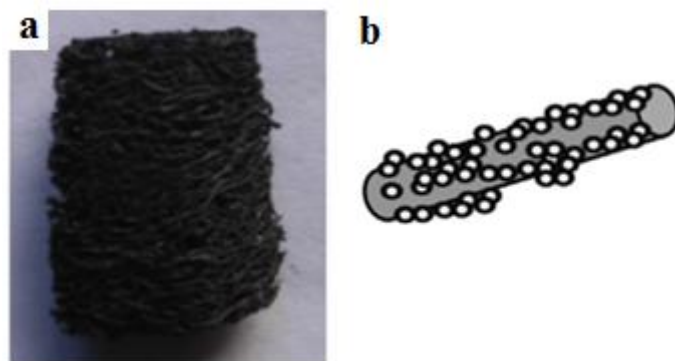


Fig. 1.7 [a] Loofah sponge carbon (LSC) -TiO₂ and [b] photographic image of LSC-TiO₂. Reproduced from [57].

The use of 3D carbon scaffold anode with hydrophilic functional -C=N group for bacterial colonisation was found to improve the extracellular electron transfer [58]. As demonstrated, three-dimensional anodes provide large accessible surface to bacterial biofilm formation [47] and, consequently, for achieving high-performance MFCs.

Carbon nanofibers modified graphite fibres, and reduced graphene oxide/carbon nanotube-coated scaffold are promising new composite anode materials. A maximum current density as high as 35.7 A m⁻² was achieved by using carbon nanofibers modified graphite fibres as anodes for MFC [26]. A power density of 335 mWm⁻³ was obtained from reduced graphene oxide/carbon nanotube-coated scaffold anode system

Composite anode of graphite fibre brush (MFC-GFB) has been used together with graphite granules (MFC-GG) in a tubular MFC to increase the power density achieved by 5.3 and 1.2 times higher than individually with MFC-GG and MFC-GFB, respectively. The enhanced performance of the system was attributed to the dense biofilm formation and low internal resistance of the system [52]. Fraiwan et al. recently compared six types of micro-/nano-structured anodes for use in micro-sized MFCs. The anodes considered include carbon nanotubes (CNTs), carbon nanofibers (CNFs), gold/poly (ε-caprolactone) microfiber (GPM), gold/poly (ε-caprolactone) nanofiber (GPN), planar gold (PG), and conventional carbon paper (CP). The performance of all anodes was tested with compact and reliable micro-liter sized MFC. Table 1.2 provides a comparison of the performance of some of the composite anodes that have been used for MFCs [43]. A homemade coating of the 3D anode was developed by using the iron net as structural support and was anchored to a layer of carbon felt [59]. Power generation was greatly influenced by the ratio of carbon powder and 30% polytetrafluoroethylene (PTFE) solution mixture. The efficiency was tested with an acetate

feed MFC, and the power generation was significantly improved with the coating of the anode. The internal resistance of the system was reduced by 59.4%, while power density increased by 1.5 times compared to the use of a non-coated iron net [59].

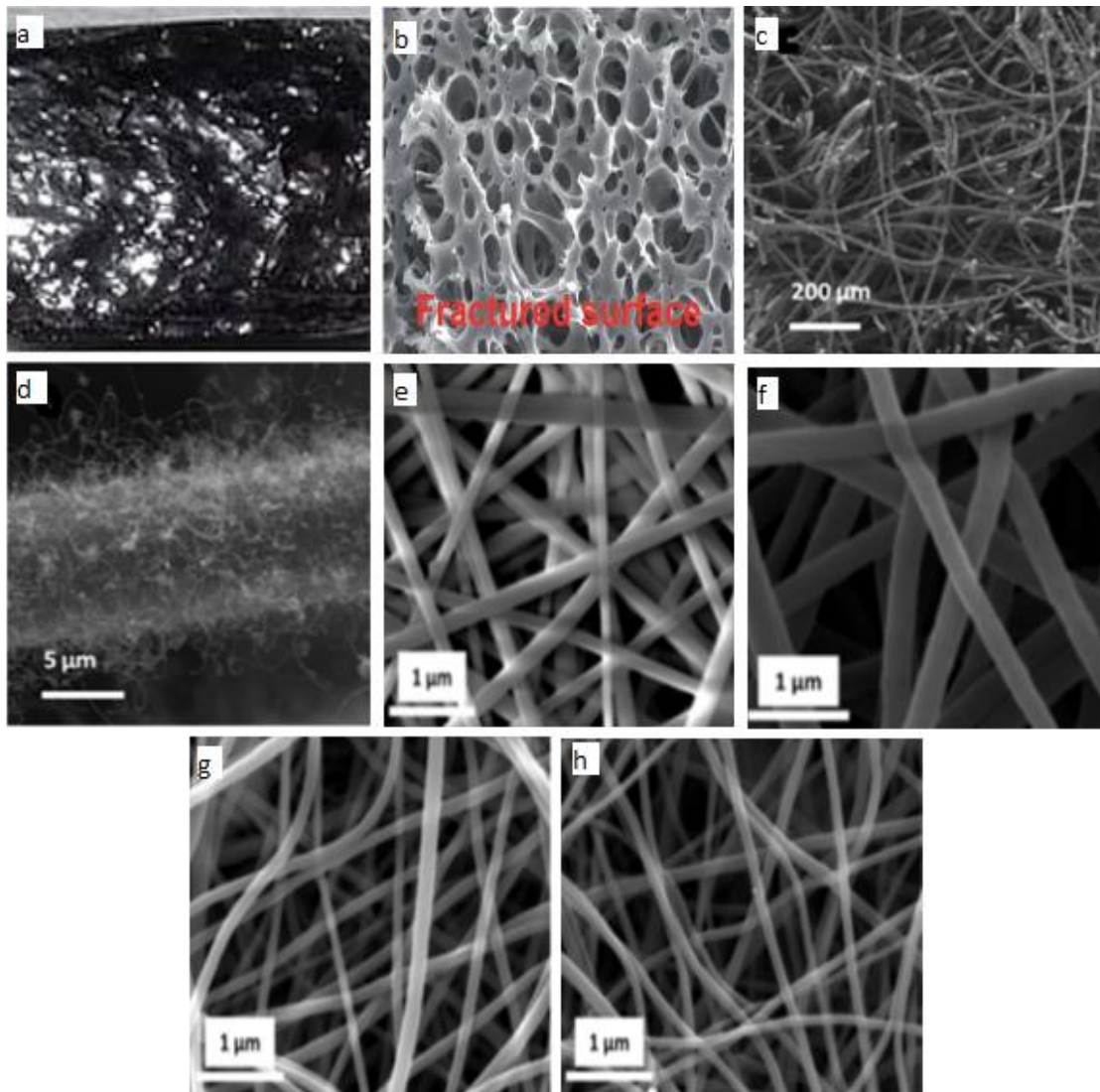


Fig. 1.8 SEM images of composite anodes [a, b] 3D carbon scaffold anodes from polyacrylonitrile, [c, d] carbon nanofibers modified graphite felt, ESEM images of [e] PAN precursor, [f] stabilized PAN, [g] carbon nanofibers (CNF), [h] activated carbon nanofibers nonwoven (ACNFN). Reproduced [a and b] from [58], [c and d] from [26], and [e, f, g and h] from [60].

Figure 1.8 shows the SEM images of some composite anodes with polymers. For example, Fig. 1.8a, b shows the 3D open-celled structure of the carbon scaffold anode which has a diameter of about 5 μm capable of permitting transport of substrate and growth of bacteria colonies that can facilitate extracellular electron transfer from the microorganisms to the anode. Fig. 1.8 (c,d)

also show that the hierarchical micro- / nanostructure displayed by CNFs/GF will also promote the attachment of bacteria to the anode and, consequently, enhance electron transfer simultaneously from the microorganisms to the anode. On the other hand, Fig. 1.8 (e-h) shows the changes in the structure of an electrospun mat as it undergoes stabilisation, carbonisation, and activation.

Table 1.2 Comparison of some reported composite anode materials used for construction of in MFC research

Composite					Performance				
Anode	Cathode	System Architecture	Source of inoculation	Substrate	Anode surface area (cm ²)	I max (A/m ²)	Pmax (mW/m ²)	Reference	
3D carbon scaffold anodes from polyacrylonitrile	Air cathode	Single chamber MFC	<i>Escherichia coli</i>	PO4-buffered basal medium	2	2.91	30.7	[58]	
carbon nanotube-textile	Carbon cloth	H shaped two chamber	Domestic wastewater	Artificial wastewater	2	7.2	1098	[23]	
Carbon nanofibers modified graphite fibres	NA	Three-electrode half-cell	Domestic wastewater	Acetate substrate	1	35.7	NA	[26]	
Multi-walled carbon nanotubes on Poreflon membrane	Carbon cloth	Single-chamber air-cathode	Domestic wastewater	synthetic acetate wastewater	20.25	NA	120.35	[5]	
Carbon nanotube-coated microporous sponge	CNT–Sponge Pt	H shaped two chamber	Domestic wastewater	Domestic wastewater	1	5.2	1240	[50]	
Graphene modified anode	carbon paper	Dual chamber MFC	<i>Escherichia coli</i>	Synthetic medium	26400*	3	2668	[32]	

Graphene-sponges	Air cathode	H shaped two chamber	Wastewater	Glucose medium	NA	1.32	1570	[61]
3D anode modified with a Nano-structured capacitive layer	Air cathode	Single chamber MFC	Activated anaerobic sludge	Acetate medium	3	27	2590	[57]
Up-flow fixed-bed microbial fuel cell	Carbon fibre felt	dual-chamber MFC	Anaerobic digester	Synthetic wastewater	NA	NA	590**	[62]
Coating-type three-dimensional anode	Air cathode	Single chamber MFC	Anaerobic sludge	synthetic acetate wastewater	64	NA	5189.4**	[59]
microporous flexible three-dimensional graphene sponge	carbon paper	Dual-chamber MFC	Anaerobic sludge	Acetate phosphate buffer	9	NA	427**	[39]
reduced graphene oxide/tin oxide nanocomposite	Pt rod	Dual-chamber MFC	<i>Escherichia coli</i>	Synthetic wastewater	6	NA	1624	[63]
graphene/polyaniline nanocomplex modified anode	Carbon felt	Dual-chamber MFC	anaerobic sludge	Synthetic wastewater	4	2.67	1390	[35]
ionic liquid functionalized graphene nanosheets	NA	electrochemical cells	<i>Shewanella oneidensis</i> MR1	NA	NA	2.8	601	[64]
Polyaniline/mesoporous tungsten trioxide	Air cathode	Single chamber MFC	<i>Escherichia coli</i>	Synthetic wastewater	9	3.71	980	[65]
flexible 3D graphene-nickel foam	Carbon cloth	dual-chamber MFC	<i>Shewanella oneidensis MR-1.</i>	Tryptic soy broth medium	10	NA	661000**	[36]

Composite graphite fibre brush and graphite granules	Carbon cloth	Tubular microbial fuel cell	Effluent from Acetate substrate enriched MFC	235**	1.43	66900**	[52]
reduced graphene oxide/carbon nanotube-coated scaffold	Air cathode	dual-chamber MFC	<i>Escherichia coli JM109</i>	Luria-Bertani (LB) broth	NA	335**	NA [33]
Multi-walled carbon nanotube/SnO₂nanocomposite	Pt rod	Dual chamber MFC	<i>Escherichia coli</i>	Synthetic media	0.314	2.9	1421 [66]
a hierarchical porous graphene/nickel (G/Ni) composite electrode	NA	H-shaped MFCs	<i>Shewanella putrefaciens</i>	Luria-Bertani (LB) broth	2	NA	3903 [67]
Graphite coated with manganese oxide/multiwall carbon nanotubes	graphite cathode	Benthic MFC	marine sediment	Natural sea water	16	0.45	109.1 [68]
activated carbon with SSM and Fe₃O₄	Air cathode	single chambered MFC	Effluent from MFC	Acetate substrate	NA	5.51	809 [69]

* cm²g⁻¹ ** mWm⁻³

1.2.2.2 Carbon nanotubes composite

Recently, the use of CNTs has attracted much interest because of their unique, excellent intrinsic properties which include high conductivity, corrosion resistance, high surface area and electrochemical stability [5]. As an example, carbon nanotube-textile (CNT-textile) have been used for development of high-performance MFCs [5,23,58]. The CNT-textile is biocompatible and has high conductivity in nature. The 3D space structure provided by the CNT-textile enables the formation of 10 times more biofilm than with an unmodified textile. Space facilitates an efficient substrate transport of biofilm and internal colonisation of a diverse group of microbial community [23,58]. CNT-textile anode has also been found to produce 10 times less charge transfer resistance (R_{ct}). The achievable maximum current density was 157% higher, while the power density was 68% higher and the energy recovery was 141% greater compared with the use of carbon cloth anode [23]. The CNT-textiles anode is undoubtedly suitable for improving MFC performance. An advanced version of this material is based on coating carbon nanotubes on macroporous sponge [70]. The CNT-sponge has lower internal resistance, improved stability, more ordered continuous 3D CNT surface and tuneable structure with improved mechanical stability. Up to 48%, higher current density has been achieved with the use of CNT-sponge in MFC compared with that obtained with CNT textile under the same conditions [23,70]. The use of nanomaterials in the anode not only improved the power generation but also exhibits tolerance to high substrate concentration. It also enhanced the performance of nanostructured CNFs/GF which enhances extracellular electron transfer from inside of the bacteria to anode hastened by the metabolism of bacteria [26].

He et al. also developed a novel up-flow fixed-bed microbial fuel cell (FB-MFC) using carbon nanotubes (CNTs) as the anode and microbial carriers for continuous treatment of wastewater and electricity generation. The main focus in designing the FBMFC was the achievement of efficient wastewater treatment, while also producing electricity. The maximum removal of chemical oxygen demand (COD) achieved by the reactor was 90%, but it was also observed that the excessive overloading caused significant electricity generation and COD removal [62].

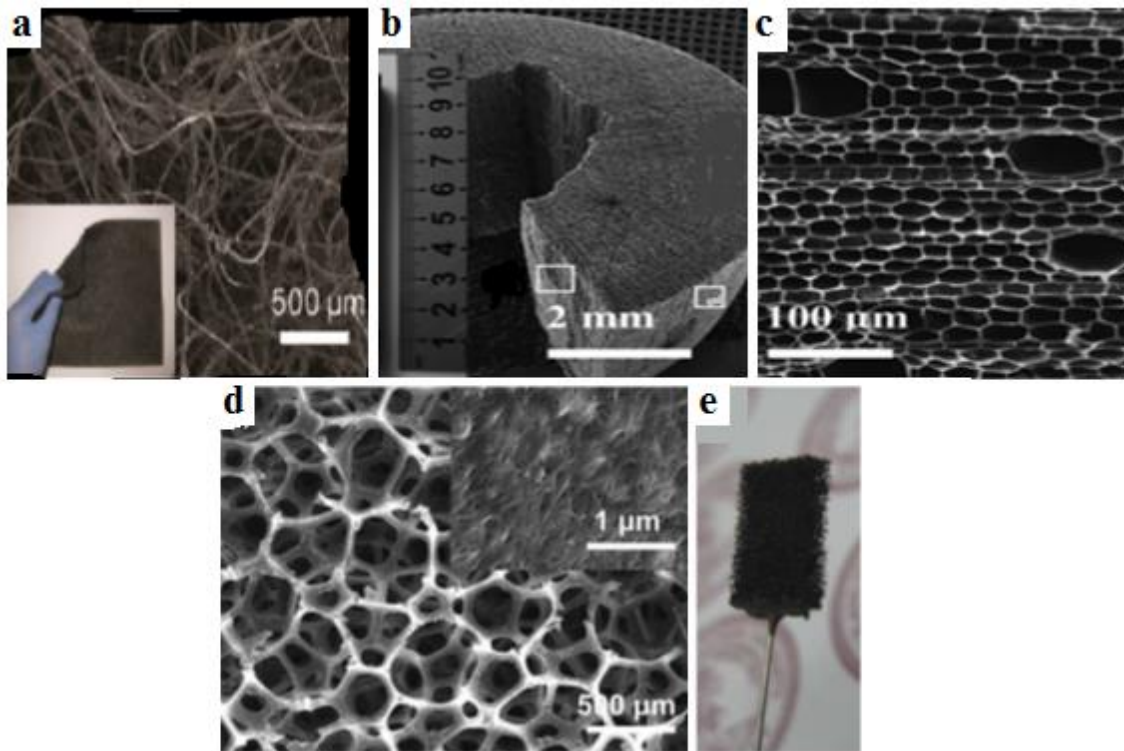


Fig. 1.9 SEM images of some composite anode material. [a] carbon nanotube-textile (CNT-textile) composite, [b] and [c] a 3D-ordered macroporous carbon derived from a natural resource as anode carbon nanotubes (CNT)-sponge electrode, [d] image of the CNT-sponge and [e] picture of a CNT-sponge electrode. Reproduced [a] from [70], [b and c] from [50] and [d and e] from [70].

The use of carbon nanofibers modified graphite fibres (CNFs/GF) composite electrode have also been found to improve performance by up to 7 times better than with the use of unmodified graphite fibres [26]. The activated carbon nanofiber nonwoven (ACNFN) is an ultra-thin, porous interconnected structure with the high bio-accessible surface area. A 3D structure of ACNFN offers maximised surface area for biofilm coverage, and when combined with high macroporosity, it enhanced performance through the reduction of mass transfer limitation [60]. Figure 1.9 shows SEM images of some composite anode material and a picture of a ready to use CNT sponge electrode (Fig. 1.9e). Interestingly, Figure 1.9d shows that the CNT sponge has a uniform macroporous structure and provide a 3-D scaffold capable of colonisation by bacteria,

1.2.2.3 Multi-walled carbon nanotubes composite

Multi-walled carbon nanotubes (MWCNTs) with carboxyl groups have been used for air-breathing MFC and have been shown to exhibit 2-fold enhancement of power density compared

to the use of carbon cloth electrode [5]. In a recent study, multi-walled carbon nanotubes/SnO₂ (MWCNTs-SnO₂/GCE) nanocomposite coated on glassy carbon electrode was employed [66]. The MWCNTs-SnO₂/GCE and bare CGE produced maximum power densities of 1421 mWm⁻² and 457 mW m⁻², respectively [66]. In another study, benthic microbial fuel cells (BMFCs) have been significantly scaled up by application of graphite coated with manganese oxide/multiwall carbon nanotubes composites [68]. The composite offered better hydrophobicity, kinetic activity, and power density when compared to a plane graphite anode. The observed improvement was due to the combined effect of electron transfer shuttle of Mn ions and their redox reactions on the reaction site (i.e., anode and biofilm) [68].

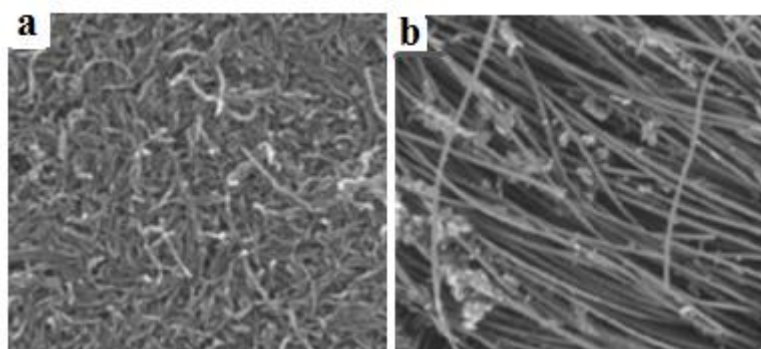


Fig. 1.10 SEM and FESEM images of MWCNTs-based nanocomposite electrodes. [a] MWCNTs on Poreflon membrane and [b] MWCNTs spray-coated on carbon cloth. Reproduced from [5].

1.2.2.4 Graphene-based anode

Graphene is a 2D crystalline allotrope of carbon which has interesting properties, such as large specific surface area (up to 2600 m²g⁻¹), remarkably high electronic conductivity (7200 S m⁻¹), and incredible mechanical strength, i.e., tensile modulus up to 35 GPa [71,72]. Recent studies have also shown that graphene has good biocompatibility [73,74] and, can, therefore, be considered as a potentially useful anode material for MFCs. It has been reported that the power density of graphene modified stainless steel mesh (GMS) was 18 times larger than obtained with a stainless steel mesh (SSM) anode and was 17 times higher compared with polytetrafluoroethylene (PTFE) modified SSM (PMS) [32]. The substantial enhancement observed in this case was due to the improved surface area of the electrode, better bacterial biofilm adhesion and efficient extracellular electron transfer [32]. The stainless steel (SS) current collector increases electrical conductivity for electrode connections, and the

performance of the system is improved by the SS current collector which reduced the internal resistance of the system.

Chen et al. developed a macroporous flexible 3D graphene sponge using an ice template as the anode. The microporous 3D graphene readily allowed the proliferation of bacteria in a random manner and led to a high biofilm coverage, resulting in an enhanced performance [39]. The cost of producing the graphene sponge (G-S) electrode was \$2000 per m³ and was, therefore, the least cost-efficient by order of magnitude than any commercial graphite-based anode material [61]. In another study, the incorporation of tin oxide (SnO₂) nanoparticles on the surface of reduced graphene oxide (R-GO-SnO₂) was used to achieve power generation which was almost 5 times higher compared with the use of unmodified reduced graphene oxide [63]. Synergistic effects between SnO₂ and graphene, as well as good biocompatibility, were responsible for the much improved bacterial biofilm formation and charge transfer efficiency [63]. Reduced graphene oxide/carbon nanotubes (R-GO-CNTs sponges) melamine sponges using dip-coating method have also been demonstrated to provide a large electrically conductive surface for *Escherichia coli* growth and electron transfer in MFC [33]. Four R-GO-CNT sponges with different thicknesses and arrangements were investigated, but the thinnest one (with a thickness of 1.5 mm) exhibited a superior performance, providing a maximum current density of 335 A m⁻³ [33].

The use of a graphene-polyaniline nanocomposite modified anode has also been proposed and found to achieve 3 times higher power generation than carbon cloth [35]. A significant increment in bacterial loading on the anode surface was observed and could be attributed to the electrostatic interactions between positively-charged ionic liquid (1-(3-aminopropyl)-3-methylimidazolium bromide) functionalized graphene nanosheets (IL-GNS). This improved interaction between bacteria and the anode resulted in the enhanced charge transfer from bacteria to anode [75].

A 3D reduced graphene oxide–nickel (R-GO-Ni) foam has also been used as an anode for MFC through precise deposition of R-GO sheets onto the nickel foam substrate [36]. The R-GO thickness, in relation to the electrode surface area, can be tuned by loading cycles. This macroporous scaffold architecture not only provides a 3D surface for microbial growth but also enhanced substrate transfer in the culture medium. The performance was substantially improved than with the use of nickel foam and other graphite based anode materials [36].

The development of a hierarchical porous graphene/nickel anode (G/Ni) was achieved by using *Shewanella putrefaciens* MFCs, which gave 13-fold higher power density than that of conventional MFC carbon cloth anode [37]. Considering the low cost of porous Ni and the low

weight percentage of graphene (5 %w), this composite electrode offers great promise for the production of high-performance MFCs for larger scale power generation [37].

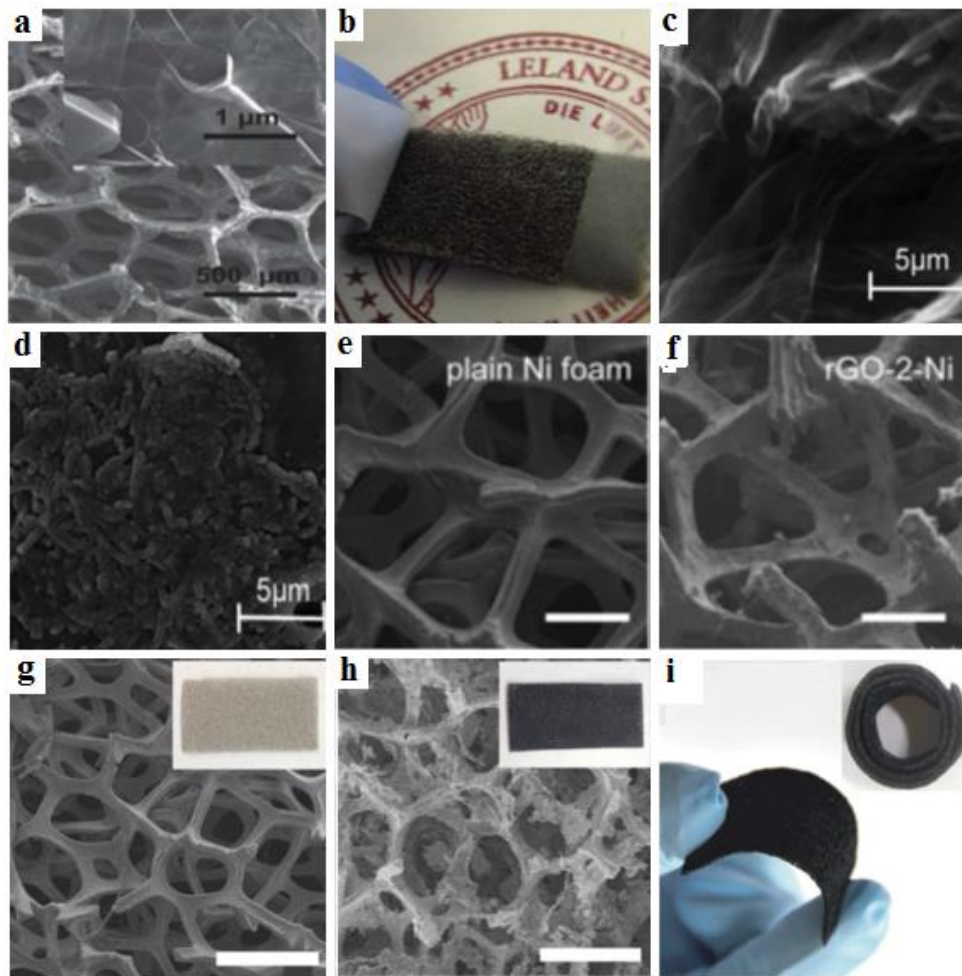


Fig. 1.11 SEM images of [a] graphene-based anodes and [b] graphene-sponge (G-S) composite electrode, [c] bare carbon cloth, [d] RGO-SnO₂/carbon cloth electrode, [e] plain nickel foam, [f] rGO-2-Ni (2 = the number of loading cycles) foams. Scale bars are 200 μm, [g] plain nickel foam, [h] digital pictures (insets) of plain nickel foam and rGO-Ni foam. Scale bars are 200 μm, and (i) digital picture of a curved rGO-Ni foam. Inset: rGO-Ni foam rolled up into a cylindrical shape. Reproduced [a, b] from [70], [c, d] from [76], and [e, f, g, h, i] from [36].

Some interesting SEM images of graphene-based anodes are shown in Figure 1.11. Notable among these, Fig. 1.11 (c,d) shows a comparison of bare carbon cloth (CC) with R-GO-SnO₂/CC electrodes that have been incubated with bacteria [63]. The presence of R-GO and SnO₂ in the latter was obvious. Figure 1.10e shows that Ni foam had a smooth surface before R-GO sheets were loaded (Fig. 1.11f). More clearly, Figure 1.10g shows that a continuous 3D

scaffold of Ni foam with variable pore size was formed. This microstructure, particularly those with the large pore size, will promote colonisation of the inner structure with bacteria and, consequently, enable efficient nutrient transfer [36]. Fig. 1.11h shows that refluxing the Ni foam in GO solution led to coverage of the whole foam scaffold with R-GO sheets. As a result, a conducting R-GO coating was formed, and this could serve as a good electron transfer layer, while also enabling colonisation by bacteria and achieving improved power generation [36]. Furthermore, Fig. 1.11i shows that the R-GO-Ni foam maintains the mechanical properties of the Ni skeleton which is flexible and can be bent or fold into different shapes to suit different MFC designs.

1.2.3 Surface modified anodes

The electrode surface plays a significant role in the overall anode quality and performance. Recently, many studies have reported that surface modification is beneficial for achieving high surface areas for bacterial adhesion and enhanced biocompatibility which favours the kinetics of electron transfer. A summary of some of the reported surface modified anodes is provided in Table 1.3. In general, surface modification with TiO₂-carbon cloth nanofiber mats achieved the best current density of 8 A m⁻², while the best power density of 1574 mW m⁻² was achieved with a surface modified with carbon nanotubes and a conducting polymer coating. The two extensive surface modifications that are commonly used are polymer coating and graphite/carbon surface treatment. Both of these types of surface modification are discussed in the following sub-sections.

Table 1.3 Comparison of the performance of some surface modified anodes in MFC

Surface modification				Performance						
Anode	Cathode	System Architecture	Source of inoculation	Substrate	Anode surface area (cm ²)	I max (A/m ²)	Pmax (mW/m ²)	Reference		
TiO₂-C/C dual nanofiber mats	NA	Three electrode half cell	<i>Escherichia coli</i> K12	Luria Bertani broth	NA	8	NA	[17]		
MCM-41† on graphite felt	Graphite felt	Dual-chamber MFC	Anaerobic digester sludge	Synthetic wastewater	1.5	NA	71.8	[77]		
NaX‡ on graphite felt	Graphite felt	Dual-chamber MFC	Anaerobic digester sludge	Synthetic wastewater	1.5	NA	215	[77]		
Polyaniline modified stainless steel fiber felt	Carbon felt	H-shaped two-chamber	Domestic wastewater	Synthetic wastewater	3.24	1.15	347	[28]		
Vertically Aligned Carbon Nanotubes	Air cathode	miniaturized microbial fuel cell	Anaerobic digestion Sludge	Acetate medium	NA	0.87	270	[56]		
Randomly Aligned Carbon Nanotubes	Air cathode	miniaturized microbial fuel cell	Anaerobic digestion Sludge	Acetate medium	NA	1.81	540	[56]		
Spin-Spray Layer-by-Layer Carbon Nanotubes	Air cathode	miniaturized microbial fuel cell	Anaerobic digestion Sludge	Acetate medium	NA	2.59	830	[56]		
Gold/poly(e-caprolactone) microfiber	Gold foil	Micro-liter size MFC	primary clarifier influent	Acetate mineral media	0.28	0.248	65	[43]		

Gold/poly(e-caprolactone) nanofiber	Gold foil	Micro-liter size	primary clarifier	Acetate mineral	0.28	0.117	29	[43]	
		MFC	influent	media					
Nano goethite into activated carbon on stainless steel mesh	Air cathode	single chambered	Effluent from	Synthetic wastewater	12.5	NA	693	[78]	
		MFC	MFC						
Activated carbon nanofiber	Air cathode	single chambered	Wastewater plant	Wastewater	3	2715**	758**	[60]	
		MFC							
surface modification of carbon mesh	Air cathode	single chambered	anaerobic sludge	Glucose phosphate	7	NA	419	[19]	
		MFC		buffer solution					
Nanostructured polyaniline-coated anode ×	platinum rod	Dual-chamber	<i>Escherichia coli</i>	Glucose containing	NA	1.4	820	[76]	
		MFC		synthetic media					
carbon veil modified with a micro-porous layer	Air cathode	single chambered	Activated sewage	human urine	4.9*	NA	60.7	[79]	
		MFC	sludge						
carbon cloth modified with a micro-porous layer	Air cathode	single chambered	Activated sewage	human urine	4.9*	NA	50.6	[79]	
		MFC	sludge						
stainless steel fibre felt	Carbon felt	H-shaped	two-chamber	Effluent from	Synthetic media	3.24	6.1	2142	[35]
			MFC						
Carbon nanotubes and polyaniline on microporous graphite felt	Carbon cloth	dual-chamber	<i>Shewanella</i>	<i>Synthetic medium</i>	11.25	NA	308	[16]	
		MFC	<i>putrefaciens</i>						
polyaniline networks onto graphene nanoribbons coated carbon paper	NA	H-shaped	dual-chamber	<i>Shewanella</i>	<i>M9 media</i>	4	1.8	172	[64]
				<i>oneidensis MR-1.</i>					

Carbon carbon paper	Nanotube/Polyaniline	carbon paper	dual-chamber MFC	<i>Escherichia coli</i>	Luria bertani broth	80	NA	1574	[24]	
Vertically Nanosheets paper	Oriented Modified Carbon	TiO ₂ Carbon paper	carbon paper MFC	dual-chamber MFC	<i>anaerobic sludge</i>	Synthetic media	9.6	3.25	690***	[80]
Nitric acid treated carbon cloth		Carbon cloth	Dual-chamber MFC	Effluent from MFC	Synthetic wastewater	112	1.31	687	[81]	

† Mobil catalytic materials number 41, ‡ Sodium X zeolite, × Nanostructured, *Cathode surface, ** A m⁻³, *** W m⁻³

1.2.3.1 Conductive polymer coatings

Conductive polymer coatings have attracted considerable attention due to their high conductivity and biocompatibility [76]. Composite polyaniline (PANI)-mesoporous tungsten trioxide (m-WO₃) has been developed and used as a precious metal-free catalyst [65]. PANI was loaded on m-WO₃ via chemical oxidation of PANI. The catalytic activity of the composite was elucidated by using electrochemical techniques. Significant improvement in performance was observed with the composite based on the combination of m-WO₃ and PANI. The m-WO₃ exhibited good biocompatibility, while PANI has a good electrical conductivity [65]. The changes in morphology caused by this combination is illustrated in Figure 1.12. The m-WO₃ displayed a sachima-shaped morphology (Fig. 1.12a) which became less distinct when loaded with PANI (Fig. 1.12b). Nevertheless, the ordered pores and pore size were still evident.

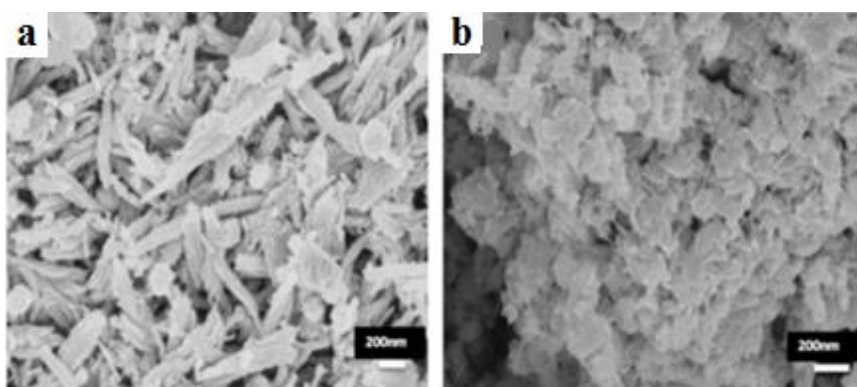


Fig. 1.12 SEM [a] micrographs of m-WO₃ and [b] 20%w PANI/m-WO₃ composite. Reproduced from [65].

Polyaniline (PANI) coated electrodes have been shown to enhance power generation significantly. By using a nanostructured PANI-modified glassy carbon anode, power generation was significantly increased [76]. Measurement by electrochemical impedance spectroscopy revealed that the charge transfer was significantly enhanced by the nanostructured polyaniline coating [76].

The Electrodeposition of PANI networks onto graphene nanoribbons (GNRs)-coated carbon paper (CP/GNRs/PANI) was found to enhance power generation than with the use of GNR and CP [64]. The enhancement was attributed to the positively charged PANI backbone which improved interaction affinity with negatively charged bacterial cells and, thus, enhanced the direct electron transfer via outer membrane cytochromes. Conductive GNRs greatly improved the conductivity of the CP/GNRs/PANI electrode in the neutral medium [64]. This observation indicates that the synergistic effect of both components was responsible for the substantial

improvement in energy generation [64]. Carbon nanotubes/polyaniline carbon paper (CNT/PANI carbon paper) was utilised and compared with other traditional carbon paper/cloth in another study [24]. The results demonstrated that a lower ohmic loss and enhanced power generation was obtained with CNT/PANI carbon paper [24]. Modification of graphite felt (GF) with PANI was followed by the electrophoretic deposition of CNTs. The surface modification resulted in a rough and nano-cilia containing film on the GF. It transformed the surface from hydrophobic to hydrophilic. The use of CNTs increased the surface area for biofilm coverage, as well as for achieving a higher electrical conductivity. The achieved maximum power density of 257 mW m^{-2} corresponds to an increase of 343% and 186%, respectively, when compared with those achieved with the pristine GF MFC and the PANI/GF MFC, respectively [16]. Also, polyaniline modified stainless steel fibre felt (SSFFs) has been found to offer a low activation overpotential which readily resulted in charge transfer at the biofilm and anode interface [28]. Figure 1.13 shows SEM images of the surface modification of anodes. For example, Fig. 1.13 (a, b) shows that the modified stainless-steel fibre felts (SSFFs) have a rough micro-structured surface which is readily conducive to bacteria colonisation and improved interaction between resulting biofilm and the electrode.

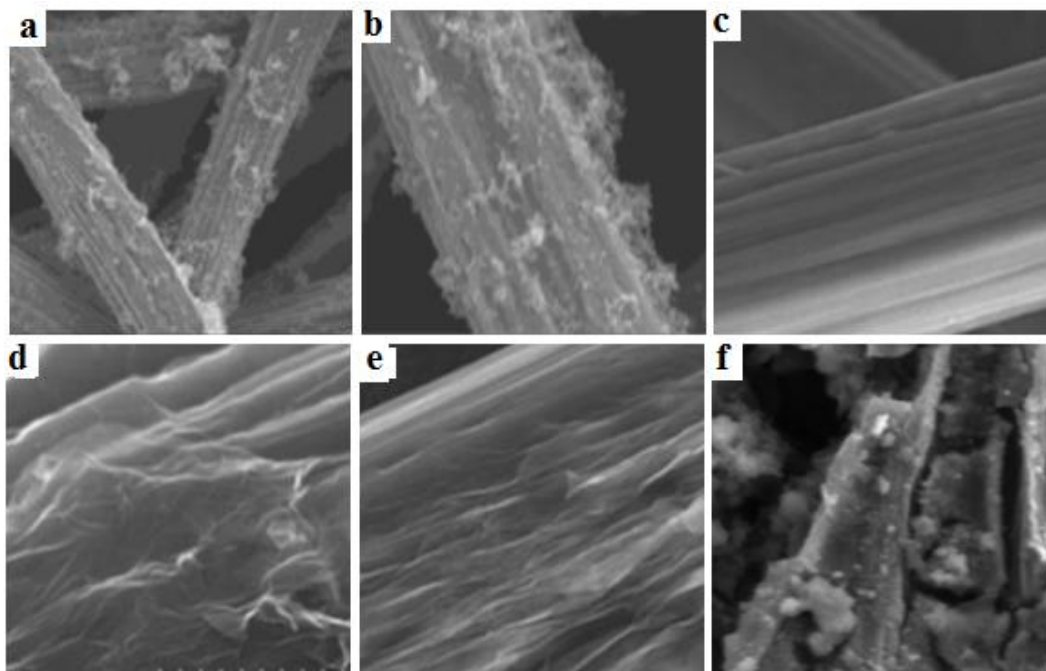


Fig. 1.13 SEM images of the stainless-steel fiber felts (SSFFs) before and after polyaniline modification. [a, b] PANI/SSFF, [c] CP, [d] CP/GNS, and [e] CP/IL-GNS, and [f] CNT/PANI carbon paper electrode. Reproduced [a, b] from [28], [c, d, e] from [82] and [f] CNT/PANI carbon paper electrode. Reproduced [a, b] from [28], [c, d, e] from [82] and [f] from [24].

1.2.3.2 Graphite/carbon surface treatment

Vertically oriented TiO₂ nanosheets modified carbon paper forms vertically penetrating pores that offer a large contact area to bacteria for direct electron transfer [80]. This is particularly helpful for improving nutrient distribution, achieving high biocompatibility and favouring electron transport pathways in a recent study [80]. The maximum power output density of mixed consortia inoculated microbial fuel cell was increased by 63% by employing a TiO₂-NSs/CP as a bioanode, compared with the use of a bare CP as a bioanode. In another study dual nanofiber mats of TiO₂(rutile)-C(semi-grafito)/C(semi-grafito) was used for MFC anode [17], one fibre composed mostly of Ti, O, and C, while the composition of the other fibre was mainly based on C. The dual nanofiber demonstrated a better performance than a single nanofiber. The maximum current density achieved in this study was 8 A m⁻² [17].

In a recent study, two zeolites, namely mobil catalytic materials number 41 (MCM-41) and Sodium X zeolite (NaX), were used to modify graphite felt anodes [77]. The achieved maximum power density and coulombic efficiencies were 152% and 36% higher than those obtained with the unmodified anodes, respectively. The improved performance was due to its microporous structure, super hydrophilicity and enhanced biofilm coverage [77]. Activated carbon (AC) with SSM (AcM) and Fe₃O₄ anode has also been explored for MFCs, and the performance of the system was attributed to the enhancement of capacitance [69]. Nano-goethite with 0, 2.5, 5.0 and 7.5% (mass percentage) were added into the activated carbon (AC) powder and rolled onto stainless steel mesh. The resulting composite anodes produced 36% higher power than with an unmodified AC anode. The increased performance was achieved because of decreased charge transfer resistance (R_{ct}) and increased exchange current density (I_0) [78].

Some studies have demonstrated that MFC start-up time can be lowered by electrochemically oxidizing carbon mesh in nitric acid or ammonium nitrate. It was demonstrated in one study [81] that the anodes modified by this approach achieved a Coulombic efficiency of 71%. Oxygen-containing functional groups present on the carbon surface may be responsible for the improved overall performance of the system [19]. Carbon cloth (CC) anodes treated with concentrated nitric acid and heated in a muffle furnace (CC-H), gave 0.42–0.46 V for CC, 0.52–0.58 V for CC-A and 0.80 V for CC-H across a 1000 Ω resistance. SEM images confirmed that the high biofilm density on CC-H was responsible for the higher voltage and current generation [81].

Also carbon veil (CV) and carbon cloth (CC) modified with a micro-porous layer (MPL) have been used for MFCs and the power generation from the modified anodes almost doubled those achieved with the unmodified electrodes [79].

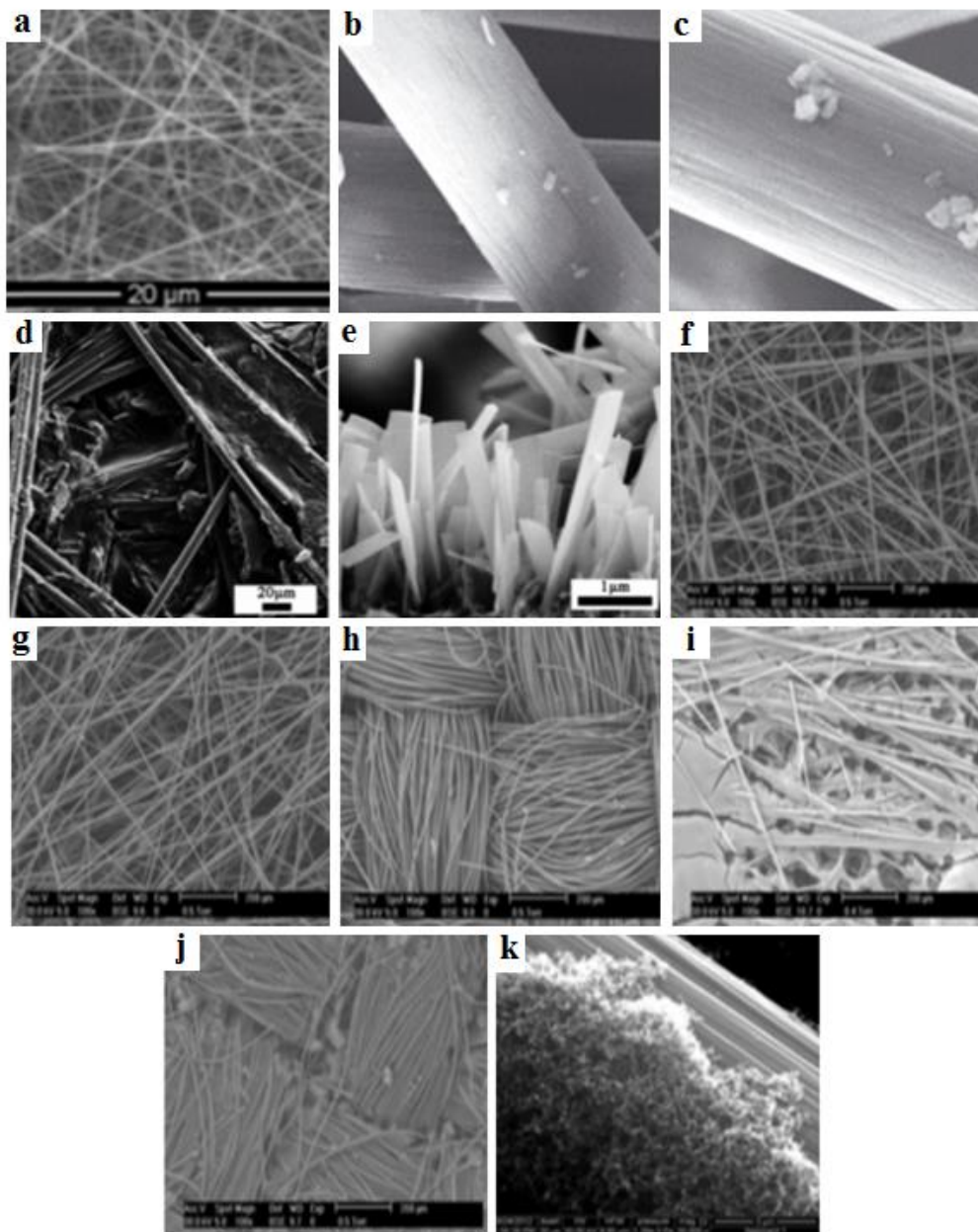


Fig. 1.14 [a] Micrographs of TiO₂-C/C dual nanofiber calcined at 1000°C for 3 h at N₂ atmosphere, [b] MCM-41, [c] NaX, FESEM images of the bare CP electrode, [d] TiO₂-NSs/CP electrode, [e] TiO₂-NSs/CP electrode obtained under optimal conditions, SEM images of electrodes, [f] CV20 (20 layered carbon veil), [g] CV30 (30 layered carbon veil), [h] CC, [i] CV20-MPL, [j] CC-MPL, and [k] MPL structure on CC-MPL. Reproduced [a] from [17], [b, c] reproduced from [77], [d, e] from [80], and [f, g, h, i, j, k] from [79].

The 3D macroporous anodes based on stainless steel fibre felt coating carbon nanoparticles (graphene, carbon nanotube, or activated carbon) on stainless steel fibre felts (SSFFs) provided large accessible surface area for biofilm growth due to their morphologies and structures, as well as interfacial substrate transport. It also offers advantages in terms of kinetics, such as low overpotential and high reactivity [27].

Figure 1.14 shows the SEM images of surface treated anodes. The presence of interconnected and entangled dual nano-fibre which formed a non-woven mat is obvious in Figure 1.14a. On the other hand, Figure 1.14b shows that the carbon fibres were more densely woven on the carbon cloth than on carbon veil (Fig. 1.14 f, h). In contrast, those formed on microporous layered (MPL) surface were uneven and more porous which may result in a better and higher surface area for bacterial growth. Overall, stainless steel fibre felt, carbon nanotube/polyaniline carbon paper, and nanostructured polyaniline-coated anode were some of the high performing anodes based on a surface modification that achieved power densities of 2142 mW m^{-2} , 1574 mW m^{-2} and 820 mW m^{-2} , respectively [35].

1.2.4 Metal-based anode

In the last ten years, many metals such as titanium [10], gold [82,83], and copper [31] have been considered for use as anodes in MFCs. Most of these metals were unsuitable because of their corrosive nature. In contrast, stainless steel has attracted increasing interest for use as an anode material for microbial fuel cells [21]. The performance of some of the reported metal-based anodes are summarised in Table 1.4. Evidently, the performance of stainless steel as an anode material stands out from the rest. Pocaznoi et al. have compared stainless steel anode with carbon cloth and graphite plate for use as anodes for MFC with the use of soil landfill and acetate as substrate. Figure 1.15 shows the ability of carbon and stainless-steel materials to form microbial anodes under identical conditions.

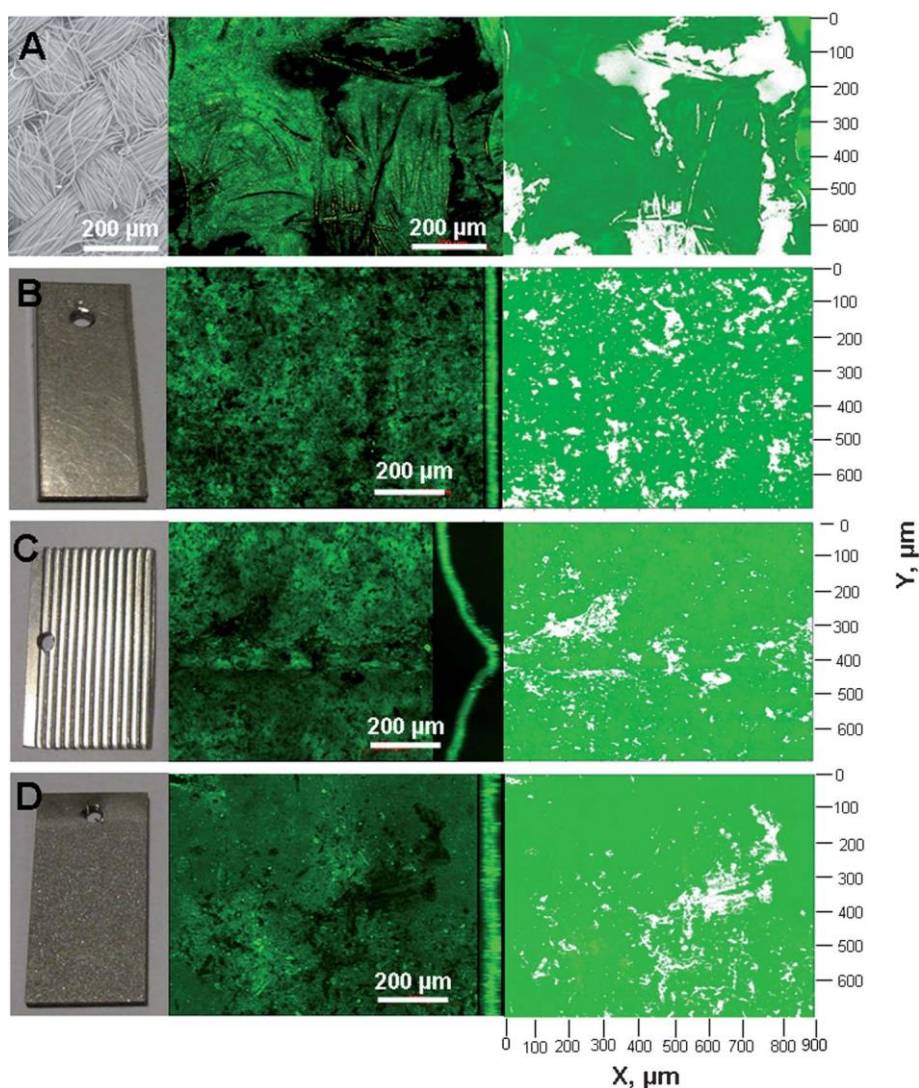


Fig. 1.15 Macroscopic and fluorescence images of anodes with and without biofilms on [a] carbon cloth, [b] smooth stainless steel, [c] macrostructured smooth stainless steel and [d] microstructured smooth stainless steel. Images from left to right are: macroscopic view of the clean electrode, epifluorescence image and treated image for assessment of biofilm surface coverage ratio. Reproduced from [21].

In all cases, the biofilm formation was reasonably uniform with almost complete coverage. This study found that carbon cloth anode produced a current density of 33.7 A m^{-2} , while SS anode produced 20.6 A m^{-2} [21]. The achieved high power with the 3D structure carbon cloth was due to its high surface area. Electrochemical testing of stainless steel at $+0.1 \text{ V vs. SCE}$ provided up to 35 A m^{-2} [21]. It has also been demonstrated that oxidised stainless steel is a more effective anode material, and a facile SS modification gave a current density up to 45.3 mA cm^{-3} at ambient temperature. This is the highest current generation reported to date [29]. From all studies, it is clear that stainless steel is a more efficient and cost-effective anode

material for the future development of MFCs. However, some key factors must still be considered, such as corrosion resistance, and achievable surface area to achieve high-performance MFCs. There is still a lot of room and scope for improvement in metal anode development. Planar gold was found to be the best performing metal anode with a power density of 8000 mW m^{-2} .

Table 1.4 Comparisons of the performance of some metal-based anodes used for MFCs

Metal-based							Performance			
Anode	Cathode	System Architecture	Source inoculation	of	Substrate	Anode surface area (cm ²)	I max (A/m ²)	Pmax (mW/m ²)	Reference	
Stainless steel	NA	Three-electrode cell	Soil leachate		Acetate substrate	2.5	35	NA	[21]	
Oxidised stainless steel	NA	3-pin electrochemical cells	Effluent from MFC		M1 medium	2	0.0453*	NA	[29]	
Bare gold	Air cathode	miniaturized microbial fuel cell	Anaerobic digestion Sludge		Acetate medium	NA	1.11	480	[56]	
Planar gold	Gold foil	Micro-litre size MFC	primary influent	clarifier	Acetate mineral media	0.28 cm ²	0.117	8000	[43]	

* A/cm³

1.3 Challenges and future directions

One of the long-term goals of MFC technology is to advance capabilities that will enable the utilisation of the vast volumes of wastewater that are readily available globally, as a basis for generating alternate large-scale energy. If achieved, this will have the dual benefits of “deriving energy from the problem itself,” while also alleviating the various environmental impacts often associated with wastewater. However, before the operation of a commercial plant can be realised, many challenges are yet to be overcome. To date, the implementation of large-scale MFC technology has been hindered by low power generation and high material costs. Further research is therefore still needed to develop low cost, sustainable, high-performance materials that can be used for the development of efficient MFC systems.

Recent studies have demonstrated that the use of 3D materials for MFC anodes have huge potential for supporting the development of high-performance MFCs in the future because of their demonstrated ability to increase power generation by several orders of magnitude. In this regard, further future consideration must also be given to the development of MFC stacks as a way of increasing the net power generation of MFC systems to the level required for large-scale operation. However, to design efficient MFC stack which can be deployed in wastewater treatment train, further engineering will be required to minimise kinetics losses. Another important consideration is the deterioration of the performance in long-term operation caused by membrane biofouling. To this end, the development or adoption of an adequate method to prevent biofouling of cation exchange membrane becomes an urgent necessity.

1.4. Conclusion

The proper and efficient choice of an anode and the material from which it is made is a critical factor in the effort to achieve high-performance MFCs. The choice of the wrong anode material will render this possibility redundant. As the kinetics of the microbes employed in MFCs are much sluggish than those achievable with a cathode material or cathode catalyst, the use of 3D anodes has been demonstrated to date to be very beneficial and capable of increasing power generation by several orders of magnitude compared with the use of 2D plane anodes. Admittedly, there is still much to be done to improve efficiency further before large-scale power generation from wastewater can be realised. Also, consideration of intrinsic parameters, such as kinetics, internal resistance, surface anatomy and interaction of surface with biofilm, are also necessary.

Further development of new cost-effective and efficient materials are also needed for the construction of new renewable and sustainable MFCs which can be deployed in wastewater treatment plants.

References

- [1] S. Aziz, A.R. Memon, S.F. Shah, S.A. Soomro, A. Parkash, Prototype designing and operational aspect of microbial fuel cell - review paper, *Sci.Int.(Lahore)*. 25 (2013) 49–56.
- [2] S.P. Sukhatme, Meeting India's future needs of electricity through renewable energy sources, *Curr. Sci.* 101 (2011).
- [3] H.-Y. Tsai, C.-C. Wu, C.-Y. Lee, E.P. Shih, Microbial fuel cell performance of multiwall carbon nanotubes on carbon cloth as electrodes, *J. Power Sources*. 194 (2009) 199–205. doi:10.1016/j.jpowsour.2009.05.018.
- [4] Y. Zhao, K. Watanabe, R. Nakamura, S. Mori, H. Liu, K. Ishii, K. Hashimoto, Three-dimensional conductive nanowire networks for maximizing anode performance in microbial fuel cells, *Chem. - A Eur. J.* 16 (2010) 4982–4985.
- [5] N. Thepsuparungsikul, N. Phonthamachai, H.Y. Ng, Multi-walled carbon nanotubes as electrode material for microbial fuel cells, *Water Sci. Technol.* 65 (2012) 1208–1214. doi:10.2166/wst.2012.956.
- [6] H. Liu, R. Ramnarayanan, B.E. Logan, Production of Electricity during Wastewater Treatment Using a Single Chamber Microbial Fuel Cell, *Environ. Sci. Technol.* 38 (2004) 2281–2285. doi:10.1021/es034923g.
- [7] B. Min, B.E. Logan, Continuous electricity generation from domestic wastewater and organic substrates in a flat plate microbial fuel cell., *Environ. Sci. Technol.* 38 (2004) 5809–5814. doi:Doi 10.1021/Es0491026.
- [8] C.I. Torres, A.K. Marcus, H.S. Lee, P. Parameswaran, R. Krajmalnik-Brown, B.E. Rittmann, A kinetic perspective on extracellular electron transfer by anode-respiring bacteria, *FEMS Microbiol. Rev.* 34 (2010) 3–17. doi:10.1111/j.1574-6976.2009.00191.x.
- [9] Microbial fuel cell as new technology for bioelectricity generation: A review, *Alexandria Eng. J.* 54 (2015) 745–756. doi:10.1016/J.AEJ.2015.03.031.
- [10] A. ter Heijne, H.V.M. Hamelers, M. Saakes, C.J.N. Buisman, Performance of non-porous graphite and titanium-based anodes in microbial fuel cells, *Electrochim. Acta.* 53 (2008) 5697–5703. doi:10.1016/j.electacta.2008.03.032.
- [11] X. Wang, S. Cheng, Y. Feng, M.D. Merrill, T. Saito, B.E. Logan, Use of Carbon Mesh Anodes and the Effect of Different Pretreatment Methods on Power Production in Microbial Fuel Cells, *Environ. Sci. Technol.* 43 (2009) 6870–6874. doi:10.1021/es900997w.

- [12] F. Li, Y. Sharma, Y. Lei, B. Li, Q. Zhou, Microbial Fuel Cells: The Effects of Configurations, Electrolyte Solutions, and Electrode Materials on Power Generation, *Appl. Biochem. Biotechnol.* 160 (2010) 168–181. doi:10.1007/s12010-008-8516-5.
- [13] J. Wei, P. Liang, X. Huang, Recent progress in electrodes for microbial fuel cells., *Bioresour. Technol.* 102 (2011) 9335–44. doi:10.1016/j.biortech.2011.07.019.
- [14] B. Logan, S. Cheng, V. Watson, G. Estadt, Graphite Fiber Brush Anodes for Increased Power Production in Air-Cathode Microbial Fuel Cells, *Environ. Sci. Technol.* 41 (2007) 3341–3346. doi:10.1021/es062644y.
- [15] Y. Liu, F. Harnisch, K. Fricke, U. Schröder, V. Climent, J.M. Feliu, The study of electrochemically active microbial biofilms on different carbon-based anode materials in microbial fuel cells, *Biosens. Bioelectron.* 25 (2010) 2167–2171. doi:10.1016/j.bios.2010.01.016.
- [16] H.F. Cui, L. Du, P.B. Guo, B. Zhu, J.H.T. Luong, Controlled modification of carbon nanotubes and polyaniline on macroporous graphite felt for high-performance microbial fuel cell anode, *J. Power Sources.* 283 (2015) 46–53. doi:10.1016/j.jpowsour.2015.02.088.
- [17] N. a. Garcia-Gomez, I. Balderas-Renteria, D.I. Garcia-Gutierrez, H. a. Mosqueda, E.M. Sánchez, Development of mats composed by TiO₂ and carbon dual electrospun nanofibers: A possible anode material in microbial fuel cells, *Mater. Sci. Eng. B.* 193 (2015) 130–136. doi:10.1016/j.mseb.2014.12.003.
- [18] D. Jiang, B. Li, Novel electrode materials to enhance the bacterial adhesion and increase the power generation in microbial fuel cells (MFCs), *Water Sci. Technol.* 59 (2009) 557–563. doi:10.2166/wst.2009.007.
- [19] J. Luo, M. Chi, H. Wang, H. He, M. Zhou, Electrochemical surface modification of carbon mesh anode to improve the performance of air-cathode microbial fuel cells, *Bioprocess Biosyst. Eng.* 36 (2013) 1889–1896. doi:10.1007/s00449-013-0963-x.
- [20] G.G. Kumar, V.G.S. Sarathi, K.S. Nahm, Recent advances and challenges in the anode architecture and their modifications for the applications of microbial fuel cells, *Biosens. Bioelectron.* 43 (2013) 461–475. doi:10.1016/j.bios.2012.12.048.
- [21] D. Pocaznoi, A. Calmet, L. Etcheverry, B. Erable, A. Bergel, Stainless steel is a promising electrode material for anodes of microbial fuel cells, *Energy Environ. Sci.* 5 (2012) 9645. doi:10.1039/C2EE22429A.

- [22] S. Chen, G. He, Q. Liu, F. Harnisch, Y. Zhou, Y. Chen, M. Hanif, S. Wang, X. Peng, H. Hou, U. Schröder, Layered corrugated electrode macrostructures boost microbial bioelectrocatalysis, *Energy Environ. Sci.* 2 (2012) 9769–9772. doi:10.1039/c2ee23344d.
- [23] X. Xie, L. Hu, M. Pasta, G.F. Wells, D. Kong, C.S. Criddle, Y. Cui, Three-dimensional carbon nanotube-textile anode for high-performance microbial fuel cells, *Nano Lett.* 11 (2011) 291–296. doi:10.1021/nl103905t.
- [24] C.-T. Wang, R.-Y. Huang, Y.-C. Lee, C.-D. Zhang, Electrode Material of Carbon Nanotube/Polyaniline Carbon Paper Applied in Microbial Fuel Cells, *J. Clean Energy Technol.* 1 (2013) 206–210.
- [25] H. Song, Y. Zhu, J. Li, Electron transfer mechanisms, characteristics and applications of biological cathode microbial fuel cells – A mini review, *Arab. J. Chem.* (2015) 1–8. doi:10.1016/j.arabjc.2015.01.008.
- [26] Y. Shen, Y. Zhou, S. Chen, F. Yang, S. Zheng, H. Hou, Carbon nanofibers modified graphite felt for high performance anode in high substrate concentration microbial fuel cells, *Sci. World J.* 2014 (2014). doi:10.1155/2014/130185.
- [27] J. Hou, Z. Liu, S. Yang, Y. Zhou, Three-dimensional macroporous anodes based on stainless steel fiber felt for high-performance microbial fuel cells, *J. Power Sources.* 258 (2014) 204–209. doi:10.1016/j.jpowsour.2014.02.035.
- [28] J. Hou, Z. Liu, Y. Li, Polyaniline Modified Stainless Steel Fiber Felt for High-Performance Microbial Fuel Cell Anodes, *J. Clean Energy Technol.* 3 (2015) 165–169. doi:10.7763/JOCET.2015.V3.189.
- [29] P. Ledezma, B.C. Donose, S. Freguia, J. Keller, Oxidised stainless steel: A very effective electrode material for microbial fuel cell bioanodes but at high risk of corrosion, *Electrochim. Acta.* 158 (2015) 356–360. doi:10.1016/j.electacta.2015.01.175.
- [30] M.A. Moqsud, K. Omine, N. Yasufuku, M. Hyodo, Y. Nakata, Microbial fuel cell (MFC) for bioelectricity generation from organic wastes, *Waste Manag.* 33 (2013) 2465–2469. doi:10.1016/j.wasman.2013.07.026.
- [31] X. Zhu, B.E. Logan, Copper anode corrosion affects power generation in microbial fuel cells, *J. Chem. Technol. Biotechnol.* 89 (2014) 471–474.
- [32] Y. Zhang, G. Mo, X. Li, W. Zhang, J. Zhang, J. Ye, X. Huang, C. Yu, A graphene modified anode to improve the performance of microbial fuel cells, *J. Power Sources.* 196 (2011)

- 5402–5407. doi:10.1016/j.jpowsour.2011.02.067.
- [33] H.T. Chou, H.J. Lee, C.Y. Lee, N.H. Tai, H.Y. Chang, Highly durable anodes of microbial fuel cells using a reduced graphene oxide/carbon nanotube-coated scaffold, *Bioresour. Technol.* 169 (2014) 532–536. doi:10.1016/j.biortech.2014.07.027.
- [34] H. Yuan, Z. He, Graphene-modified electrodes for enhancing the performance of microbial fuel cells, *Nanoscale*. 7 (2015) 7022–7029. doi:10.1039/c4nr05637j.
- [35] J. Hou, Z. Liu, P. Zhang, A new method for fabrication of graphene/polyaniline nanocomplex modified microbial fuel cell anodes, *J. Power Sources*. 224 (2013) 139–144. doi:10.1016/j.jpowsour.2012.09.091.
- [36] H. Wang, G. Wang, Y. Ling, F. Qian, Y. Song, X. Lu, S. Chen, Y. Tong, Y. Li, High power density microbial fuel cell with flexible 3D graphene-nickel foam as anode., *Nanoscale*. 5 (2013) 10283–90. doi:10.1039/c3nr03487a.
- [37] Y. Qiao, X.-S. Wu, C.-X. Ma, H. He, C.M. Li, A hierarchical porous graphene/nickel anode that simultaneously boosts the bio- and electro-catalysis for high-performance microbial fuel cells, *RSC Adv.* 4 (2014) 21788. doi:10.1039/c4ra03082f.
- [38] G. Gnana kumar, C.J. Kirubakaran, S. Udhayakumar, C. Karthikeyan, K.S. Nahm, Conductive Polymer/Graphene Supported Platinum Nanoparticles as Anode Catalysts for the Extended Power Generation of Microbial Fuel Cells, *Ind. Eng. Chem. Res.* 53 (2014) 16883–16893. doi:10.1021/ie502399y.
- [39] W. Chen, Y.-X. Huang, D.-B. Li, H.-Q. Yu, L. Yan, Preparation of a macroporous flexible three dimensional graphene sponge using an ice-template as the anode material for microbial fuel cells, *RSC Adv.* 4 (2014) 21619. doi:10.1039/c4ra00914b.
- [40] J.M. Sonawane, E. Marsili, P. Chandra Ghosh, Treatment of domestic and distillery wastewater in high surface microbial fuel cells, *Int. J. Hydrogen Energy*. 39 (2014) 21819–21827. doi:10.1016/j.ijhydene.2014.07.085.
- [41] R. Karthikeyan, B. Wang, J. Xuan, J.W.. Wong, P.K.H. Lee, M.K.H. Leung, Interfacial electron transfer and bioelectrocatalysis of carbonized plant material as effective anode of microbial fuel cell, *Electrochim. Acta.* 157 (2015) 314–323. doi:10.1016/j.electacta.2015.01.029.
- [42] Q. Liao, J. Zhang, J. Li, D. Ye, X. Zhu, B. Zhang, Increased performance of a tubular microbial fuel cell with a rotating carbon-brush anode, *Biosens. Bioelectron.* 63 (2015) 558–

561. doi:10.1016/j.bios.2014.08.014.
- [43] A. Fraiwan, S.P. Adusumilli, D. Han, A.J. Steckl, D.F. Call, C.R. Westgate, S. Choi, Microbial power-generating capabilities on micro-/nano-structured anodes in micro-sized microbial fuel cells, *Fuel Cells*. 14 (2014) 801–809. doi:10.1002/fuce.201400041.
- [44] A. Deeke, T.H.J.A. Sleutels, T.F.W. Donkers, H.V.M. Hamelers, C.J.N. Buisman, A. Ter Heijne, Fluidized capacitive bioanode as a novel reactor concept for the microbial fuel cell, *Environ. Sci. Technol.* 49 (2015) 1929–1935. doi:10.1021/es503063n.
- [45] F. Zhang, X. Xia, Y. Luo, D. Sun, D.F. Call, B.E. Logan, Improving startup performance with carbon mesh anodes in separator electrode assembly microbial fuel cells, *Bioresour. Technol.* 133 (2013) 74–81. doi:10.1016/j.biortech.2013.01.036.
- [46] V. Lanas, B.E. Logan, Evaluation of multi-brush anode systems in microbial fuel cells, *Bioresour. Technol.* 148 (2013) 379–385. doi:10.1016/j.biortech.2013.08.154.
- [47] X. Chen, D. Cui, X. Wang, X. Wang, W. Li, Porous carbon with defined pore size as anode of microbial fuel cell, *Biosens. Bioelectron.* 69 (2015) 135–141. doi:10.1016/j.bios.2015.02.014.
- [48] J. Liu, F. Zhang, W. He, X. Zhang, Y. Feng, B.E. Logan, Intermittent contact of fluidized anode particles containing exoelectrogenic biofilms for continuous power generation in microbial fuel cells, *J. Power Sources*. 261 (2014) 278–284. doi:10.1016/j.jpowsour.2014.03.071.
- [49] J. Zhang, J. Li, D. Ye, X. Zhu, Q. Liao, B. Zhang, Enhanced performances of microbial fuel cells using surface-modified carbon cloth anodes: A comparative study, *Int. J. Hydrogen Energy*. 39 (2014) 19148–19155. doi:10.1016/j.ijhydene.2014.09.067.
- [50] S. Chen, G. He, X. Hu, M. Xie, S. Wang, D. Zeng, H. Hou, U. Schröder, A three-dimensionally ordered macroporous carbon derived from a natural resource as anode for microbial bioelectrochemical systems, *ChemSusChem*. 5 (2012) 1059–1063. doi:10.1002/cssc.201100783.
- [51] Jun Zhang, Tubular bamboo charcoal for anode in microbial fuel cells, *J. Power Sources*. 272 (2014) 277–282. doi:10.1016/j.jpowsour.2014.08.115.
- [52] J. Li, C. Liu, Q. Liao, X. Zhu, D. Ye, Improved performance of a tubular microbial fuel cell with a composite anode of graphite fiber brush and graphite granules, *Int. J. Hydrogen Energy*. 38 (2013) 15723–15729. doi:10.1016/j.ijhydene.2013.05.067.

- [53] S. Chen, H. Hou, F. Harnisch, S. a. Patil, A. a. Carmona-Martinez, S. Agarwal, Y. Zhang, S. Sinha-Ray, A.L. Yarin, A. Greiner, U. Schröder, Electrospun and solution blown three-dimensional carbon fiber nonwovens for application as electrodes in microbial fuel cells, *Energy Environ. Sci.* 4 (2011) 1417–1421. doi:10.1039/c0ee00446d.
- [54] X.H. Peng, X.Z. Chu, P.F. Huang, K. Shan, Improved Power Performance of Activated Carbon Anode by Fe₂O₃ Addition in Microbial Fuel Cells, *Appl. Mech. Mater.* 700 (2014) 170–174. doi:10.4028/www.scientific.net/AMM.700.170.
- [55] A. ElMekawy, H.M. Hegab, X. Dominguez-Benetton, D. Pant, Internal resistance of microfluidic microbial fuel cell: Challenges and potential opportunities, *Bioresour. Technol.* 142 (2013) 672–682. doi:10.1016/j.biortech.2013.05.061.
- [56] H. Ren, S. Pyo, J.I. Lee, T.J. Park, F.S. Gittleson, F.C.C. Leung, J. Kim, A.D. Taylor, H.S. Lee, J. Chae, A high power density miniaturized microbial fuel cell having carbon nanotube anodes, *J. Power Sources.* 273 (2015) 823–830. doi:10.1016/j.jpowsour.2014.09.165.
- [57] J. Tang, Y. Yuan, T. Liu, S. Zhou, High-capacity carbon-coated titanium dioxide core-shell nanoparticles modified three dimensional anodes for improved energy output in microbial fuel cells, *J. Power Sources.* 274 (2015) 170–176. doi:10.1016/j.jpowsour.2014.10.035.
- [58] Y.-Q. Wang, H.-X. Huang, B. Li, W.-S. Li, Novel developed three-dimensional carbon scaffold anodes from polyacrylonitrile for microbial fuel cells, *J. Mater. Chem. A.* 3 (2015) 5110–5118. doi:10.1039/C4TA06007E.
- [59] J. Yu, Y. Tang, Coating-type three-dimensional acetate-driven microbial fuel cells, *J. Biosci. Bioeng.* 120 (2015) 135–139. doi:10.1016/j.jbiosc.2014.12.008.
- [60] S.S. Manickam, U. Karra, L. Huang, N.-N. Bui, B. Li, J.R. McCutcheon, Activated carbon nanofiber anodes for microbial fuel cells, *Carbon N. Y.* 53 (2013) 19–28. doi:10.1016/j.carbon.2012.10.009.
- [61] X. Xie, G. Yu, N. Liu, Z. Bao, C.S. Criddle, Y. Cui, Graphene–sponges as high-performance low-cost anodes for microbial fuel cells, *Energy Environ. Sci.* 5 (2012) 6862. doi:10.1039/c2ee03583a.
- [62] Y. He, Z. Liu, X. hui Xing, B. Li, Y. Zhang, R. Shen, Z. Zhu, N. Duan, Carbon nanotubes simultaneously as the anode and microbial carrier for up-flow fixed-bed microbial fuel cell, *Biochem. Eng. J.* 94 (2015) 39–44. doi:10.1016/j.bej.2014.11.006.

- [63] A. Mehdinia, E. Ziaei, A. Jabbari, Facile microwave-assisted synthesized reduced graphene oxide/tin oxide nanocomposite and using as anode material of microbial fuel cell to improve power generation, *Int. J. Hydrogen Energy*. 39 (2014) 10724–10730. doi:10.1016/j.ijhydene.2014.05.008.
- [64] C. Zhao, P. Gai, C. Liu, X. Wang, H. Xu, J. Zhang, J.-J. Zhu, Polyaniline networks grown on graphene nanoribbons-coated carbon paper with a synergistic effect for high-performance microbial fuel cells, *J. Mater. Chem. A*. 1 (2013) 12587–12594. doi:10.1039/C3TA12947K.
- [65] Y. Wang, B. Li, L. Zeng, D. Cui, X. Xiang, W. Li, Polyaniline/mesoporous tungsten trioxide composite as anode electrocatalyst for high-performance microbial fuel cells, *Biosens. Bioelectron.* 41 (2013) 582–588. doi:10.1016/j.bios.2012.09.054.
- [66] A. Mehdinia, E. Ziaei, A. Jabbari, Multi-walled carbon nanotube/SnO₂ nanocomposite: A novel anode material for microbial fuel cells, *Electrochim. Acta*. 130 (2014) 512–518. doi:10.1016/j.electacta.2014.03.011.
- [67] Y. Qiao, X.-S. Wu, C.-X. Ma, H. He, C.M. Li, A hierarchical porous graphene/nickel anode that simultaneously boosts the bio- and electro-catalysis for high-performance microbial fuel cells, *RSC Adv.* 4 (2014) 21788. doi:10.1039/c4ra03082f.
- [68] Y. Fu, J. Yu, Y. Zhang, Y. Meng, Graphite coated with manganese oxide/multiwall carbon nanotubes composites as anodes in marine benthic microbial fuel cells, *Appl. Surf. Sci.* 317 (2014) 84–89. doi:10.1016/j.apsusc.2014.08.044.
- [69] X. Peng, H. Yu, X. Wang, Q. Zhou, S. Zhang, L. Geng, J. Sun, Z. Cai, Enhanced performance and capacitance behavior of anode by rolling Fe₃O₄ into activated carbon in microbial fuel cells, *Bioresour. Technol.* 121 (2012) 450–453. doi:10.1016/j.biortech.2012.06.021.
- [70] X. Xie, M. Ye, L. Hu, N. Liu, J.R. McDonough, W. Chen, H.N. Alshareef, C.S. Criddle, Y. Cui, Carbon nanotube-coated macroporous sponge for microbial fuel cell electrodes, *Energy Environ. Sci.* 5 (2012) 5265. doi:10.1039/c1ee02122b.
- [71] L. Xiao, J. Damien, J. Luo, H.D. Jang, J. Huang, Z. He, Crumpled graphene particles for microbial fuel cell electrodes, *J. Power Sources*. 208 (2012) 187–192. doi:10.1016/j.jpowsour.2012.02.036.
- [72] D. Li, M.B. Müller, S. Gilje, R.B. Kaner, G.G. Wallace, Processable aqueous dispersions

- of graphene nanosheets, *Nat. Nanotechnol.* 3 (2008) 101–105. doi:10.1038/nnano.2007.451.
- [73] S. Cheng, H. Liu, B.E. Logan, Increased power generation in a continuous flow MFC with advective flow through the porous anode and reduced electrode spacing, *Environ. Sci. Technol.* 40 (2006) 2426–2432. doi:10.1021/es051652w.
- [74] J. Liu, Y. Qiao, C.X. Guo, S. Lim, H. Song, C.M. Li, Graphene/carbon cloth anode for high-performance mediatorless microbial fuel cells., *Bioresour. Technol.* 114 (2012) 275–80. doi:10.1016/j.biortech.2012.02.116.
- [75] C. Zhao, Y. Wang, F. Shi, J. Zhang, J.-J. Zhu, High biocurrent generation in *Shewanella*-inoculated microbial fuel cells using ionic liquid functionalized graphene nanosheets as an anode, *Chem. Commun. Chem. Commun.* 49 (2013) 6668–6670.
- [76] A. Mehdinia, M. Dejaloud, A. Jabbari, Nanostructured polyaniline-coated anode for improving microbial fuel cell power output, *Chem. Pap.* 67 (2013) 1096–1102.
- [77] X. yuan Wu, F. Tong, T. shun Song, X. ying Gao, J. jing Xie, C.C. Zhou, L. xiong Zhang, P. Wei, Effect of zeolite-coated anode on the performance of microbial fuel cells, *J. Chem. Technol. Biotechnol.* 90 (2015) 87–92. doi:10.1002/jctb.4290.
- [78] X. Peng, H. Yu, X. Wang, N. Gao, L. Geng, L. Ai, Enhanced anode performance of microbial fuel cells by adding nanosemiconductor goethite, *J. Power Sources.* 223 (2013) 94–99. doi:10.1016/j.jpowsour.2012.09.057.
- [79] J. You, C. Santoro, J. Greenman, C. Melhuish, P. Cristiani, B. Li, I. Ieropoulos, Microporous layer (MPL)-based anode for microbial fuel cells, *Int. J. Hydrogen Energy.* 39 (2014) 21811–21818. doi:10.1016/j.ijhydene.2014.07.136.
- [80] T. Yin, Z. Lin, L. Su, C. Yuan, D. Fu, Preparation of vertically oriented TiO₂ nanosheets modified carbon paper electrode and its enhancement to the performance of MFCs, *ACS Appl. Mater. Interfaces.* 7 (2015) 400–408. doi:10.1021/am506360x.
- [81] H. Cai, J. Wang, Y.F. Bu, Q. Zhong, Treatment of carbon cloth anodes for improving power generation in a dual-chamber microbial fuel cell, *J. Chem. Technol. Biotechnol.* 88 (2013) 623–628. doi:10.1002/jctb.3875.
- [82] S.R. Crittenden, C.J. Sund, J.J. Sumner, Mediating Electron Transfer from Bacteria to a Gold Electrode via a Self-Assembled Monolayer, *Langmuir.* 22 (2006) 9473–9476. doi:10.1021/la061869j.

- [83] H. Richter, K. McCarthy, K.P. Nevin, J.P. Johnson, V.M. Rotello, D.R. Lovley, Electricity Generation by *Geobacter sulfurreducens* Attached to Gold Electrodes, *Langmuir*. 24 (2008) 4376–4379. doi:10.1021/la703469y.

Aims of study

Triggered global energy crisis today attract the field of renewable bioenergy as one of the approaches to decrease the current global warming crisis. MFCs is very recent development in biotechnology and highly attracting area. The prerequisites for commercialization of MFCs are high performance, and material of construction should be low for example electrodes and membranes.

From the literature review, it is learned that the stainless steel (SS) is the promising electrodes for microbial fuel cells application due to its excellent mechanical strength, good conductivity, high rigidity and stability. The metal-based anodes remain largely unaddressed in the MFC research. The major issues with the use of low-grade SS anodes are relatively poor biocompatibility due to hydrophobic nature, prone to corrosion and 2D nature. However, it can be addressed by using anti-corrosion conductive coatings. For instance, the conductive polymer coating, primarily by polyaniline (PANi) and polypyrrole (PPy) has been tried on carbon and composite based anodes in MFCs. These polymers possess high electron mobility, facile chemical synthesis, stability, biocompatibility, anti-corrosion nature, excellent electrokinetics and sustainability. In particular, the PANi modified anodes have been demonstrated to enhance the microbial adhesion to the surface and consequently the bioelectrocatalytic performance. The SS wool offers compelling advantages such as a very high surface area, low cost, and malleability, which allows it to be moulded to any shape according to the system architecture. The thesis aims at the use of conductive polymers for MFCs electrode preparation application defined below.

- Process optimisation for polyaniline (PANi) and polypyrrole (PPy) modified stainless steel electrodes using electropolymerisation of aniline and pyrrole respectively. Moreover, to be explored in MFCs to study startup time of the reactors with respective electrodes.
- Additionally, it also plans to investigate the effect of external resistance on the kinetics of the Pristine SS, PANi and PPy anodes under various operating conditions such as, under open circuit mode, under optimum external resistance, and with very low resistance
- Further, the developed PANi and PPy anodes are to be explored in air cathode MFCs to study long-term energy production and electrochemical behaviour in synthetic (M9 media) wastewater.
- Apart from the use of PANi in anode modification, PANi coating can be explored as a cathode

to replace conventional platinum air cathode. The optimum aniline polymerisation time and its associated electrochemical performance in terms of exchange current density will be investigated in aqueous proton conductor.

- The optimised PANi loading and Pt cathode will be studied in MFCs for a long time using synthetic (M9 media) wastewater.
- The final and important objective is to develop 12 V MFC stack using stainless steel wool modified with conductive polymer (PANi or PPy) anode. The stack will be run on real landfill leachate collected from local landfill site.

Chapter 2

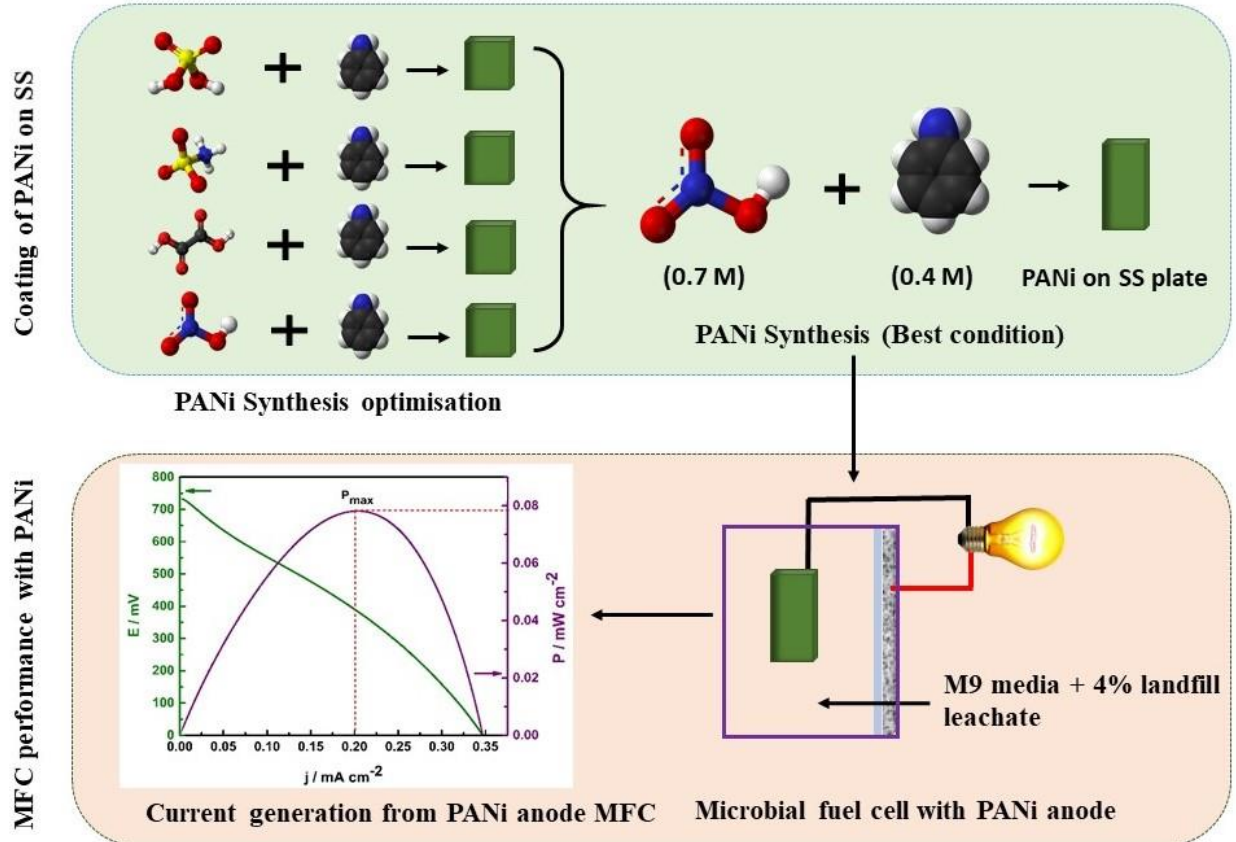
Exploring the use of polyaniline-modified stainless-steel plates as low-cost, high performance anodes for microbial fuel cells

[Published as, J.M. Sonawane, S. Al-Saadi, R.K. Singh, P.C. Ghosh, S.B. Adeloju, Exploring the use of polyaniline-modified stainless-steel plates as low-cost, high-performance anodes for microbial fuel cells, Electrochim. Acta. (2018) 268, 484-493, Elsevier]

Abbreviation:

Ag/ AgCl	Silver/ silver chloride
ANi	Aniline
CV	Cyclic voltammetry
EIS	Electrochemical impedance spectroscopy
FTIR	Fourier transform infrared spectroscopy
j_{max}	Maximum current density
MFCs	Microbial fuel cells
OCV	Open circuit voltage
PANi	Polyaniline
PANi/ GF	Polyaniline graphite felt
PANI/CC	Polyaniline carbon cloth
PANI/CNT	Polyaniline carbon nanotubes
PANI/CNT/CP	Carbon Nanotube/Polyaniline Carbon Paper
PANI _{che} /SSFF	Polyaniline synthesised by chemical polymerisation
PANI _{ele} /SSFF	Polyaniline synthesised by electrochemical polymerisation
P_{max}	Maximum power density
R _{ct}	Charge Transfer Resistance
R _s	Solution resistance
SS-P/PANi	Stainless steel plate coated with polyaniline
SS-P	Stainless steel plate

Graphical abstract



Abstract

The provision of optimum medium for microbial growth and maintenance of long-term stability for microbial fuel cells (MFCs) is very much dependent on the chosen anode material. However, the chosen material must also be readily available and cheap in order to attract wider use and broader adoption of MFCs. In this study, we explored the use of polyaniline (PANi) modified stainless steel plates (SS-Ps) as potential low-cost anodes for MFCs, with capability for effective promotion of microbial growth and retention of long-term stability. Careful and selective choice of acid and aniline concentrations for galvanostatic polymerisation produced highly uniform and adherent conductive PANi coating on SS-P which are desirable for use as anodes in MFC. The resulting PANi modified SS-P (SS-P/PANi) was evaluated as a low-cost anode for MFCs in simulated wastewater which composed of a M9 media and 4% landfill leachate. The SS-P/PANi anode performed efficiently in a MFC, achieving a 13-fold higher current generation than with a pristine SS-P anode during the startup phase. Also, it achieved higher OCV_{max} of 730 ± 42 mV, j_{max} of 0.14 ± 0.12 mA cm^{-2} and a P_{max} of 0.078 ± 0.011 mW cm^{-2} . In comparison, the SS-P anode achieved lower OCV_{max} of 649 ± 37 mV, j_{max} of 0.009 ± 0.011 mA cm^{-2} and P_{max} of 0.010 ± 0.008 mW cm^{-2} . Furthermore, the achieved current and power densities with the SS-P/PANi anode were superior to those obtained with a previously reported PANi modified stainless steel fibre felt (SSFF) anode. Thus, demonstrating the suitability of the SS-P/PANi electrode for adoption as a low-cost, high-performance anode for MFCs.

2.1 Introduction

The current limitations to the widespread use and commercialisation of microbial fuel cell (MFC) technology are high material costs and low efficiency [1]. The development of MFCs faces many challenges at the material level, particularly with the use of relatively expensive electrode materials. Furthermore, at the anode, active electrogenic bacterial communities are required to use their metabolism to break down organic materials and produce electrons [2]. It is therefore highly desirable that the chosen anode material be biocompatible, chemically stable, less prone to corrosion in complex corrosive media, have low activation overpotential and low charge transfer resistance [3].

Pocazoni et al. [4] have recently proposed that stainless steel (SS) be a promising electrode material for the development of highly efficient anodes for MFCs. However, SS possesses many inherent properties that may hinder its use in MFCs for large-scale power generation [5]. For example, in comparison with traditional carbon-based anodes, the biocompatibility of SS is poor, and this often leads to poor electroactive biofilm coverage on SS anode surface. Also, SS has high charge transfer resistance, high activation overpotential, hydrophobic nature, and corrodes in complex media [5]. It has been suggested that these properties of SS can be improved by coating with a conductive polymer such as polyaniline [5–7]. Although the recent use of PANi modified/ composite electrodes have been reported for construction of MFCs for power generation from organic waste matter [8–11], the selection of cheap, widely available material for the anode is still an issue. In an attempt to find a solution, Song et al. [10] developed an inkjet - printing approach for producing conducting and porous PANi/carbon paper anode for MFCs [6]. However, the adoption of such paper-based anode is limited and restricted to limited applications.

Among the materials that have been used with PANi coatings for MFC anodes, the use of PANi modified SS-based anode is uncommon and the basis of their performance is still not well understood. The only one previously reported study [5] modified a SS fibre felt (SSFF) which has a rough surface with PANi by both chemical and electrochemical oxidative polymerisation. The modified anodes gave large electroactive surface area, a biocompatible interface for electroactive bacterial colonisation, enhanced power output and decreased internal resistance [5]. However, the surface roughness of the SSFF may limit the ability to obtain a more uniform and adherent PANi that will ensure optimum performance as an anode in a MFC. We anticipate that further improvement in performance can still be achieved by modifying a stainless-steel plate (SS-P)

which has less or no surface roughness with a more uniform and adherent PANi coating to provide a basis for cheap access to MFC anodes. The consideration of SS-P anode for this purpose is particularly attractive because of its unique intrinsic properties, such as low charge transfer resistant [12], hydrophilic nature [13] and high biocompatibility [14].

The approach chosen for PANi modification of SS can also significantly influence its performance when employed for MFCs. Electrochemical polymerisation of ANi on SS can be achieved by either galvanostatic (applied constant current), potentiostatic (applied constant potential) and potentiodynamic (applied variable potential) polymerisation [9,15]. The conductive nature of the resulting polymer film can be monitored by recording either a chronoamperogram [16,17] or a chronopotentiogram [18,19] during film growth by potentiostatic or galvanostatic polymerisation, respectively, to attain optimum conductivity. The use of galvanostatic polymerisation has particularly been recognised as being more efficient for producing more uniform conductive polymer coatings on objects of variable shapes and dimensions [20]. The conductivity of the coating, as well as its chemical resistance and anticorrosion properties, are also influenced by the chosen monomer, aniline (ANi), concentration and applied current density [21].

In this study, we explored the use of PANi-modified SS-P anode for further improving MFC performance beyond that achieved previously with the SS fibre felt anode [9]. Also, we aim, by this study, to gain a better understanding of the nature and characteristics of the PANi-modified SS-P anode, as well as its specific influence on the MFC performance. This will therefore involve a detailed investigation of the factors that influence the formation of uniform and adherent PANi coatings on SS-P in different acid electrolytes, as well as those affecting their stabilities. The influence of more dynamic PANi coating parameters, such as thickness and choice of polymerisation time on PANi coating longevity on SS-P will also be investigated. Furthermore, an in-depth characterisation of the nature and durability of the PANi coating on SS-P will be conducted by cyclic voltammetry, time-dependent electrochemical impedance spectroscopy, Fourier transformed infrared (FTIR) spectroscopy, and contact angle measurement. Finally, the effectiveness of the PANi-modified SS-P as an anode in a MFC will be investigated in simulated wastewater, and this will include a comparison of the MFC performances of the SS-P anodes with and without PANi modification.

2.2 Materials and methods

2.2.1 Electrochemical cell setup and electrode preparation

The electropolymerisation of ANi was performed with a three-electrode cell assembly. The working electrode is an SS plate with dimensions of 1 x 1.5 x 0.1 cm. The SS sheet was purchased from Ladhani Metal Corporation (Mumbai, India). The SS-Ps were polished using metallographic abrasive paper with grit sizes of 320, 400, 600, 800 and 1200. The SS-Ps were subsequently subjected to ultrasonication for 15 mins in acetone to degrease. The reference electrode was a miniature Ag/AgCl reference electrode (RRPEAGCL, Pine Research Instrumentation, Durham, USA). The auxiliary electrode was a platinum rod. All electrochemical experiments were performed with a BiologicVMP3 potentiostat-galvanostat (BioLogic, Claix, France) fitted with EC-Lab V 10.44 software for data processing. All solutions were purged with nitrogen for 10 mins to remove oxygen before the commencement of polymerisation.

2.2.2 Cathode fabrication

The air cathodes used in this study were fabricated by a previously reported method [22]. A 20% platinised carbon powder, Vulcan XC-72 (Sigma-Aldrich, Australia) was coated on a 10 x 12 cm carbon paper (GDS 210, CeTech, Taichung, Taiwan). A 0.5 mg cm⁻² uniform Pt loading was applied using a 5% Nafion solution as a binder (Sigma-Aldrich, Australia). The electrodes were subsequently placed in a hot air oven to ensure complete drying for six hours. Nafion NRE-212 (Sigma-Aldrich, Australia) were hot-pressed with the electrodes on one side using a hot press (Carver, Inc, Wabash, USA) under 10 kg cm⁻² at 140 °C for 3 min. Fabricated membrane electrode assemblies (MEA) were cut into a size of 3 x 2.5 cm. The cathode was crammed into an acrylic and aluminium mesh (which act as a current collector) in the MFC reactor.

2.2.3 Electropolymerisation of Polyaniline (PANi)

For electropolymerisation of ANi, reagent grade aniline (Sigma-Aldrich, Sydney, Australia.) and various solutions, including sulfuric acid, sulfamic acid, nitric acid and oxalic acid (Sigma-Aldrich, Sydney, Australia) were used. PANi was synthesised by galvanostatic polymerisation of ANi with an applied current density of 2.5 mA cm⁻² (constant current) for 15 minutes in an aqueous acidic solution containing aniline monomer. The chosen current density was optimised by varying between 0.5 and 3 mA cm⁻². The criteria for choosing the optimum applied current density was

based on the achievement of the condition for forming an emeraldine PANi coating, which is highly conducting and stable than other forms of PANi. The use of low current density resulted in the formation of leucoemeraldine - white/clear and colorless $(C_6H_4NH)_n$ and (per)nigraniline – PANi blue/violet $(C_6H_4N)_n$. In contrast, the use of an applied current density of 2.5 and 3 mA cm⁻² gave emeraldine PANi – green for the emeraldine salt, or blue for the emeraldine base $[(C_6H_4NH)_2(C_6H_4N)]_n$. Therefore, we chose an applied current density of 2.5 mA cm⁻² to obtain emeraldine PANi coating on the SS-P.

Four different acids, including sulfamic, sulfuric, oxalic and nitric acids, were used for the growth of the PANi coating on SS-P with varying aniline concentration. Similarly, while keeping the established optimum ANi concentration constant, the concentration of each acid was varied from 0.1 M to 0.7 M to identify their influences on the nature and characteristics of the resulting PANi coatings. The recorded chronopotentiograms during the film growth were analysed to identify the most conductivity film for each acid. The influence of ANi concentration was then investigated from 0.1 M to 0.5 M for the PANi growth while using the identified optimum concentration for each acid. The recorded chronopotentiograms were again analysed to determine the optimum ANi concentration for each acid.

2.2.4 Contact angle measurement and Scanning electron microscopy

Water contact angles of the PANi coating were measured at room temperature (19 °C) and 40% relative humidity, using sessile drop method on a telescopic goniometer C60 (Kino Industry Co. Ltd, Norcross, GA, USA). Each sample was measured three times to ensure good reproducibility. Scanning electron microscopy (SEM) images were also obtained from a FEG-SEM (JSM-7600F) Scanning Electron Microscope (JEOL Ltd., Tokyo, Japan).

2.2.5 Fourier Transform Infrared Spectroscopy (FTIR)

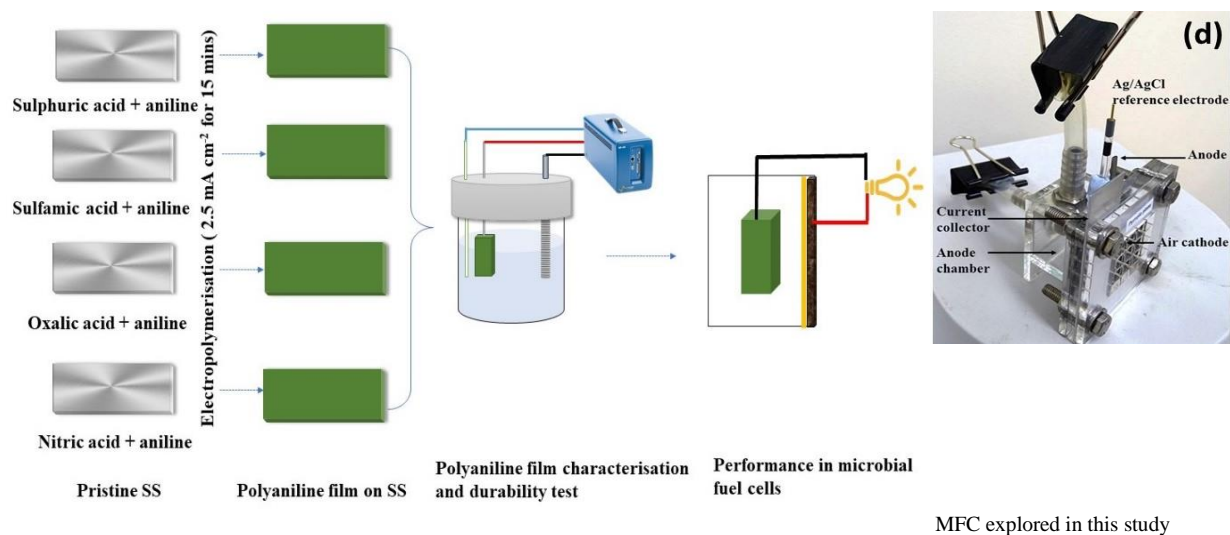
A Vertex 80 (Bruker Corporation, Massachusetts, United States) FTIR spectrometer instrument was used to record FTIR of pristine stainless steel, and PANi coated SS-Ps. FTIR spectra were obtained by attenuated total reflectance (ATR) method with a resolution of 4 cm⁻¹. The wave numbers were in the range of 4000–650 cm⁻¹ for PANi. Baseline corrections were made carefully, and peaks were determined with the aid of an Opus software (Bruker Corporation, Massachusetts, USA).

2.2.6 Time-dependent electrochemical impedance spectroscopy

Time-dependent electrochemical impedance spectroscopy (EIS) and data processing were conducted with a Biologic VMP-3 potentiostat-galvanostat (BioLogic, Claix, France) fitted with EC-Lab V 10.44 software. The change in the charge transfer resistance (R_{ct}) of the PANi coatings on the working electrodes was determined by EIS measurements. This was conducted immediately after immersion of the PANi coated plate in 0.1 M NaCl and measured after every 24 hours for 7 days without any disturbance of the electrochemical cell. The EIS measurement on the working electrode was done at a frequency of 100 MHz to 10 mHz with a sinusoidal perturbation amplitude of 10 mV at 6 points per decade. For EIS data analysis, the equivalent circuits used are shown later in Fig. 2.7a.

2.2.7 Setup and operation of MFCs

The single chamber air cathode MFCs were constructed by using acrylic sheets. In one set of experiment, SS-P anodes without coating were used, while in the other set PANi modified stainless steel plate (SS-P/PANi) were employed. The empty bed volume of each reactor was 27 cm³. The projected surface area of the anodes and air cathodes were 3.5 cm² and 7.5 cm², respectively. For MFC inoculation, 4% landfill leachate (collected from the (Suez Environment, Melbourne, Australia) was added to the synthetic wastewater (M9 medium) which contained acetate (25 mM) as a sole carbon source. The media made up in distilled water contained NH₄Cl: 0.31 g, KCl: 0.13 g, NaH₂PO₄.H₂O: 2.69 g, Na₂HPO₄: 4.33 g, and 12.5 mL of each trace metal and vitamin solutions [23]. The experiments were conducted at room temperature 25 ± 2 °C. The media was purged with N₂ for 30 min before inoculation, and the MFCs were sparged for 10 min after inoculation to increase the primary activity of obligate anaerobes and minimise aerobic oxidation of organic matter.



Scheme 2.1 Schematic for surface modification of SS-Ps with PANi by galvanostatic polymerisation of ANi, characterisation, and exploration of PANi modified SS-P as an anode in a microbial fuel cell.

The MFCs were operated initially in an open circuit mode for two batch cycles to allow electrogenic bacteria to grow on the electrode. After the second cycle, 90% of the media was replenished with fresh media, and then 100 Ω external resistors were attached. All experiments were conducted in triplicates. The MFCs were connected with a data logger (GL-820 Graphtec, Japan) to take readings at 30 mins interval. The overall scheme for the formation of the PANi-modified SS-Ps and their use for MFCs are illustrated in Scheme 2.1.

2.3 Results and discussion

Previous studies of the early stages of PANi formation have revealed progressive nucleation of the films, depending upon the electrolyte concentration and monomer composition, which resulted in different shapes of PANi cluster formation [24,25]. Depending on the monomer concentration, the nucleation process changes from progressive at lower concentrations to instantaneous nucleation at higher concentrations [24]. However, other studies have shown that the nucleation step of PANi also depends on the counter ion of the dopant and type of acid dopant used in the electrodeposition of the polymer which directly affects polymer growth and the associated morphology [26]. It has also been established that the activation overpotential and mass transfer controlled early stage of the PANi growth results in the formation of a compact layer [27]. Given the possible diversity of outcomes in the growth of PANi, it was necessary to carefully consider the influence of the chosen

electrolytes on the nature of PANi coating formed by galvanostatic polymerisation of ANi on SS-P anodes. This is necessary to ensure that the best PANi coating is obtained for use as an MFC anode, and also to serve as a means of gaining a better understanding of the underlying properties through a detailed investigation of the electrochemical and other advanced analytical characteristics.

2.3.1 PANi film formation

2.3.1.1 PANi film formation with sulphuric acid

The galvanostatic polymerisation was used to form PANi coatings on SS plates by varying sulphuric acid concentration from 0.1 M to 0.7 M while keeping ANi concentration constant at 0.1 M. The resulting chronopotentiograms are shown in Fig. 2.1(a). The achieved activation potentials in the presence of acid concentrations ≥ 0.2 M are close to 1.0 V. Evidently, the use of 0.1 M sulphuric acid was unsuitable for forming a conductive PANi film, as the activation potential was as high as 1.5 V. The lowest activation potential was obtained in the presence of 0.3 - 0.7 M sulphuric acid. Considering that 0.3 M sulphuric acid gave the lowest stabilisation potential of 0.646 V, it was chosen as the optimum sulphuric acid concentration for the formation of PANi coating on the SS plates.

Subsequently, the sulphuric acid concentration was kept constant at 0.3 M, while the ANi concentration was varied from 0.1 to 0.5 M. The variation of ANi concentration had no significant effect on the formation of PANi coating on SS [Fig. 2.1(b)]. Consequently, it was established that the use of a monomer solution which contained 0.3 M sulphuric acid and 0.2 M ANi was optimum for effective coating of PANi on the SS plate at an applied current density of 2.5 mA cm^{-2} .

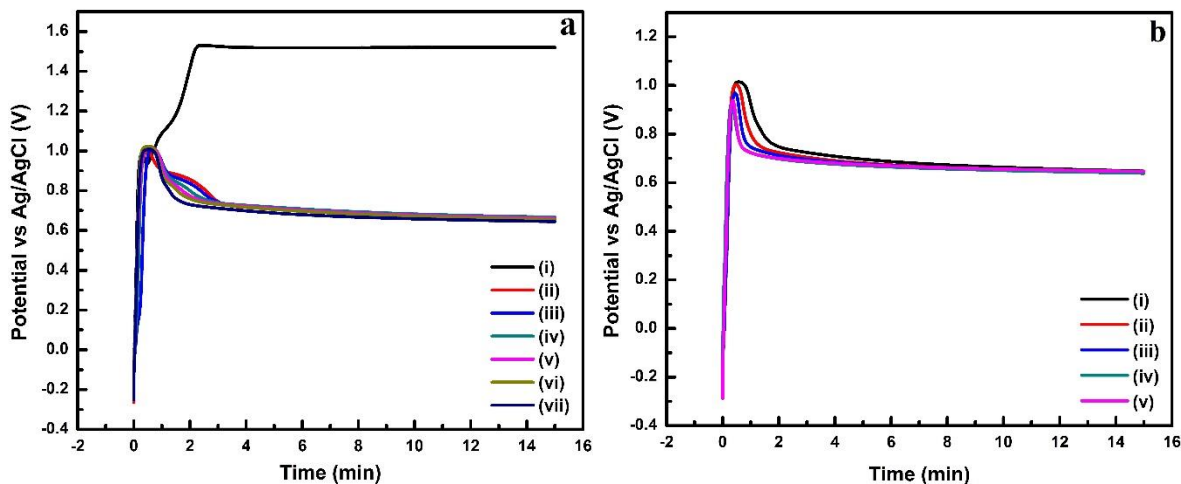


Fig. 2.1 Chronopotentiograms obtained for formation of PANi layer on SS plate with (a) varying sulfuric acid concentration in presence of 0.1 M ANi and (b) varying ANi concentration in presence of 0.3 sulphuric acid. Concentrations of sulphuric acid in (a) are: (i) 0.1, (ii) 0.2, (iii) 0.3, (iv) 0.4, (v) 0.5, (vi) 0.6 and (vii) 0.7 M. ANi concentration in (b) are: (i) 0.1, (ii) 0.2, (iii) 0.3, (iv) 0.4 and (v) 0.5 M.

In a previous study, 0.2 M ANi in 0.4 M sulphur acid was used to form polyaniline-graphene nanocomposite coatings by cyclic voltammetry on SS working electrode between -0.8 – 1.6 V at 0.05 V S^{-1} for ten cycles [28]. The nanocomposite coatings exhibited excellent corrosion resistance in corrosive media [28]. In another study, the electropolymerisation of PANi on SS was carried in 0.5 M and 1 M sulphuric acid under potentiodynamic conditions within a potential range of -0.2 to 1.0 V for various cycles [29]. The PANi film formed on SS was useful for anodic protection in corrosive media [29]. However, in both cases, the required sulphuric acid concentrations were higher than needed for galvanostatic polymerisation in the present study.

2.3.1.2 PANi film formation using sulfamic acid

Galvanostatic polymerisation formed PANi coating on SS by using 0.1 – 0.7 M sulfamic acid, while keeping ANi concentration constant at 0.1 M at an applied current density of 2.5 mA cm^{-2} for 15 mins. The chronopotentiograms obtained during the film formation are shown in Fig. 2.2(a). The observed activation potential in the presence of sulfamic acid was different for each concentration. The lowest activation potential of 0.6 V was observed in 0.7 M sulfamic acid. Non-conducting films were formed when 0.1 - 0.4 M sulfamic acid was used [Fig. 2.2(b)]. The optimum sulfamic acid concentration for forming PANi coating on SS was 0.7 M which gave the lowest stabilisation potential; Consequently, by keeping the sulphamic acid concentration constant at 0.7 M, the ANi concentration was varied from 0.1 M to 0.5 M.

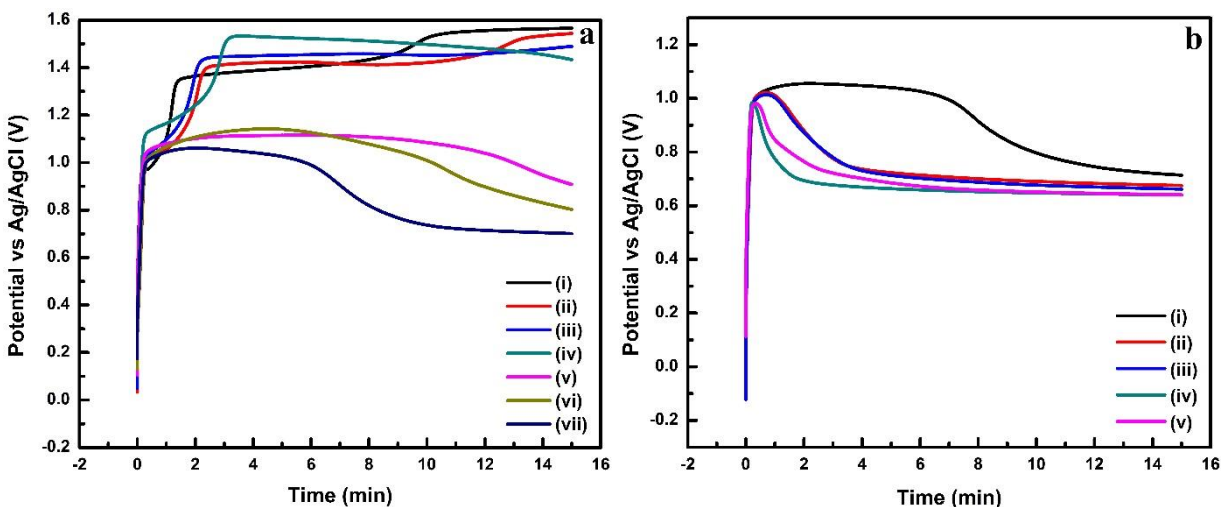


Fig. 2.2 Chronopotentiograms obtained for the formation of PANi layer on SS plate with (a) varying sulfamic acid concentration in the presence of 0.1 M ANi and (b) varying ANi concentration in the presence of 0.7 M sulphamic acid. Sulphamic acid concentrations (a): (i) 0.1, (ii) 0.2, (iii) 0.3, (iv) 0.4, (v) 0.5, (vi) 0.6, and (vii) 0.7 M. ANi concentrations in (b): (i) 0.1, (ii) 0.2, (iii) 0.3, (iv) 0.4, and (v) 0.5 M.

The most stable and conductive PANi film was formed with 0.4 M ANi in the presence of 0.7 M sulphamic acid, as reflected by the lowest activation (1 V) and stabilisation potentials (0.6 V) obtained with the application of a current density of 2.5 mA cm^{-2} . Relatively few attempts have been made to electro-synthesis PANi on stainless steel with sulfamic acid. In a previous study, 0.5 M sulfamic acid was used to synthesise PANi on SS surface by cyclic voltammetry at a scan rate of 20 mV s^{-1} . The potential ranged between -0.30 and 1.40 V in the presence of 0.15 M aniline [30]. In another study, PANi electrodeposition was achieved in 0.1 M ANi and 1 M sulfamic acid by using three different sweeping potentials: i) -0.2 to $+0.8$, ii) -0.2 to $+1.0$, and iii) -0.2 to $+1.4 \text{ V}$ at a scan rate of 20 mV s^{-1} [31]. In both cases, the required ANi concentrations were much lower than needed in the present study for galvanostatic polymerisation. Also, in one case [31], the required sulfamic acid was much higher.

2.3.1.3 PANi film formation with oxalic acid

The galvanostatic polymerisation was also used to deposit PANi coating on SS plate in the presence of oxalic acid. The oxalic acid concentrations were varied from $0.1 - 0.7 \text{ M}$, while keeping ANi concentration constant at 0.1 M . A steady current of 2.5 mA cm^{-2} was applied to achieve electropolymerisation for 15 mins. The effect of variation of oxalic acid concentration is

shown in Fig 2.3(a). Evidently, the obtained activation potentials were high and variable in the presence of 0.1 - 0.3 M oxalic acid, which is indicative of the formation of overoxidised non-conductive films. In contrast, the use of oxalic acid concentration from 0.4 to 0.7 M gave similar activation and stabilisation potentials. Due to the reduced solubility of oxalic acid in water, 0.3 M oxalic acid was chosen. The ANi concentration was subsequently varied from 0.1 M to 0.5 M. Evidently, only 0.5 M ANi gave a high activation potential which led to the formation of the overoxidised film. The resulting chronopotentiograms are shown in Fig. 2.3(b).

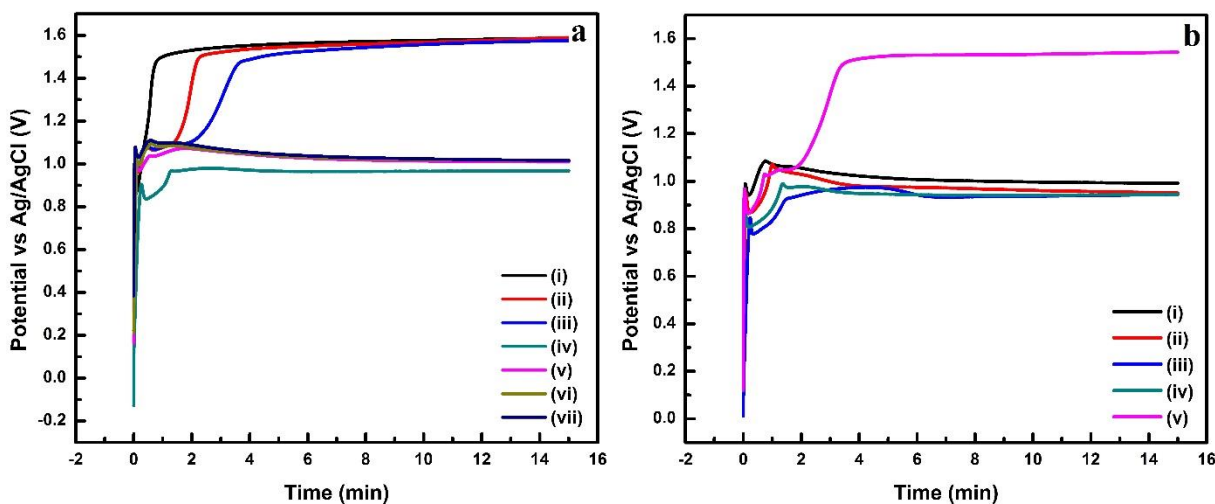


Fig. 2.3 Chronopotentiograms obtained for the formation of PANi layer on SS plate with (a) varying oxalic acid concentration in the presence of 0.1 M ANi and (b) varying ANi concentration in the presence of 0.3 M oxalic acid. Oxalic acid concentrations in (a): (i) 0.1, (ii) 0.2, (iii) 0.3, (iv) 0.4, (v) 0.5, (vi) 0.6, and (vii) 0.7 M. ANi concentration in (b): (i) 0.1, (ii) 0.2, (iii) 0.3, (iv) 0.4, and (v) 0.5 M.

The use of 0.1 M ANi in the presence of 0.3 M oxalic acid enabled the formation of the most stable and conductive PANi film. Few studies have been made on electropolymerisation of PANi with oxalic acid, but none of the studies has validated the wide-ranging effect of ANi concentration on the resulting film. In one study, PANi film was formed by electropolymerisation from 0.1 M aniline containing 0.5 M oxalic acid on an iron rod [32]. In another study, PANi film was deposited on carbon steel by cyclic voltammetry using 0.1M ANi in 0.2 M oxalic acid. at a scan rate of 10 mVs⁻¹ from -0.6 – 1.6 V. [33]. While the required ANi concentration in the previous study is consistent with the one achieved for galvanostatic polymerisation in the present study, the required oxalic acid concentration in one case [32] is notably higher.

2.3.1.4 PANi film formation with nitric acid

Deposition of PANi coating on SS was again accomplished by galvanostatic polymerisation in the presence of a nitric acid with an applied current density of 2.5 mA cm^{-2} for 15 mins. The acid concentration was varied from 0.1-0.7 M while keeping ANi concentration constant at 0.1 M. Fig 2.4(a) shows the effect of variation of nitric acid concentration. Evidently, the achieved activation potentials were high and variable in the presence of 0.1-0.3 M nitric acid, which is indicative of the formation of the overoxidised film. In contrast, the use of 0.4 to 0.7 M nitric acid gave lower activation and stabilisation potentials. Both potentials reduced significantly with increasing nitric acid concentration from 0.4 to 0.7 M. The lowest activation and stabilisation potentials were obtained with 0.7 M nitric acid and was therefore chosen as optimum. With the subsequent variation of ANi concentration from 0.1 to 0.5 M, it was observed that only 0.1 M ANi gave higher activation and stabilisation potentials than with higher ANi concentrations where the activation and stabilisation potentials are lower and very close. The resulting chronopotentiograms are shown in Fig. 2.4(b). Evidently, the use of 0.4 M ANi in the presence of 0.7 M nitric acid gave the best PANi coating.

Table 2.1 summarises the optimum acid and ANi concentrations achieved in this study for obtaining the best PANi coatings on the SS-Ps. Evidently, the highest acid and ANi concentrations required for forming PANi coating on the SS-Ps were obtained with sulfamic and nitric acids, while the least acid requirements were observed with sulfuric and oxalic acids. Although the ANi concentration required for formation of PANi coating with oxalic acid was lower than required with sulfuric acid, the conductivity of the PANi coating (based on stabilisation potential) obtained with the latter was much better.

The largest difference between the activation and stabilisation potential of 393 mV was obtained for the PANi coating obtained with nitric acid, followed by 340 mV with sulfamic acid, 322 mV with sulfuric acid and only 30 mV with oxalic acid. As the change in potential is reflective of the conductivity of the PANi coating, the most conductive coating was obtained with 0.4 M ANi in 0.7 M nitric acid, while the least conductive PANi coating was obtained with 0.1 M ANi in 0.3 M oxalic acid. For this reason, further use and consideration of the PANi coating in this study was based on the use of 0.4 M ANi in 0.7 M nitric acid. The required 0.4 M ANi in 0.7 M nitric acid for achieving optimum PANi coating on SS-P by galvanostatic polymerisation in this study is distinctively higher than 0.1 M ANi in 0.3 M nitric acid [33] and 0.3 ANi in 0.1 M nitric acid [34]

used in previous studies for PANi coating on SS. However, it is important to note that in one of the previous cases, the resulting PANi film was powdery even after curing at 170 °C for ten mins [33], while in the other, the PANi film was brittle, and have low lateral conductivities [34]. These defects can be attributed to the low ANi and acid concentrations used in those studies [34,35]. These observations demonstrate that, when using nitric acid for the growth of PANi coating, the acid concentration must be higher than the ANi concentration to produce the desired uniform and adherent PANi coating. These observations highlight the need for a more careful selection of electropolymerisation conditions for surface modification of SS-P with PANi. Figure 2.4 shows the influence of variation of nitric acid and ANi concentrations on the galvanostatic formation of PANi coating on SS-Ps. Evidently, the conductivity of the resulting PANi coating increased with increasing nitric acid concentration, resulting in increasingly lower stabilisation potential. The lowest stabilisation potential was obtained in 0.7 M nitric acid and which consequently gave the most conductive coating. In contrast, the use of nitric acid concentration between 0.1 and 0.3 M was, as illustrated in Figure 2.1(a), undesirable as they result in the formation of overoxidised PANi coating with poor conductivity. This observation sheds light to the difficulties experienced in previous studies [33,34] in obtaining a uniform, conductive and adherent PANi coating. Such poor quality PANi coating will not provide the desired efficient anode performance in MFC. Figure 2.4(b) demonstrates that under optimum nitric acid concentration, there were only smaller differences in the resulting stabilisation potential and, hence, on the conductivity of the PANi coating when varying ANi concentration was employed. Nevertheless, it was still obvious in this case that the conductivity of the PANi coating increased with increasing ANi concentration, reaching an optimum stabilisation potential between 0.4 and 0.5 M ANi.

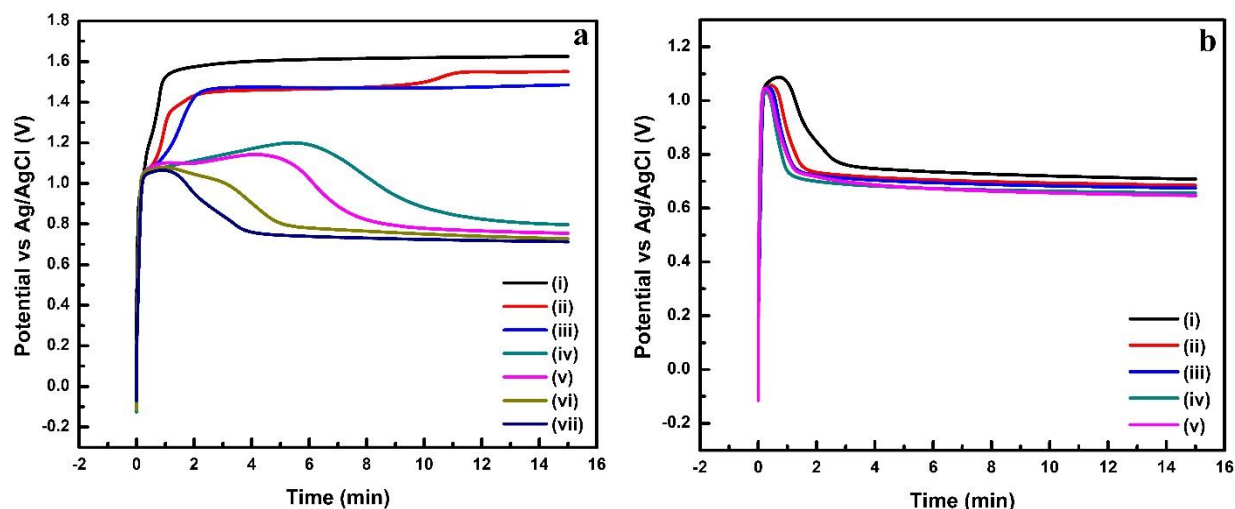


Fig. 2.4 Chronopotentiograms obtained for formation of PANi layer on SS plate with (a) varying nitric acid concentration in the presence of 0.1 M ANi and (b) varying ANi concentration in the presence of 0.7 M nitric acid. Nitric acid concentrations in (a): (i) 0.1, (ii) 0.2, (iii) 0.3, (iv) 0.4, (v) 0.5, (vi) 0.6, and (vii) 0.7 M. ANi concentrations in (b): (i) 0.1, (ii) 0.2, (iii) 0.3, (iv) 0.4, and (v) 0.5 M.

Table 2.1 Optimum activation and stabilisation potentials obtained for PANi formation on SS plate from different acids and ANi concentrations.

Acids	Concentration (M)	ANi Concentration (M)	Activation Potential (E_a/V)	Stabilisation Potential (E_s/V)
Sulfuric acid	0.3	0.2	0.968	0.646
Sulfamic acid	0.7	0.4	0.980	0.640
Oxalic acid	0.3	0.1	0.974	0.944
Nitric acid	0.7	0.4	1.04	0.647

2.3.2 Characterisation of PANi coatings

2.3.2.1 Cyclic voltammetry

Figure 2.5 shows the cyclic voltammogram obtained for the PANi-modified SS-P in 0.7 M nitric acid at a scan rate of 5 mV s^{-1} . Evidently, the cyclic voltammogram produced peaks that are attributed to different oxidation states of PANi. Notably, the main peak for the polyemeraldine salt, which represents the only conducting state of the polymer, appeared at about 0.3 V. The redox peaks at about 0.3 V and 0.2 V are therefore attributed to the polyemeraldine/ polyemeraldine

states. Also, other redox features were present, although less pronounced possibly due to growth on SS-P.

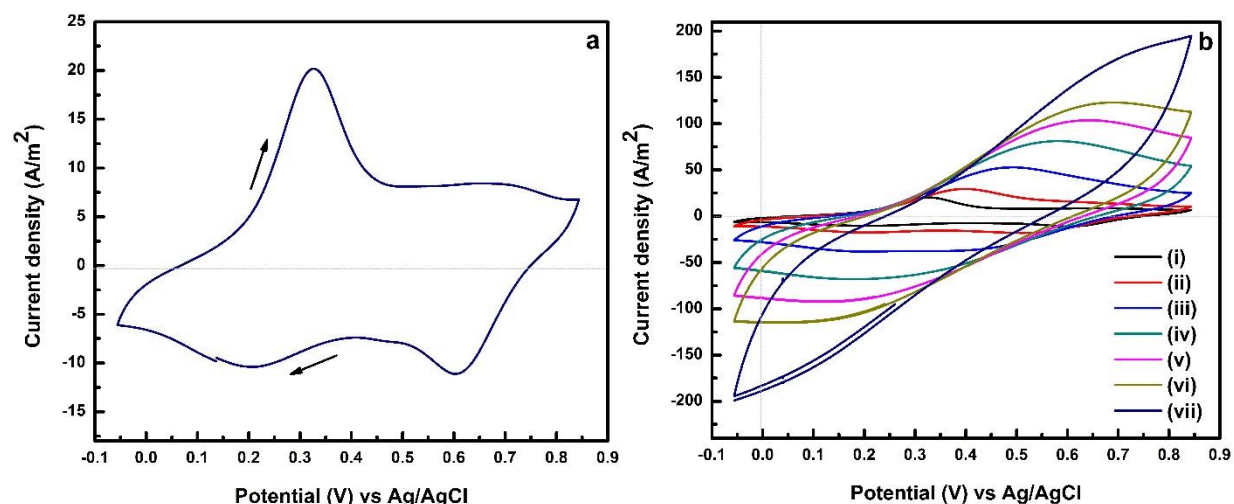


Fig. 2.5 Cyclic voltammograms obtained for PANi-coated SS in 0.7 nitric acid. (a) cyclic voltammogram obtained at 5 mV/s scan rate, and (b) cyclic voltammograms obtained at: (i) 5, (ii) 10, (iii) 25, (iv) 50, (v) 75, (vi) 100, and (vii) 200 mV/s.

The cyclic voltammograms obtained for the PANi-coated SS-P at different scan rates are shown in Fig. 2.5(b). The increase in the peak currents, as well as a shift in peak potential with increasing scan rate, are evident. At a scan rate, higher than 100 mV s⁻¹, the peak currents disappeared, and the redox process was not evident. Thus, indicating that electrode reversibility is lost at a scan rate higher than 100 mV s⁻¹.

2.3.2.2 Fourier-transform infrared spectroscopy (FTIR)

The FTIR spectrum obtained for the PANi coating produced on a SS-P with 0.4 M ANi in 0.7 M nitric acid is shown in Fig. 2.6(a). The vibrations due to C-C stretching and C-H deformation in benzenoid rings were detected at 1623 and 1192 cm⁻¹ [36]. The peak at 1598 cm⁻¹ was attributed to C=N stretching of the quinoid ring [37]; the peak at 1513 cm⁻¹ was due to C=C stretching of the benzenoid group [38]; the peaks at 1397 cm⁻¹ and 1348 cm⁻¹ were due to C=C stretching vibration of quinoid rings and benzenoid rings [39]. Also, the polaronic $\nu(\text{C}\sim\text{N}^+)$ vibration was observed at 1348 cm⁻¹ [36]. The peak observed at 1186 cm⁻¹ was due to the stretching frequency of C-O and indicates the presence of organic acids in the PANi film, while the peak at 1156 cm⁻¹ was due to S=O bonding for camphor sulphonic acid [37]. The characteristic absorption bands of PANi

observed at 830, and 700 cm^{-1} are attributed to the C-H out of plane bending in the benzenoid ring. It was reported that the presence of benzenoid and quinoid units provide evidence for the emeraldine structure of PANi [37].

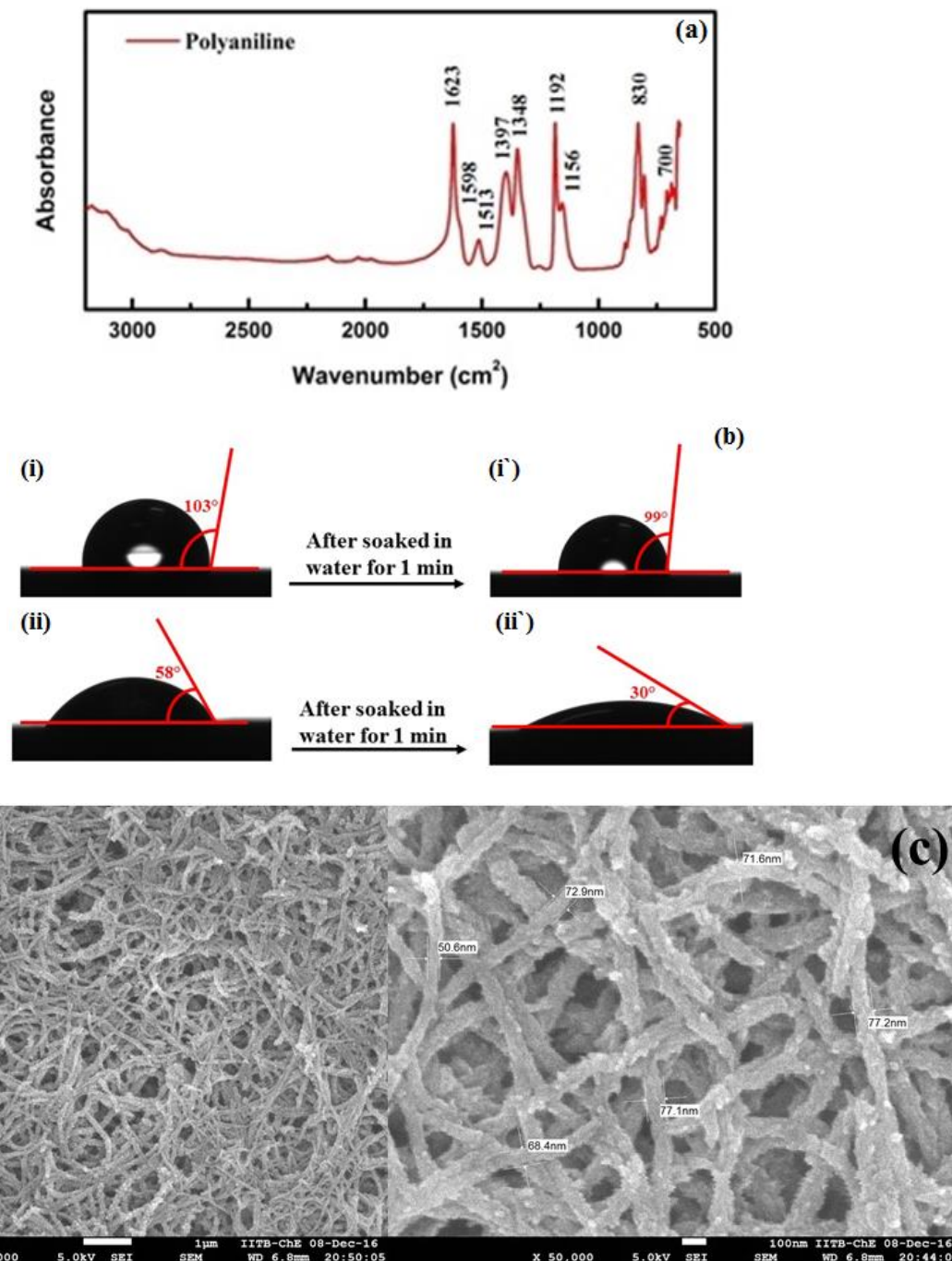


Fig. 2.6 Characterisation of PANi modified SS-P. (a) FTIR spectrum, (b) contact angle measurement for pristine SS-P (i, i') and PANi modified SS-P (ii, ii') and (c) SEM images of PANi modified SS-P.

2.3.2.3 Contact angle measurement

Fig. 2.6(b) shows the contact angle measurements obtained for pristine SS-P (i, i') and SS-P/PANi (ii, ii'). The SS-P displayed a hydrophobic (103°) surface. Even after soaking (99°) in water it remained hydrophobic ($\theta > 90^\circ$). In contrast, the initial contact angle observed for the SS-P/PANi was 58° . After soaking in water for 1 min, the measured contact angle changed to 30° . This is due to the presence of the PANi nanofibres which provided a larger surface area and, hence, resulted in much rapid uptake of water and change in the measured contact angle. The SS-P/PANi was therefore clearly hydrophilic ($\theta < 90^\circ$) because it soaked up water. Evidently, the SS-P/PANi remained essentially hydrophilic before and after exposure to the aqueous medium. The much higher change in coating resistance observed was obviously due to the stronger hydrophilic nature of the coating.

2.3.2.4 Scanning Electron Microscope

The SS-P/PANi was also characterised by scanning electron microscopy. The surface topography shows the presence of surface nanofibers on top of a compact layer. The thickness of the fibres ranges from 56-77 nm, as shown in Fig. 2.6(c). The presence of the nanofibres gave a larger exposed area which accounts for the observed higher current measurements, as will be demonstrated later.

2.3.3 Evaluation of coating durability

As the prime property commonly displayed by conductive polymers is electrical conductivity, electrochemical impedance spectroscopy was used to evaluate the coating kinetics, coating stability and associated electrochemical reactions [40,41]. The equivalent circuit (EC) used to evaluate R_{ct} is illustrated in Fig.2.7(a) [42,43]. The EC model used was $R(Q(R(QR)))$, which consists of the solution resistance (R_s) connected in series with the parallel connection of the constant phase element of the polarisation resistance (R_p). This is subsequently connected with the parallel connection of the constant phase element of the double layer capacitor (Cdl) and the charge transfer resistance (R_{ct}). In this model, the capacitor is replaced by the constant phase element to surface reactivity, surface heterogeneity, roughness, electrode porosity and potential distribution associated with the electrode geometry. The constant phase element (Q) considers the interfacial irregularities such as porosity and roughness of the intact PANi film. All PANi coatings were immersed in a corrosive (0.1 M NaCl) solution at ambient temperature. The aim was to determine

initial R_{ct} and monitor changes in R_{ct} with time when exposed to the corrosive solution. This was achieved by subjecting the samples regularly, after 24 hrs, to EIS measurements at varying scanning frequency from 1 MHz to 10 mHz. The collected data was analysed with the EC lab software V 10.44. The R_{ct} [shown in Fig. 2.7(b)] was estimated using the equivalent circuit and was monitored for seven days. The initial R_{ct} obtained for the SS-P/PANi produced in nitric, oxalic, sulfamic and sulfuric acids were 6.25 ± 1.38 , 35.64 ± 0.81 , 11.99 ± 1.29 and 6.64 ± 0.34 Ohm.cm², respectively. After 7 days, as indicated in Table 2, the R_{ct} increased substantially to 51.60 ± 17.38 , 546.43 ± 29.28 , 101.05 ± 16.92 and 192.10 ± 12.01 Ohm.cm², respectively. It was found that the R_{ct} of the SS-P/PANi synthesised with oxalic acid changed by 1433%, whereas the least change (726%) was obtained for the SS-P/ PANi formed with nitric acid. It was therefore obvious that the SS-P/PANi coating produced from 0.4 M aniline in 0.7 M nitric acid exhibited the best stability in terms of electrochemical activity. This is consistent with the explanation provided earlier for establishing the PANi coating formed in this monomer as the most conducting. This is also supported by the EIS measurements. Fig. 2.7(b) shows the changes in R_{ct} obtained with the different PANi coatings over a 7-day period. There is an obvious consistency between the observed film conductivity trend reported earlier in Table 1 and the trend of the measured charge transfer resistance shown in Figure 2.7(b). Evidently, the most conducting PANI film formed in nitric acid gave the lowest charge transfer resistance, while the least conducting PANi coating formed in oxalic acid gave the highest charge transfer resistance. The equivalent circuits fitted with the Bode plots of PANi are shown in Fig. 2.7(a). The Bode plots suggest that the response shifted from a higher frequency to lower frequency with time due to stimulated defects in the coating where water molecules and ions easily penetrated through the film. The R_{ct} can be attributed to the charge transfer owing to the ionic transfer through the coating pores, and it decreased with increasing time. Electrolyte and oxygen penetrated the SS-P through the cracks in the coatings to reach the metals and, subsequently, led to the coating deterioration [44].

Table 2.2 Changes in charge transfer resistance [R_{ct} (Ohm.cm²)] for PANi formed in different acids

Days	Sulfuric acid	Sulfamic acid	Oxalic acid	Nitric Acid
0	6.64	11.99	35.64	6.25
1	11.29	15.69	48.83	8.61
2	13.96	18.06	65.09	13.10
3	53.74	28.59	192.94	30.89
4	83.09	54.51	300.73	42.40
5	108.79	71.34	349.79	44.31
6	163.85	88.10	379.07	56.24
7	192.10	101.05	546.43	51.60

The durability of the SS-P/PANi was further investigated by using phase and Bode plots from EIS measurements. Fig. 2.7(c) and 2.7(d) show the phase and Bode plots obtained for the SS-P/PANi produced in nitric acid and subsequently immersed in a 0.1 M NaCl solution. The impedance of the SS-P/PANi increased with increasing exposure time in NaCl solution, suggesting a steady decline in the conductivity. The Bode plots consist of two-time constants for SS-P/PANi, the high-frequency time constant related to the coating/electrolyte interphase, whereas the low-frequency time constant was associated with the metal/electrolyte interphase. After 3 days of immersion of SS-P/PANi in NaCl solution, the time constant at low frequencies become more pronounced due to the reaction at the metal-electrolyte interphase. The observed increase in the R_{ct} can be attributed to the penetration of the SS-P/PANi by Cl^- ions which led to the exposure of the underlying SS-P to the NaCl solution. The results in Fig. 2.7(c) and 2.7(d) demonstrated that the metal remained intact during the PANi degradation step. If the metal degraded during the testing period, the impedance would have been higher than that of the pristine SS-P. The measured impedance for the pristine SS-P was 3.7 (log /Ohm cm⁻²) but varied from 0.7 to 1.75 (log /Ohm cm⁻²) for the SS-P/PANi coating. Even from the Bode plot, the phase shift was -18° to -30° for the SS-P/PANi, whereas for the pristine SS-P, it was -77° at the same frequency. At high frequencies, the phase shifts for both pristine SS-P and the SS-P/PANi were similar, and it ranges between 4° and 6°. The results indicated that the PANi coating exhibited high electrical conductivity and displayed significant stability even after seven days in a corrosive solution

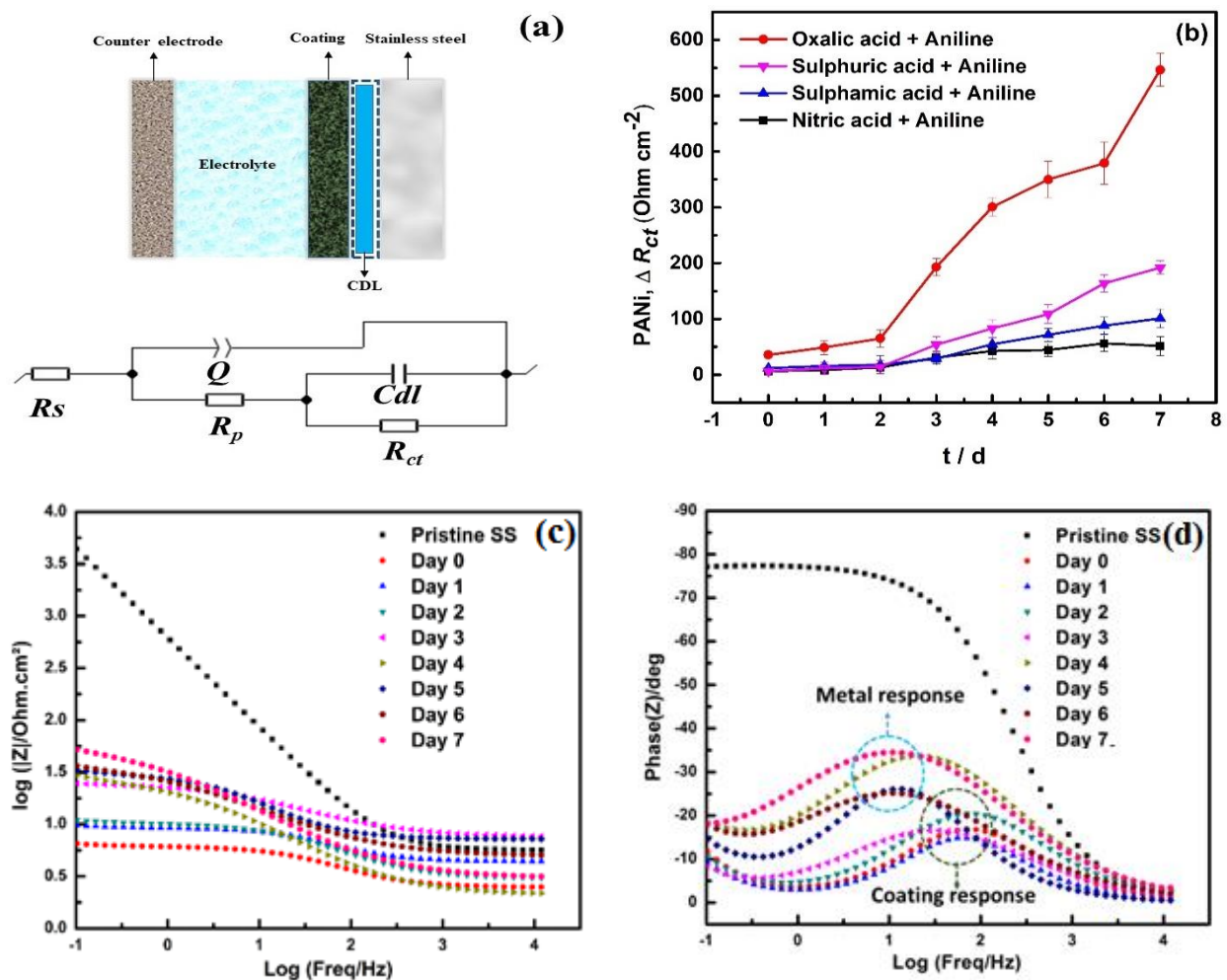


Fig. 2.7 Electrochemical characterisation of PANi coating on SS. (a) Equivalent circuit used for impedance measurement, (b) change in PANi coating resistance as a function of time, (c) frequency dependences of the impedance and (d) phase shift in the Bode plots of PANi film synthesised in nitric acid.

2.3.4 Microbial fuel cells with SS-P/PANi anode

The MFCs with the SS-P/PANi and pristine SS-P anodes were conducted in synthetic wastewater (M9 medium) which contained acetate (25 mM) as a sole carbon source, and to which 4% landfill leachate was added as a source of bacteria. Two cycles were run without resistance at ambient temperature to initiate biofilm growth. The maximum OCVs achieved in the first cycle were 608 mV and 664 mV with the SS-P and SS-P/PANi anodes, respectively. Figure 2.8(a) shows the OCV variations obtained with both anodes over a 12-day period. Notably, upon addition of 25 mM in the second successive batch cycle (after 5 days), the OCV increased to 649 mV and 730 mV with

the SS-P and SS-P/PANi anodes, respectively, on the 7th and 8th day of operation of the MFCs. The results in Figure 2.8(a) also show some correlations in time for the SS-P anode and the SS-PANI anode during the independent measurements. This can be explained based on the three possible major losses in a microbial fuel cell, which includes activation, ohmic and mass transfer modes. The SS-PANI anode possess low activation potential and because it has high conductivity, its OCV is slightly higher than that of SS-P. However, the root cause of OCV is the reaction of a substrate in the system. Obviously, in the first cycle, the OCV is mainly based on a substrate (minimal contribution from bacterial growth) and, as both reactors have the same substrate, there is some correlations in the first cycle. In contrast, in the second cycle, the SS-PANI anode shows a prolong stationary voltage phase signatures of the enrichment of electroactive biofilm formation compared to the SS-P anode.

Subsequently, the solutions in the MFCs were replaced with fresh media and a 100 Ω resistor was applied to each MFC. The MFC with the SS-P/PANI anode achieved a successful start-up of the current generation on the first day, as shown by the current generation curves in Fig. 2.8(b). Even after inoculation, the MFC with the SS-P/PANI anode did not show a lag phase. This may be due to the established biofilm growth from the previous two successive OCV cycles where no resistance was applied. With the applied R_{ext} (100 Ω), a slow exponential trend was observed in the current generation and after three days the current (~ 0.14 mA) was stable for two days, which is the stationary phase of the MFC with the SS-P/PANI anode. However, on the 4th day, a sharp decline in the current was observed in this MFC, which was attributed to the substrate depletion. In contrast, negligible current generation was observed in the MFC with the SS-P anode. This anode gave very slow current generation, and even after 7 days of incubation, no increment was observed. A number of studies [9,45,46] have suggested that the PANi surface enhances the start-up time of MFCs by favouring extracellular electron transfer from bacteria to anode material. It can, therefore, be concluded that the faster start-up time achieved with the SS-P/PANI anode resulted because of its high bio-electrochemical activity which is reflective of its high biocompatibility to electrogenic bacteria. The observations in this study, therefore, demonstrate that the MFC with SS-P/PANI anode enhanced the startup time due to the presence of the PANi coating.

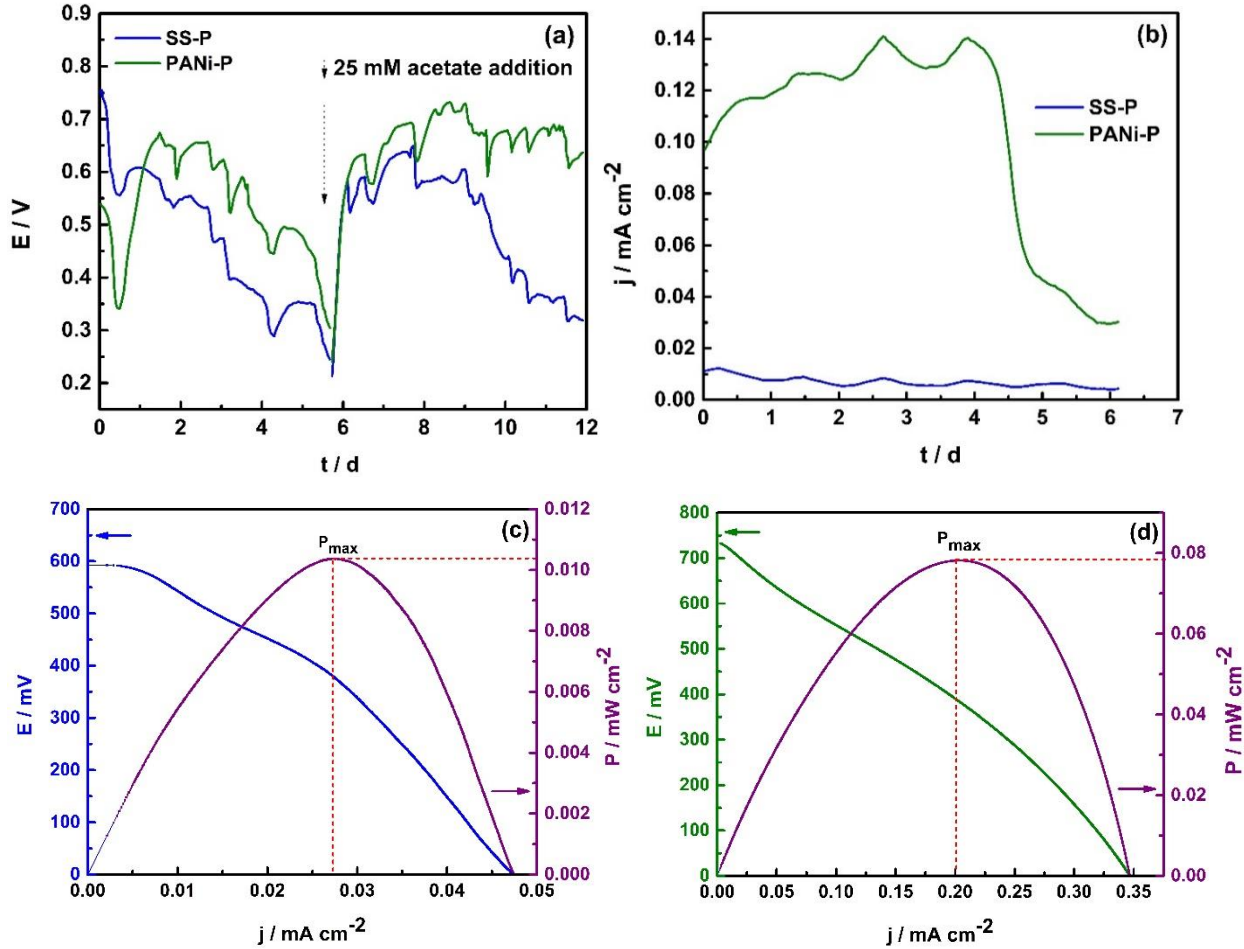


Fig. 2.8 Performance of the MFCs with the SS-P and SS-P/PANi anodes. (a) Open circuit voltage output during the start-up phase of the MFCs system, (b) current generation from MFCs system with 100Ω resistance connected across the cell, (c) polarisation curves of the MFCs with SS-P anode, and (d) polarisation curves of the MFCs with SS-P/PANi anode.

Polarisation curves were obtained from the MFCs with the SS-P and SS-P/PANi anodes during the second batch cycle on the 3rd day. The maximum power density obtained with the SS-P anode was $0.010 \pm 0.008 \text{ mW cm}^{-2}$ under $0.027 \pm 0.0022 \text{ mA cm}^{-2}$. Fig. 2.8(c) shows the polarisation curve obtained with the SS-P anode. The maximum power density achieved with this anode was $0.0103 \pm 0.0017 \text{ mW cm}^{-2}$. In contrast, the MFC with the SS-P/PANi anode produced a maximum power density of $0.078 \pm 0.011 \text{ mW cm}^{-2}$ under $0.199 \pm 0.026 \text{ mA cm}^{-2}$ normalised by cathode area. The polarisation curve obtained with the SS-P/PANi anode is shown in Fig. 2.8(d). The current generation across 100Ω was 0.008 mA cm^{-2} and 0.14 mA cm^{-2} with the SS-P and SS-P/PANi anodes, respectively. The performance enhancement is attributed to the PANi coating

which lowers the start-up time of the MFC, as evident in the observed current generation from 1st day. Also, the biological oxidation of acetate appeared to be accelerated by the presence of the PANi coating.

2.3.4.1 Comparison with previous studies

The previously reported performances achieved by using PANi anodes in MFCs are summarised in Table 3. The performances are compared on the basis of the type of MFCs, the substrate used, current density, power density and number of days of operation. The enrichment time is reflected by the start-up phase of electrogenic bacteria anode.

As the data in Table 3 demonstrate, the SS-P/PANi anode exhibited a power density significantly higher than those achieved with PANi/che/SSFF, PANi/ele/SSFF, and PANi/CNT in the first 6 days of MFC batch cycle. The performance could be further improved by several magnitude after successive batch cycles which promotes biofilm growth on the anode.

It is interesting to note from the data in Table 3 that the chemically synthesised PANi coating on SSFF gave much higher maximum current density than the electrochemically synthesised coating, but the latter gave much higher maximum power density than with the chemically synthesised coating. In contrast, the electrochemically synthesised PANi coating on SS-P in our study gave much higher maximum current density than both PANi coatings on SSFF, while also achieving much higher maximum power density than the chemically synthesised coating on SSFF. The difference appeared to be due to the use of galvanostatic polymerisation for the growth of PANi coating in our study. It produces a more uniform and more adherent PANi coating.

Table 2.3 Comparison of the performances of PANi modified anodes in MFCs.

Type of MFC	Vol. of reactor (mL)	Days of operation	Anode material	Anode area (cm ²)	Max. Current density (mA cm ⁻²)	Max. power density (mW cm ⁻²)	Reference
H-shaped	90	14	PANi _{che} /SSFF	3.24	0.149	0.0360	[5]
H-shaped	90	14	PANi _{ele} /SSFF	3.24	0.0035	0.0800	[5]
Tri-electrode	NA	<1	PANi/CN T	1	NA	0.0042	[47]
Dual chamber	100	03	PANi/C NT/CP	80	NA	0.157	[48]
Dual chamber	110	30	PANi/CC	25	0.0944	0.516 [†]	[45]
Single chamber	83	09	PANi/GF	12.5	NA	0.400 [†]	[9]
Single chamber	27	06	PANi/SS-P	3.5	0.199*	0.078*	This study**

* Values obtained from polarisation curves

** Normalised by cathode area

† Volumetric power density (mW m⁻³)

2.4 Conclusion

Highly conductive and stable PANi coated SS plates have been successfully prepared by galvanostatic polymerisation of ANi (0.4 ANi and 0.7 M nitric acid). FTIR and CV measurements confirmed the formation of emeraldine structure on the PANi coated SS-P. Electrochemical impedance spectroscopy were useful in understanding the mechanism of coating deterioration over time. The preliminary test of the SS-P/PANi anode in a MFC gave a P_{\max} of 0.078 ± 0.011 mW cm⁻², whereas SS-P anode produced a P_{\max} of 0.010 ± 0.008 mW cm⁻². Investigations are in progress to determine long-term performance to achieve maximum current from the SS-P/PANi anode and consideration of using SS wool modified with PANi to achieve a higher surface anode for more improved microbial fuel cells.

References

- [1] M. Ghasemi, M. Ismail, S.K. Kamarudin, K. Saeedfar, W.R.W. Daud, S.H.A. Hassan, L.Y. Heng, J. Alam, S.E. Oh, Carbon nanotube as an alternative cathode support and catalyst for microbial fuel cells, *Appl. Energy*. 102 (2013) 1050–1056. doi:10.1016/j.apenergy.2012.06.003.
- [2] M. Rahimnejad, A. Adhami, S. Darvari, A. Zirepour, S.E. Oh, Microbial fuel cell as new technology for bioelectricity generation: A review, *Alexandria Eng. J.* 54 (2015) 745–756. doi:10.1016/j.aej.2015.03.031.
- [3] J.M. Sonawane, A. Yadav, P.C. Ghosh, S.B. Adeloju, Recent advances in the development and utilization of modern anode materials for high performance microbial fuel cells, *Biosens. Bioelectron.* 90 (2017) 558–576. doi:10.1016/j.bios.2016.10.014.
- [4] D. Pocaznoi, A. Calmet, L. Etcheverry, B. Erable, A. Bergel, Environmental Science Stainless steel is a promising electrode material for anodes of microbial fuel cells, (2012) 9645–9652. doi:10.1039/c2ee22429a.
- [5] J. Hou, Z. Liu, Y. Li, Polyaniline Modified Stainless Steel Fiber Felt for High-Performance Microbial Fuel Cell Anodes, *J. Clean Energy Technol.* 3 (2015) 165–169. doi:10.7763/JOCET.2015.V3.189.
- [6] R.-B. Song, K. Yan, Z.-Q. Lin, J.S. Chye Loo, L.-J. Pan, Q. Zhang, J.-R. Zhang, J.-J. Zhu, Inkjet-printed porous polyaniline gel as an efficient anode for microbial fuel cells, *J. Mater. Chem. A*. 4 (2016) 14555–14559. doi:10.1039/C6TA05770E.
- [7] Y. Wang, B. Li, L. Zeng, D. Cui, X. Xiang, W. Li, Polyaniline/mesoporous tungsten trioxide composite as anode electrocatalyst for high-performance microbial fuel cells, *Biosens. Bioelectron.* 41 (2013) 582–588. doi:10.1016/j.bios.2012.09.054.
- [8] P. Zamani, D. Higgins, F. Hassan, G. Jiang, J. Wu, S. Abureden, Z. Chen, Electrospun Iron–Polyaniline–Polyacrylonitrile Derived Nanofibers as Non–Precious Oxygen Reduction Reaction Catalysts for PEM Fuel Cells, *Electrochim. Acta.* 139 (2014) 111–116. doi:10.1016/j.electacta.2014.07.007.
- [9] P. Wang, H. Li, Z. Du, Polyaniline synthesis by cyclic voltammetry for anodic modification in microbial fuel cells, *Int. J. Electrochem. Sci.* 9 (2014) 2038–2046.
- [10] A. Mostafaei, A. Zolriasatein, Synthesis and characterization of conducting polyaniline nanocomposites containing ZnO nanorods, *Prog. Nat. Sci. Mater. Int.* 22 (2012) 273–280.

- doi:10.1016/j.pnsc.2012.07.002.
- [11] J. Hou, Z. Liu, P. Zhang, A new method for fabrication of graphene/polyaniline nanocomplex modified microbial fuel cell anodes, *J. Power Sources*. 224 (2013) 139–144. doi:10.1016/j.jpowsour.2012.09.091.
- [12] H. Wang, J. Lin, Z.X. Shen, Polyaniline (PANi) based electrode materials for energy storage and conversion, *J. Sci. Adv. Mater. Devices*. 1 (2016) 225–255. doi:10.1016/j.jsamd.2016.08.001.
- [13] W. Zhong, X. Chen, S. Liu, Y. Wang, W. Yang, Synthesis of highly hydrophilic polyaniline nanowires and sub-micro/nanostructured dendrites on poly(propylene) film surfaces, *Macromol. Rapid Commun*. 27 (2006) 563–569. doi:10.1002/marc.200500796.
- [14] †,‡ Hua-jie Wang, ‡,§ Li-wen Ji, ‖ and Da-feng Li, § Jin-Ye Wang*, Characterization of Nanostructure and Cell Compatibility of Polyaniline Films with Different Dopant Acids, (2008). doi:10.1021/JP0750957.
- [15] P.K. Sharma, G. Gupta, V. V. Singh, B.K. Tripathi, P. Pandey, M. Boopathi, B. Singh, R. Vijayaraghavan, Synthesis and characterization of polypyrrole by cyclic voltammetry at different scan rate and its use in electrochemical reduction of the simulant of nerve agents, *Synth. Met*. 160 (2010) 2631–2637.
- [16] D.A. Kaplin, S. Qutubuddin, Electrochemically synthesized polypyrrole films: effects of polymerization potential and electrolyte type, *Polymer (Guildf)*. 36 (1995) 1275–1286.
- [17] X. Luo, X.T. Cui, Electrochemical deposition of conducting polymer coatings on magnesium surfaces in ionic liquid., *Acta Biomater*. 7 (2011) 441–6.
- [18] A.H. El-Shazly, H.A. Al-Turaif, Improving the Corrosion Resistance of Buried Steel by Using Polyaniline Coating, *Int. J. Electrochem. Sci*. 7 (2012) 211–221.
- [19] C. García-Hernández, C. García-Cabezón, C. Medina-Plaza, F. Martín-Pedrosa, Y. Blanco, J.A. de Saja, M.L. Rodríguez-Méndez, Electrochemical behavior of polypyrrol/AuNP composites deposited by different electrochemical methods: Sensing properties towards catechol, *Beilstein J. Nanotechnol*. 6 (2015) 2052–2061.
- [20] R. Balint, N.J. Cassidy, S.H. Cartmell, *Acta Biomaterialia* Conductive polymers : Towards a smart biomaterial for tissue engineering, *Acta Biomater*. 10 (2014) 2341–2353.
- [21] S. Chen, J. Zhu, T. Zhou, B. He, W. Huang, B. Wang, Preparation and properties study of polyaniline conductive anti-fouling coatings, *Int. J. Electrochem. Sci*. 7 (2012) 8170–8184.

- [22] J.M. Sonawane, E. Marsili, P. Chandra Ghosh, Treatment of domestic and distillery wastewater in high surface microbial fuel cells, *Int. J. Hydrogen Energy*. 39 (2014) 21819–21827. doi:10.1016/j.ijhydene.2014.07.085.
- [23] F. Harnisch, C. Koch, S.A. Patil, T. Hübschmann, S. Müller, U. Schröder, Revealing the electrochemically driven selection in natural community derived microbial biofilms using flow-cytometry, *Energy Environ. Sci.* 4 (2011) 1265. doi:10.1039/c0ee00605j.
- [24] Z. Mandić, L. Duić, F. Kovačiček, The influence of counter-ions on nucleation and growth of electrochemically synthesized polyaniline film, *Electrochim. Acta*. 42 (1997) 1389–1402.
- [25] R. Córdova, M.A. del Valle, A. Arratia, H. Gómez, R. Schrebler, Effect of anions on the nucleation and growth mechanism of polyaniline, *J. Electroanal. Chem.* 377 (1994) 75–83. doi:10.1016/0022-0728(94)03425-7.
- [26] A.. Motheo, J.. Santos, E.. Venancio, L.H.. Mattoso, Influence of different types of acidic dopant on the electrodeposition and properties of polyaniline films, *Polymer (Guildf)*. 39 (1998) 6977–6982.
- [27] C. Kvarnström, György Inzelt, Conducting polymers. A new era in electrochemistry, *J. Solid State Electrochem.* 14 (2009) 917–917.
- [28] Y. Jafari, S.M. Ghoreishi, M. Shabani-Nooshabadi, Electrochemical deposition and characterization of polyaniline-graphene nanocomposite films and its corrosion protection properties, *J. Polym. Res.* 23 (2016) 91. doi:10.1007/s10965-016-0983-8.
- [29] A.Y. Obaid, E.H. El-Mossalamy, S.A. Al-Thabaiti, I.S. El-Hallag, A.A. Hermas, A.M. Asiri, Electrodeposition and Characterization of Polyaniline on Stainless Steel Surface via Cyclic, Convulsive Voltammetry and SEM in Aqueous Acidic Solutions, *Int. J. Electrochem. Sci.* 9 (2014) 1003–1015.
- [30] A.T. Ozyilmaz, G. Ozyilmaz, O. Yigitoglu, Synthesis and characterization of poly(aniline) and poly(o-anisidine) films in sulphamic acid solution and their anticorrosion properties, *Prog. Org. Coatings*. 67 (2010) 28–37.
- [31] S.K. Dhawan, D.C. Trivedi, Synthesis and properties of polyaniline obtained using sulphamic acid, *J. Appl. Electrochem.* 22 (1992) 563–570.
- [32] M.C. Bernard, A. Hugot-LeGoff, S. Joiret, N.N. Dinh, N.N. Toan, Polyaniline layer for iron protection in sulfate medium, *Synth. Met.* 102 (1999) 1383–1384.

- [33] A.P. Srikanth, V. Raman, S. Tamilselvi, S. Nanjundan, N. Rajendran, Anti-Corrosion Methods and Materials Electropolymerization and corrosion protection of polyaniline and its copolymer on carbon steel, *Materials (Basel)*. 55 (2008) 111–115.
- [34] G. Troch-Nagels, R. Winand, A. Weymeersch, L. Renard, Electron conducting organic coating of mild steel by electropolymerization, *J. Appl. Electrochem.* 22 (1992) 756–764.
- [35] H. Lu, Y. Zhou, S. Vongehr, K. Hu, X. Meng, Electropolymerization of PANI coating in nitric acid for corrosion protection of 430 SS, *Synth. Met.* 161 (2011) 1368–1376. doi:10.1016/j.synthmet.2011.05.003.
- [36] G. Niaurah, Z. Kuprionis, V. Kod, R. Mazeikiene, Application of Sum-Frequency Generation Spectroscopy for the Structural Studies of Polyaniline, *Materials (Basel)*. 9 (2003) 436–440.
- [37] A. Mostafaei, F. Nasirpouri, Epoxy/polyaniline-ZnO nanorods hybrid nanocomposite coatings: Synthesis, characterization and corrosion protection performance of conducting paints, *Prog. Org. Coatings*. 77 (2014) 146–159.
- [38] Y. Lv, Fe 3+ -Selective enhanced Fluorescent probes based on rhodamine derivatives, *Quim. Nov.* 38 (2015) 1297–1299.
- [39] Y. Ma, M. Qiao, Y. Chen, C. Hou, B. Zhang, Q. Zhang, Fabrication of electromagnetic Fe₃O₄ @polyaniline nanofibers with high aspect ratio, *RSC Adv.* 5 (2015) 9986–9992.
- [40] A.S. Sarac, M. Ates, B. Kilic, Electrochemical impedance spectroscopic study of polyaniline on platinum, glassy carbon and carbon fiber microelectrodes, *Int. J. Electrochem. Sci.* 3 (2008) 777–786.
- [41] A. Mischczyk, K. Darowicki, Use of impedance spectroscopy to evaluate the durability of protective coatings after thermal shock, *Corros. Sci.* 40 (1998) 663–672.
- [42] L.M. Duc, V.Q. Trung, Layers of Inhibitor Anion – Doped Polypyrrole for Corrosion Protection of Mild Steel, *Intech.* (2013). doi:10.5772/54573.
- [43] M. Shabani-Nooshabadi, F. Karimian-Taheri, Electrosynthesis of a polyaniline/zeolite nanocomposite coating on copper in a three-step process and the effect of current density on its corrosion protection performance, *RSC Adv.* 5 (2015) 96601–96610. doi:10.1039/C5RA14333K.
- [44] D. Ramesh, Evaluation of Corrosion Stability of Water Soluble Epoxy-Ester Primer through Electrochemical Studies, *Mater. Sci. Appl.* 03 (2012) 333–347.

- [45] B. Lai, X. Tang, H. Li, Z. Du, X. Liu, Q. Zhang, Power production enhancement with a polyaniline modified anode in microbial fuel cells, *Biosens. Bioelectron.* 28 (2011) 373–377. doi:10.1016/j.bios.2011.07.050.
- [46] Y. Qiao, S.-J. Bao, C.M. Li, Electrocatalysis in microbial fuel cells—from electrode material to direct electrochemistry, *Energy Environ. Sci.* 3 (2010) 544. doi:10.1039/b923503e.
- [47] Y. Qiao, C.M. Li, S.-J. Bao, Q.-L. Bao, Carbon nanotube/polyaniline composite as anode material for microbial fuel cells, *J. Power Sources.* 170 (2007) 79–84. doi:10.1016/j.jpowsour.2007.03.048.
- [48] C.-T. Wang, R.-Y. Huang, Y.-C. Lee, C.-D. Zhang, Electrode Material of Carbon Nanotube/Polyaniline Carbon Paper Applied in Microbial Fuel Cells, *J. Clean Energy Technol.* 1 (2013) 206–210.

Chapter 3

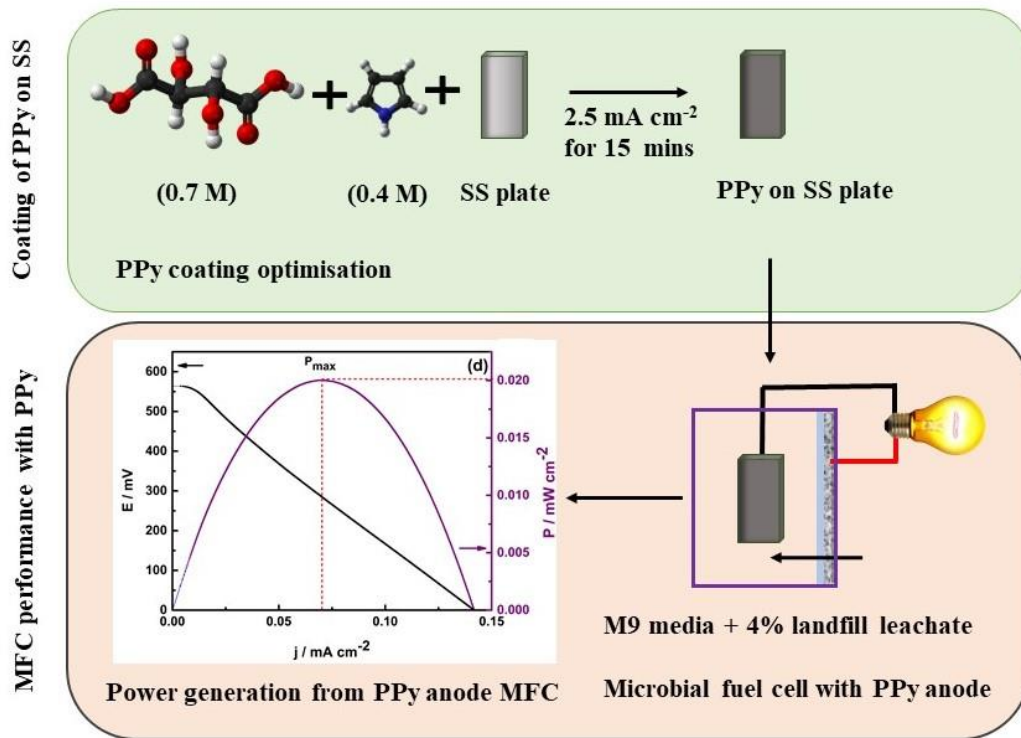
Synthesis and utilisation of polypyrrole coated stainless steel as a low-cost anode for high-performance microbial fuel cells

[To be submitted as, J.M. Sonawane, R.K. Singh, P.C. Ghosh, S.B. Adeloju, Synthesis and utilisation of polypyrrole coated stainless steel as a low-cost anode for high-performance microbial fuel cells, ChemElectroChem, Willey]

Abbreviation:

Ag/ AgCl	Silver/ silver chloride
EIS _{TD}	Time-dependent electrochemical impedance spectroscopy
FTIR	Fourier transform infrared spectroscopy
j_{max}	Maximum current density
MFCs	Microbial fuel cells
MoC	material of construction
MoC	Material of construction
OCV	Open circuit voltage
P_{max}	Maximum power density
PPy	Polypyrrole
Py	Pyrrole
R _{ct}	Charge Transfer Resistance
R _s	Solution resistance
SS/PPy-P	Stainless steel coated polypyrrole plate
SS-P	Stainless steel plate

Graphical abstract



Abstract

In this study, we explored the use of polypyrrole coating on stainless steel as a basis for producing low-cost anode for MFC, with the ability to effectively promote microbial growth and retain long-term stability. The PPy coated stainless steel plate (SS/PPy-P) was evaluated as a potential low-cost anode for MFCs in a M9 media which contained 4% landfill leachate. Comparison of the SS/PPy-P anode with a pristine (uncoated) SS-P anode revealed much higher OCV_{max} of 664 ± 27 mV, j_{max} of 0.027 ± 0.002 mA cm⁻² and a P_{max} of 0.012 ± 0.009 mW cm⁻² compared with an OCV_{max} of 624 ± 47 mV, j_{max} of 0.070 ± 0.028 mA cm⁻² and P_{max} of 0.020 ± 0.023 mW cm⁻² obtained in the absence of PANi coating. Notably, during the startup phase, a 3-fold increase in current generation was achieved with SS/PPy-P over the SS-P anode. Undoubtedly, the coating of the SS-P with PPy (as SS/PPy-P) substantially improved its performance and its potential utilisation as a low-cost anode for MFCs.

3.1 Introduction

The anode plays a significant role in the performance of MFCs [1], as the anode chamber is where electrogenic bacterial communities breakdown organic matters to generate electricity[2]. It is therefore crucial that the anode employed has high biocompatibility [3,4], high chemical stability [3,5], corrosion resistance to diverse wastewaters [3,6], low charge transfer resistance (R_{ct}) [7], and low activation overpotential [8].

Despite a recent suggestion that stainless steel (SS) is a promising anode material for construction of high-performance MFCs [9,10], it exhibits several intrinsic properties which can be a hurdle for large-scale MFC construction, such as poor biocompatibility compared with traditional carbon-based anode materials. The poor biocompatibility of SS often leads to a poor electrogenic bacterial biofilm formation [11]. Also, SS has high charge transfer resistance, hydrophobic nature, high activation overpotential and corrodes in complex liquid media. However, these issues can be addressed by coating SS with polypyrrole. Since PPy has been broadly demonstrated as a biocompatible and exceptional electrical conducting medium [12].

In comparison with SS, PPy-coated anodes usually have low R_{ct} , high exchange current density (j_o), high electrical conductivity and high biocompatibility that are known to improve the performance of MFCs. However, the coating of PPy on SS has not been widely employed as an anode in MFCs. To the best of the authors' knowledge, there is no report available on the PPy-coated stainless steel (SS) anode for MFC studies.

The use of conducting polymers has gained substantial interest in recent years due to they're unique chemical and physical properties that have resulted in various applications. Among the commonly considered conducting polymers, polypyrrole (PPy) and polyaniline (PANi) have attracted the most interest to date. The use of PPy-coated electrodes as anodes for microbial fuel cells (MFCs) has continued to attract some interests. Some the reported use of PPy-coated electrodes as anodes in MFCs for generation of electricity include the use of PPy/reduced graphene oxide (rGO) composites [13], polyurethane/graphite/PPy composite [14], PPy hydrogels/ carbon nanotubes composite [15], MnO₂/PPy composite-modified anode [16], PPy-coated Carbon Nanofiber [17] and PPy-coated CNT composite [18]. Although composites of PANi anodes have been explored for MFCs, the PPy coating on SS is the simple and facile approach. The PPy coating would protect the SS from a range of complex media/ wastewaters. Also, SS could be a promising and cost-effective alternative for high-performance MFCs.

Although galvanostatic polymerisation is well known in the literature, it is not commonly used for coating SS for use as MFC anodes. To our knowledge, a thorough investigation of the coating of PPy on stainless steel has never been undertaken. There is, therefore, a need for a detailed study of the durability of PPy coating and mechanism of coating removal. The understanding of the mechanism of coating removal may be useful in identifying the best PPy coated electrode for MFCs application. This may also be useful in improving the durability of the PPy coating, which may be achieved by optimising coating thickness for the desired time and in specific liquid media such as aggressive wastewater, landfill leachate, etc.

In this study, we have investigated the electropolymerisation of Py in L-(+)-Tartaric acid for coating PPy on SS. In-depth, electrochemical and analytical characterisation of the PPy-coated SS will be undertaken by time-dependent impedance spectroscopy (EIS_{TD}), Fourier transformed infrared (FTIR) spectroscopy, electron microscopy, contact angle measurement and 3D profilometry to obtain a comprehensive analysis of the nature and robustness of the coatings. The optimised PPy coating on SS explored for use as an anode in a MFC with M9 media+4% landfill leachate, and as a preliminary investigation, its performance will be measured in terms of voltage and current generation for short duration to study the effect of PPy on MFC startup.

3.2 Materials and Methods

3.2.1 Electrochemical cell setup and sample preparation

Tri-electrode cell assembly was used for the electropolymerisation of PPy on SS plate. The SS plates with a dimension of 1 x 1.5 x 0.1 cm were used as a working electrode. The SS-304 sheet was procured from Ladhani Metal Corporation (Mumbai, Maharashtra, India). The SS plates were polished using metallographic abrasive paper from grit sizes of 320, 400, 600, 800 and 1200. After polishing SS, plates were subjected to ultrasonication in acetone to degrease the samples before electropolymerisation. The miniature Ag/AgCl reference electrode (RRPEAGCL, Pine Research Instrumentation, Durham, USA) was used for voltage measurement. A platinum electrode was served as the counter electrode. A BiologicVMP3 potentiostat (BioLogic, Claix, France) was used throughout the electrochemical experiments. EC-Lab V 10.44 software was fitted with potentiostat for the operation and analysis of the produced data. All solutions were purged with nitrogen gas before the beginning of polymerisation.

3.2.2 Electropolymerisation of Polypyrrole (PPy)

For electropolymerisation of PPy, reagent grade pyrrole (Sigma-Aldrich, Sydney, Australia) and reagent grade L-(+)-Tartaric acid (Sigma-Aldrich, Sydney, Australia) were used. PPy was synthesised by galvanostatic polymerisation with an applied constant current density of 2.5 mA cm⁻² in aqueous solutions containing Py monomer. PPy was synthesis with 0.1 M Py, while varying L-(+)-Tartaric acid from 0.1 to 0.7 M. Upon observed lowest activation and stabilising voltage considered the best condition for PPy synthesis. In later stage L-(+)-Tartaric acid concentration kept constant and varied Py concentration from 0.1 to 0.5 M. After 15 mins of film growth, the chronopotentiograms were analysed, and the lowest potential indicative of highest film conductivity for each condition and accordingly concentration was optimised.

3.2.3 Surface profilometry and contact angle measurement

An InfiniteFocus microscope (Alicona, Raaba/Graz, Austria) was used to characterise the surface properties of the PPy film. Images were taken at a different magnification ranging from 10X, 20X and 50X. CAD/CAM suite (Alicona, Raaba/Graz, Austria) was used to analyse the surface profile of the PPy film. Water contact angle of the PPy film was measured at ambient temperature (19 °C) and 40% relative humidity. Sessile drop method on a telescopic goniometer C60 (USA Kino Industry Co. Ltd, Norcross, GA) was used. Three samples were tested for reproducibility of the results.

3.2.4 Fourier Transform Infrared Spectroscopy (FTIR)

FTIR analysis used to study the spectral effect on the PPy film on SS plate. A Vertex 80 (Bruker Corporation, Massachusetts, United States) FTIR spectrometer was employed to record FTIR of SS plate, and SS coated with PPy. The attenuated total reflectance (ATR) method was used to obtained FTIR spectra with a resolution of 4 cm⁻¹. The wavenumbers were kept in the range of 4000–650 cm⁻¹. The Opus software (Bruker Corporation, Massachusetts, United States) was used to determined FTIR peaks, after careful corrections of the baseline.

3.2.5 Cathode fabrication

The air cathodes were fabricated by the method reported previously [19,20]. In brief, Vulcan XC-72, fine platinised carbon powder with 20 wt % Platinum content (Sigma-Aldrich, Sydney, Australia) was used for coating on carbon paper. Nafion solution (5%) was used as a binder

(Sigma-Aldrich, Sydney, Australia). The Nafion solution was mixed with Pt powder in isopropyl alcohol; the resulted Pt ink was ultrasonicated with a probe sonicator for minimum 15 mins. The ink coated on 12 x 10 cm carbon paper (GDS 210, CeTech, Taichung, Taiwan) with 0.5 mg cm^{-2} loading. Utmost care was taken for uniform loading of Pt over carbon paper surface. The coated electrodes placed in a hot air oven for six hours at $60 \text{ }^\circ\text{C}$ to ensure complete drying. After drying monolayer of 5 %, Nafion solution was applied and again placed in a hot air oven for 15 mins. Subsequently, the electrodes were hot pressed on Nafion membrane NRE-212 (Sigma-Aldrich, Australia) under 10 kg cm^{-2} at $140 \text{ }^\circ\text{C}$ for 3 min using Carver hot press (Carver, Inc, Wabash, USA). Hotpressed electrodes were cut in 3 x 2.5 cm. Made cathodes were sandwiched in the aluminium mesh (act as a cathode current collector) and acrylic flange in the MFCs reactors.

3.2.6 Experimental setup and operation of MFCs

Clear 4 mm acrylic sheets were used to fabricate MFCs reactors. The acrylic sheets were cut using the laser technology and described dimensions of pieces were used to construct MFCs. The base of MFC was made of three pieces stacked together with a dimension of 6.8 x 6.8. The top and bottom made up of 3 x 2.5 cm acrylic pieces. A cube with inner dimension 3 x 3 x 3 was fixed. This acted as an anode chamber with a working volume of 27 cm^3 . The rectangular void was placed on the opening of the assembled structure. The void served as a house for air cathode. On top of the cathode, the aluminium mesh was placed, and the acrylic flange was tightened with nut and bolts. The MFCs are equipped with inlet and outlet for the refilling of media. The projected surface area of anodes was 3.5 cm^2 , whereas the air cathode surface area was 7.5 cm^2 . The performance of MFC was evaluated with normalised cathode surface area.

3.2.7 Operation of MFCs

All MFCs were fed with synthetic wastewater (M9 media) containing sodium acetate (25 mM) as a sole carbon source. The composition of the M9 media per L of distilled water is as follows: NH_4Cl : 0.31 g, KCl : 0.13 g, $\text{NaH}_2\text{PO}_4 \cdot \text{H}_2\text{O}$: 2.69 g, Na_2HPO_4 : 4.33 g, and 12.5 mL of each trace metal and vitamin solutions [21,22]. The study suggested that landfill leachate is the most promising substrate for microbial fuel cells [19]. The 4% landfill leachate (collected from the landfill site, Suez Environment, Melbourne, Australia) was inoculated as a source of bacteria in M9 media. All experiments were conducted at room temperature $25 \pm 2 \text{ }^\circ\text{C}$. The reactors were

flushed with N₂ gas for five mins, and media was purged with N₂ for 30 mins before inoculation to ensure removal of O₂ to minimise aerobic oxidation of M9 media. The experiments were conducted in a fed-batch mode. After a batch cycle, 90 % media replaced with new M9 media. Initially, MFCs were operated under open circuit mode for two cycles then 100 Ω external resistor was applied to evaluate current generation after biofilm formation in two successive cycles. All experiments were conducted in triplicates. A set of experiment was carried out with M9 media without bacterial inoculum as a control experiment.

3.3 Results and discussion

3.3.1 PPy film formation with L-(+)-Tartaric acid

Electropolymerisation of PPy on SS plate was carried out in L-(+)-Tartaric acid from 0.1 M – 0.7 M, while Py concentration was kept constant. 2.5 mA cm⁻² constant current was applied for 15 mins. The galvanostatic polymerisation was used to deposit PPy over SS plate using Py in L-(+)-Tartaric acid. Various concentration ranging from 0.1 – 0.7 M. The L-(+)-Tartaric acid concentration was varied from 0.1 – 0.7 M in the presence of 0.1 M Py. Fig 3.1a. Shows that the use of 0.1 to 0.4 M L-(+)-Tartaric acid gave distinctly higher activation and stabilisation potentials that gradually decreases with increasing L-(+)-Tartaric acid concentration up to 0.4 M. In contrast, the use of 0.5-0.7 M L-(+)-Tartaric acid gave very close activation and stabilisation potentials. Subsequent variation of pyrrole concentration from 0.1 M to 0.5 M revealed that 0.1 M pyrrole gave high activation potential and did not appear to form a conductive PPy film, as reflected by the increasing electrode potential in Fig. 3.1b. In contrast, the use of 0.2 – 0.5 M Py gave very close activation potentials but slightly different stabilisation potentials. Overall, a monomer solution which contained 0.4 Py and 0.7 M L-(+)-Tartaric acid gave the most stable and conductive PPy coatings on SS plate.

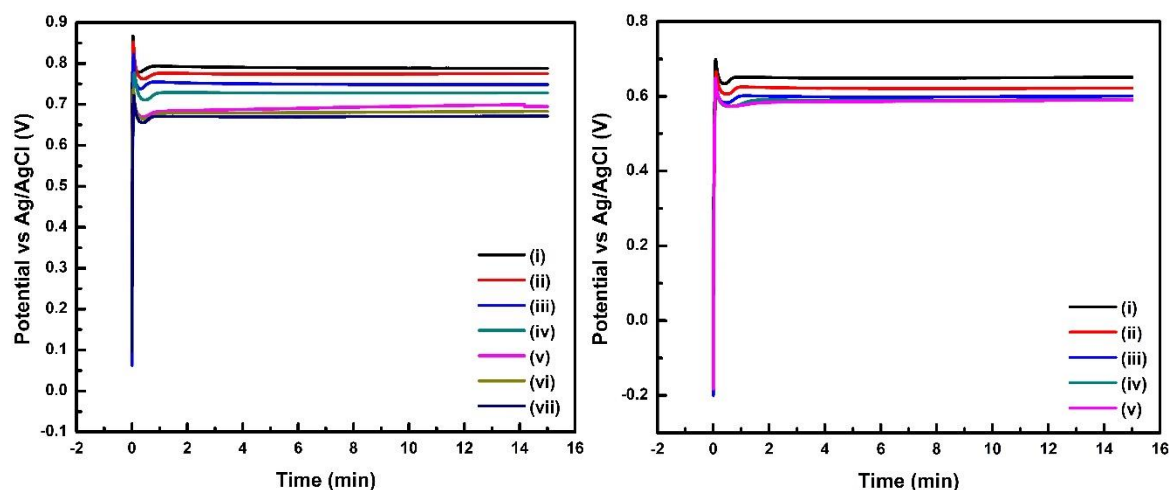


Fig. 3.1 Chronopotentiograms obtained for the formation of a PPy layer on SS plate with (a) varying L-(+)-Tartaric acid concentration in the presence of 0.1 M Py and (b) varying Py concentration in the presence of 0.7 M L- (+)-Tartaric acid. L-(+)-Tartaric acid concentrations in (a): (i) 0.1, (ii) 0.2, (iii) 0.3, (iv) 0.4, (v) 0.5, (vi) 0.6, and (vii) 0.7 M. Py concentrations in (b): (i) 0.1, (ii) 0.2, (iii) 0.3, (iv) 0.4, and (v) 0.5 M.

The conditions for achieving optimum PPy coatings on SS plates with L-(+)-Tartaric acid are summarised in Table 3.1.

Table 3.1 Optimum activation and stabilisation potentials obtained for PPy formation on SS plate from L-(+)-Tartaric acid with different Py concentrations.

Acid/Salt	Concentration (M)	Py Concentration (M)	Activation Potential (Ea/V)	Stabilisation Potential (Es/V)
L-(+)-Tartaric acid	0.7	0.4	0.704	0.658

3.3.2 PPy coating characterisation

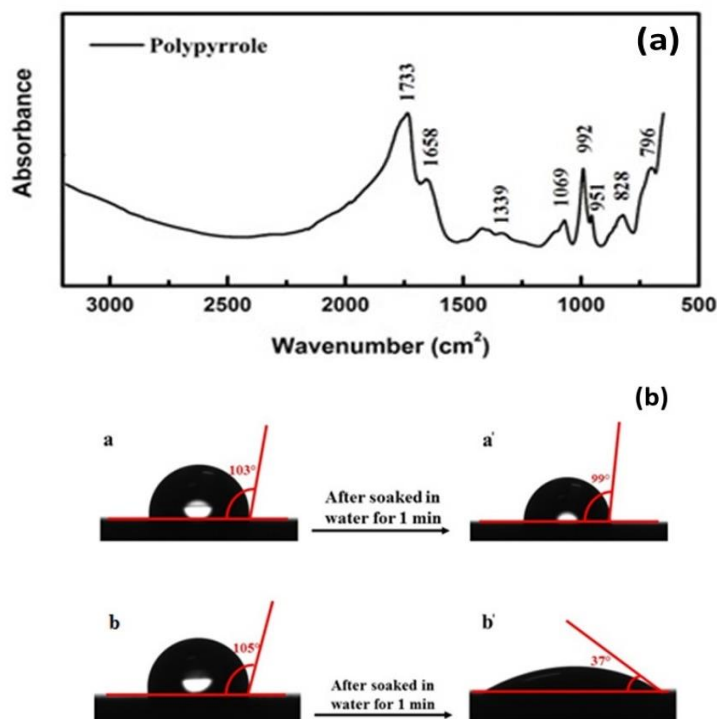
3.3.2.1 Fourier Transform Infrared Spectroscopic Studies of PPy Films

Infrared analysis was carried out on the PPy film synthesised from 0.4 M Py and 0.7 L-(+)-Tartaric acid concentrations. To identify the spectral effect on PPy film. (Only spectra of PPy formed from L-(+)-Tartaric acid is shown). The spectra (Fig. 3.2a) with Gaussian deconvolution of absorption bands centered at 1733 cm^{-1} are assigned to the free and site-specific interactions of the carbonyl group [23]. The strong band observed at 1658 cm^{-1} are attributed to the C=O stretch. The

absorption peak at 1658 cm^{-1} was due to a -C=O linkage in the PPy film. The C=O structure at the $\beta\text{-C}$ of pyrrole ring is typically due to the oxidation of polypyrrole [24]. The bands at 1339 and 1069 cm^{-1} correspond to =C-H in-plane vibrations, while the band at 828 cm^{-1} is due to out of plane vibrations indicating polymerisation of pyrrole [25]. The bands located at 951 cm^{-1} are attributed to the C-H out of plane deformation of Py units. Thus, the FTIR spectroscopic study confirms the presence of PPy coating on the SS plate [24]. The peak at 796 cm^{-1} corresponds to C-H out of plane ring deformation [26]. Hence, the above characteristic peaks confirm the PPy film on SS.

3.3.2.2 Contact angle measurement

Fig. 3.2b shows contact angle of SS plate (a, a') and SS/PPy-P (b, b'). The SS plates show hydrophobic (103°) surface. Even after soaking (99°) in water it remained hydrophobic ($\theta > 90^\circ$). Its initial contact angle was 105° (hydrophobic $\theta < 90^\circ$), and after soaking in water, the contact angle dropped to 37° (hydrophilic, $\theta \leq 90^\circ$). So, the PPy coated SS plate has a tendency to become hydrophilic when exposing to the aqueous medium. This observation explains the significant differences in the coating resistance observed for the PPy coatings when exposed to an aqueous NaCl solution. The much higher change in coating resistance observed for the PPy-coated plate was clearly due to the stronger hydrophilic nature of the coating.



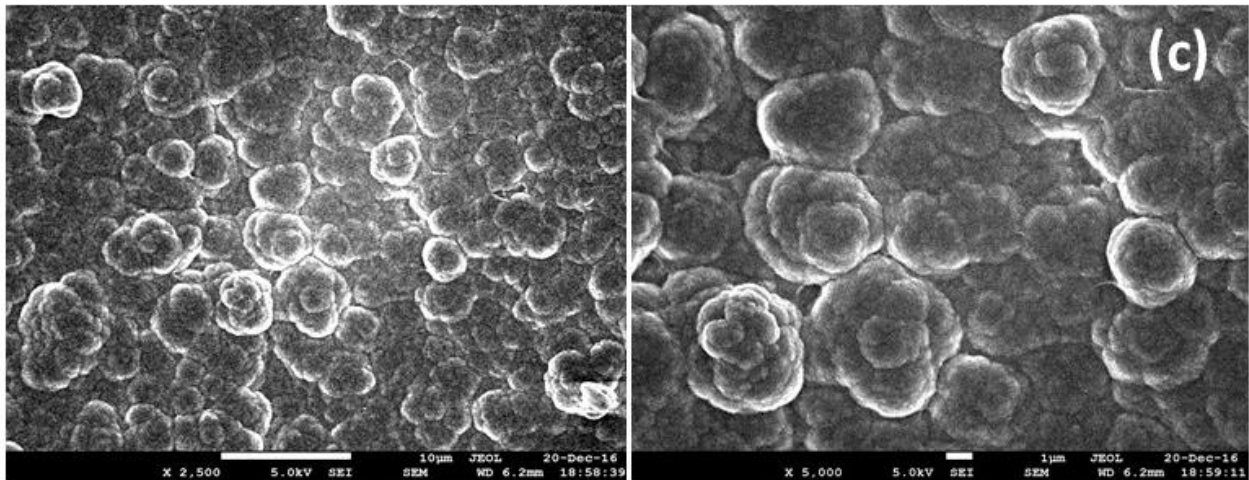


Fig. 3.2 Characterisation of PPy film on SS plate (a) FTIR spectra of PPy film on SS plate, and (b) Contact angle measurement of (i, i') SS plate and (ii, ii') PPy plate (c) SEM images of PPy on SS plate.

3.3.2.3 Scanning Electron Microscope

A scanning electron microscope was used to characterise the synthesised PPy on SS synthesised from galvanostatic electropolymerisation using 0.4 M PPy in 0.7 M L-(+)-Tartaric acid. The surface topography shows high surface nanofibers. The SEM micrographs reveal the PPy compact cauliflower structure as shown in Fig. 3.3c.

3.3.3 Evaluation of coating durability by time-dependent electrochemical spectroscopy

As the prime property displayed by conductive polymers is electrical conductivity, the use of electrochemical impedance spectroscopy was explored to evaluate the coating kinetics, coating stability and associated electrochemical reactions [27,28]. The equivalent circuit in Fig.3.3a used to assess R_{ct} . Both synthesised PPy coatings were immersed in a corrosive (0.1 M NaCl) solution at ambient temperature. The aim was to determine initial coating resistance and monitor change in coating resistance over a period in the corrosive solution. So, to achieve this goal, the samples were subjected, after every 24 hrs. EIS measurements at varying scanning frequency from 1 MHz to 10 mHz. The collected data was analysed with the EC lab software. The R_{ct} was estimated using an equivalent circuit (shown in Fig. 3.3a). The R_{ct} change was monitored for 7 days. The change in coating resistance is shown in Fig. 3.3b. Bode plots suggest that the response was shifted from

a higher frequency to lower frequency over a period due to stimulated defects in the coating at the place where water molecules and ions easily transferred through the film. The frequency response and bode plot is given in Fig. 3.3 a and b, respectively. R_{ct} can be attributed to the charge transfer resistance owing to the ionic transfer through the coating pores, and it normally decreases with the increase in the time. Electrolyte and oxygen penetrate through the cracks from coatings reach the metals which leading to the initiation of the deterioration [29].

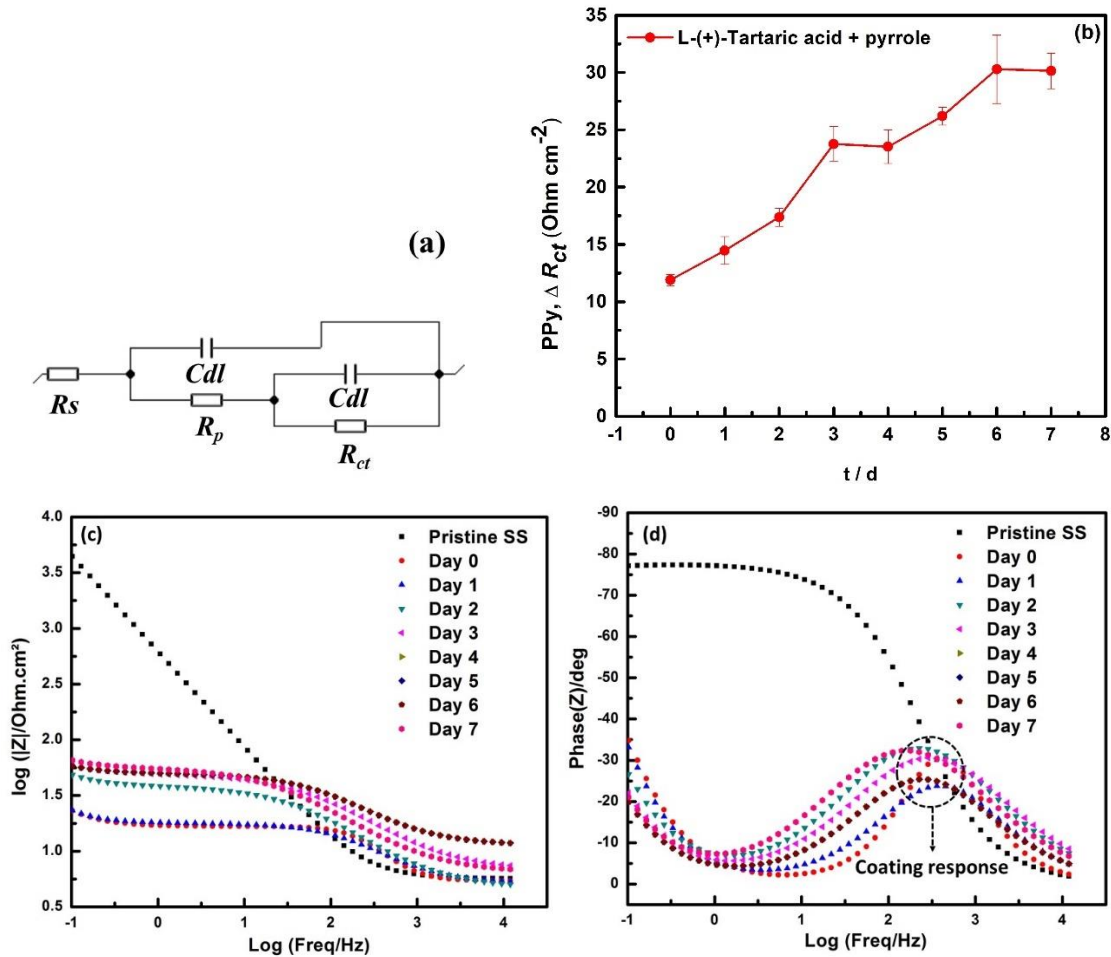


Fig. 3.3 Electrochemical analysis of PPy coating by time dependant electrochemical spectroscopy; a) The equivalent circuit utilised for impedance; b) Change in PPy charge transfer resistance as a function of time in 0.1 M NaCl; c) measurement Frequency dependences of the impedance and d) phase shift in the Bode plots of PPy film synthesised from 0.4 M pyrrole in 0.7 M L-(+)-Tartaric acid

Table 3.2 Change in charge transfer resistance [R_{ct} (Ohm.cm²)] for PPy formed in L-(+)-Tartaric acid.

Days	L-(+)-Tartaric acid (PPy)
0	11.89
1	14.46
2	17.37
3	23.75
4	23.52
5	26.19
6	30.28
7	30.14

3.4 Performance of microbial fuel cells

The uncoated SS plate (SS-P) and PPy coated SS plate (SS/PPy-P) anodes were explored for MFC performance. The MFCs operated in M9 media with 25 mM acetate and 4% landfill leachate as a source of bacteria. In a previous MFC study, it was demonstrated that landfill leachate is an efficient substrate for MFCs [19]. Two batch cycles were initially run without external resistance at ambient temperature to allow for the establishment of biofilm on the anodes. The maximum OCVs achieved with the SS-P anode were 608 ± 32 mV and 664 ± 27 mV from the first and second cycles, respectively. In contrast, the SS/PPy-P anode gave maximum OCVs of 355 ± 33 mV and 624 ± 47 mV from the first and second batch cycles, respectively. The OCV curves are shown in Fig. 3.4a. After two successive cycles, the MFCs were again fed with 25 mM sodium acetate, and an external resistor of 100 Ω was applied to both systems. The MFC with the SS/PPy-P anode did not show lag phase with the addition of fresh sodium acetate solution, which may be attributed to the successful biofilm formation during the two successive batch cycles conducted in the absence of an external resistance load. Remarkably, the SS/PPy-P system accomplished a successful start-up of the current generation on the first day, as shown in the current generation curves in Fig. 3.4b. A stationary current is observed during the current generation (~ 0.025 mA cm⁻²) for three days. After the stationary phase, a sharp fall in current was on the fourth day of the operation with the

SS/PPy-P anode, possibly due to the substrate depletion and generation of toxic substances from the bacterial metabolic activities.

In contrast, the MFC with the SS-P anode generated much less current. On the first day, only a current of $0.012 \pm 0.009 \text{ mA cm}^{-2}$ was produced. A later slow decline was observed for the remaining six days of operation. These findings prove that the use of the SS/PPy-P anode significantly lowers the startup time of the MFC due to the more efficient bacterial growth on the anode surface, as well as the efficient extracellular electron transfer from the biofilm to the anode. The polarisation curves obtained, as shown in Fig. 3.4c, on the third day of operation of the MFCs during the second batch cycle, revealed that the SS-P anode gave a P_{max} of $0.010 \pm 0.008 \text{ mW cm}^{-2}$ under $0.027 \pm 0.0022 \text{ mA cm}^{-2}$ current density normalised by cathode area. In contrast, as shown in Fig. 6d, the SS/PPy-P anode gave a P_{max} of $0.020 \pm 0.023 \text{ mW cm}^{-2}$ under $0.070 \pm 0.028 \text{ mA cm}^{-2}$ normalised by cathode area.

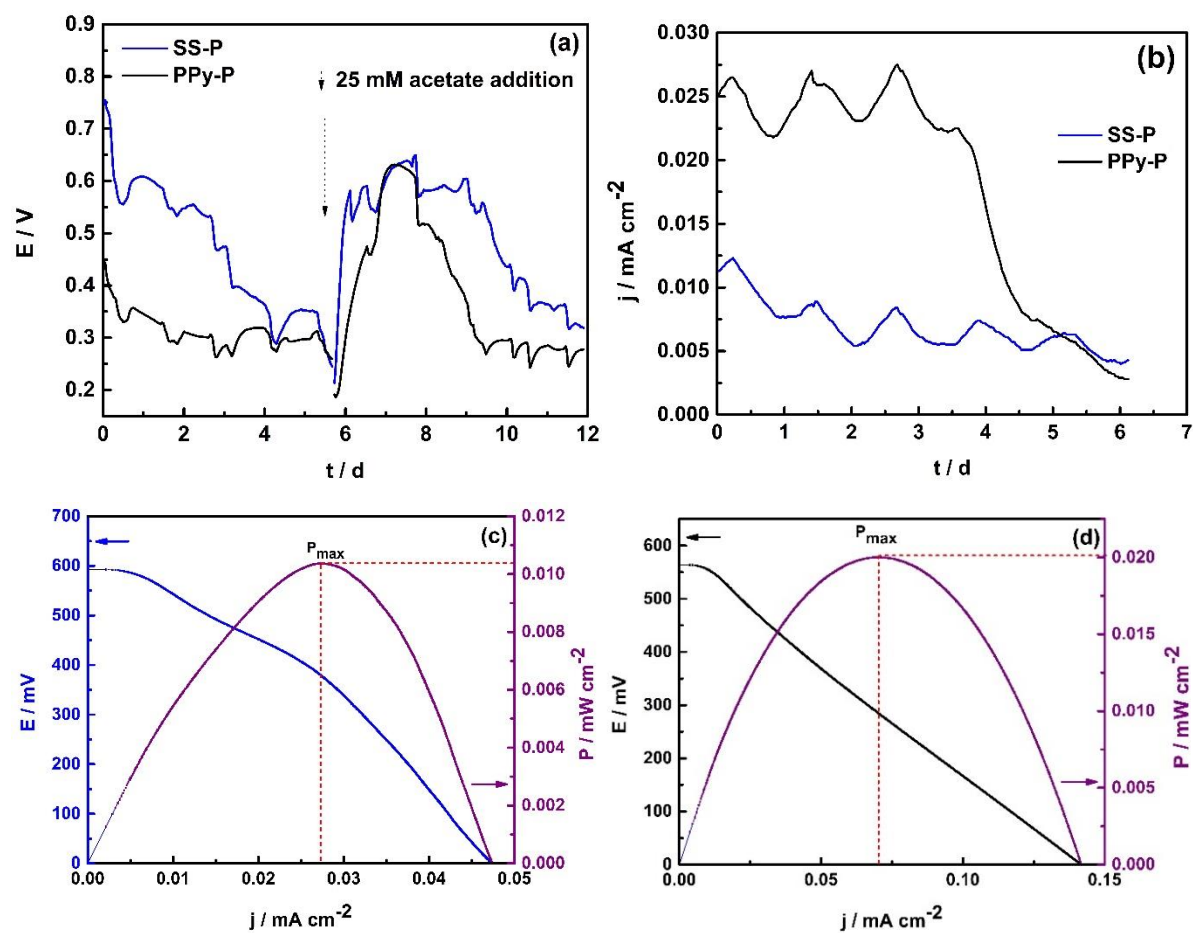


Fig. 3.4 Performance of the MFCs fortified with SS-P anode and SS/PPy-P anodes. a) Open circuit voltage output during the start-up phase of the MFCs system. b) current generation from MFCs

system by connecting $100\ \Omega$ across the cell. c) Polarisation curves of the MFCs with SS-P anode. d) Polarisation curves of the MFCs with SS/PPy-P anode.

3.5 Conclusion

The PPy coating on SS-304 has been successfully prepared by galvanostatic polymerisation of PPy monomer solution Py monomer solution 0.4 M Py in 0.7 M L-(+)-Tartaric acid under $2.5\ \text{mA cm}^{-2}$ constant current density for 15 mins. The coated PPy/SS-P after immersed in 0.1 M NaCl solution and the time-dependent $\text{EIS}_{(\text{TD})}$ performed after every 24 hours' time for seven days to study the change in coating resistance. The FTIR measurements confirm the formation of PPy on SS plate. Thus, suggesting a significant difference in the longevity of the coating in both dopant media. Therefore, PPy prepared in 0.4 M Py in 0.7 M L-(+)-Tartaric acid is qualified for long-term protection to corrosive media and could be useful for MFCs anode. 3D profilometry and Bode plots revealed the mechanism of coating deterioration over the time. The contact angle measurement with SS/PPy-P was hydrophobic and only became hydrophilic when immersed in water for few mins. The optimised SS/PPy-P anode in preliminary test in MFCs gave a P_{max} of $0.020 \pm 0.023\ \text{mW cm}^{-2}$, whereas SS-P anode produced a P_{max} of $0.010 \pm 0.008\ \text{mW cm}^{-2}$. The careful synthesis of PPy on SS is a crucial factor for achieving best MFC performance. However, long-term performance studies are required to achieve maximum power generation from SS/PPy-P anode MFCs in real wastewater. Further, PPy coating on high surface SS materials can be considered a better option for improving MFC performance.

References

- [1] P. Liang, M. Fan, X. Cao, X. Huang, Y. Peng, S. Wang, Q. Gong, J. Liang, [Electricity generation by the microbial fuel cells using carbon nanotube as the anode]., *Huan Jing Ke Xue= Huanjing Kexue.* 29 (2008) 2356–60. <http://www.ncbi.nlm.nih.gov/pubmed/18839600> (accessed November 5, 2017).
- [2] D. Ucar, Y. Zhang, I. Angelidaki, An overview of electron acceptors in microbial fuel cells, *Front. Microbiol.* 8 (2017) 643. doi:10.3389/fmicb.2017.00643.
- [3] A. Baudler, I. Schmidt, M. Langner, A. Greiner, U. Schröder, Does it have to be carbon? Metal anodes in microbial fuel cells and related bioelectrochemical systems, *Energy Environ. Sci.* 8 (2015) 2048–2055. doi:10.1039/C5EE00866B.
- [4] H. Yuan, Z. He, Graphene-modified electrodes for enhancing the performance of microbial fuel cells, *Nanoscale.* 7 (2015) 7022–7029. doi:10.1039/c4nr05637j.
- [5] Mustakeem, Electrode materials for microbial fuel cells: Nanomaterial approach, *Mater. Renew. Sustain. Energy.* 4 (2015) 22. doi:10.1007/s40243-015-0063-8.
- [6] C. Santoro, C. Arbizzani, B. Erable, I. Ieropoulos, Microbial fuel cells: From fundamentals to applications. A review, *J. Power Sources.* 356 (2017) 225–244. doi:10.1016/j.jpowsour.2017.03.109.
- [7] Y.-R. He, X. Xiao, W.-W. Li, G.-P. Sheng, F.-F. Yan, H.-Q. Yu, H. Yuan, L.-J. Wu, Enhanced electricity production from microbial fuel cells with plasma-modified carbon paper anode, *Phys. Chem. Chem. Phys.* 14 (2012) 9966. doi:10.1039/c2cp40873b.
- [8] A. Mahadevan, D.A. Gunawardena, S. Fernando, Technology and Application of Microbial Fuel Cells, *Technol. Appl. Microb. Fuel Cells.* (2014) 13–32. doi:10.5772/57200.
- [9] D. Pocaznoi, A. Calmet, L. Etcheverry, B. Erable, A. Bergel, Environmental Science Stainless steel is a promising electrode material for anodes of microbial fuel cells, (2012) 9645–9652. doi:10.1039/c2ee22429a.
- [10] J.M. Sonawane, A. Yadav, P.C. Ghosh, S.B. Adeloju, Recent advances in the development and utilization of modern anode materials for high performance microbial fuel cells, *Biosens. Bioelectron.* 90 (2017) 558–576. doi:10.1016/j.bios.2016.10.014.
- [11] J. Hou, Z. Liu, Y. Li, Polyaniline Modified Stainless Steel Fiber Felt for High-Performance Microbial Fuel Cell Anodes, *J. Clean Energy Technol.* 3 (2015) 165–169. doi:10.7763/JOCET.2015.V3.189.

- [12] R. Bin Song, Y.C. Wu, Z.Q. Lin, J. Xie, C.H. Tan, J.S.C. Loo, B. Cao, J.R. Zhang, J.J. Zhu, Q. Zhang, Living and Conducting: Coating Individual Bacterial Cells with In Situ Formed Polypyrrole, *Angew. Chemie - Int. Ed.* 56 (2017) 10516–10520. doi:10.1002/anie.201704729.
- [13] G. Gnana Kumar, C.J. Kirubaharan, S. Udhayakumar, K. Ramachandran, C. Karthikeyan, R. Renganathan, K.S. Nahm, Synthesis, structural, and morphological characterizations of reduced graphene oxide-supported polypyrrole anode catalysts for improved microbial fuel cell performances, *ACS Sustain. Chem. Eng.* 2 (2014) 2283–2290. doi:10.1021/sc500244f.
- [14] P. Pérez-Rodríguez, V.M. Ovando-Medina, S.Y. Martínez-Amador, J.A. Rodríguez-de la Garza, Bioanode of polyurethane/graphite/polypyrrole composite in microbial fuel cells, *Biotechnol. Bioprocess Eng.* 21 (2016) 305–313. doi:10.1007/s12257-015-0628-5.
- [15] X. Tang, H. Li, Z. Du, W. Wang, H.Y. Ng, Conductive polypyrrole hydrogels and carbon nanotubes composite as an anode for microbial fuel cells, *RSC Adv.* 5 (2015) 50968–50974. doi:10.1039/C5RA06064H.
- [16] W. Chen, Z. Liu, G. Su, Y. Fu, X. Zai, C. Zhou, J. Wang, Composite-modified anode by MnO₂/polypyrrole in marine benthic microbial fuel cells and its electrochemical performance, *Int. J. Energy Res.* 41 (2017) 845–853. doi:10.1002/er.3674.
- [17] S.-H. Roh, Electricity Generation from Microbial Fuel Cell with Polypyrrole-Coated Carbon Nanofiber Composite., *J. Nanosci. Nanotechnol.* 15 (2015) 1700–3. <http://www.ncbi.nlm.nih.gov/pubmed/26353717> (accessed December 10, 2016).
- [18] Y. Zou, C. Xiang, L. Yang, L.-X. Sun, F. Xu, Z. Cao, A mediatorless microbial fuel cell using polypyrrole coated carbon nanotubes composite as anode material, *Int. J. Hydrogen Energy.* 33 (2008) 4856–4862. doi:10.1016/j.ijhydene.2008.06.061.
- [19] J.M. Sonawane, S.B. Adeloju, P.C. Ghosh, Landfill leachate: A promising substrate for microbial fuel cells, *Int. J. Hydrogen Energy.* (2017). doi:10.1016/j.ijhydene.2017.03.137.
- [20] J.M. Sonawane, E. Marsili, P. Chandra Ghosh, Treatment of domestic and distillery wastewater in high surface microbial fuel cells, *Int. J. Hydrogen Energy.* 39 (2014) 21819–21827. doi:10.1016/j.ijhydene.2014.07.085.
- [21] F. Harnisch, C. Koch, S.A. Patil, T. Hübschmann, S. Müller, U. Schröder, Revealing the electrochemically driven selection in natural community derived microbial biofilms using flow-cytometry, *Energy Environ. Sci.* 4 (2011) 1265. doi:10.1039/c0ee00605j.

- [22] Y. Liu, F. Harnisch, K. Fricke, R. Sietmann, U. Schröder, Improvement of the anodic bioelectrocatalytic activity of mixed culture biofilms by a simple consecutive electrochemical selection procedure, *Biosens. Bioelectron.* 24 (2008) 1006–1011. doi:10.1016/j.bios.2008.08.001.
- [23] A. Ramoa, S. D. A. S.; Barra, G. M. O.; Merlini, C.; Livi, S.; Soares, B. G.; Pegoretti, Novel electrically conductive polyurethane/montmorillonite-polypyrrole nanocomposites, *Express Polym. Lett.* 9 (2015) 945.
- [24] P. Raotole, P.P. Patil, A.B. Gaikwad, Polypyrrole Coatings on Low Carbon Steel from Aqueous Oxalate Solution, *Int. J. Emerg. Technol. Adv. Eng.* 9001 (2250).
- [25] Template-free aqueous synthesis of conductive polymer nanoparticles, (2012).
- [26] Z. Li, J. Cai, P. Cizek, H. Niu, Y. Du, T. Lin, A self-supported, flexible, binder-free pseudo-supercapacitor electrode material with high capacitance and cycling stability from hollow, capsular polypyrrole fibers, *J. Mater. Chem. A.* 3 (2015) 16162–16167.
- [27] A.S. Sarac, M. Ates, B. Kilic, Electrochemical impedance spectroscopic study of polyaniline on platinum, glassy carbon and carbon fiber microelectrodes, *Int. J. Electrochem. Sci.* 3 (2008) 777–786.
- [28] A. Miszczyk, K. Darowicki, Use of impedance spectroscopy to evaluate the durability of protective coatings after thermal shock, *Corros. Sci.* 40 (1998) 663–672.
- [29] D. Ramesh, Evaluation of Corrosion Stability of Water Soluble Epoxy-Ester Primer through Electrochemical Studies, *Mater. Sci. Appl.* 03 (2012) 333–347.

Chapter 4

Electrokinetic behaviour of conducting polymer modified stainless steel anodes during the enrichment phase in microbial fuel cells

[Submitted and under review as, J.M. Sonawane, P.C. Ghosh, S.B. Adeloju, Electrokinetic behaviour of conducting polymer modified stainless steel anodes during the enrichment phase in microbial fuel cells, Electrochimica Acta, Elsevier, Accepted]

Nomenclature:

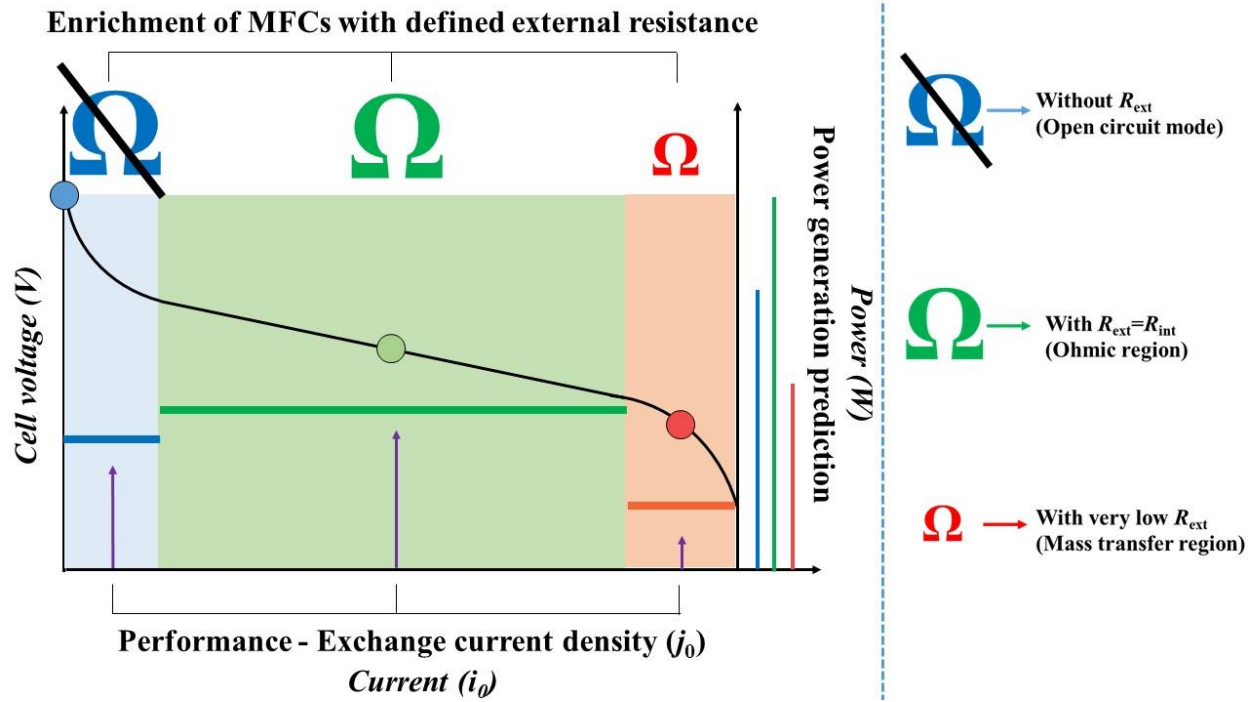
$(\neq R_{\text{ext}})$	Operated in activation region [No R_{ext} , Ω]
$(\gg R_{\text{ext}})$	Operated in mass transfer region [very low R_{ext} , Ω]
$(R_{\text{ext}}=R_{\text{int}})$	Operated in Ohmic region [$R_{\text{ext}}=R_{\text{int}}$, Ω]
F	Faraday's constant [$96,485 \text{ C mol}^{-1}$]
i_0	Exchange current [mA]
j_0	Exchange current density [mA cm^{-2}]
$j_{0\text{max}}$	Maximum exchange current density [mA cm^{-2}]
K_0	Rate constant [m s^{-1}]
R	Ideal gas constant [$8.31 \text{ J mol}^{-1} \text{ K}^{-1}$]
R	Resistance [Ω]
R_{ct}	Charge transfer resistance [Ω]
R_{ext}	External resistance [Ω]
R_{int}	Internal resistance [Ω]
T	Absolute temperature [K]
η	Overpotential [mV]

Abbreviation:

2D	Two dimensional
3D	Three dimensional
Ag/ AgCl	Silver/ silver chloride
ARB	Anode respiring bacteria
BV	Butler-Volmer equation
CNT	Carbon nanotubes
COD	Chemical oxygen demand
CPHs/CNTs	PPy hydrogels/carbon nanotubes
E	Electrode potential (mV)
EIS	Electrochemical impedance spectroscopy
FTIR	Fourier transform infrared spectroscopy
LSV	Linear sweep voltammetry
MFCs	Microbial fuel cells

OCV	Open circuit voltage
PAN	polyacrylonitrile
PANi	Polyaniline
PPy	Polypyrrole
PPy/AQDS	polypyrrole/anthraquinone-2,6-disulphonic disodium salt
PS	Polysaccharides
PSC	Potential step chronoamperometry
R_{ct}	Charge Transfer Resistance
R_s	Solution resistance
SS/PANi-P	Stainless steel coated polyaniline plate
SS/PANi-W	Stainless steel coated polyaniline wool
SS/PPy-P	Stainless steel coated polypyrrole plate
SS/PPy-W	Stainless steel coated polypyrrole wool
SS-P	SS plate
SS-P	Stainless steel plate
SS-W	Stainless steel wool
SS-W	Stainless steel wool
T	Temperature (K)
X_{red}	concentration of the redox couple (mM)

Graphical abstract



Abstract

Two of the major bottlenecks in achieving large-scale power generation with MFCs to date are the low power output and the usually long start-up time, both of which are mainly associated with poor bacterial kinetics and inefficient anode electrode materials. We have demonstrated in this study that the electron transfer kinetics of stainless steel (SS) can be significantly improved by modification with polyaniline (PANi) and polypyrrole (PPy). Furthermore, we have demonstrated that the kinetics of the bacterial growth can be significantly enhanced by the application of a carefully selected external resistance (R_{ext}), resulting in significantly shorter start-up time. The half-cell reactors used for the investigations were enriched under different conditions including without R_{ext} (Open circuit mode), with $R_{ext}=R_{int}$ (Ohmic region), and with very low R_{ext} (mass transfer region). The MFC anodes enriched under $R_{ext}=R_{int}$ gave maximum exchange current density (j_{0max}) on the 4th day of operation. The calculated j_{0max} for SS wool, PANi-wool, and PPy-wool anodes were $0.03 \pm 0.02 \text{ mA cm}^{-2}$, $1.05 \pm 0.04 \text{ mA cm}^{-2}$ and $0.5 \pm 0.04 \text{ mA cm}^{-2}$, respectively. The lowest charge transfer resistance (R_{ct}) of $0.23 \Omega \text{ cm}^{-2}$ was obtained with SS/PANi-wool anode which exhibited the highest electron transfer kinetics and better compatibility than SS/PPy-wool. The high current drawn from the system during the biofilm establishment phase did not support electroactive biofilm formation because it prevented the growing anode-respiring bacteria (ABR) from providing sufficient electron flow to the counter electrode.

4.1. Introduction

Over the past decade, electron transfer process in microbial fuel cells (MFCs) has been studied extensively [1–3]. It has been established that the imposition of external resistance (R_{ext}) influences the ability of the anode to act as an electron acceptor and electron flux through the circuit [4]. While it is known that the chosen electrode material influences the MFC performance, conductivity, and the nature of the resulting biofilm [5,6], its anodic performance can also be controlled by imposing an external resistance to the system [4,7]. When applied, the external resistance directly influences the current generation and the removal of chemical oxygen demand (COD) by controlling the flow of electrons from the anode to the cathode [8,9]. Furthermore, the MFC design and operational conditions affect the bacterial dynamics and metabolism [10,11].

Although it has only recently been reported [12] that stainless steel (SS) is a promising electrode material for MFCs, it has been increasingly realised that there are several issues with the use of SS for this purpose. For example, when compared with carbon-based anode materials, SS has poor compatibility, which results in an inadequate electroactive bacterial colonisation on its surface. [13] However, it is possible to improve the better compatibility of SS by surface modification with conducting polymers [14–16]. Modification of SS plates with PANi and PPy films has been considered in some studies [13,17–20] for improving compatibility and increasing apparent surface area accessible for bacterial colonisation. In recent years, there has been an increasing interest in using conductive polymers as anode materials in MFCs. A SS-polyaniline (SS-PANi) anode has been used in a MFC [13], and 3D macroporous anodes were also constructed by coating PANi on a SS fibre felt. These modified electrodes provided large surface areas for microbes to grow in 3D, as well as providing a large electrochemically active surface area for reaction and interfacial electron transfer [13]. HSO_4^- doped polyaniline modified carbon cloth anode has been successfully used to achieve a maximum power density of $0.0056 \text{ mW cm}^{-3}$ [21]. Also, the required start-up time was reduced by two days, and the R_{int} decreased from 261Ω to 90Ω [22]. Also, PPy and nanostructured PPy have been employed as anodes in MFC [23]. In another case, a composite electrode with poly(methylene blue) and PPy electrodeposited onto a stainless steel electrode was used in MFCs [24].

Molognoni et al. [25] have recently demonstrated the influence of external resistance on the start-up time of MFC. By matching R_{ext} with internal resistance (R_{int}) upon application of the calculated resistance, it has been demonstrated that MFC power output and coulombic efficiency were

increased. Furthermore, the maximum flow of electrons from the anode to the cathode can also be reduced by application of R_{ext} . Therefore, to minimise energy losses, it is desirable to operate an MFC at an optimal resistance where $R_{\text{ext}}=R_{\text{int}}$. [25]. Remarkably, it has been reported that the influence of R_{ext} on pure culture MFC is not significant since it is limited for defined electron transfer process [26,27]. However, the application of R_{ext} is important for mixed culture communities because of its complex and synergistic current generation from various communities of bacteria in the same growing condition. Some studies have suggested that the cellular electron transfer rate is higher with the application of a larger external load which resulted in a thick mature biofilm, whereas poor biofilm developed at lower R_{ext} . [27,28] As the R_{ext} of the system affects the substrate consumption by the bacterial community, it also directly influences the kinetics of the bacterial community and the overall anode kinetics [4,9]. Therefore, the application of R_{ext} directly affects the enrichment of bacterial communities at different R_{ext} [29]. Many researchers have studied the influence of R_{ext} on the microorganism growth and diversity [8,9,27]. It was observed that when enriched under lower R_{ext} , the biomass produced in the MFC was less than in conventional anaerobic digestion [8]. So, it is possible to trace the complexity of anodes used in MFCs. Most studies concluded that a change in microorganism diversity was observed when applied external resistance was changed [4,9,29,30]. However, the effect of the imposition of external resistance on the electrokinetic behaviour of conducting polymer-modified SS electrodes, as well as its role in facilitating microorganism diversity and its influence on start-up time when used in MFCs, has never been considered. This may be critical for the successful adoption of conducting polymer-modified SS anodes for achieving optimum MFC performance.

In a previous study [20], we demonstrated the use of polyaniline (PANi) modified stainless steel plates (SS-Ps) as low-cost anodes for MFCs and achieved a reasonably efficient microbial growth and retention of long-term stability. In the present study, we explore the use of two conducting polymers, PANi and PPy, for surface modification of SS electrodes as a basis for improving their biocompatibilities, surface area and performance. To understand the influence of the nature of the chosen SS material on the achieved performances, we considered two types of stainless steel as SS plate (SS-P) and SS wool (SS-W). The performances of the resulting SS-P, SS-W, SS-PANi-P, SS-PANi-W, SS-PPy-P and SS-PPy-W electrodes were investigated as anodes for MFCs. The effect of the imposition of R_{ext} on electroactive bacterial kinetics in terms of exchange current densities were studied by using a M9 media and landfill leachate as the source of bacteria.

Electrochemical measurements, such as anodic Tafel plots, and electrochemical impedance spectroscopy were employed to gain a more detailed understanding of the kinetic behaviour of the bacterial community under different operating conditions with the SS, SS-PANi and SS-PPy anodes. Furthermore, to gain a full understanding of the complexity of biofilm formation on the anodes under various operating conditions, Fourier transform infrared spectroscopy (FTIR) spectroscopy was employed.

4.2 Experimental

4.2.1 Synthesis of PANi and PPy on SS

A SS-304 sheet was purchased from Ladhani Metal Corporation (Mumbai, India). The SS sheet plates were polished progressively using metallographic abrasive paper with grit sizes of 320, 400, 600, 800 and 1200. The working electrode dimensions were 1.0 x 1.5 x 0.1 cm. The SS-W was purchased from a local market from Mumbai, India. The apparent surface area of the SS-W was 25 cm². All SS plates and wools were cleaned in absolute ethanol by ultrasonication for 15 mins. For modification of SS with polyaniline (PANi) and polypyrrole (PPy), reagent grade 0.4 M aniline monomer and 0.4 M pyrrole monomer solution were used in 0.7 M nitric acid and 0.7 M L-(+)-Tartaric acid, respectively (Sigma-Aldrich, Melbourne, Australia). PANi and PPy were synthesised by galvanostatic polymerisation of the monomer solutions at an applied constant current of 2.5 mA cm⁻² for a polymerisation time of 15 mins.

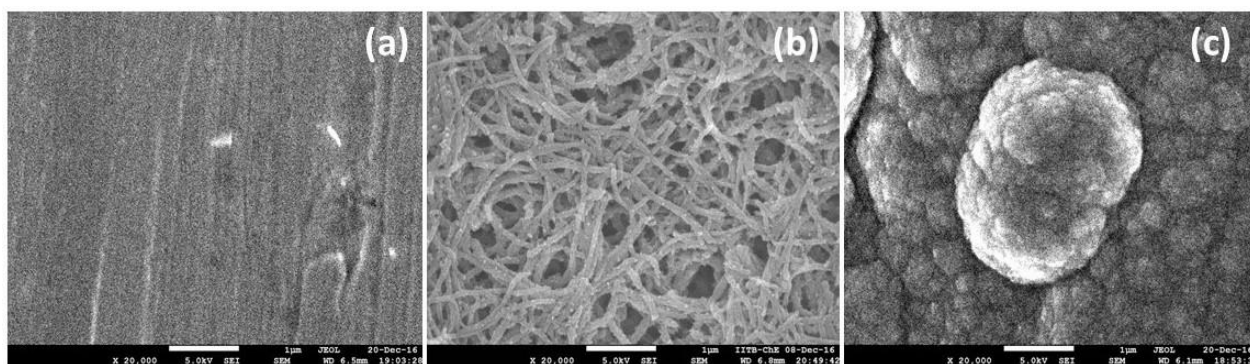


Fig. 4.1 Characterisation of anode materials by SEM. (a) Pristine SS, (b) SS-PANi, and (c) SS-PPy.

The scanning electron micrographs obtained from the pristine SS, SS-PANi, and SS-PPy are shown in Fig. 4.1. It is obvious from the micrographs that the coating of SS with PANi and PPy

resulted in distinct morphological changes that are consistent with those attributed to each conducting polymer.

4.2.2 MFC configuration

All experiments were performed with eighteen identical MFC half cells made of plastic reagent bottles (each with an empty bed volume of 50 mL). The cells were housed with a SS-P, SS-W, SS-P coated with PANi (SS/PANi-P), SS-W coated with PANi (SS/PANi-W), SS-P coated with PPy (SS/PPy-P), and SS-W coated with PPy (SS/PPy-W). Miniature Ag/AgCl electrodes (RRPEAGCL, Pine Research Instrumentation, Durham, USA) were used as reference electrodes. A titanium mesh was used as a counter electrode in each cell. For all electrochemical measurements, a potentiostat (VMP3, Biologic, Claix, France) fitted with EC-Lab Software V10.44 for data processing was used. All cells and M9 solutions were sparged with nitrogen for 10 mins to remove oxygen before the commencement of each experiment.

4.2.3 Operation

Triplicate of each MFC with the different SS anodes were enriched using a M9 media [31] under different conditions and 25 mM sodium acetate served as a sole carbon source. 4% Landfill leachate was used as inoculum in the M9 media, as previously demonstrated that landfill leachate is a promising feed for MFCs [32]. The landfill leachate was sampled from a local landfill site (Suez Environment, Melbourne, Australia). The M9 media + 4% landfill leachate and the cells were sparged with nitrogen gas for ten minutes to maintain anaerobic conditions inside the cells. Fig. 4.2 provides the graphical representation of a typical polarisation curve and the operating points employed for all MFCs at the defined resistor. Typical MFCs follows kinetic losses such as activation, Ohmic, and mass transfer losses [33,34]. In order to simulate similar conditions, we enrich electrogenic bacterial growth on each anode by applying specific external resistance during the enrichment step. The MFCs enriched without externally applied resistance is referred to as enrichment in the activation region. Those enriched when $R_{\text{ext}}=R_{\text{int}}$ is referred to as enrichment in the Ohmic region, while those enriched with the application of very low external resistance is referred to as enrichment in the mass transfer region. All MFCs were enriched in triplicate under each condition with each for seven days in an incubator at 37 °C.

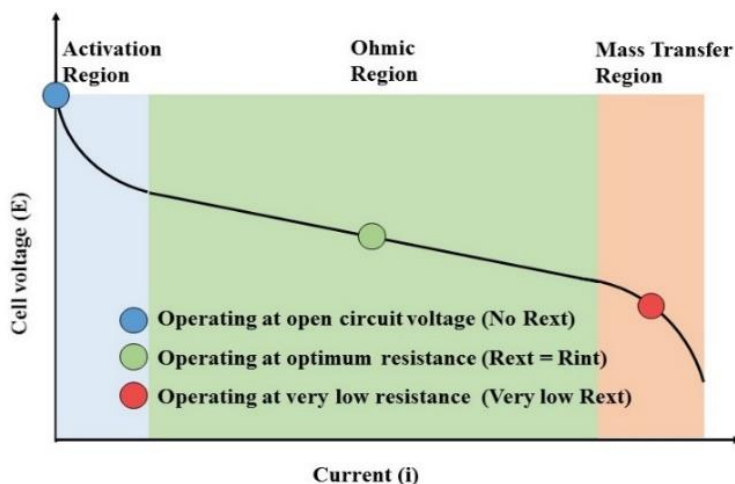


Fig. 4.2 Operating points employed for MFC performance evaluation: 1. All sets of MECs enriched in the activation region (without external resistance) 2. All sets of MECs enriched in the Ohmic region, where $R_{ext}=R_{int}$ 3. All sets of MFCs enriched with the application of very low resistance in the mass transfer region.

4.2.4 MFC performance evaluation

4.2.4.1 Maximum current generation from the different SS anodes

All cells with SS anodes as working electrodes and titanium mesh as the counter electrode were connected to the potentiostat for chronoamperometric measurements to determine the maximum current generated from each cell. Potential step chronoamperometry (PSC) was used to evaluate the maximum currents passed through the working electrodes. The voltage applied to the working electrodes was varied from 100 mV to 0.7 V for 10 s with Ag/AgCl electrode as a reference electrode. The voltage step was 0.100 V, and the current was recorded at 5 μ A interval. The maximum current flow was recorded for each anode (working electrode). By Ohm's law, the required applied resistance was calculated for each anode from the maximum current. Table 4.1 provides the applied resistance employed with each anode for a seven day period.

4.2.4.2 Electrochemical characterisation

Anodic Tafel plots were recorded for all cells on day zero after immediate addition of substrate. After performing electrochemical measurements, the desired resistances were connected to the respective cells placed in an incubator at 37 $^{\circ}$ C. The MFCs were enriched for 23 hrs to permit microbial colonisation on the surfaces of the anodes without disturbance. Afterward, the applied resistance was carefully detached from each cell, and all MFCs were left to stabilise for 1 hour at

ambient temperature to reach maximum open circuit potential. Then, further electrochemical measurements were conducted on the cells to identify the effect of the incubation time and applied R_{ext} on the bacterial community. EIS was used to determine noticeable changes in the impedance, while LSV was employed to obtain Tafel curves. After these measurements, all MFCs were again re-connected to the same resistance values used previously and then enriched for a further 23 hrs. This procedure was repeated until the measured electrochemical performances had completely depreciated. Then, time-dependent electrochemical impedance spectroscopy was employed for measuring observable changes in impedance of all MFCs. All measurements were recorded in an open circuit mode. All anodes were employed as working electrodes and used each time in conjunction with a Ag/AgCl as a reference electrode and a titanium mesh as a counter electrode. The EIS measurement was conducted to identify the effect of electrogenic bacterial enrichment, which resulted from the applied R_{ext} , on changes in the impedance measurements. The measurement was conducted at a frequency of 100 MHz to 10 mHz and a sinus amplitude of 10 mV at 6 points per decade. The cells were run again for 15 minutes in OCV mode. Subsequently, Tafel plots were recorded for each cell by sweeping the voltage from open circuit potential to 150 mV at a scan rate of 1 mV s⁻¹. After application of an overpotential (η), positive deviation from OCV to 150 mV shows an initial lag of η and further Tafel lines became linear. By using the Tafel equation, the X-axis intercept is the log of the current exchange densities ($\ln j_0$). The Tafel plots were analysed by using the EC-Lab® software (Bio-Logic Science instruments). Similar control experiments were run in the sterile M9 media. A slight variation of the coatings in the M9 media was observed. All the experimental values were corrected by subtracting the results obtained for the control experiments.

4.2.4.3 Tafel Plot

Tafel plot, as derived from the equation below [35], was employed for measurement of the reaction kinetics at the various anodes:

$$\ln\left(\frac{i}{i_0}\right) = \beta\left(\frac{F\eta}{RT}\right)$$

where i_0 is exchange current density, i is the electrode current density (mA m⁻²), α is the electron transfer coefficient, R is the ideal gas constant (8.31 J mol⁻¹ K⁻¹), F is the Faraday's constant (96,485 C mol⁻¹), T is the absolute temperature, K and η is the activation overpotential. Ag/AgCl

electrode was used as the reference electrode and was placed in the half-cell of the MFC during the measurements. The purpose of using Tafel plot was to calculate the i_0 and R_{ct} values. The i_0 is a fundamental parameter in the rate of electrooxidation or electroreduction of a chemical species at an electrode in equilibrium. The charge transfer resistance (R_{ct}) was calculated from the following equation: [36]

$$R_{ct} = \frac{RT}{nFi_0}$$

where n is the number of electrons.

By analysis of the Tafel plot, the exchange current density (j_0) was calculated. Based on the Tafel-type linear equation obtained from the graphs, the slope was F/RT , and the y-axis intercept was the logarithm of the exchange current.

4.2.4.4 Polarisation behaviour of the anodes

Electrochemical measurements, including the polarisation behaviour of the anodes (Tafel plots), were carried out to determine the electrokinetics of the anodes in individual MFCs under variable enrichment conditions. MFCs were enriched under three conditions: (i) at activation zone without applied resistance (OCV, $\neq R_{ext}$), (ii) at Ohmic region, where $R_{ext}=R_{int}$, and (iii) in the mass transfer zone, i.e., very low R_{ext} ($\gg R_{ext}$). The EIS results revealed a significant change in impedance for the different anodes under the varying conditions.

For each cell, the Tafel plot was recorded after 24 hours as described in section 2.4.2, the exchange current density, j_0 , was determined by extrapolation to $\eta = 0$ of linear regression ($R^2 > 0.99$) from $\eta = 0 - 150$ mV. By applying 150 mV overpotential to the working electrode, the j_0 values then depend on charge limited electrochemical process where mass transfer is limited during the measurement. As j_0 is indicative of the rate of electron exchange between the bacterial cells at equilibrium, a higher j_0 value would indicate the involvement of a faster electron exchange rate, [37] a lower activation energy barrier for forward reaction and a high electrochemical reaction rate [37,38]. The j_0 trend can thus be correlated with the classical bacterial growth curve during the start-up phase of MFCs. The growth curve is solely based on bacterial kinetics which occurs in a few hours or days, and it depends on several intrinsic and extrinsic factors [39].

4.2.4.5 Fourier transform infrared spectroscopy (FTIR)

Vertex 80 (Bruker Corporation) FTIR spectrometer was used to record FTIR spectra of pristine stainless steel (SS-304), SS/PANi and SS/PPy anodes after incubation in M9 media for seven days under various operating conditions. The measurements were performed at 22 °C in an air-conditioned room. The attenuated total reflectance (ATR) mode with a resolution of 4 cm⁻¹ was used to record all FTIR spectra. The recorded wavenumbers were in the range of 4000–650 cm⁻¹ for all samples. For each anode, three different points were examined intricately, and an average spectrum was calculated. The baseline corrections were made carefully, and peaks were determined with the aid of the Opus software (Bruker Corporation, Massachusetts, United States).

4.3 Result and discussion

4.3.1 Maximum current generation

The maximum currents produced with the SS-P, SS-W, SS/PANi-P, SS/PANi-W, SS/PPy-P and SS/PPy-W anodes were recorded by applying a linear sweep voltammetry to the individual anode from 0.1 to 0.7 V. The voltammograms showing the maximum current densities (j_{\max}) obtained for the different anodes are shown in Fig. 4.3. Evidently, the SS/PANi-P and SS/PANi-W anodes gave j_{\max} at 0.6 V. This is consistent with the j_{\max} obtained at 0.6 – 0.7 V in other studies [40,41]. Considering an applied voltage of 0.6 V, the respective j_{\max} for all anodes were used to calculate the resistance of the system. The j_{\max} obtained for SS-P, SS-W, SS/PPy-P and SS/PPy-W anodes were 0.26 ± 0.14 , 1.03 ± 0.11 , 1.12 ± 0.09 , and 6.41 ± 0.24 mA cm⁻², respectively. It was obvious from these results that the PPy coatings resulted in substantial increase in the j_{\max} by a factor of over 4-6, with the higher increase observed with the SS/PPy-W. In contrast, the PANi coatings resulted in higher j_{\max} values of 3.35 ± 0.24 mA cm⁻² and 8.75 ± 0.32 mA cm⁻² for the SS/PANi-P and SS/PANi-W anodes, respectively. These represent increases of between 8 and 13 due to the PANi coating. From the current obtained at 0.6 V, the applicable resistance (R) were calculated by using the Ohms law, and the resulting resistance values were considered as optimum ($R_{\text{ext}}=R_{\text{int}}$) for a maximum current generation for the respective anodes. All applied resistance were ± 10 % of calculated values from the I-V curve.

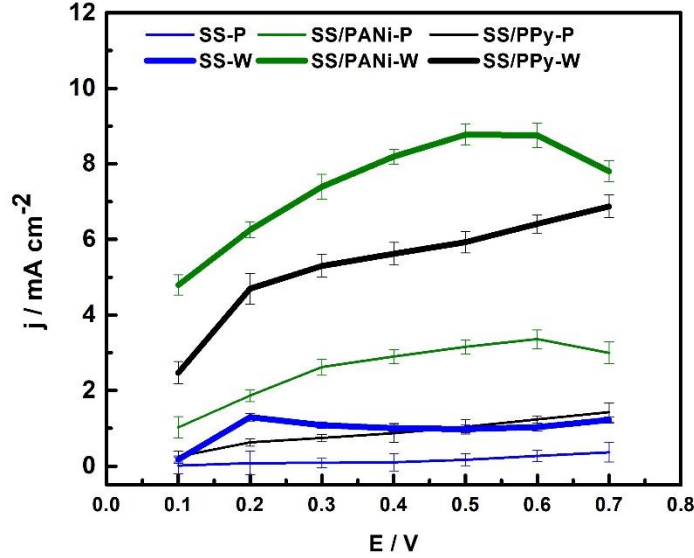


Fig. 4.3 I-V curves obtained with SS-P, SS-W, SS/PANi-P, SS/PANi-W, SS/PPy-P and SS/PPy-W anodes used to determine maximum current.

Table 4.1 Applied resistance to the MFCs for evaluation of kinetics under various conditions

Electrode	Mode of operation	R_{ext} (Ohm)	Electrode	Mode of operation	R_{ext} (Ohm)
SS-P	Without resistance	NA	SS-W	Without resistance	NA
SS-P	$R_{ext}=R_{int}$	800	SS-W	$R_{ext}=R_{int}$	100
SS-P	$R_{ext}=\text{very low}$	90	SS-W	$R_{ext}=\text{very low}$	10
SS/PANi-P	Without resistance	NA	SS/PANi-W	Without resistance	NA
SS/PANi-P	$R_{ext}=R_{int}$	60	SS/PANi-W	$R_{ext}=R_{int}$	10
SS/PANi-P	$R_{ext}=\text{very low}$	10	SS/PANi-W	$R_{ext}=\text{very low}$	5
SS/PPy-P	Without resistance	NA	SS/PPy-W	Without resistance	NA
SS/PPy-P	$R_{ext}=R_{int}$	200	SS/PPy-W	$R_{ext}=R_{int}$	20
SS/PPy-P	$R_{ext}=\text{very low}$	20	SS/PPy-W	$R_{ext}=\text{very low}$	5

4.3.2. Bioelectroperformance of anode materials during incubation

4.3.2.1 Exchange current densities of anode materials

All the anode materials were enriched under activation zone ($\neq R_{ext}$), external load with $R_{ext}=R_{int}$ and very low load under mass transfer mode. The j_0 values obtained under the various operating resistors are given in Table 2. The j_0 values obtained for SS-P system under OCV and mass transfer

conditions were similar, whereas relatively higher j_0 values were obtained when enriched under $R_{\text{ext}}=R_{\text{int}}$. The j_0 values obtained for MFC with SS-P anodes enriched without load were almost stable for 1-5 days before deteriorating. The system enriched under $R_{\text{ext}}=R_{\text{int}}$ reached a maximum j_0 on the 4th day, as shown in Fig. 4.4(a). The changes in j_0 values for all system is given in Fig. 4.4. It is important to note here that the $j_{0_apparent}$ referred to in this Fig. 4.4 is the exchange current density normalised by the actual surface area of the electrode instead of the electrochemical or BET surface area. A high electrogenic activity was observed when enriched at $R_{\text{ext}}=R_{\text{int}}$. All systems demonstrated a short lag phase followed by a transient exponential phase. Long stationary phase was observed without much increment upon enrichment in all SS-P systems.

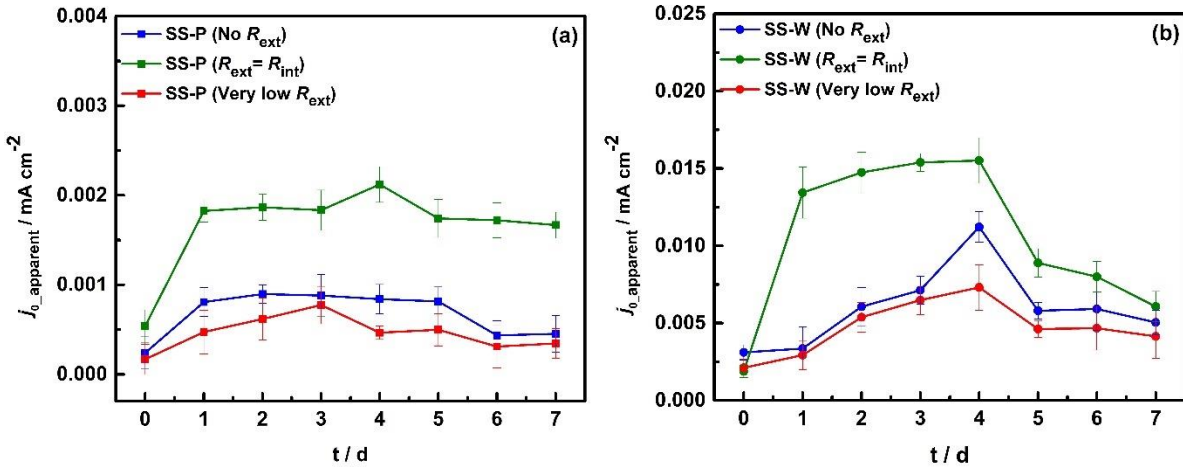


Fig. 4.4 Variation of j_0 values obtained for all SS based MFC systems with time. (a) MFCs with SS-P anodes, and (b) MFCs with SS-W anodes.

In contrast, the j_0 values obtained for SS-W system under OCV and mass transfer conditions, as given in Table 4.2, were distinctly different with the latter giving lower value, but the j_0 values obtained when enriched under $R_{\text{ext}}=R_{\text{int}}$ was also slightly higher. Fig. 4.4(b) shows that the data obtained from Tafel plot for SS-W anodes enriched in the activation zone ($\neq R_{\text{ext}}$), and in the mass transfer region ($\gg R_{\text{ext}}$) followed the same j_0 trend with a 24-hr lag phase. Both systems demonstrated a slow exponential phase with transient stationary phase, followed by a logarithmic decline. On the other hand, the MFCs with the SS-W anode enriched in the Ohmic region ($R_{\text{ext}}=R_{\text{int}}$) behaved differently with a j_0 value of $0.015 \pm 0.001 \text{ mA cm}^{-2}$. The variation of the j_0 of the MFC with the SS-W anode with time is shown in Fig. 4.4(b). The sudden increase in the j_0

observed on the 1st day for the SS-W anode enriched under $R_{ext}=R_{int}$ signified a transient lag phase where the bacteria on the surface has adjusted to the new environment. From day 1 to 3, an exponential phase was observed followed by a stationary phase for one day.

Table 4.2 shows that when coated with PANi, the j_0 values obtained for SS/PANi-P increased considerably for all conditions. Notably, the j_0 values obtained for the SS/PANi-P system under OCV and Ohmic region ($R_{ext}=R_{int}$) were similar, whereas the j_0 values obtained under mass transfer condition was evidently lower. From the Tafel plot, the variation of j_0 values for MFCs with SS/PANi-P anodes is shown in Fig. 4.5(a). The lag phase in j_0 obtained for all conditions showed similar trend on the first day of the enrichment. Upon further enrichment, the lag phase of j_0 was observed in the MFC enriched under OCV mode and $R_{ext}=R_{int}$. The stationary phase was observed for 2-4 days, 2-3 days and 3-4 days in the MFC systems enriched without ($\neq R_{ext}$), $R_{ext}=R_{int}$ and very low resistance ($\gg R_{ext}$), respectively. The death phase is followed by a stationary phase in all SS/PANi-P systems due to nutrient deficiency in the reactor.

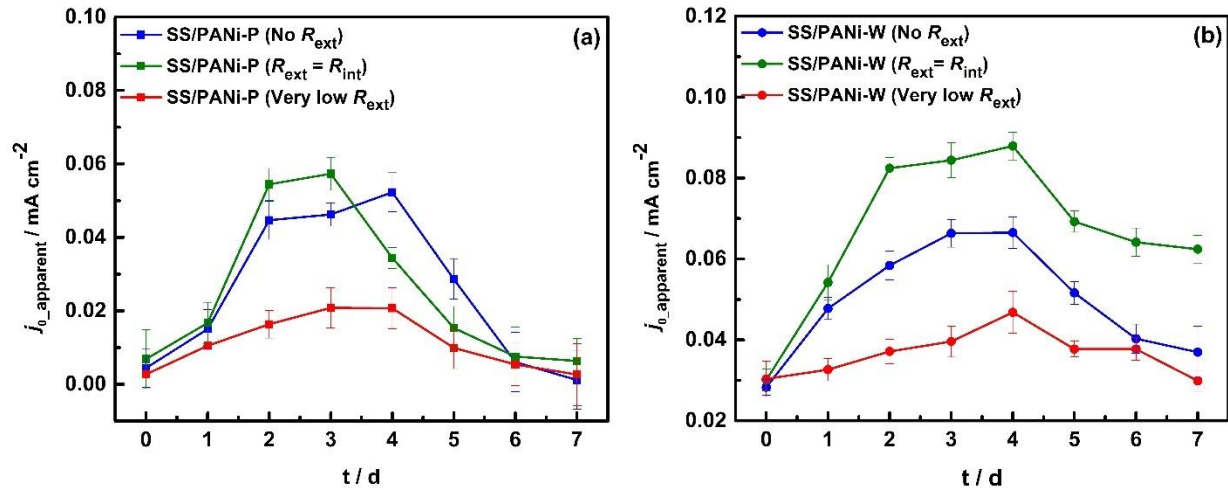


Fig. 4. 5 Variation of j_0 values obtained for all PANi anodes with time. (a) MFCs with SS/PANi-P anodes, and (b) MFCs with SS/PANi-W anodes.

Similarly, Table 4.2 shows that when coated with PANi, the j_0 values obtained for SS/PANi-W also increased considerably for all conditions. However, in this case, the j_0 values obtained for the SS/PANi-P system in the Ohmic region ($R_{ext}=R_{int}$) were higher than those obtained under OCV condition, but the j_0 values obtained under mass transfer condition was again evidently lower. Fig. 4.5(b) shows the variation of j_0 values obtained with the SS/PANi-W anodes under different conditions. Compared with the SS-W anodes, the SS/PANi-W anodes enriched under activation

zone ($\neq R_{\text{ext}}$) and $R_{\text{ext}}=R_{\text{int}}$ demonstrated a transient lag phase followed by an exponential phase. A reasonably stable j_0 phase was observed between the 3rd and 4th day. On the other hand, the anodes enriched under very low resistance demonstrated a lag phase for only one day, followed by a slow exponential phase. Under all conditions, the $j_{0\text{max}}$ was observed on the 4th day, and a logarithmic decline was observed after that.

Table 4.2 shows that the SS-P anodes coated with PPy resulted in a considerably less increase in the j_0 values than obtained with SS/PANi-P anodes for all conditions by a factor of 7-13. More importantly, the j_0 values obtained for the SS/PPy-P system in the Ohmic region ($R_{\text{ext}}=R_{\text{int}}$), under OCV condition, and under mass transfer condition were only slightly different, with the highest j_0 values obtained in the Ohmic region. The variation of $j_{0\text{max}}$ for SS/PPy-P anodes is shown in Fig. 4.5(a) and, notably, the highest j_0 was obtained under all conditions on the 4th day of enrichment.

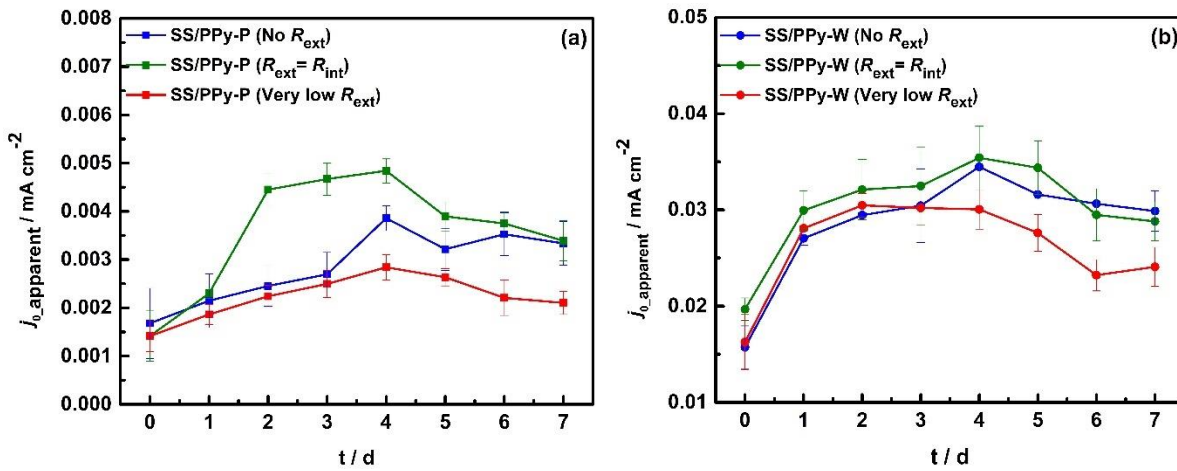


Fig. 4.6 Variation of j_0 values obtained for all PPy anodes with time. (a) MFCs with SS/PPy-P anodes, and (b) MFCs with SS/PPy-W anodes.

In contrast, Table 4.2 shows that the SS-W anodes coated with PPy resulted in a considerably more increase in the j_0 values than obtained for SS/PPy-P anodes for all conditions by a factor of 7-10. This was due to the larger surface area provided by the SS-W anode. However, the j_0 values obtained for the SS/PPy-W anodes in the Ohmic region ($R_{\text{ext}}=R_{\text{int}}$), under OCV condition, and under mass transfer condition were again only slightly different, with little difference between the highest j_0 values obtained in the Ohmic region and those obtained under OCV condition. Fig. 4.6(b) shows the variation of j_0 values obtained with the SS/PPy-W anodes. Again, the $j_{0\text{max}}$ values of the SS/PPy-W anodes were obtained on the 4th day of enrichment under all conditions.

All the SS/PPy-W anodes behave differently to the SS/PPy-P anodes under the different conditions with a transient lag phase. After enrichment for 24 hrs, all systems showed an exponential phase of j_0 values, followed by an extended stable phase from day 1 to day 4. Upon further enrichment, a slight logarithmic decline was observed in all cases after day 4. The results demonstrate that reasonably short start-up time is achieved by coating with a conducting polymer and this is attributed to the 3D surface in the MFC chamber. The lower and more stable j_0 values obtained with the SS/PPy-W anodes suggest that the anodes have relatively lower compatibility compared to the SS/PANi-W anodes. However, the SS/PPy-P anodes enriched under $R_{ext}=R_{int}$ followed a classical bacterial growth curve and, thus, suggests that the anodes required enrichment under optimised external resistance to avoid delay in the start-up phase. The anodes enriched under OCV and with very low resistance demonstrated an extended lag phase or start-up time, as well as indistinguishable exponential phase, stationary phase, and logarithmic decline even after enrichment for seven days. This indicates that long start-up time is required if the MFC is operated under OCV conditions or with very low external resistance.

Table 4.2 Changes in exchange current densities after incubation of MFCs with applied external resistance

Plate-based Anode materials and applied resistance		j_{0max} after incubation (mA cm ⁻²)	Wool-based Anode materials and applied resistance		j_{0max} after incubation (mA cm ⁻²)
SS-P			SS-W		
NA	($\neq R_{ext}$)	0.0008 ± 0.0004	NA	($\neq R_{ext}$)	0.011 ± 0.003
800 Ω	($R_{ext}=R_{int}$)	0.0021 ± 0.0004	100 Ω	($R_{ext}=R_{int}$)	0.015 ± 0.001
90 Ω	($\gg R_{ext}$)	0.0007 ± 0.0003	10 Ω	($\gg R_{ext}$)	0.007 ± 0.001
SS/PANi-P			SS/PANi-W		
NA	($\neq R_{ext}$)	0.052 ± 0.005	NA	($\neq R_{ext}$)	0.066 ± 0.003
60 Ω	($R_{ext}=R_{int}$)	0.057 ± 0.004	10 Ω	($R_{ext}=R_{int}$)	0.088 ± 0.003
10 Ω	($\gg R_{ext}$)	0.021 ± 0.005	5 Ω	($\gg R_{ext}$)	0.047 ± 0.005
SS/PPy-P			SS/PPy-W		
NA	($\neq R_{ext}$)	0.004 ± 0.003	NA	($\neq R_{ext}$)	0.034 ± 0.002
200 Ω	($R_{ext}=R_{int}$)	0.005 ± 0.003	20 Ω	($R_{ext}=R_{int}$)	0.035 ± 0.003
20 Ω	($\gg R_{ext}$)	0.003 ± 0.004	5 Ω	($\gg R_{ext}$)	0.030 ± 0.002

4.3.2.2 Charge transfer resistance of anode materials

The changes in the charge transfer resistance (R_{ct}) values for all the SS anodes used under (a) OCV mode ($\neq R_{ext}$), (b) the Ohmic region ($R_{ext}=R_{int}$) and (c) the mass transfer region ($\gg R_{ext}$) are given in Table 4.3. In all cases, the R_{ct} decreased considerably after enrichment for 2-4 days. Furthermore, as indicated by the data in Table 4.3, the R_{ct} was lowest for all SS-P and SS-W anodes after enrichment when operated in the Ohmic region ($R_{ext}=R_{int}$). Also, the coating of the SS-P and SS-W anodes with PANi and PPy resulted in considerable reduction of the R_{ct} , with the lowest reduction achieved with PANi coating. Thus, indicating that both the operation in the Ohmic region and the coating with conducting polymer considerably improved conductivity and supports improved electrokinetic behaviour of the anodes.

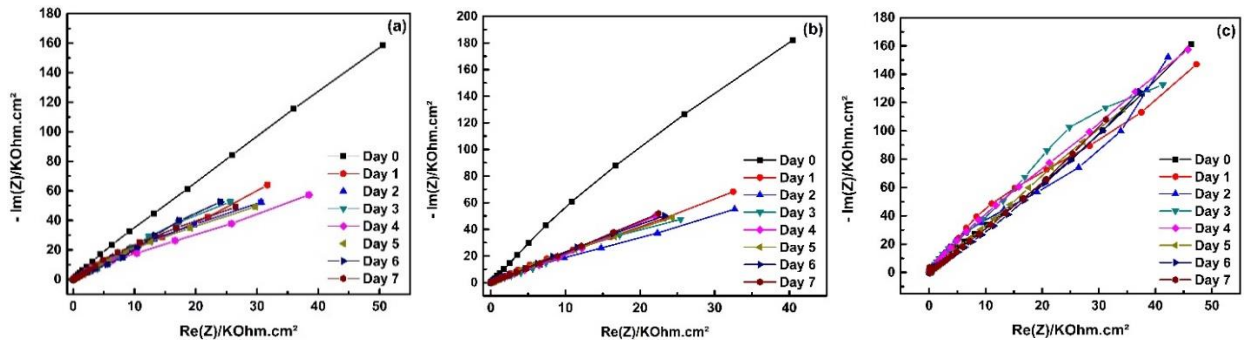


Fig. 4.7 EIS plots for stainless steel-based anodes. (a) the system operated under OCV mode, (b) system operated under $R_{ext}=R_{int}$, and (c) system operated under very low R_{ext} .

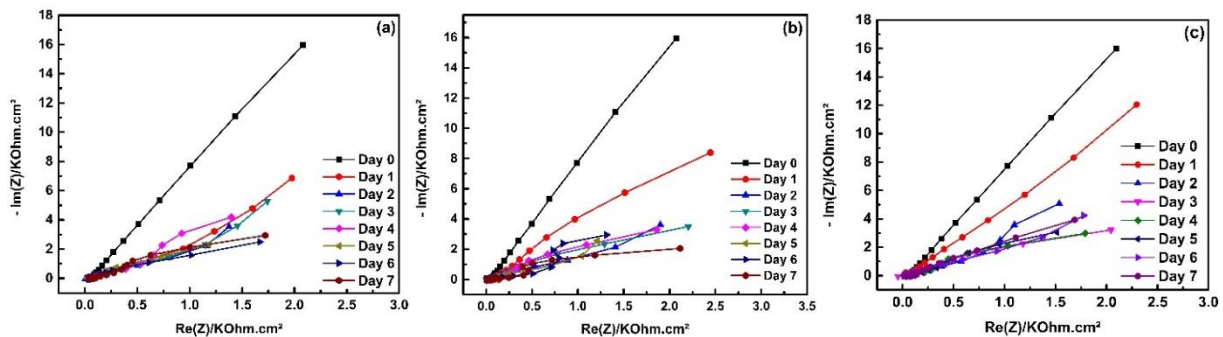


Fig. 4.8 EIS plots of SS wool-based anode system. (a) the system operated under OCV mode, (b) system operated under 100Ω , and (c) system operated under 10Ω .

For the SS-P anodes used under various conditions, the R_{ct} was lowest on the second and third day of operation. The low R_{ct} indicates that maximum electrokinetic activity was observed. The Nyquist plots obtained for the SS-P and SS-W systems enriched under the different conditions are shown in Fig. 4.7a-c, and Fig. 4.8a-c, respectively. The Nyquist plots of the SS-P systems revealed the dominance of mass transfer control, i.e., diffusion inactive electrode and an electrolyte which indicate a poor reaction kinetics. Changes in impedance were observed for the anodes enriched under activation region ($\neq R_{ext}$), and those enriched under the Ohmic region showed significant changes. However, a minuscule change in impedance was observed for those enriched under mass transfer zone. The change in R_{ct} as a function of time is given in Table 4.3, and 4.4 provides the observed changes in the R_{ct} for all plate-based and wool based anode as a function of time.

Table 4.3 Variation of charge transfer resistance (R_{ct}) in plate based anode system

Days	SS ($\neq R_{ext}$)	SS ($R_{ext}=R_{ext}$)	SS ($>>R_{ext}$)	PANi ($\neq R_{ext}$)	PANi ($R_{ext}=R_{ext}$)	PANi ($>>R_{ext}$)	PPy ($\neq R_{ext}$)	PPy ($R_{ext}=R_{ext}$)	PPy ($\neq R_{ext}$)
0	536	614	553	29.03	24.65	27.18	76.39	90.37	96.31
1	159	70.1	271	8.53	7.67	12.22	59.69	55.80	68.99
2	143	68.6	208	2.87	2.36	7.85	52.38	28.84	57.29
3	146	70.1	166	2.78	2.24	6.17	47.53	27.48	51.33
4	153	60.5	276	3.45	3.73	6.20	33.25	26.51	45.19
5	158	73.8	258	4.48	8.37	12.98	39.85	32.91	48.61
6	295	74.6	414	21.25	17.02	23.76	36.35	34.22	58.07
7	283	76.8	371	40.61	20.15	48.61	38.42	37.86	61.11

Plate based anode. ($R_{ct} / \Omega \text{ cm}^{-2}$)

($\neq R_{ext}$) - Operated at open circuit voltage (No R_{ext})

($R_{ext}=R_{ext}$) - Operated at optimum resistance ($R_{ext}=R_{int}$)

($>>R_{ext}$) - Operated at very low resistance (very low R_{ext})

The Nyquist plots obtained for the SS/PANi-P and SS/PANi-W systems enriched in the activation zone ($\neq R_{ext}$), Ohmic region ($R_{ext}=R_{int}$) and the mass transfer region ($>>R_{ext}$) are shown in Fig. 4.9(a-c), and Fig. 4.10(a-c), respectively. When compared with the SS/PANi-P systems, the Nyquist plots obtained for the SS/PANi-W systems demonstrated similar characteristics with significantly lower impedance values. The change in the R_s for all MFCs with the SS/PANi-W anodes upon incubation is indicative of the high bacterial growth in the cells which altered the pH of the M9 media. Since the cells were in a single chamber, no proton was consumed at the cathode.

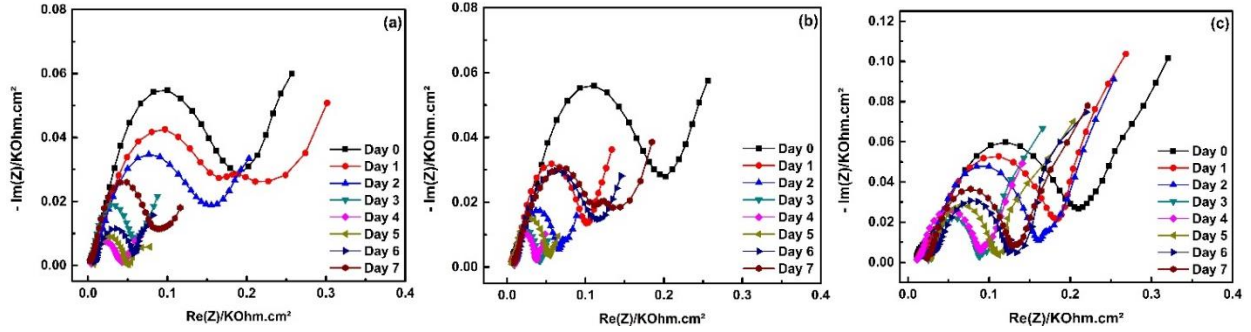


Fig. 4.9 EIS plots of PANi based anode system. (a) the system operated under OCV mode, (b) system operated under 60Ω , and (c) system operated under 10Ω .

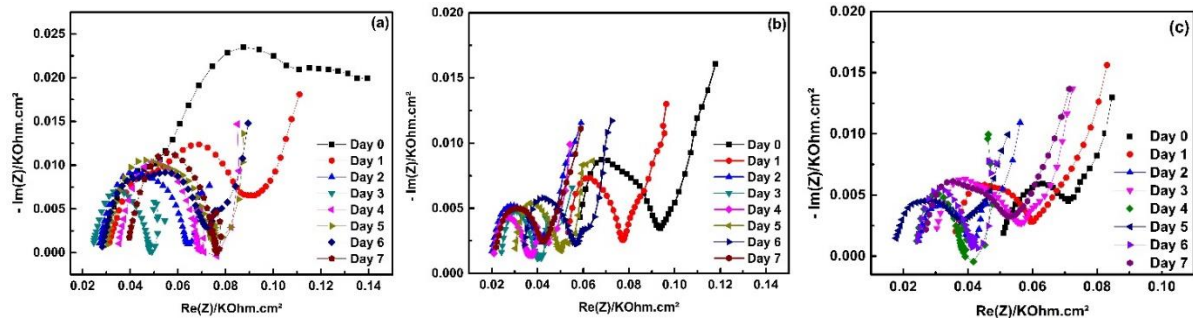


Fig. 4.10 EIS plots of SS-PANi-W based anode system. (a) the system operated under OCV mode, (b) system operated under 10Ω , and (c) system operated under 5Ω .

The Nyquist plots obtained for the SS/PANi-P anodes, when compared with the SS-P anodes, revealed faster charge transfer kinetics and the processes were under kinetic control with recessive mass transfer control. Also, the observed semi-circle under the high-frequency regions indicates the capacitive behaviour of the electrodes in all conditions. Changes in impedance were observed in all systems to a different degree and, thus, indicate that biofilm was grown on the anode surfaces. Table 4.5 provides the observed changes in the R_{ct} for all SS/PANi-P anodes as a function of time.

Table 4.4 Variation of charge transfer resistance (R_{ct}) in SS-wool based anode system

Days	SS ($\neq R_{ext}$)	SS ($R_{ext}=R_{ext}$)	SS ($\gg R_{ext}$)	PANi ($\neq R_{ext}$)	PANi ($R_{ext}=R_{ext}$)	PANi ($\gg R_{ext}$)	PPy ($\neq R_{ext}$)	PPy ($R_{ext}=R_{ext}$)	PPy ($\neq R_{ext}$)
0	41.3	39.3	51.8	4.54	4.26	4.23	8.16	6.52	7.89
1	38.3	9.5	43.8	2.69	2.37	3.93	4.75	4.29	4.57
2	21.1	8.7	23.9	2.20	1.56	3.46	4.36	4.00	4.21
3	18.0	8.3	19.8	1.93	1.52	3.24	4.22	3.95	4.25
4	11.4	8.3	17.6	1.93	1.46	2.74	3.72	3.63	4.27
5	22.1	14.4	27.8	2.49	1.85	3.40	4.06	3.73	4.65
6	21.7	16.0	27.5	3.19	2.00	3.40	4.19	4.35	5.53
7	25.4	21.1	30.9	3.47	2.06	4.29	4.30	4.46	5.33

Wool based anode. ($R_{ct} / \Omega \text{ cm}^{-2}$)

($\neq R_{ext}$) - Operated at open circuit voltage (No R_{ext})

($R_{ext}=R_{ext}$) - Operated at optimum resistance ($R_{ext} = R_{int}$)

($\gg R_{ext}$) - Operated at very low resistance (very low R_{ext})

The Nyquist plots obtained for the SS/PPy-P anodes enriched in the activation zone ($\neq R_{ext}$), Ohmic region ($R_{ext}=R_{int}$) and in the mass transfer region ($\gg R_{ext}$) are shown in Fig. 4.11(a-c) and Fig. 4.12(a-c), respectively. The Nyquist plots obtained for the SS/PPy-W anodes demonstrated similar behaviour to those of the SS/PPy-P anodes, but with significantly lower impedance values. Interestingly, the R_s also changed considerably upon enrichment for all SS/PPy-W anodes as for the SS/PANi-W anodes.

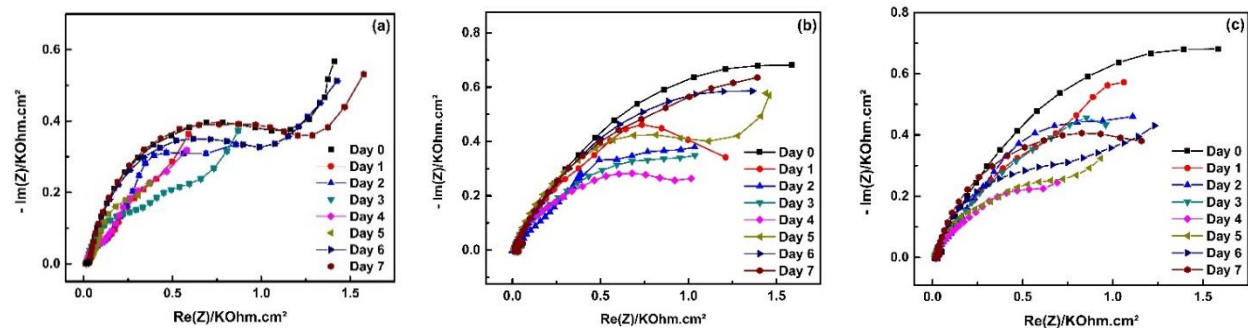


Fig. 4.11 EIS plots of PPy based anode system. (a) system operated under OCV mode, (b) system operated under 200 Ω , and (c) system operated under 20 Ω .

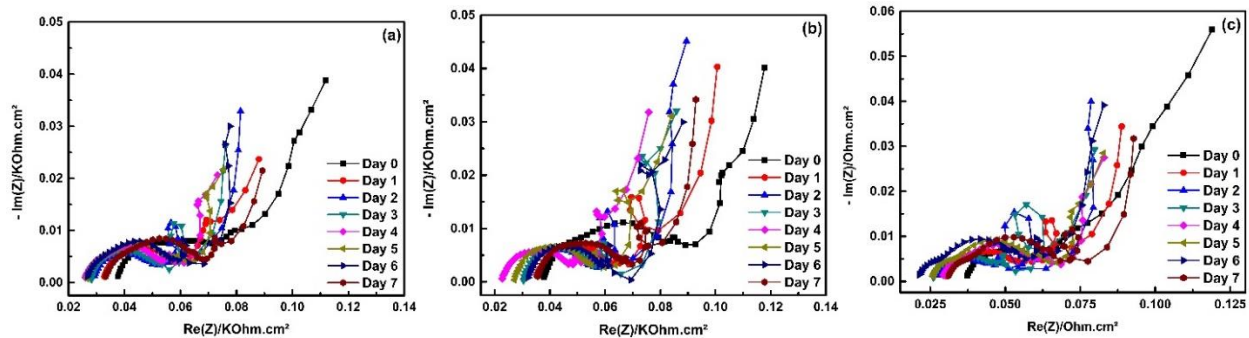


Fig. 4.12 EIS plots of SS/PPy-W based anode system. (a) system operated under OCV mode, (b) system operated under 20 Ω , and (c) system operated under 10 Ω .

When compared with the SS-P systems, the Nyquist plots obtained for the SS/PPy-P anodes showed lower impedance values which can be attributed to faster charge transfer kinetics due to the presence of PPy. The large semi-circle in the high-frequency regions indicates the capacitive behaviour of all anodes enriched under various conditions. The decrease in the R_{ct} values is also attributed to the charge generated by the biofilm [42,43].

Table 4.5 Changes in charge transfer resistance after incubation of MFCs with applied external resistance

Plate-based Anode materials and applied resistance	Initial R_{ct} ($\Omega \text{ cm}^{-2}$)	R_{ct} after incubation ($\Omega \text{ cm}^{-2}$)	Wool-based Anode materials and applied resistance	Initial R_{ct} ($\Omega \text{ cm}^{-2}$)	R_{ct} after incubation ($\Omega \text{ cm}^{-2}$)
SS-P			SS-W		
NA ($\neq R_{ext}$)	536	146	NA ($\neq R_{ext}$)	41.3	11.4
800 Ω ($R_{ext}=R_{int}$)	614	68.6	100 Ω ($R_{ext}=R_{int}$)	39.3	8.3
90 Ω ($\gg R_{ext}$)	553	166	10 Ω ($\gg R_{ext}$)	51.8	17.6
SS/PANi-P			SS/PANi-W		
NA ($\neq R_{ext}$)	29.03	2.78	NA ($\neq R_{ext}$)	4.54	1.93
60 Ω ($R_{ext}=R_{int}$)	24.65	2.24	10 Ω ($R_{ext}=R_{int}$)	4.26	1.46
10 Ω ($\gg R_{ext}$)	27.18	6.17	5 Ω ($\gg R_{ext}$)	4.23	2.74
SS/PPy-P			SS/PPy-W		
NA ($\neq R_{ext}$)	76.39	33.25	NA ($\neq R_{ext}$)	8.16	3.72
200 Ω ($R_{ext}=R_{int}$)	90.37	33.25	20 Ω ($R_{ext}=R_{int}$)	6.52	3.63
20 Ω ($\gg R_{ext}$)	96.31	45.19	5 Ω ($\gg R_{ext}$)	7.89	4.25

4.4 Fourier Transform Infrared (FTIR) Spectroscopic Studies

Attenuated total reflectance Fourier transform infrared spectroscopy (ATR-FITR) is a classical tool for analysing biofilm complexity based on the evaluation of macromolecular fingerprints,

such as proteins, nucleic acids, and polysaccharides that related to the accumulated biomass [44,45]. This technique was used in this study to identify changes associated with the use of the SS-P, SS/PANi-P, and SS/PPy-P anodes under different operating conditions. As previously indicated, all anodes used in the MFCs were enriched under the OCV mode, the Ohmic region ($R_{\text{ext}}=R_{\text{int}}$) and the mass transfer region (Low R_{ext}).

The FTIR spectra [Fig. 6(a)] obtained for the SS-P anodes used for MFCs under all conditions showed a peak for heteropolysaccharides at 1740 cm^{-1} [46]. The peaks obtained near 1660 cm^{-1} (amide I) were mainly due to C=O stretch; at 1530 cm^{-1} was for amide II; at 1432 cm^{-1} was due in part to C-H deformation; the $1,100\text{--}900\text{ cm}^{-1}$ region is referred to as the PS band (P=O symmetric stretch, C-C and C-O stretch ring stretching vibrations of polysaccharides and the P=O stretch of phosphodiester) [47]. The major groups of biomolecules associated with these bands are protein (amide I and II), nucleic acids (the region around 1240 and 1008 cm^{-1}), and polysaccharides (the region from $1,100$ to 850 cm^{-1}) [47]. The polysaccharides are reflective of the bacterial growth on the surfaces of the anodes.

The FTIR spectra [Fig. 4.13(b)] obtained for SS/PANi-P anodes under variable enrichment conditions showed a peak for heteropolysaccharide at 1596 cm^{-1} [46]. The peaks at 1505 and 1430 cm^{-1} were assigned to aromatic ring C=C [48]. The peak at $1,235\text{ cm}^{-1}$ was due to P=O asymmetric stretch, C-O-C stretch, and amide III [C-N bend and N-H stretch]. The peak at $1,165\text{ cm}^{-1}$ to 830 cm^{-1} regions was below the PS band (P=O symmetric stretch, C-C and C-O stretch). Presence of nucleic acids was evident in regions around $1,248$ and 988 cm^{-1} ; the peak at $1,505\text{ cm}^{-1}$ was due to amide II; N-H bend and C-N stretch; at $1,459\text{ cm}^{-1}$ was due to C-H bend; at $1,295\text{ cm}^{-1}$ was due to P=O asymmetric stretch, C-O-C stretch, and amide III [C-N bend and N-H stretch] [47].

Fig. 4.13(c) shows the FTIR spectra obtained for SS/PPy-P anodes enriched in the OCV mode, Ohmic region, and mass transfer mode, respectively. The peaks were poorly developed in the SS/PPy-P anode compared to those of SS-P and SS/PANi-P anodes as shown in Fig. 4.13(a,b). The peak at 1539 cm^{-1} was due to amide II; at 1432 cm^{-1} was due in part to C-H deformation; at the region from 1150 to 870 cm^{-1} was due in part to C-O-C, C-O, ring stretching vibrations of polysaccharides and the P=O stretch of phosphodiester); and presence of nucleic acids was evident in regions around 1098 and 984 cm^{-1} .

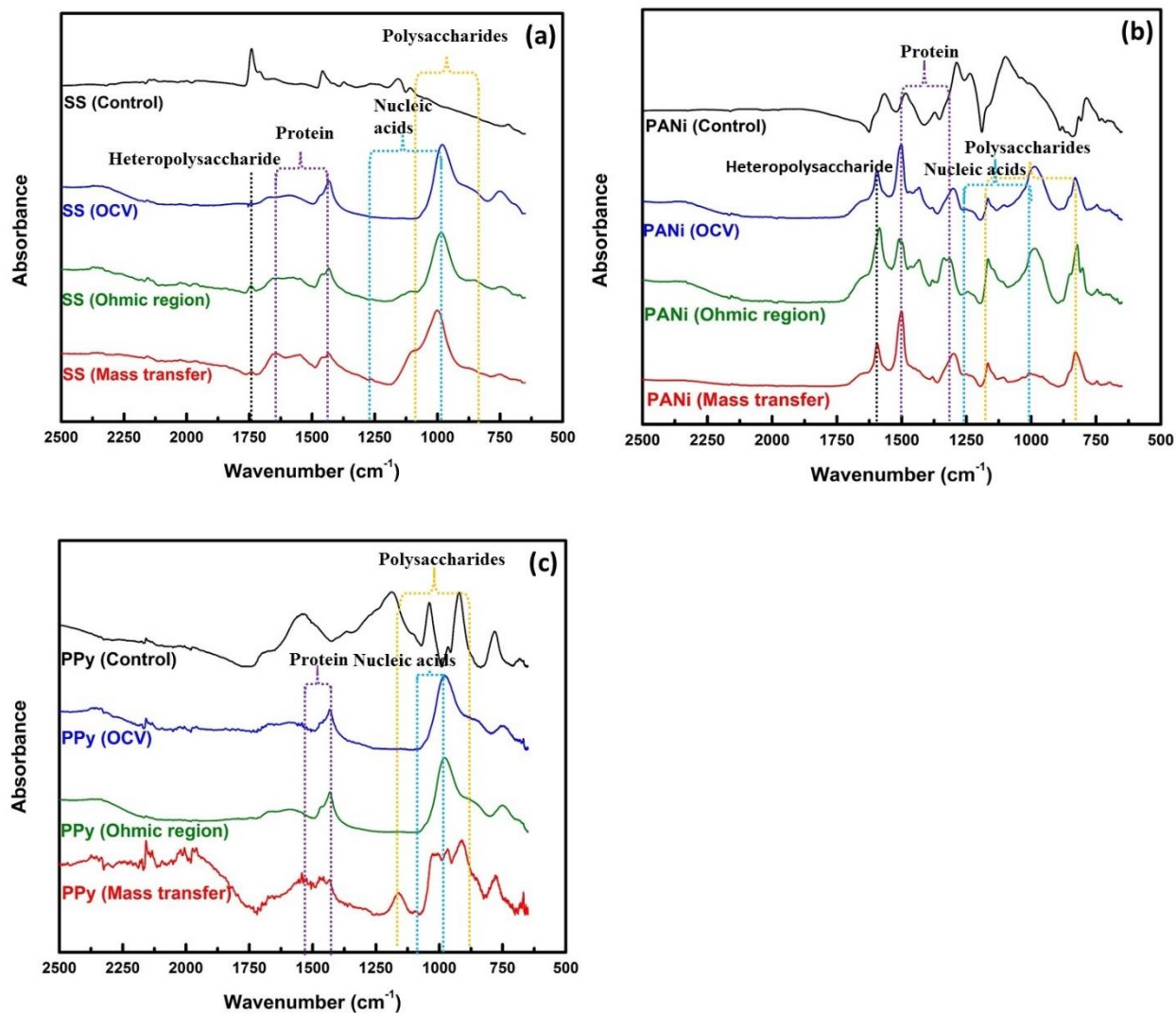


Fig. 4.13 ATR-FTIR spectra obtained for SS anodes enriched under three different conditions. An electrode harvested at the end of the 7th day of the experiment; (a) SS-P anode, (b) SS/PANi-P anode, and (c) SS/PPy-P anode.

Polysaccharides are the principal component of extracellular polymeric substances (EPSs) secreted by microbes [49]. The SS-P and PANi-P anodes used in the MFCs showed many similar FTIR peaks. In both cases, prominent peaks of polysaccharides, nucleic acid, and proteins were observed. However, for the SS-PPy anode, the heteropolysaccharide peak was poorly developed, possibly due to lower microbial growth. Li et al. [50] have demonstrated that anode biofilm enrichment from the same inoculum on different anode materials results in various bacterial diversity. A large number of bacteria and diversity was found on modified anodes than on

unmodified anodes [50]. Interestingly, the SS-PANi anode showed various signatures of complex biomolecules and complex biofilm. Even the SS-PANi anode shows excellent compatibility from anode enriched under very low resistance with the poor intensities of the biomolecules bands. However, the SS-PPy anode gave slightly better j_0 compared with that obtained with the SS plate anode due to the low R_{ct} and greater hydrophilicity for bacterial attachment.

4.5 Conclusion

This study has demonstrated that the performance of SS can be significantly improved by modification with conducting polymers. The PANi and PPy modified SS electrodes acquired higher compatibility, charge transferability and low activation overpotential. The electrokinetics of the SS-P, SS/PANi-P, SS/PPy-P, SS-W, SS/PANi-W and SS/PPy-W anodes investigated in M9+4% landfill leachate with 2.5% acetate demonstrate considerable improvement with both the conducting polymer modification of SS and the imposition of external resistance. The j_0 achieved with the use of the SS/PANi-W anode was 121% higher than with pristine SS-W anode on the fourth day of operation under the Ohmic region ($R_{ext}=R_{int}$). Pristine SS-W and SS/PANi-W anodes exhibited similar activity upon application of external resistance. The lower R_{ct} obtained for SS/PANi-P and SS/PANi-W anodes compared with SS-P, SS-W, SS/PPy-P and SS/PPy-W anodes are indicative of their higher electron transfer kinetics.

The study also demonstrated that the application of R_{ext} was useful for lowering the start-up time of the MFCs. However, the application of very low resistance has the tendency to increase the start-up time. The FTIR analysis identified the signature biomolecules (heteropolysaccharide, proteins, nucleic acids and polysaccharides) associated with the bacterial growth with the identified order of biofilm formation being greater for PANi>SS>PPy. The PANi modified SS-W anode proved to be a more efficient and cheap anode material for MFCs and is a very promising anode for microbial fuel cell development. However, further investigations are required to more clearly elucidate its actual performance in MFCs, and this aspect will be considered in the future study.

References

- [1] H. Song, Y. Zhu, J. Li, Electron transfer mechanisms, characteristics and applications of biological cathode microbial fuel cells – A mini review, *Arab. J. Chem.* (2015) 1–8. doi:10.1016/j.arabjc.2015.01.008.
- [2] O. Choi, B.-I. Sang, Extracellular electron transfer from cathode to microbes: application for biofuel production., *Biotechnol. Biofuels.* 9 (2016) 11. doi:10.1186/s13068-016-0426-0.
- [3] K.C. Wrighton, J.C. Thrash, R.A. Melnyk, J.P. Bigi, K.G. Byrne-Bailey, J.P. Remis, D. Schichnes, M. Auer, C.J. Chang, J.D. Coates, Evidence for direct electron transfer by a gram-positive bacterium isolated from a microbial fuel cell, *Appl. Environ. Microbiol.* 77 (2011) 7633–7639. doi:10.1128/AEM.05365-11.
- [4] S. Jung, J.M. Regan, Influence of external resistance on electrogenesis, methanogenesis, and anode prokaryotic communities in microbial fuel cells., *Appl. Environ. Microbiol.* 77 (2011) 564–71. doi:10.1128/AEM.01392-10.
- [5] J.M. Sonawane, A. Yadav, P.C. Ghosh, S.B. Adeloju, Recent advances in the development and utilization of modern anode materials for high performance microbial fuel cells, *Biosens. Bioelectron.* 90 (2017) 558–576. doi:10.1016/j.bios.2016.10.014.
- [6] C. Santoro, S. Babanova, K. Artyushkova, J.A. Cornejo, L. Ista, O. Bretschger, E. Marsili, P. Atanassov, A.J. Schuler, Influence of anode surface chemistry on microbial fuel cell operation, *Bioelectrochemistry.* 106 (2015) 141–149. doi:10.1016/j.bioelechem.2015.05.002.
- [7] X. Xie, G. Yu, N. Liu, Z. Bao, C.S. Criddle, Y. Cui, Graphene–sponges as high-performance low-cost anodes for microbial fuel cells, *Energy Environ. Sci.* 5 (2012) 6862. doi:10.1039/c2ee03583a.
- [8] K.P. Katuri, K. Scott, I.M. Head, C. Picioreanu, T.P. Curtis, Microbial fuel cells meet with external resistance, (2011). doi:10.1016/j.biortech.2010.10.147.
- [9] H. Rismani-Yazdi, A.D. Christy, S.M. Carver, Z. Yu, B.A. Dehority, O.H. Tuovinen, Effect of external resistance on bacterial diversity and metabolism in cellulose-fed microbial fuel cells, *Bioresour. Technol.* 102 (2011) 278–283. doi:10.1016/j.biortech.2010.05.012.
- [10] S. Ishii, S. Suzuki, T.M. Norden-Krichmar, T. Phan, G. Wanger, K.H. Nealson, Y. Sekiguchi, Y.A. Gorby, O. Bretschger, Microbial population and functional dynamics

- associated with surface potential and carbon metabolism., *ISME J.* 8 (2014) 963–78. doi:10.1038/ismej.2013.217.
- [11] K.-J. Chae, M.-J. Choi, J.-W. Lee, K.-Y. Kim, I.S. Kim, Effect of different substrates on the performance, bacterial diversity, and bacterial viability in microbial fuel cells, *Bioresour. Technol.* 100 (2009) 3518–3525. doi:10.1016/j.biortech.2009.02.065.
- [12] D. Pocaznoi, A. Calmet, L. Etcheverry, B. Erable, A. Bergel, Environmental Science Stainless steel is a promising electrode material for anodes of microbial fuel cells, (2012) 9645–9652. doi:10.1039/c2ee22429a.
- [13] J. Hou, Z. Liu, Y. Li, Polyaniline Modified Stainless Steel Fiber Felt for High-Performance Microbial Fuel Cell Anodes, *J. Clean Energy Technol.* 3 (2015) 165–169. doi:10.7763/JOCET.2015.V3.189.
- [14] I. Ul Ahad, A. Bartnik, H. Fiedorowicz, J. Kostecki, B. Korczyk, T. Ciach, D. Brabazon, Surface modification of polymers for biocompatibility via exposure to extreme ultraviolet radiation, *J. Biomed. Mater. Res. Part A.* 102 (2014) 3298–3310. doi:10.1002/jbm.a.34958.
- [15] A.-D. Bendrea, L. Cianga, I. Cianga, Review paper: Progress in the Field of Conducting Polymers for Tissue Engineering Applications, *J. Biomater. Appl.* 26 (2011) 3–84. doi:10.1177/0885328211402704.
- [16] T. Govindarajan, R. Shandas, A Survey of Surface Modification Techniques for Next-Generation Shape Memory Polymer Stent Devices, *Polymers (Basel).* 6 (2014) 2309–2331. doi:10.3390/polym6092309.
- [17] Y. Jafari, S.M. Ghoreishi, M. Shabani-Nooshabadi, Electrochemical deposition and characterization of polyaniline-graphene nanocomposite films and its corrosion protection properties, *J. Polym. Res.* 23 (2016) 91. doi:10.1007/s10965-016-0983-8.
- [18] K. Dutta, P.P. Kundu, A Review on Aromatic Conducting Polymers-Based Catalyst Supporting Matrices for Application in Microbial Fuel Cells, *Polym. Rev.* 54 (2014) 401–435. doi:10.1080/15583724.2014.881372.
- [19] J.M. Sonawane, S.A. Patil, P.C. Ghosh, S.B. Adeloju, Low-cost stainless-steel wool anodes modified with polyaniline and polypyrrole for high-performance microbial fuel cells, *J. Power Sources.* 379 (2018) 103–114. doi:10.1016/j.jpowsour.2018.01.001.
- [20] J.M. Sonawane, S. Al-Saadi, R.K. Singh, P.C. Ghosh, S.B. Adeloju, Exploring the use of polyaniline-modified stainless steel plates as low-cost, high-performance anodes for

- microbial fuel cells, *Electrochim. Acta.* (2018). doi:10.1016/j.electacta.2018.01.163.
- [21] K. Scott, G.A. Rambu, K.P. Katuri, K.K. Prasad, I.M. Head, Application of Modified Carbon Anodes in Microbial Fuel Cells, *Process Saf. Environ. Prot.* 85 (2007) 481–488. doi:10.1205/psep07018.
- [22] B. Lai, X. Tang, H. Li, Z. Du, X. Liu, Q. Zhang, Biosensors and Bioelectronics Power production enhancement with a polyaniline modified anode in microbial fuel cells, *Biosens. Bioelectron.* 28 (2011) 373–377. doi:10.1016/j.bios.2011.07.050.
- [23] Y. Zou, J. Pisciotta, I. V. Baskakov, Nanostructured polypyrrole-coated anode for sun-powered microbial fuel cells, *Bioelectrochemistry.* 79 (2010) 50–56.
- [24] G. Kennell, Godwin, Evitts, Microbial fuel cell with a polypyrrole/poly(methylene blue) composite electrode, *Reports Electrochem. Volume 2* (2012) 3. doi:10.2147/RIE.S33526.
- [25] D. Molognoni, S. Puig, M.D. Balaguer, A. Liberale, A.G. Capodaglio, A. Callegari, J. Colprim, Reducing start-up time and minimizing energy losses of Microbial Fuel Cells using Maximum Power Point Tracking strategy, *J. Power Sources.* 269 (2014) 403–411. doi:10.1016/j.jpowsour.2014.07.033.
- [26] P. Aelterman, S. Freguia, J. Keller, W. Verstraete, K. Rabaey, The anode potential regulates bacterial activity in microbial fuel cells, *Appl. Microbiol. Biotechnol.* 78 (2008) 409–418. doi:10.1007/s00253-007-1327-8.
- [27] T. Liu, Y.-Y. Yu, D. Li, H. Song, X. Yan, W.N. Chen, The effect of external resistance on biofilm formation and internal resistance in *Shewanella* inoculated microbial fuel cells, *RSC Adv.* 6 (2016) 20317–20323. doi:10.1039/c5ra26125b.
- [28] J.S. Mclean, G. Wanger, Y.A. Gorby, M. Wainstein, J. Mcquaid, S. ichi Ishii, O. Bretschger, H. Beyenal, K.H. Nealson, Quantification of electron transfer rates to a solid phase electron acceptor through the stages of biofilm formation from single cells to multicellular communities, *Environ. Sci. Technol.* 44 (2010) 2721–2727. doi:10.1021/es903043p.
- [29] D.Y. Lyon, F. Buret, T.M. Vogel, J.-M. Monier, Is resistance futile? Changing external resistance does not improve microbial fuel cell performance, 2010. doi:10.1016/j.bioelechem.2009.09.001.
- [30] Z. Ren, H. Yan, W. Wang, M.M. Mench, J.M. Regan, Characterization of microbial fuel cells at microbially and electrochemically meaningful time scales, *Environ. Sci. Technol.* 45 (2011) 2435–2441. doi:10.1021/es103115a.

- [31] S. Chen, G. He, Q. Liu, F. Harnisch, Y. Zhou, Y. Chen, M. Hanif, S. Wang, X. Peng, H. Hou, U. Schröder, Layered corrugated electrode macrostructures boost microbial bioelectrocatalysis, *Energy Environ. Sci.* 2 (2012) 9769–9772. doi:10.1039/c2ee23344d.
- [32] J.M. Sonawane, S.B. Adeloju, P.C. Ghosh, Landfill leachate: A promising substrate for microbial fuel cells, *Int. J. Hydrogen Energy.* (2017). doi:10.1016/j.ijhydene.2017.03.137.
- [33] P. Ledezma, N. Degrenne, P. Bevilacqua, F. Buret, B. Allard, J. Greenman, I. Ieropoulos, Dynamic polarisation reveals differential steady-state stabilisation and capacitive-like behaviour in microbial fuel cells, *Sustain. Energy Technol. Assessments.* 5 (2014) 1–6. doi:10.1016/j.seta.2013.10.008.
- [34] P. Clauwaert, P. Aelterman, T.H. Pham, L. De Schampelaire, M. Carballa, K. Rabaey, W. Verstraete, Minimizing losses in bio-electrochemical systems: The road to applications, *Appl. Microbiol. Biotechnol.* 79 (2008) 901–913. doi:10.1007/s00253-008-1522-2.
- [35] M. Ehsani, Y. Gao, S.E. Gay, A. Emadi, *Modern Electric, Hybrid Electric, and Fuel Cell Vehicles: Fundamentals, Theory, and Design, Second Edition*, CRC Press, 2009. <http://www.amazon.com/dp/1420053981%5Cnhttp://www.amazon.com/dp/0849331544> (accessed February 23, 2017).
- [36] L. Hui, *Proton Exchange Membrane Fuel Cells: Contamination and Mitigation Strategies*, CRC Press, 2010.
- [37] S.V. Raghavulu, P.S. Babu, R.K. Goud, G.V. Subhash, S. Srikanth, S.V. Mohan, Bioaugmentation of an electrochemically active strain to enhance the electron discharge of mixed culture: process evaluation through electro-kinetic analysis, *RSC Adv.* 2 (2012) 677. doi:10.1039/c1ra00540e.
- [38] N.Q. Minh, T. Takahashi, Chapter 9 - Stack design and fabrication BT - *Science and Technology of Ceramic Fuel Cells*, in: Elsevier Science, 1995: pp. 233–306. doi:http://dx.doi.org/10.1016/B978-044489568-4/50010-4.
- [39] R.J.L. Paulton, The bacterial growth curve, *J. Biol. Educ.* 25 (1991) 92–94. doi:10.1080/00219266.1991.9655183.
- [40] S. Basu, *Recent trends in fuel cell science and technology*, Springer New York, New York, NY, 2007. doi:10.1007/978-0-387-68815-2.
- [41] S.C. Bhatia, 1 – Energy resources and their utilisation, in: *Adv. Renew. Energy Syst.*, 2014: pp. 1–31. doi:10.1016/B978-1-78242-269-3.50001-2.

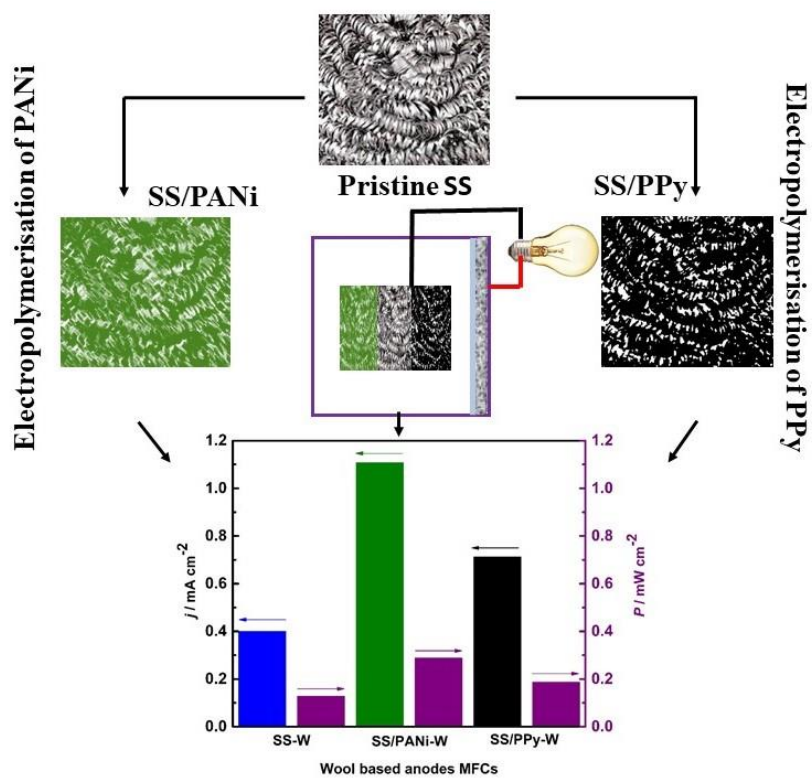
- [42] R.P. Ramasamy, Z. Ren, M.M. Mench, J.M. Regan, Impact of initial biofilm growth on the anode impedance of microbial fuel cells, *Biotechnol. Bioeng.* 101 (2008) 101–108. doi:10.1002/bit.21878.
- [43] B. Wei, J.C. Tokash, F. Zhang, Y. Kim, B.E. Logan, Electrochemical analysis of separators used in single-chamber, air-cathode microbial fuel cells, *Electrochim. Acta.* 89 (2013) 45–51. doi:10.1016/j.electacta.2012.11.004.
- [44] F. Quilès, F. Humbert, A. Delille, Analysis of changes in attenuated total reflection FTIR fingerprints of *Pseudomonas fluorescens* from planktonic state to nascent biofilm state, *Spectrochim. Acta - Part A Mol. Biomol. Spectrosc.* 75 (2010) 610–616. doi:10.1016/j.saa.2009.11.026.
- [45] J.J. Ojeda, M. Dittrich, Fourier transform infrared spectroscopy for molecular analysis of microbial cells, *Methods Mol. Biol.* 881 (2012) 187–211. doi:10.1007/978-1-61779-827-6_8.
- [46] M. Szymanska-Chargot, A. Zdunek, Use of FT-IR Spectra and PCA to the Bulk Characterization of Cell Wall Residues of Fruits and Vegetables Along a Fraction Process, *Food Biophys.* 8 (2013) 29–42. doi:10.1007/s11483-012-9279-7.
- [47] A. Delille, F. Quilès, F. Humbert, In situ monitoring of the nascent *Pseudomonas fluorescens* biofilm response to variations in the dissolved organic carbon level in low-nutrient water by attenuated total reflectance-Fourier transform infrared spectroscopy., *Appl. Environ. Microbiol.* 73 (2007) 5782–8. doi:10.1128/AEM.00838-07.
- [48] H.G. Upritchard, J. Yang, P.J. Bremer, I.L. Lamont, A.J. McQuillan, Adsorption of Enterobactin to Metal Oxides and the Role of Siderophores in Bacterial Adhesion to Metals, *Langmuir.* 27 (2011) 10587–10596. doi:10.1021/la202352j.
- [49] L. Zhang, X. Zhu, J. Li, Q. Liao, D. Ye, Biofilm formation and electricity generation of a microbial fuel cell started up under different external resistances, *J. Power Sources.* 196 (2011) 6029–6035. doi:10.1016/j.jpowsour.2011.04.013.
- [50] C. Li, L. Zhang, L. Ding, H. Ren, H. Cui, Effect of conductive polymers coated anode on the performance of microbial fuel cells (MFCs) and its biodiversity analysis, *Biosens. Bioelectron.* 26 (2011) 4169–4176. doi:10.1016/j.bios.2011.04.018.

Chapter 5

Low-cost stainless-steel wool anodes modified with polyaniline and polypyrrole for high-performance microbial fuel cells

[Published as, JM Sonawane, SA Patil, PC Ghosh, SB Adeloju, Low-cost stainless-steel wool anodes modified with polyaniline and polypyrrole for high-performance microbial fuel cells, Journal of Power Sources 379, 103-114, 2018]

Graphical abstract



Abstract

A conducting polymer coated stainless-steel wool (SS-W) is proposed for use as a low-cost anode for microbial fuel cells (MFCs). When coated with polyaniline (PANi) and polypyrrole (PPy), the pristine SS-W, SS/PANi-W, and SS/PPy-W anodes produced maximum current densities of 0.30 ± 0.04 , 0.67 ± 0.05 , 0.56 ± 0.07 mA cm⁻², respectively, in air-cathode MFCs. Also, based on achieved power density, both SS/PANi-W, and SS/PPy-W achieved 0.288 ± 0.036 mW cm⁻² and 0.187 ± 0.017 mW cm⁻², respectively, which were superior to 0.127 ± 0.011 mW cm⁻² obtained with pristine SS-W. Further, in comparison with SS-P based anodes, all SS-W based anodes gave improved power densities under similar experimental conditions by at least 70%. Moreover, the charge transfer resistance of the SS-W was much lower (240 ± 25 Ω cm⁻²) than for the SS-P (3192 ± 239 Ω cm⁻²). The determined $j_{0(\text{apparent})}$ values obtained for SS/PANi-W (0.098 ± 0.007 mA cm⁻²) and SS/PPy-W (0.036 ± 0.004 mA cm⁻²) anodes were also much higher than that obtained for the pristine SS-W (0.020 ± 0.005 mA cm⁻²), as well as than those of all SS-P based anodes. The observed enhancement of the bioelectrocatalytic performances were well supported by physicochemical and electrochemical characterisation.

Nomenclature:

Cdl	Double layer capacitor
F	Faraday's constant [96,485 C mol ⁻¹]
i_0	Exchange current [mA]
j_0	Exchange current density [mA cm ⁻²]
Q	Constant phase element
R	Ideal gas constant [8.31 J mol ⁻¹ K ⁻¹]
R	Resistor [Ω]
R_{ct}	Charge transfer resistance [Ω]
R_s	Solution resistance [Ω]
T	Absolute temperature [K]
W	Warburg diffusion element [Ω]
η	Overpotential [mV]

Abbreviations:

CPHS/CNTs	Conductive polypyrrole hydrogels/carbon nanotubes
EET	Extracellular electron transfer
MWCNTs	Multiwalled carbon nanotubes
NT-MPMs	Multi-walled MnO ₂ /polypyrrole/MnO ₂ nanotubes
PANi	Polyaniline
PANi/ GF	Polyaniline graphite felt
PANI/CC	Polyaniline carbon cloth
PANI/CNT/CP	Polyaniline carbon nanotubes
PANI/CP	Polyaniline carbon paper
PANI _{che} /SSFF	Polyaniline synthesised by chemical polymerisation
PANI _{ele} /SSFF	Polyaniline synthesised by electrochemical polymerisation
PPy	Polypyrrole
PPy/AQDS	Polypyrrole/anthraquinone-2,6-disulphonic disodium salt
PPy/MnO ₂	Polypyrrole Manganese dioxide composite
PPy/RVC	Polypyrrole-Coated Reticulated Vitreous Carbon
PPy-CNTs	Polypyrrole carbon nanotubes

SS	Stainless steel
SS/PANi-P	Stainless steel modified polyaniline plate
SS/PANi-W	Stainless steel modified polyaniline wool
SS/PPy-P	Stainless steel modified polypyrrole plate
SS/PPy-W	Stainless steel modified polypyrrole wool
SSFF	Stainless steel fibre felt
SS-FO	Flame oxidised stainless steel
SS-P	Stainless steel plate
SS-W	Stainless steel wool

5.1 Introduction

Despite the considerable scientific and technological advancements that have been made in microbial fuel cell (MFC) research over the years, several issues, such as high material costs and low power outputs have limited their wider adoption and applications [1]. The performance of MFC is affected by many intrinsic (such as microorganisms and chosen construction materials) and operational factors [2–7]. The microorganisms-anode interaction is amongst the most important factors that determine the bioelectrocatalytic performance of these systems [8,9]. Exploration of different materials and approaches to find the most suitable anode material has thus been a major area of challenge in MFC research [1].

The required qualities for an ideal anode material include possession of properties such as biocompatibility, high electrical conductivity [10], large surface area for wide coverage by exoelectrogenic bacteria [11], corrosion resistance [12], suitable mechanical strength and toughness [13,14], and, in addition, the chosen material must be relatively cheap to achieve low-cost scalability for practical applications [15]. A number of two and three-dimensional (2D and 3D) materials have been investigated for use as anodes for MFCs. The most widely used 2D carbon-based anode materials, such as graphite plates and rods, carbon cloth [16] have considerable limitations in relation to their low accessible surface area for microbial biofilm colonisation, high charge transfer resistance, high activation, and mass transfer overpotential [17]. To overcome some of the aforementioned limitations, surface modification of materials and the use of 3D carbon-based materials as anodes have gained widespread consideration. Different 3D materials, such as electrospun carbon fibre mats [18], carbon fibre veil [19], graphite fibre brush [20] and rotating spiral carbon brush have recently been used as anodes [21]. In order to reduce the precursor costs, attempts have been made successfully to construct 3D anodes from natural materials, such as king mushroom, wild mushroom and corn stem [22]. Composite anodes, such as carbon scaffold from polyacrylonitrile [23], carbon nanofibers modified graphite [24], activated carbon nanofibers nonwoven [25], nitrogen-doped graphene aerogels [26], and carbon-metal composites, such as carbon yarn with stainless steel [27], have also been investigated. These research efforts, in particular on 3D materials, have resulted in remarkable improvement in the current or power densities achieved in MFCs. The enhanced performance with 3D and composite electrodes is attributed primarily to their high surface area for efficient colonisation of bacterial communities, enhanced biocompatibility and electrical conductivity [27–31]. By increasing the

surface area and controlling the pore size of these materials the substrate access for electrogenic bacteria can be enhanced, which in turn results in relatively low mass transfer limitations [32,33]. However, major limitations of 3D carbon materials include their brittle structure which has less strength and low conductivity leading to high Ohmic resistance. Metal-based electrodes are able to address these issues as recently demonstrated by Baudler et al. [34].

Pocaznoi et al. [35] reported that stainless steel is the most commonly used metal-based anode material for MFCs due to its excellent mechanical strength, good conductivity, high rigidity and stability [1,36]. Major issues with the use of low-grade SS anodes include its relatively poor biocompatibility due to the hydrophobic nature and proneness to corrosion. The biocompatibility issue can be addressed by heat treatment or flame oxidation as proposed by Guo et al. [37].

Recently, various methods have been reported for modification of SS based anode materials, such as flame-oxidation, flame deposition, binder and binder-free nanocarbon coating [37–42]. The flame oxidation of SS results into node like sites, which mainly consisted of hematite (Fe_2O_3) on the surface of SS. The resulting anode produced a maximum power density of 0.106 mW cm^{-2} [38]. In the other study, flame oxidation of SS generated iron oxide nanoparticles on the surface and a current density of 1.92 mA cm^{-2} [37]. In another approach, carbon nanostructures were formed on SS using flame synthesis and a maximum power density of $0.0187 \text{ mW cm}^{-2}$ was achieved [39]. Carbon nanofibers were also coated onto SS by chemical vapour deposition, and the modified anode generated a maximum current density of 1.28 mA cm^{-2} [40]. All of the above studies were investigated under controlled potentiostatic testing conditions. A carbon black-stainless steel mesh composite anode was prepared by using a binder-free dipping method, and when employed in a continuous magnetic stirring batch-mode MFC, it gave maximum power density of 0.321 mW cm^{-2} [41]. Graphene with polytetrafluoroethylene (binder) coating on a SS mesh was also used, and it gave a maximum power density of $0.2668 \text{ mW cm}^{-2}$ [42].

In comparison with routinely used SS plate (SS-P) and mesh materials, SS wool (SS-W) offers compelling advantages, such as very high surface area, low cost, and malleability, which allows it to be moulded into any shape according to the system architecture. To the best of our knowledge SS-W has never been employed as an anode material in MFCs and also never previously coated with conducting polymers, but its high surface area and relatively low-cost warrant consideration as an alternative cheap anode. Furthermore, conducting polymer coatings, such as polyaniline (PANi) and polypyrrole (PPy), have been shown to be effective for corrosion reduction for carbon

and composite based MFC anodes [43]. These polymers possess high electron mobility, stability, biocompatibility, anticorrosion nature, excellent electrokinetics and can be produced by facile chemical or electrochemical synthesis. In particular, PANi modified anodes were found to enhance microbial adhesion to the surface and, consequently, improve the bioelectrocatalytic performance [44,45]. It is anticipated that the coating of the SS-W with conducting polymers will minimise corrosion and improve performance through enhanced microbial adhesion.

In this study, we explore the very high surface area and malleability offered by SS-W, for the first time, as a basis for developing high performance and low-cost MFC anode. To further improve the anode performance via enhanced microbial adhesion, we investigate the use of galvanostatic polymerisation of aniline (ANi) and pyrrole (Py) for coating the SS-W with PANi and PPy. The suitability of the uncoated and coated SS-W as MFC anodes were investigated by thorough physicochemical and electrochemical characterisation by scanning electron microscopy, profilometry, contact angle measurements, electrochemical impedance spectroscopy and Tafel curve analysis. Also, to gain an in-depth understanding of the performances of the uncoated and coated anodes, a comparison was made between the pristine SS-W, SS/PANi-W, and SS/PPy-W. The performances of the SS/PANi-W and SS/PPy-W anodes were further compared with those of the most commonly used pristine SS-P anodes. Furthermore, the bioelectrocatalytic performances of the SS-W, SS/PANi-W, and SS/PPy-W anodes were investigated for the first time in MFCs by monitoring the achieved current densities and polarisation behaviour in air-cathode MFCs.

5.2 Materials and methods

5.2.1 Electrode materials

SS plate (SS-304; Metline Industries, Mumbai) and SS wool (domestic use; Scotch-Brite, India) were used as base anode materials (projected surface area of 3.5 cm^2). The measured thickness of the single fibre of SS-W was 126.6 ± 3.34 micron, and the density was 2.39 gm cm^{-3} . The thickness of the overall anode was 0.8 cm. The SS-P was used as a reference anode material to compare with the performance of SS-W anodes. All SS-Ps were polished progressively by using metallographic abrasive paper of grit sizes of 320, 400, 600, 800 and 1200. Polished SS-Ps and SS-Ws were subjected to ultrasonication for 15 minutes in acetone to degrease the SS samples before electropolymerisation. A miniature saturated Ag/AgCl (sat. KCl) was used as a reference electrode

(RRPEAGCL, Pine Research Instrumentation, Durham, USA). The counter electrode used for the electrochemical experiment was a titanium mesh (Amac, Croydon, Australia).

5.2.2 Polyaniline (PANi) and polypyrrole (PPy) anode modification

All electrochemical experiments were performed with the Biologic SP-150 potentiostat (BioLogic, Claix, France) equipped with an EC-Lab 10.44 software. All solutions were purged with nitrogen for 15 minutes to remove oxygen before the commencement of polymerisation. For electropolymerisation of aniline on SS-P and SS-W, reagent grade aniline and nitric acid (Sigma-Aldrich, Mumbai, India) were used. PANi was synthesised by applying a constant current of 2.5 mA cm⁻² in 0.4 M ANi in 0.7 M nitric acid (previously optimised) for 15 minutes. Polypyrrole was electropolymerised in 0.4 M pyrrole in 0.7 L-(+)-Tartaric acid using the same conditions. Fig. 5.1(a, b, c) shows the pristine SS-W, SS-W coated with polyaniline (SS/PANi-W), and SS-W coated with polypyrrole (SS/PPy-W), respectively.

5.2.3 Cathode fabrication

The air cathodes were fabricated by following a previously reported method [27]. Briefly, fine platinised (Vulcan XC-72) carbon powder, Pt content 20% wt. (Sigma-Aldrich, Australia) was coated onto a 12 x 10 cm commercial carbon paper (GDS 210, CeTech, Taichung, Taiwan). The Pt loading was maintained at 0.5 mg cm⁻² using 5% Nafion solution as a binder (Sigma-Aldrich, Australia). All coated electrodes were incubated in a hot air oven for 6 hours at 60 °C to ensure complete drying. Subsequently, the dried electrodes were hot pressed on one side using Nafion NRE-212 (Sigma-Aldrich, Australia) under 10 kg cm⁻² at 140 °C for 3 minutes using a Carver hot press (Carver, Inc, Indiana, USA). Fabricated membrane electrode assemblies (MEA) were cut into 3 x 2.5 cm (projected surface area of 7.5 cm⁻²). The cathode was sandwiched into an acrylic mesh and aluminium mesh (which act as a current collector) in the MFC reactor.

5.2.4 Characterisation of anode materials

Alicona microscopy was used to characterise the topography of all SS plate electrode, SS/PANi-P and SS/PPy-P with 20x, 50x and 10x magnifications. Multiple three-dimensional scans, for triplicates of the samples, were obtained. Utmost care was taken to avoid surface contamination of electrodes. Scanning electron microscopy (SEM) images were obtained with a JSM - 760F FEG Scanning Electron Microscope (SEM) at a 1-micrometre resolution at 100,00X magnification. It

was difficult to characterise the SS wool electrodes correctly by these methods due to its structure and entanglement of the wool mesh. Therefore, photographs of SS wool anodes were taken to ensure uniform coating with the conducting polymer, as shown in Fig. 5.1 (a, b, c). Evidently, the use of galvanostatic polymerisation was effective for achieving a uniform coating of SS-W with PANi and PPy.

5.2.5 MFC reactor configuration

The design of the air-cathode MFC is shown in Fig. 5.1(d). Acrylic sheets were cut by using laser technology and then used to construct MFCs. The base of the MFC was made up of three sheets stacked together with the dimensions of 6.8 x 6.8 cm². The top and bottom sheets consist of a mesh structure of dimensions 3 x 2.5 cm². A rectangular void of same dimensions as that of the mesh was made in the bottom sheet. The coated cathode was placed in this void to help in the circulation of current. Above these sheets, a cube with inner dimension 3 x 3 x 3 cm was fixed. This assembly acted as an anode chamber with a working volume of 27 cm³. This cubical box was equipped with two circular voids for the effluent inflow and outflow. The experimental setup is shown in Fig. 5.1(e).

5.2.6 Operation of MFCs

MFCs were fed with synthetic wastewater (M9 medium) containing sodium acetate (25 mM) as a sole carbon source. The composition of the M9 medium per L of distilled water is as follows - NH₄Cl: 0.31 g, KCl: 0.13 g, NaH₂PO₄.H₂O: 2.69 g, Na₂HPO₄: 4.33 g, and 12.5 mL of each trace metal and vitamin solutions [46,47]. The landfill leachate (4%; collected from the landfill site, Turbhe, Mumbai) was inoculated as a source of bacteria in M9 media. It was demonstrated in a recent study that landfill leachate is a most promising substrate for MFCs [48] and, hence, we employed the leachate as a source of bacterial inoculum in this study. All experiments were conducted at an average ambient temperature of 27 °C. The media was sparged with N₂ for 30 min before inoculation, and the MFCs were sparged for 10 minutes after inoculation to increase the primary activity of obligate anaerobes and minimise aerobic oxidation of organic matter. The experiments were conducted in a fed-batch mode (by replenishing 90% of the spent medium by fresh M9 medium after every batch cycle). The MFCs operated initially in an open circuit mode and then in a closed-circuit mode with a 100 Ω external resistor. All experiments were conducted

in triplicates. Control experiments were carried out with each anode material only in M9 media without landfill leachate inoculum.

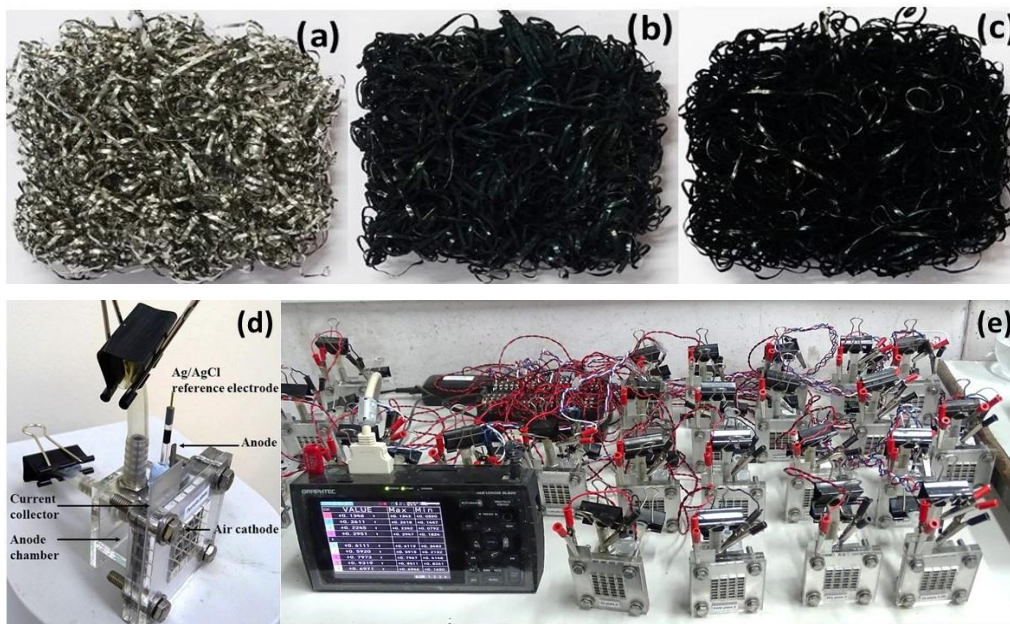


Fig. 5.1 Anode materials and MFC systems used in this study. Stainless steel wool (SS-W) anodes: (a) pristine SS-W, (b) SS-W coated with polyaniline, (c) SS-W coated with polypyrrole, (d) the system architecture of the MFC, and (e) the experimental setup for MFCs along with a data logger.

5.2.7 Analytics and calculations

Initially, both MFCs with SS-P and SS-W based anodes were operated under an open circuit voltage (OCV) mode for two cycles (each cycle = 6 d) to establish biofilm on the anodes without any external load [27]. OCV was measured at 30 min intervals using a data logger (Graphtec GL-820). After two successive cycles, a 100 Ω resistor was connected to each MFC set-up, and the voltage was recorded. Current (I) was calculated by Ohm's law: $I=V/R$; where R is external resistance, and V is the voltage across the anode and cathode. The current and power generation data are normalised by the projected surface area of the cathode (7.5 cm²). MFCs with high surface anodes were normalised to the cathode surface area for performance assessment [49,50].

All electrochemical experiments were conducted with a Biologic SP-150 potentiostat-galvanostat (BioLogic, Claix, France) fitted with EC-Lab V 10.44 software. Current and power density curves were obtained using linear sweep voltammetry (LSV) recorded at a scan rate of 1 mV s⁻¹ within a potential window from OCV to 0 V. These were measured during the 9th batch cycle when a stable

and maximum current was observed. Tafel plots of anodes in all systems were recorded using LSV (scanning from OCV to 150 mV at a scan rate of 1 mV s⁻¹) before the inoculation of MFCs and during the 9th batch cycle of the MFC experiments. After application of η (overpotential), positive deviation from OCV to 150 mV shows an initial lag of η and subsequent Tafel lines become linear. With the application of the Tafel equation, the X-axis intercept was determined as the log of the current exchange densities ($\ln j_0$). Similar control experiments were performed in sterile M9 media. The slight variation of coatings in M9 media could be traced. All the experimental Tafel values were subtracted from the control sets.

Anodic Tafel plot, as derived from the equation below, was employed to measure the reaction kinetics [51].

$$\ln\left(\frac{i}{i_0}\right) = \beta\left(\frac{F\eta}{RT}\right)$$

where i_0 is exchanged current, i is the electrode current density (mA cm⁻²), β is the electron transfer coefficient, R is the ideal gas constant (8.31 J mol⁻¹ K⁻¹), F is the Faraday's constant (96485 C mol⁻¹), T is the absolute temperature, K (303 K) and η is the activation overpotential. The purpose of using a Tafel plot is to calculate the i_0 value. The i_0 is a fundamental parameter in the rate of electro-oxidation or electro-reduction of a chemical species on an electrode at equilibrium. The charge transfer resistance (R_{ct}) was calculated from the following equation [51].

$$R_{ct} = \frac{RT}{nFi_0}$$

where n is the number of electrons and other parameters as described above.

The charge transfer resistance of the anodes was determined by electrochemical impedance spectroscopy (EIS). The measurement was conducted immediately after the addition of microbial inoculum and during the 9th cycle when the maximum current was achieved with each system. All measurements were carried out at OCV conditions by removing R_{ext} , and the systems were allowed to stabilise to attain the maximum OCV. These measurements on the working electrode were performed at a frequency of 100 MHz to 10 mHz with a sinusoidal perturbation amplitude of 10 mV at 6 points per decade. For EIS data analysis, two different equivalent circuits were used [Fig. 5.2(a, b)].

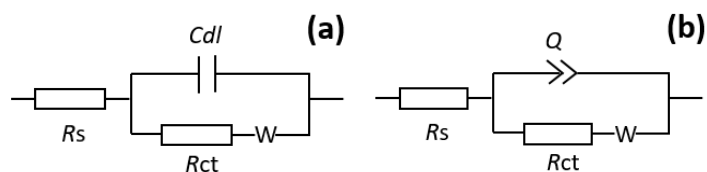


Fig. 5.2 The electrical equivalent circuit used to analyse the EIS data: a) for uncoated SS electrodes, and b) for PANi and PPy coated SS electrodes.

For control, double layer capacitance (Cdl) of SS electrodes was considered, while for SS coated with PANi and PPy electrodes, constant phase element (Q) was considered. R_s and R_{ct} represent the solution resistance and the charge transfer resistance, respectively. A Warburg element (W) was employed to evaluate the diffusion resistance. Both types of the equivalent circuits composed of a solution element (solution resistance, R_s) in series with a charge transfer element (charge transfer resistance R_{ct} in parallel with a double layer capacitance Cdl or constant phase element Q) followed by a Warburg diffusion element (diffusion resistance W in parallel with Cdl or Q).

5.3. Results and discussion

5.3.1 Morphological features, surface area and hydrophilicity of polymer coated SS-P anodes

The SEM images shows that the SS/PANi-P [Figure 5.3(b)] coating has a fibrous and porous structure, while the SS/PPy-P [Figure 5.3(c)] has a cauliflower-like structure. The differences in the structure of the polymer coatings may account for the differences in the average surface roughness observed in the profilometric images for PANi and PPy coated SS-P surfaces. Nevertheless, the observations from the SEM images clearly indicate that the polymer coatings resulted in the increased surface area for the anodes and, consequently, provided more area for the biofilm growth and adhesion of bacteria than with the uncoated SS-P.

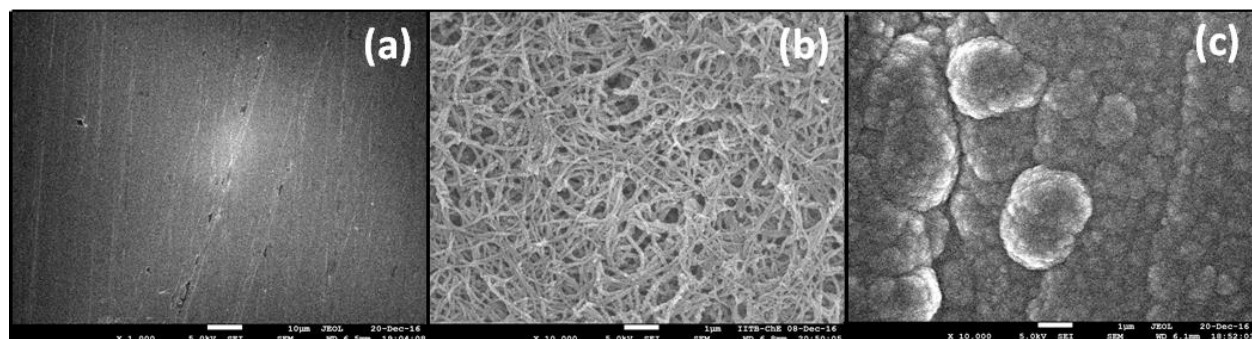
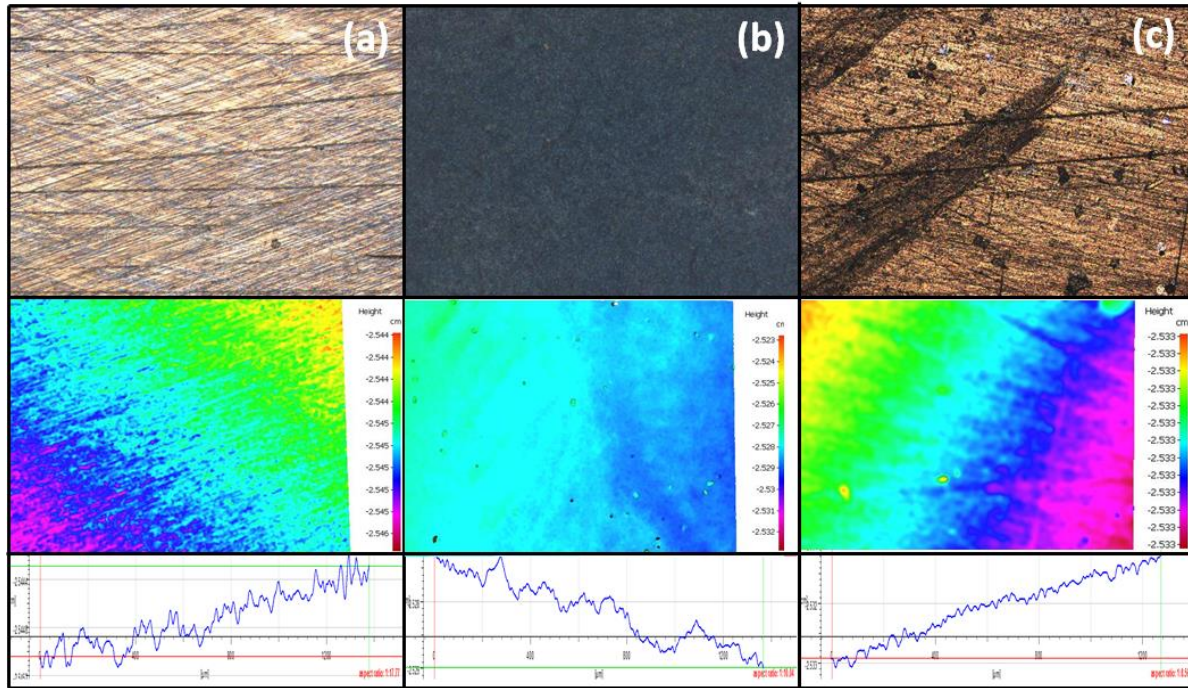


Fig. 5.3 Scanning electron microscopy images of (a) SS-P, (b) SS/PANi-P, and (c) SS/PPy-P anode materials.

Figure 5.4A provides the profilometric images for SS-P, SS/PANi-P, and SS/PPy-P. The images show the difference in the surface profiles of these anode materials at mm/ μ m scale. From these results, the average roughness of SS-P, SS/PANi-P and SS/PPy-P were 505 ± 37 , 604 ± 52 , and 438 ± 28 nm, respectively. Evidently, the surface profile for the SS/PANi-P was the roughest due to the increased roughness of the PANi coating. In contrast, the PPy coating resulted in a decreased roughness due to the more uniform nature of the PPy coating.

The polymer coated SS-P also showed a decrease in the contact angles from 86° for uncoated SS-P to 38° for SS/PANi-P and to 47° for SS/PPy-P (Figure 5.4B). These significant decreases in contact angles indicate that the nature of the polymer coatings changed from being hydrophobic to hydrophilic SS surfaces. An increase in the hydrophilicity of electrodes is known to improve the growth of electroactive biofilm [9]. The polymer modification of SS-W anodes would also result in similar improved morphological features observed with SS-P and, thus, make them similarly conducive to biofilm growth.

A



B

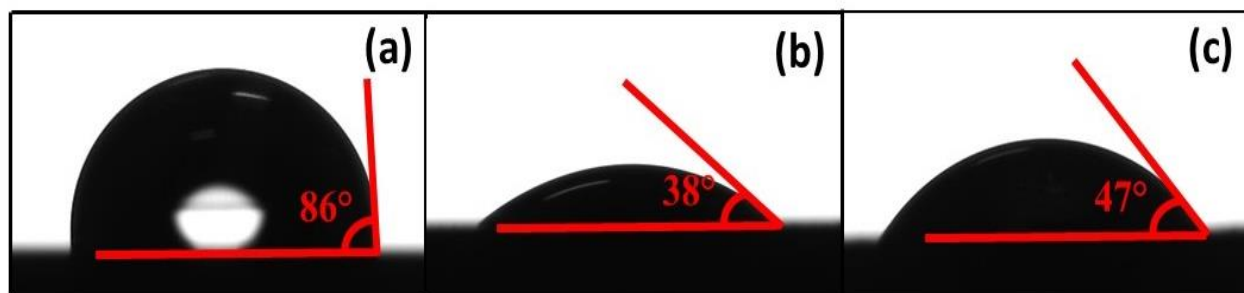


Fig. 5.4 (A) Profilometer images, and (B) Contact angles of (a) SS-P, (b) SS/PANi-P, and (c) SS/PPy-P anode materials.

5.3.2 Bioelectrocatalytic performances of SS-W and SS-P anodes

During the first cycle of the OCV mode of operation, the observed initial high OCVs with all anodes were most likely due to the aerobic conditions in the reactors. Figure 5.5 (a and b) shows that the initial potentials observed for both SS-P and SS-W based anodes slowly decreased with time. This is due to a lag phase during which the bacteria adjusted or become acclimatised to a new environment. After this lag phase and with the addition of 25 mM acetate, the OCVs increased exponentially for the next three days followed by a short stationary phase for all polymer coated SS anodes during the second cycle. For example, the average OCV obtained for the SS/PANi-P anode increased from 520 ± 42 mV to 737 ± 27 mV in the second cycle. Similarly, the OCV obtained for the SS/PANi-W anode increased from 260 ± 13 mV to 595 ± 09 mV. Among the conducting polymers, the PANi coated anodes developed a higher OCV for both SS-P and SS-W anodes. However, the OCV for uncoated SS-P and SS-W anodes deteriorated from 757 ± 36 mV to 664 ± 42 mV and 985 ± 43 mV to 927 ± 38 mV, respectively, during both cycles. These results clearly indicate that the initial biofilm attachment is better with the polymer coated SS anodes than with the uncoated anodes. The higher OCV in SS/PANi-W could be due to corrosion, and it can also be seen from Tafel plot. The deterioration of the OCVs of the SS-P and SS-W MFC anodes may be due to corrosion of SS in the M9 media.

After the two OCV batch cycles, all MFCs were then operated in a closed-circuit mode with an application of a R_{ext} of 100Ω for eight batch cycles, with each cycle lasting for ~5 days [(Figure 5.5 (c and d)]. In general, both uncoated and polymer coated SS-W based anodes gave higher current densities than their counterpart SS-P based anodes. In particular, PANi coated anodes gave

higher current densities than the PPy coated anodes. Notably, the SS-P anodes produced less current compared to the SS/PANi-P and SS/PPy-P anodes [Figure 5.5(c)]. Both the SS/PANi-P and SS/PPy-P anodes produced their maximum current densities during the 9th and 10th batch cycles (0.4 mA cm⁻² and 0.1 mA cm⁻², respectively). However, the start-up time for the current generation was faster with the SS/PANi-P anodes than with the SS/PPy-P anodes (3rd vs. the 7th cycle). This is most likely due to comparatively more biocompatible nature of PANi than with PPy and its faster biofilm formation during the OCV cycles. All the SS-W based anodes exhibited an instant current generation from the 3rd cycle, indicating that there was no delay in the start-up of the bioelectrocatalysis. This can be attributed to their 3D accessible areas that provided more anchoring points to the microbial cells and, thus, enabling more biofilm growth. The maximum current densities generated by SS-W, SS/PANi-W, and SS/PPy-W anodes were 0.30 ± 0.04 , 0.67 ± 0.05 and 0.56 ± 0.07 mA cm⁻², respectively. After the 6th cycle, no further increment in current generation was observed in all SS-W based anodes. In addition to providing more surface area (within a similar geometrical area compared to that of SS-P anode) for biofilm coverage, the higher current generation by all SS-W anodes can also be attributed to their macroporous and fibrous nature [Figure 5.1(a, b, c)] that promotes efficient mass transfer. The SS-P anodes perform poorly on these accounts due to their 2D nature. The control experiments ran in parallel with all anodes without microbial inoculum did not generate any current (data not shown).

The stable maximum current densities from day 35 of both PANi and PPy systems suggests that there is no influence of coating deterioration (if any) on the bioanode performance. Long-term MFCs tests are, however, needed to check the stability of such coatings on the anodes and to validate their applicability by running MFCs for a long time. The PANi and PPy coating method used in this work was precisely developed after extensive optimisation steps and subjected to durability testing in corrosive solution. The coatings on the metal surfaces with exopolysaccharides are reported to protect the surfaces from corrosion or fouling by lowering ionic diffusion rates [52]. Also, exopolysaccharides slime maintains a hydrophobic environment at the coating interface, where they act as an adhesive which protects PANi and PPy [52,53]. The exopolysaccharide secretion from exoelectrogens on the anode in MFC systems may render protection for PANi and PPy coatings, and, thus, prevent their degradation.

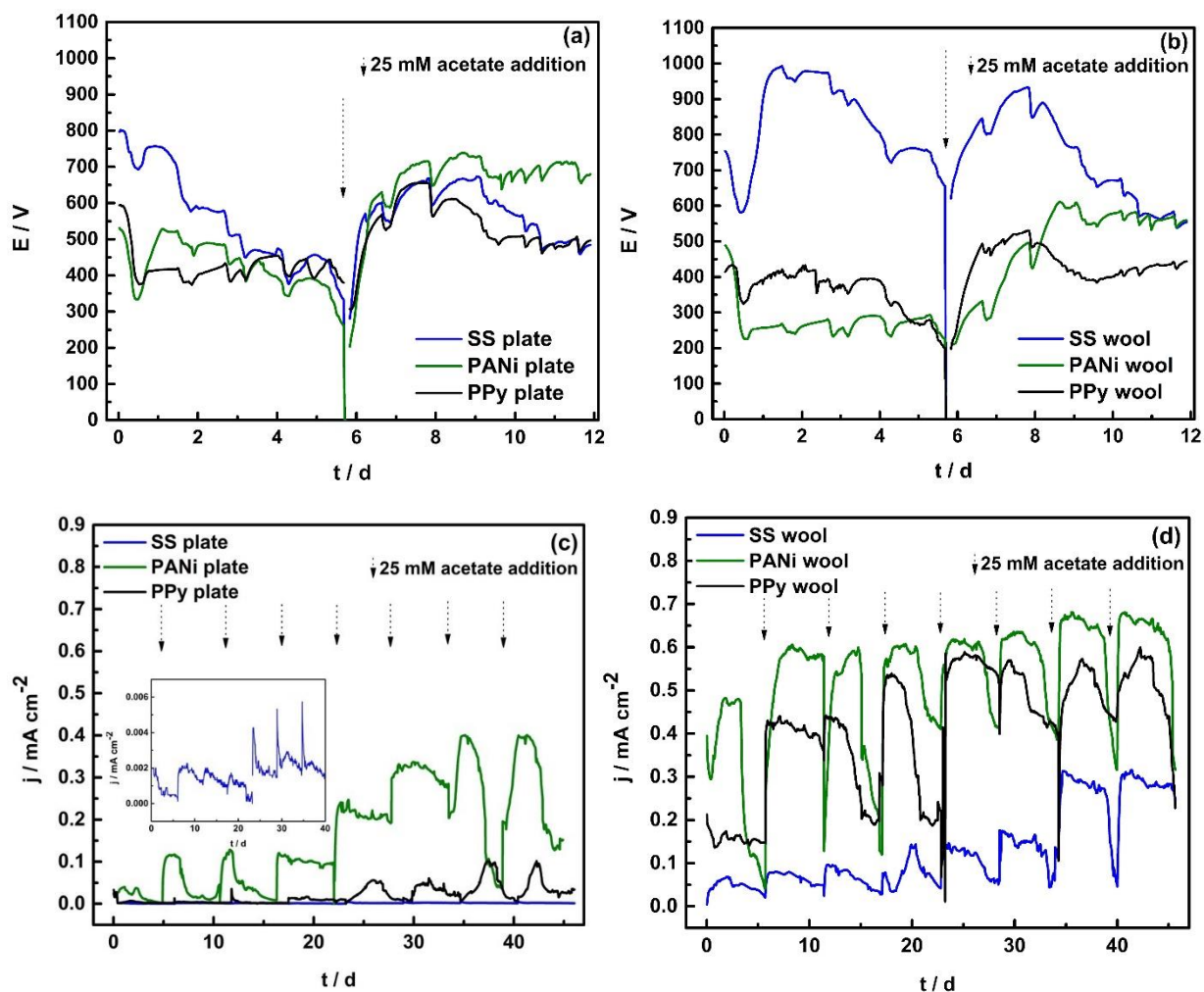
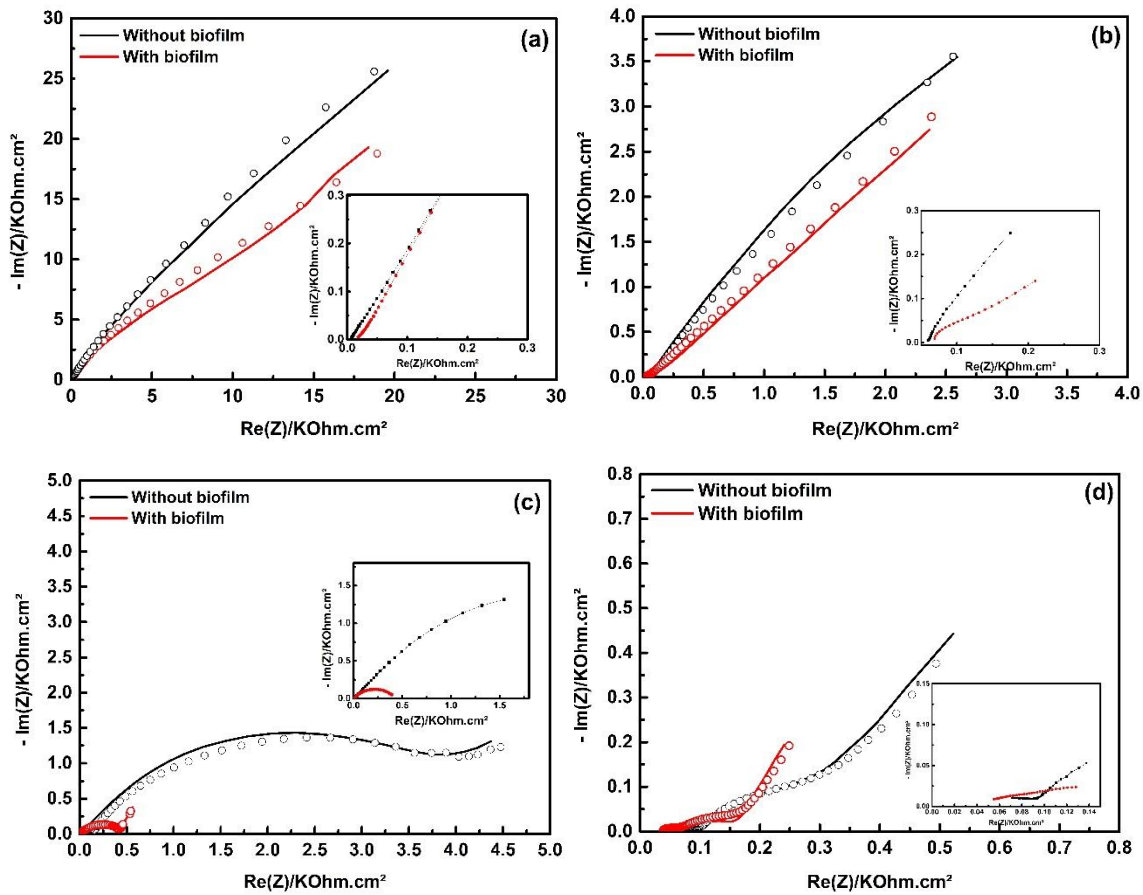


Fig. 5.5 Variation of open circuit voltages of (a) SS-P and (b) SS-W anode based MFCs monitored for two cycles. Bioelectrocatalytic performances presented in terms of current densities for (c) SS-P and (d) SS-W anode-based air-cathode MFCs operated under constant resistance mode (100Ω).

5.3.3 Charge transfer resistance of SS-W and SS-P anodes

Nyquist plots obtained from the EIS measurements of all anodes conducted at the start of the experiments and during the 9th and the 10th batch cycles are shown in Fig. 5.6. The charge transfer resistance (R_{ct}) data for the SS-P and SS-W based anodes derived from the Nyquist plots are given in Table 5.1. EIS fitting was carried out using EC-Lab 10.44 software. The fitted data for the experimental data (dotted lines) has a deviation of 1 or less than 1, indicating a good fit. The Nyquist plots obtained for the SS-P anode on day zero and after the 9th batch cycle showed a semicircle at high frequencies, which resembles charge transfer processes on the anode surface [Fig. 5.6(a)]. After the semicircle, mainly a capacitive linear segment is observed in medium and

low-frequency regions. The R_{ct} value decreased from 3192 ± 239 to $1438 \pm 143 \Omega \text{ cm}^{-2}$ after 45 days of MFC operation. The SS-W anode showed similar behaviour at relatively low impedance, which is due to a better charge transfer on the 3D surface [Fig. 5.6(b)]. R_{ct} value for this anode changed from $240 \pm 25 \Omega \text{ cm}^{-2}$ to $162 \pm 18 \Omega \text{ cm}^{-2}$. From both Nyquist plots, it was evident that the Warburg diffusion is predominantly present even after 45 days of MFC operation. It can be correlated to the relatively low j_0 value obtained for the uncoated SS anodes and strong hydrophobicity of SS, which limits the bacterial colonisation on the anodes and, consequently, leading to slower bioelectrocatalytic process. This, in turn, exhibited high impedance in mid-to-low frequency regions. It has been shown that the R_{ct} of SS anode can be decreased by acid treatment from 10.7Ω to 2.2Ω [36]. Low R_{ct} favours the electron transfer process from electroactive biofilm to the external circuit, resulting in a higher current generation.



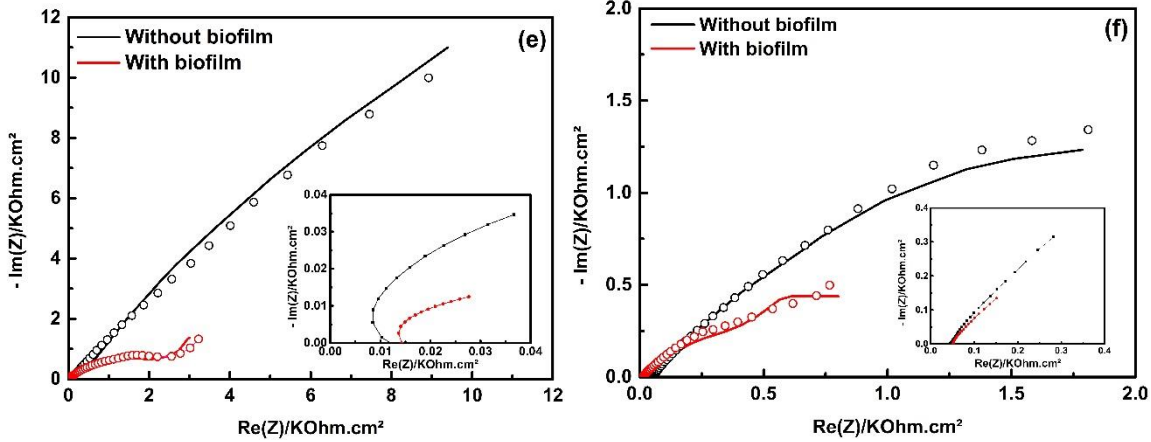


Fig. 5.6 Nyquist plots of EIS spectra for all SS based anodes: (a) SS-P, (b) SS-W, (c) SS/PANi-P, (d) SS/PANi-W, (e) SS/PPy-P, and (f) SS/PPy-W.

Table 5.1 Charge transfer resistance (R_{ct}) obtained for the bare anodes (without biofilm) and bioanodes (with biofilms).

Anode material	R_{ct} bare anode ($\Omega \text{ cm}^{-2}$)	R_{ct} bioanode* ($\Omega \text{ cm}^{-2}$)
SS-P	3192 ± 239	1438 ± 143
SS-W	240 ± 25	162 ± 18
SS/PANi-P	252 ± 32	99 ± 13
SS/PANi-W	67 ± 16	22 ± 4
SS/PPy-P	400 ± 36	132 ± 17
SS/PPy-W	142 ± 17	57 ± 13

*measured after 45 days of MFC operation

In the case of SS/PANi-P, the R_{ct} value ($252 \pm 32 \Omega \text{ cm}^{-2}$) on day 0 was much less compared to that obtained for the SS-P anode. It decreased further to $99 \pm 13 \Omega \text{ cm}^{-2}$ at the end of MFC experiments. For SS/PANi-W anode the initial R_{ct} value ($67 \pm 16 \Omega \text{ cm}^{-2}$) was even lower, which decreased further to $22 \pm 04 \Omega \text{ cm}^{-2}$. The lower R_{ct} values obtained for the PANi coated anodes strongly support the higher current densities achieved with these anodes. It has been reported that the larger reactive surface area of PANi coated anodes leads to higher electron transfer efficiency, which results in the higher power density of MFCs [31]. For SS/PPy-P the initial R_{ct} value of $400 \pm 36 \Omega \text{ cm}^{-2}$ decreased to $132 \pm 17 \Omega \text{ cm}^{-2}$, whereas for SS/PPy-W anode it decreased from $142 \pm$

17 $\Omega \text{ cm}^{-2}$ to $57 \pm 13 \Omega \text{ cm}^{-2}$ after 45 days of MFC operation. Initially, the charge transfer process of the substrate oxidation is the rate-limiting step since a few bacteria are involved in the process. The successive biofilm formation on the anode decreases the activation losses due to biocatalytic activity on its surface. It is clear that the lower impedance enhanced the performance of the anodic bioelectrocatalytic activity after incubation for a longer period.

5.3.4 Electrokinetic behaviour of PANi coated SS-W based anodes

From the Tafel-type linear equation obtained from the LSV in Figures 5.7a and 5.7b, the slope is F/RT , and the y-axis intercept is the logarithm of the exchange current. For each MFC, Tafel plot was recorded at the start of the experiment. The exchange current density (j_0) was determined by extrapolation to $\eta = 0$ of a linear regression ($R^2 > 0.99$) between $\eta = 150 \text{ mV}$. By application of 150 mV overpotential, the j_0 values depend on the charge limited electrochemical process where mass transfer is limited during measurements. The j_0 value signifies the rate of electron exchange from the biofilm to the electrode at equilibrium. A higher value of j_0 means faster electron exchange rate. The $j_{0(\text{apparent})}$ value also predicts the lower activation energy barrier for the forward reaction. The average j_0 values based on triplicate measurements are used to plot the Tafel curves. The Tafel plots for SS-P and SS-W based anodes are shown in Fig. 5.7a and 5.7b, respectively. The $j_{0(\text{apparent})}$ values for these anode systems calculated from Tafel plots are shown in Fig. 5.7c and 5.7d, respectively.

The initial $j_{0(\text{apparent})}$ values for the SS-P, SS/PANi-P and SS/PPy-P were 0.0006 ± 0.0001 , 0.002 ± 0.001 , and $0.0008 \pm 0.0001 \text{ mA cm}^{-2}$, respectively. After 45 days of MFC operation, these values increased to 0.002 ± 0.002 , 0.050 ± 0.002 and $0.006 \pm 0.004 \text{ mA cm}^{-2}$, respectively. There was no significant change in the initial $j_{0(\text{apparent})}$ value after the MFC incubation for the SS-P anode. The electrokinetic value and hydrophilic nature of the SS-P anode clearly suggest that these are unfavourable conditions for biofilm development. The SS/PANi-P shows remarkable increment in $j_{0(\text{apparent})}$ in comparison to the SS/PPy-P system indicating its excellent electrokinetic properties. The initial $j_{0(\text{apparent})}$ for SS-W, SS/PANi-W and SS/PPy-W were 0.0007 ± 0.0010 , 0.040 ± 0.009 , $0.020 \pm 0.009 \text{ mA cm}^{-2}$, respectively. They increased to 0.020 ± 0.005 , 0.098 ± 0.007 and $0.036 \pm 0.003 \text{ mA cm}^{-2}$ after 45 days of MFC operation, respectively. In contrast to the SS-P plate-based anodes, the $j_{0(\text{apparent})}$ values obtained for the SS-W based anodes increased significantly after MFC

operations due to the unpolished morphological nature of SS-W and the 3D accessible surface area for microbes to grow on their surfaces.

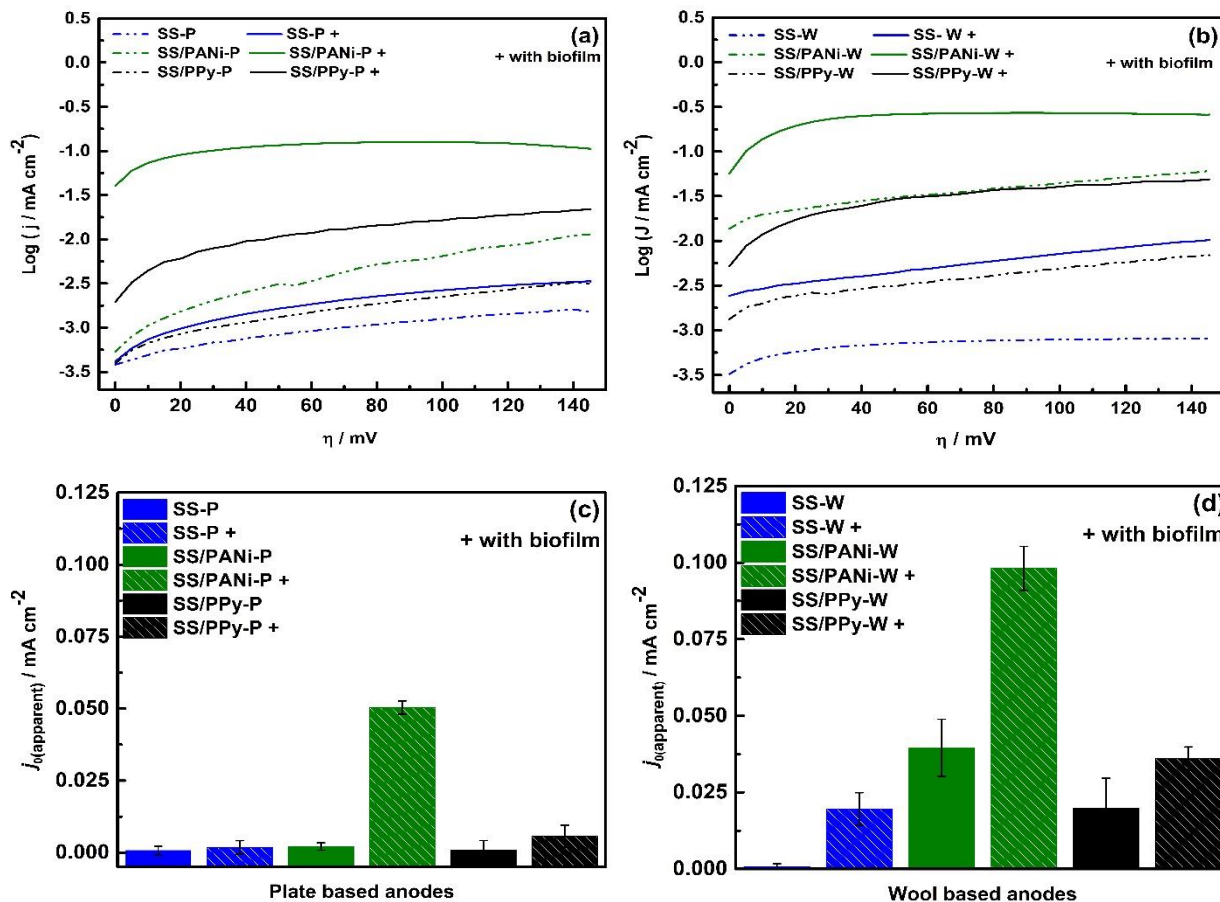


Fig. 5.7 Electrokinetics behaviour of SS-P based and SS-W based anodes. Tafel plots of SS-P based (a) and SS-W based (b) anodes. The $j_{0(\text{apparent})}$ values of SS-P based (c) and SS-W based (d) anodes. All figures include data for anodes without and with biofilm (suffixed by '+').

As expected, SS/PANI-W anode showed an increment in $j_{0(\text{apparent})}$ value. The initial $j_{0(\text{apparent})}$ of SS/PANI-W anode was also high because of its highly conductive nature. In the case of SS/PPy-W, the $j_{0(\text{apparent})}$ doubled from the initial value. The enhanced electrokinetics polymer coated anodes can be directly correlated with the biocompatibility of these electrodes for electroactive microbes. The achieved enhanced electrokinetics can be expressed in the following order: SS/PANI anodes > SS/PPy anodes > uncoated SS anodes.

5.3.5 Polarisation behaviour of all SS based anodes

The polarisation curves of all anodes are shown in Fig. 5.8. The MFC with the SS-P anode experienced doubling back (power overshoot) due to exceeding anodic electron depletion of the cathodic overpotential. The doubling back is generated by the kinetic limitation at the anode [54]. The SS-P faces the doubling back at a current density of around $0.1189 \text{ mA cm}^{-2}$ leading to a maximum power density of 0.036 mW cm^{-2} [Fig. 5.8(a)]. The polarisation of SS/PANi-P anode exhibits distinct activation; Ohmic and mass transport limited zones [Fig. 5.8(b)]. The maximum OCV obtained, in this case, was 749 mV. The activation region roughly falls from OCV to 600 mV. After activation, the system goes in the Ohmic region followed by mass transfer limit zone from 300 mV. It was observed that the maximum power density lies in the Ohmic region for SS/PANi-P system (0.187 mW cm^{-2} at 0.51 mA cm^{-2}). This behaviour suggests that high bacterial kinetic activity is involved compared to the use of the uncoated SS-P anode. The SS/PPy-P anode also experienced a power overshoot immediately after reaching a maximum power density of 0.071 mW cm^{-2} at 0.25 mA cm^{-2} , but it further led to the non-generation of doubling back [(Fig. 5.8(c)]. This observation indicates that the anode and cathodic kinetics remain at similar levels [54]. Hence, the SS/PPy-P anode can produce a significant current. However, it may also indicate that the anode was rate-limiting [55], and this led to the non-generation of doubling back.

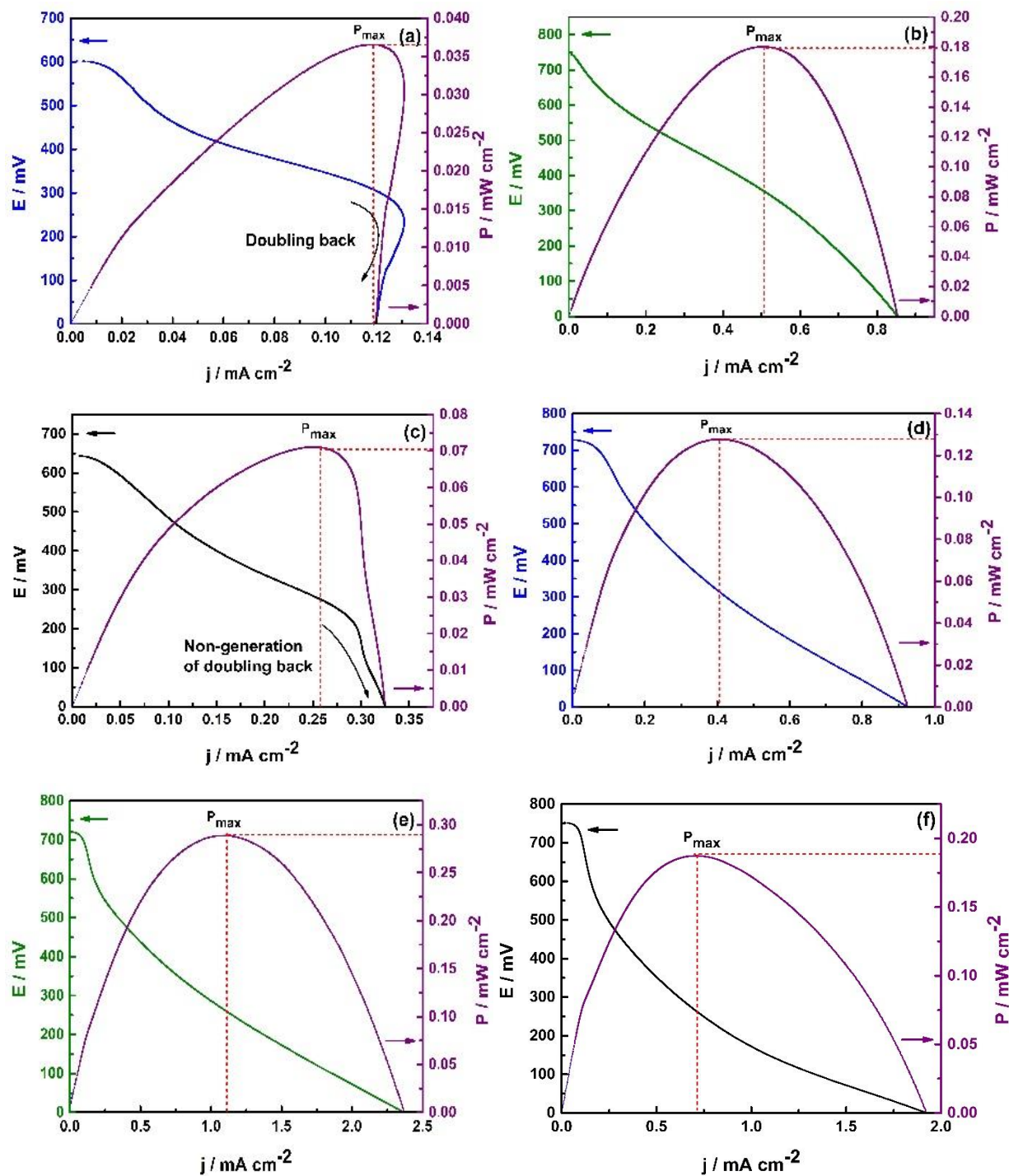


Fig. 5.8 Polarisation curves for the SS-P (a), SS/PANi-P (b), SS/PPy-P (c), SS-W (d), SS/PANi-W (e), and SS/PPy-W (f) anode based systems. The maximum power outputs expressed in terms of $mW\ cm^{-2}$ are 0.036 ± 0.004 , 0.180 ± 0.019 , 0.071 ± 0.012 , 0.127 ± 0.011 , 0.288 ± 0.036 and 0.187 ± 0.017 for the respective anode systems.

The polarisation in all SS-W based anode systems exhibits distinct activation, Ohmic, and mass transfer zones. In all MFC systems, the maximum power densities were controlled by the Ohmic limitations. The SS-W system displayed a maximum power density of 0.127 mW cm^{-2} at 0.406 mA cm^{-2} [Fig. 5.8(d)]. The SS/PANi-W system produces a maximum power density of 0.288 mW cm^{-2} at 1.115 mA cm^{-2} [Fig. 5.8(e)]. In the case of SS/PPy-W system the maximum power density achieved was 0.187 mW cm^{-2} at 0.714 mA cm^{-2} [Fig. 5.8(f)].

5.3.6 Comparison with previous work

Tables 5.2 summarises the maximum bioelectrocatalytic performances reported in terms of current and power densities for different SS based anodes in MFCs. Anode materials such as silver [34], copper [34], SS-P [35] and SS foam [56] were explored in the tri-electrode systems. Higher current densities (one order of magnitude higher than achieved with the SS-W in this study) were achieved with these materials. It should be noted here that all those studies were conducted under controlled potential polarisation conditions.

Tables 5.3 and 5.4 further provide a comparative overview of the bioelectrocatalytic performance of PANi and PPy modified anodes in different MFCs reported by other researchers. The pristine SS-wool represents the highest performing anode in conventional two-chambered and single-chambered air cathode MFCs (Table 5.2). Amongst different PANi modified composite materials, the SS/PANi-W, tested in this study, exhibits the highest power density. This comparative analysis shows that the unmodified or PANi modified SS wool based anodes outperform their counterparts in acetate-fed MFCs. This high bioelectrocatalytic performance, coupled with its low-cost clearly demonstrates the effectiveness of SS-W as a promising cheap anode material for MFCs.

Table 5.2 Comparison of bioelectrocatalytic performance of different SS based and some other metallic anodes used for MFCs

Type of MFC	Vol. of reactor (mL)	Anode material	Anode area (cm ²)	Max. Current density (mA cm ⁻²)	Max. power density (mW cm ⁻²)	Reference
Tri-electrode	250	Silver	1.5	1.1	NA	[34]
Tri-electrode	250	Copper	1.5	1.5	NA	[34]
Tri-electrode	150	SS-P	2.5	2.060	NA	[35]
Tri-electrode	500	SS foam	2	8.2	NA	[56]
Marine	NA	Austenitic SS	1200	0.014	0.0023	[57]
H-shaped	90	SSFF	3.24	0.003	0.0008	[31]
Single chamber	125	SS-FO	25	0.392	0.1060	[38]
Single chamber	125	SS foil	13	0.100	NA	[58]
H-shaped	90	SSFF	3.24	0.115	0.0347	[45]
Single chamber	27	SS-P	3.5	0.118*	0.036*	This study**
Single chamber	27	SS-W	7.5	0.400*	0.127*	This study**

* Values obtained from polarisation curves

** Normalised by cathode area

Table 5.3 Comparison of bioelectrocatalytic performance of PANi modified anodes in MFCs.

Type of MFC	Vol. of reactor (mL)	Anode material	Anode area (cm ²)	Max. Current density (mA cm ⁻²)	Max. power density (mW cm ⁻²)	Reference
H-shaped	90	PANi _{che} /SSFF	3.24	0.149	0.0360	[45]
H-shaped	90	PANi _{ele} /SSFF	3.24	0.0035	0.0800	[45]
H-shaped	NA	Inkjet-printed PANi/CP	NA	0.0396	0.0693	[44]
Tri-electrode	NA	PANi/CNT	1	NA	0.0042	[59]
Dual chamber	100	PANi/CNT/CP	80	NA	0.157	[60]

Dual chamber	110	PANI/ CC	25	0.0944	0.516 [†]	[61]
Single chamber	83	PANi/GF	12.5	NA	0.400 [†]	[62]
Single chamber	27	PANi/SS-P	3.5	0.507*	0.180*	This study**
Single chamber	27	PANi/SS-W	7.5	1.108*	0.288*	This study**

* Values obtained from polarisation curves

** Normalised by cathode area

[†] Volumetric power density (mW m⁻³)

Table 5.4 Comparison of bioelectrocatalytic performance of PPy modified anodes in MFCs.

Type of MFC	Vol. of reactor (mL)	Anode material	Anode area (cm ⁻²)	Max. Current density (mA cm ⁻²)	Max. power density (mW cm ⁻²)	Reference
Dual chamber	0.5	PPy/RVC	0.0154	NA	1.200	[63]
Dual chamber	75	PPy/AQDS	47.5	0.2742	0.1303	[64]
Benthic	NA	PPy/MnO ₂	9	0.060	0.0562	[65]
H-shaped	10	PPy/CNTs	12.25	0.1278	0.0228	[66]
Single chamber	20	NT-MPMs	7	NA	32700 [†]	[67]
Dual chamber	32	CPHs/CNTs	36.8	0.1600	0.1898	[68]
Single chamber	27	PPy/SS-P	3.5	0.288*	0.071*	This study**
Single chamber	27	PPy/SS-W	7.5	0.713*	0.187*	This study**

* Values obtained from polarisation curves

** Normalised by cathode area

[†] Volumetric current density (mW m⁻³)

5.4 Conclusions

We have demonstrated, for the first time, the potential use of low-cost SS-W scrubber as a cheap and efficient anode in air-cathode MFCs. The performance of the SS-W anode was far superior to that of the most commonly used SS-P anode on as the basis of achieved current density, power density, charge transfer resistance and electrokinetic behaviour. The PANi and PPy coatings of the SS-W improved their performances as anodes for MFCs considerably. In particular, the SS-W coated with PANi gave the best performance with 54% more power density than achieved with the SS/PPy-W anode. The SS-W is by far the cheapest anode reported in the literature in its class [37]. Considering the many advantages, such as tunable shape, size, design, high surface area and mechanical properties along with the commercial availability of SS-W, it is a most suited material for relatively cheap MFC anode. As the SS/PANi-W anode exhibited the highest power generation in this study, further study of its long-term stability is necessary prior to its adoption for the construction of a pilot scale MFC stack in an endeavour to achieve a high-performance MFC system with the potential capability for treating landfill leachate.

References

- [1] J.M. Sonawane, A. Yadav, P.C. Ghosh, S.B. Adeloju, Recent advances in the development and utilization of modern anode materials for high performance microbial fuel cells, *Biosens. Bioelectron.* 90 (2017) 558–576. doi:10.1016/j.bios.2016.10.014.
- [2] M. Miyahara, A. Kouzuma, K. Watanabe, Effects of NaCl concentration on anode microbes in microbial fuel cells., *AMB Express.* 5 (2015) 123. doi:10.1186/s13568-015-0123-6.
- [3] K.-J. Chae, M.-J. Choi, J.-W. Lee, K.-Y. Kim, I.S. Kim, Effect of different substrates on the performance, bacterial diversity, and bacterial viability in microbial fuel cells, *Bioresour. Technol.* 100 (2009) 3518–3525. doi:10.1016/j.biortech.2009.02.065.
- [4] S. Puig, M. Serra, M. Coma, M. Cabré, M.D. Balaguer, J. Colprim, Effect of pH on nutrient dynamics and electricity production using microbial fuel cells, *Bioresour. Technol.* 101 (2010) 9594–9599. doi:10.1016/j.biortech.2010.07.082.
- [5] S.A. Patil, F. Harnisch, B. Kapadnis, U. Schröder, Electroactive mixed culture biofilms in microbial bioelectrochemical systems: The role of temperature for biofilm formation and performance, *Biosens. Bioelectron.* 26 (2010) 803–808. doi:10.1016/j.bios.2010.06.019.
- [6] S.A. Patil, F. Harnisch, C. Koch, T. Hübschmann, I. Fetzer, A.A. Carmona-Martínez, S. Müller, U. Schröder, Electroactive mixed culture derived biofilms in microbial bioelectrochemical systems: The role of pH on biofilm formation, performance and composition, *Bioresour. Technol.* 102 (2011) 9683–9690. doi:10.1016/j.biortech.2011.07.087.
- [7] S. Bajracharya, M. Sharma, G. Mohanakrishna, X. Dominguez Benneton, D.P.B.T.B. Strik, P.M. Sarma, D. Pant, An overview on emerging bioelectrochemical systems (BESs): Technology for sustainable electricity, waste remediation, resource recovery, chemical production and beyond, *Renew. Energy.* 98 (2016) 153–170. doi:10.1016/j.renene.2016.03.002.
- [8] K.C. Wrighton, J.D. Coates, *Microbial Fuel Cells: Plug-in and Power-on Microbiology*, *Microbe.* 4 (2009) 281–287. www.asm.org/asm/ccLibraryFiles/FILENAME/000000004926/znw00609000281.pdf (accessed February 19, 2017).
- [9] K. Guo, A. PrévotEAU, S.A. Patil, K. Rabaey, Engineering electrodes for microbial electrocatalysis, *Curr. Opin. Biotechnol.* 33 (2015) 149–156.

- doi:10.1016/j.copbio.2015.02.014.
- [10] Mustakeem, Electrode materials for microbial fuel cells: Nanomaterial approach, *Mater. Renew. Sustain. Energy*. 4 (2015) 22. doi:10.1007/s40243-015-0063-8.
- [11] J.M. Pisciotta, Z. Zaybak, D.F. Call, J.Y. Nam, B.E. Logan, Enrichment of microbial electrolysis cell biocathodes from sediment microbial fuel cell bioanodes, *Appl. Environ. Microbiol.* 78 (2012) 5212–5219. doi:10.1128/AEM.00480-12.
- [12] F. Calignano, T. Tommasi, D. Manfredi, A. Chiolerio, Additive Manufacturing of a Microbial Fuel Cell-A detailed study., *Sci. Rep.* 5 (2015) 17373. doi:10.1038/srep17373.
- [13] M. Rahimnejad, A. Adhami, S. Darvari, A. Zirepour, S.E. Oh, Microbial fuel cell as new technology for bioelectricity generation: A review, *Alexandria Eng. J.* 54 (2015) 745–756. doi:10.1016/j.aej.2015.03.031.
- [14] S. Kalathil, D. Pant, Nanotechnology to rescue bacterial bidirectional extracellular electron transfer in bioelectrochemical systems, *RSC Adv.* 6 (2016) 30582–30597. doi:10.1039/C6RA04734C.
- [15] F. Offei, A. Thygesen, M. Mensah, K. Tabbicca, D. Fernando, I. Petrushina, G. Daniel, A viable electrode material for use in microbial fuel cells for tropical regions, *Energies*. 9 (2016) 35. doi:10.3390/en9010035.
- [16] D. Pant, G. Van Bogaert, Y. Alvarez-Gallego, L. Diels, K. Vanbroekhoven, Evaluation of bioelectrogenic potential of four industrial effluents as substrate for low cost microbial fuel cells operation, *Environ. Eng. Manag. J.* 15 (2016) 1897–1904.
- [17] M. Liu, M. Zhou, L. Ma, H. Yang, Y. Zhao, Architectural design of hierarchically meso-macroporous carbon for microbial fuel cell anodes, *RSC Adv.* 6 (2016) 27993–27998. doi:10.1039/c5ra26420k.
- [18] S. Chen, G. He, A.A. Carmona-Martinez, S. Agarwal, A. Greiner, H. Hou, U. Schröder, Electrospun carbon fiber mat with layered architecture for anode in microbial fuel cells, *Electrochem. Commun.* 13 (2011) 1026–1029. doi:10.1016/j.elecom.2011.06.009.
- [19] I. Ieropoulos, J. Greenman, C. Melhuish, Microbial fuel cells based on carbon veil electrodes: Stack configuration and scalability, *Int. J. Energy Res.* 32 (2008) 1228–1240. doi:10.1002/er.1419.
- [20] B. Logan, S. Cheng, V. Watson, G. Estadt, Graphite Fiber Brush Anodes for Increased Power Production in Air-Cathode Microbial Fuel Cells, *Environ. Sci. Technol.* 41 (2007)

- 3341–3346. doi:10.1021/es062644y.
- [21] Q. Liao, J. Zhang, J. Li, D. Ye, X. Zhu, B. Zhang, Increased performance of a tubular microbial fuel cell with a rotating carbon-brush anode, *Biosens. Bioelectron.* 63 (2015) 558–561. doi:10.1016/j.bios.2014.08.014.
- [22] R. Karthikeyan, B. Wang, J. Xuan, J.W.. Wong, P.K.H. Lee, M.K.H. Leung, Interfacial electron transfer and bioelectrocatalysis of carbonized plant material as effective anode of microbial fuel cell, *Electrochim. Acta.* 157 (2015) 314–323. doi:10.1016/j.electacta.2015.01.029.
- [23] Y.-Q. Wang, H.-X. Huang, B. Li, W.-S. Li, Novelty developed three-dimensional carbon scaffold anodes from polyacrylonitrile for microbial fuel cells, *J. Mater. Chem. A.* 3 (2015) 5110–5118. doi:10.1039/C4TA06007E.
- [24] Y. Shen, Y. Zhou, S. Chen, F. Yang, S. Zheng, H. Hou, Carbon nanofibers modified graphite felt for high performance anode in high substrate concentration microbial fuel cells, *Sci. World J.* 2014 (2014). doi:10.1155/2014/130185.
- [25] S.S. Manickam, U. Karra, L. Huang, N.-N. Bui, B. Li, J.R. McCutcheon, Activated carbon nanofiber anodes for microbial fuel cells, *Carbon N. Y.* 53 (2013) 19–28. doi:10.1016/j.carbon.2012.10.009.
- [26] Y. Yang, T. Liu, Q. Liao, D. Ye, X. Zhu, J. Li, P. Zhang, Y. Peng, S. Chen, Y. Li, A three-dimensional nitrogen-doped graphene aerogel-activated carbon composite catalyst that enables low-cost microfluidic microbial fuel cells with superior performance, *J. Mater. Chem. A.* 4 (2016) 15913–15919. doi:10.1039/C6TA05002F.
- [27] J.M. Sonawane, E. Marsili, P. Chandra Ghosh, Treatment of domestic and distillery wastewater in high surface microbial fuel cells, *Int. J. Hydrogen Energy.* 39 (2014) 21819–21827. doi:10.1016/j.ijhydene.2014.07.085.
- [28] Y.-Y. Yu, D.-D. Zhai, R.-W. Si, J.-Z. Sun, X. Liu, Y.-C. Yong, Three-Dimensional Electrodes for High-Performance Bioelectrochemical Systems., *Int. J. Mol. Sci.* 18 (2017). doi:10.3390/ijms18010090.
- [29] Y. Zhao, K. Watanabe, R. Nakamura, S. Mori, H. Liu, K. Ishii, K. Hashimoto, Three-dimensional conductive nanowire networks for maximizing anode performance in microbial fuel cells, *Chem. - A Eur. J.* 16 (2010) 4982–4985.
- [30] S. Chen, G. He, X. Hu, M. Xie, S. Wang, D. Zeng, H. Hou, U. Schröder, A three-

- dimensionally ordered macroporous carbon derived from a natural resource as anode for microbial bioelectrochemical systems, *ChemSusChem*. 5 (2012) 1059–1063. doi:10.1002/cssc.201100783.
- [31] J. Hou, Z. Liu, S. Yang, Y. Zhou, Three-dimensional macroporous anodes based on stainless steel fiber felt for high-performance microbial fuel cells, *J. Power Sources*. 258 (2014) 204–209. doi:10.1016/j.jpowsour.2014.02.035.
- [32] J.R. Kim, H.C. Boghani, N. Amini, K.-F. Aguey-Zinsou, I. Michie, R.M. Dinsdale, A.J. Guwy, Z.X. Guo, G.C. Premier, Porous anodes with helical flow pathways in bioelectrochemical systems: The effects of fluid dynamics and operating regimes, *J. Power Sources*. 213 (2012) 382–390. doi:10.1016/j.jpowsour.2012.03.040.
- [33] L. Huang, X. Li, Y. Ren, X. Wang, A monolithic three-dimensional macroporous graphene anode with low cost for high performance microbial fuel cells, *RSC Adv*. 6 (2016) 21001–21010. doi:10.1039/C5RA24718G.
- [34] A. Baudler, I. Schmidt, M. Langner, A. Greiner, U. Schröder, Does it have to be carbon? Metal anodes in microbial fuel cells and related bioelectrochemical systems, *Energy Environ. Sci*. 8 (2015) 2048–2055. doi:10.1039/C5EE00866B.
- [35] D. Pocaznoi, A. Calmet, L. Etcheverry, B. Erable, A. Bergel, Environmental Science Stainless steel is a promising electrode material for anodes of microbial fuel cells, (2012) 9645–9652. doi:10.1039/c2ee22429a.
- [36] X. Peng, S. Chen, L. Liu, S. Zheng, M. Li, Modified stainless steel for high performance and stable anode in microbial fuel cells, *Electrochim. Acta*. 194 (2016) 246–252. doi:10.1016/j.electacta.2016.02.127.
- [37] K. Guo, B.C. Donose, A.H. Soeriyadi, A. PrévotEAU, S.A. Patil, S. Freguia, J.J. Gooding, K. Rabaey, Flame Oxidation of Stainless Steel Felt Enhances Anodic Biofilm Formation and Current Output in Bioelectrochemical Systems, *Environ. Sci. Technol*. 48 (2014) 7151–7156. doi:10.1021/es500720g.
- [38] T. Yamashita, M. Ishida, S. Asakawa, H. Kanamori, H. Sasaki, A. Ogino, Y. Katayose, T. Hatta, H. Yokoyama, Enhanced electrical power generation using flame-oxidized stainless steel anode in microbial fuel cells and the anodic community structure, *Biotechnol. Biofuels*. 9 (2016) 62. doi:10.1186/s13068-016-0480-7.
- [39] J.L. Lamp, J.S. Guest, S. Naha, K.A. Radavich, N.G. Love, M.W. Ellis, I.K. Puri, Flame

- synthesis of carbon nanostructures on stainless steel anodes for use in microbial fuel cells, *J. Power Sources*. 196 (2011) 5829–5834. doi:10.1016/j.jpowsour.2011.02.077.
- [40] J. Wang, M. Li, F. Liu, S. Chen, Stainless Steel Mesh Supported Carbon Nanofibers for Electrode in Bioelectrochemical System, *J. Nanomater.* 2016 (2016) 1–5. doi:10.1155/2016/4246568.
- [41] S. Zheng, F. Yang, S. Chen, L. Liu, Q. Xiong, T. Yu, F. Zhao, U. Schröder, H. Hou, Binder-free carbon black/stainless steel mesh composite electrode for high-performance anode in microbial fuel cells, *J. Power Sources*. 284 (2015) 252–257. doi:10.1016/j.jpowsour.2015.03.014.
- [42] Y. Zhang, G. Mo, X. Li, W. Zhang, J. Zhang, J. Ye, X. Huang, C. Yu, A graphene modified anode to improve the performance of microbial fuel cells, *J. Power Sources*. 196 (2011) 5402–5407. doi:10.1016/j.jpowsour.2011.02.067.
- [43] S. Sawant, T. Han, M. Cho, Metal-Free Carbon-Based Materials: Promising Electrocatalysts for Oxygen Reduction Reaction in Microbial Fuel Cells, *Int. J. Mol. Sci.* 18 (2016) 25. doi:10.3390/ijms18010025.
- [44] R.-B. Song, K. Yan, Z.-Q. Lin, J.S. Chye Loo, L.-J. Pan, Q. Zhang, J.-R. Zhang, J.-J. Zhu, Inkjet-printed porous polyaniline gel as an efficient anode for microbial fuel cells, *J. Mater. Chem. A*. 4 (2016) 14555–14559. doi:10.1039/C6TA05770E.
- [45] J. Hou, Z. Liu, Y. Li, Polyaniline Modified Stainless Steel Fiber Felt for High-Performance Microbial Fuel Cell Anodes, *J. Clean Energy Technol.* 3 (2015) 165–169. doi:10.7763/JOCET.2015.V3.189.
- [46] S. Chen, G. He, Q. Liu, F. Harnisch, Y. Zhou, Y. Chen, M. Hanif, S. Wang, X. Peng, H. Hou, U. Schröder, Layered corrugated electrode macrostructures boost microbial bioelectrocatalysis, *Energy Environ. Sci.* 2 (2012) 9769–9772. doi:10.1039/c2ee23344d.
- [47] F. Harnisch, C. Koch, S.A. Patil, T. Hübschmann, S. Müller, U. Schröder, Revealing the electrochemically driven selection in natural community derived microbial biofilms using flow-cytometry, *Energy Environ. Sci.* 4 (2011) 1265. doi:10.1039/c0ee00605j.
- [48] J.M. Sonawane, S.B. Adeloju, P.C. Ghosh, Landfill leachate: A promising substrate for microbial fuel cells, *Int. J. Hydrogen Energy*. (2017). doi:10.1016/j.ijhydene.2017.03.137.
- [49] B.E. Logan, M.J. Wallack, K.Y. Kim, W. He, Y. Feng, P.E. Saikaly, Assessment of Microbial Fuel Cell Configurations and Power Densities, *Environ. Sci. Technol. Lett.* 2

- (2015) 206–214. doi:10.1021/acs.estlett.5b00180.
- [50] B.E. Logan, Exoelectrogenic bacteria that power microbial fuel cells, *Nat. Rev. Microbiol.* 7 (2009) 375–381. doi:10.1038/nrmicro2113.
- [51] L. Hui, *Proton Exchange Membrane Fuel Cells: Contamination and Mitigation Strategies*, CRC Press, 2010.
- [52] K. Bucur Claudiu, Finkenstadt Victoria, Cote Gregory - Greg, Evans, Electrochemical evaluation for corrosion resistance of bacterial exopolysaccharides on low carbon steel, *Int. Biodeterior. Biodegrad.* (2010). <https://www.ars.usda.gov/research/publications/publication/?seqNo115=258160> (accessed May 11, 2017).
- [53] V.L. Finkenstadt, C.B. Bucur, G.L. Côté, K.O. Evans, Bacterial exopolysaccharides for corrosion resistance on low carbon steel, *J. Appl. Polym. Sci.* 134 (2017) 45032. doi:10.1002/app.45032.
- [54] B. Kim, J. An, I.S. Chang, Elimination of Power Overshoot Caused by Electron Depletion of Limited Anodic Kinetic at Bio-anode through Assistance Current in Microbial Fuel Cell, *ChemSusChem.* 10 (2016) 612–617. doi:10.1002/cssc.201601412.
- [55] D. Pocaznoi, B. Erable, L. Etcheverry, M.-L. Delia, A. Bergel, Towards an engineering-oriented strategy for building microbial anodes for microbial fuel cells, *Phys. Chem. Chem. Phys.* 14 (2012) 13332. doi:10.1039/c2cp42571h.
- [56] S.F. Ketep, A. Bergel, A. Calmet, B. Erable, Stainless steel foam increases the current produced by microbial bioanodes in bioelectrochemical systems, *Energy Environ. Sci.* 7 (2014) 1633. doi:10.1039/c3ee44114h.
- [57] C. Dumas, A. Mollica, D. Féron, R. Basséguy, L. Etcheverry, A. Bergel, Marine microbial fuel cell: Use of stainless steel electrodes as anode and cathode materials, *Electrochim. Acta.* 53 (2007) 468–473. doi:10.1016/j.electacta.2007.06.069.
- [58] E. Guerrini, P. Cristiani, M. Grattieri, C. Santoro, B. Li, S. Trasatti, Electrochemical behavior of stainless steel anodes in membraneless microbial fuel cells, *J. Electrochem. Soc.* 161 (2014) H62–H67. doi:10.1149/2.096401jes.
- [59] Y. Qiao, C.M. Li, S.-J. Bao, Q.-L. Bao, Carbon nanotube/polyaniline composite as anode material for microbial fuel cells, *J. Power Sources.* 170 (2007) 79–84. doi:10.1016/j.jpowsour.2007.03.048.

- [60] C.-T. Wang, R.-Y. Huang, Y.-C. Lee, C.-D. Zhang, Electrode Material of Carbon Nanotube/Polyaniline Carbon Paper Applied in Microbial Fuel Cells, *J. Clean Energy Technol.* 1 (2013) 206–210.
- [61] B. Lai, X. Tang, H. Li, Z. Du, X. Liu, Q. Zhang, Power production enhancement with a polyaniline modified anode in microbial fuel cells, *Biosens. Bioelectron.* 28 (2011) 373–377. doi:10.1016/j.bios.2011.07.050.
- [62] P. Wang, H. Li, Z. Du, Polyaniline synthesis by cyclic voltammetry for anodic modification in microbial fuel cells, *Int. J. Electrochem. Sci.* 9 (2014) 2038–2046.
- [63] Y. Yuan, S. Kim, Polypyrrole-coated reticulated vitreous carbon as anode in microbial fuel cell for higher energy output, *Bull. Korean Chem. Soc.* 29 (2008) 168–172. doi:10.5012/bkcs.2008.29.1.168.
- [64] C. Feng, L. Ma, F. Li, H. Mai, X. Lang, S. Fan, A polypyrrole/anthraquinone-2,6-disulphonic disodium salt (PPy/AQDS)-modified anode to improve performance of microbial fuel cells, *Biosens. Bioelectron.* 25 (2010) 1516–1520. doi:10.1016/j.bios.2009.10.009.
- [65] W. Chen, Z. Liu, G. Su, Y. Fu, X. Zai, C. Zhou, J. Wang, Composite-modified anode by MnO₂/polypyrrole in marine benthic microbial fuel cells and its electrochemical performance, *Int. J. Energy Res.* 41 (2017) 845–853. doi:10.1002/er.3674.
- [66] Y. Zou, C. Xiang, L. Yang, L.-X. Sun, F. Xu, Z. Cao, A mediatorless microbial fuel cell using polypyrrole coated carbon nanotubes composite as anode material, *Int. J. Hydrogen Energy.* 33 (2008) 4856–4862. doi:10.1016/j.ijhydene.2008.06.061.
- [67] H. Yuan, L. Deng, Y. Chen, Y. Yuan, MnO₂/Polypyrrole/MnO₂ multi-walled-nanotube-modified anode for high-performance microbial fuel cells, *Electrochim. Acta.* 196 (2016) 280–285. doi:10.1016/j.electacta.2016.02.183.
- [68] X. Tang, H. Li, Z. Du, W. Wang, H.Y. Ng, Conductive polypyrrole hydrogels and carbon nanotubes composite as an anode for microbial fuel cells, *RSC Adv.* 5 (2015) 50968–50974. doi:10.1039/C5RA06064H.

Chapter 6

Fabrication of a carbon paper/polyaniline-copper composite cathode as a replacement for platinum cathode in low-temperature fuel cells

[Submitted as, JM Sonawane, D Pant, PC Ghosh, SB Adeloju, Fabrication of a carbon paper/polyaniline-copper composite cathode as a replacement for platinum cathode in low-temperature fuel cells, Journal of Material Chemistry A, Elsevier]

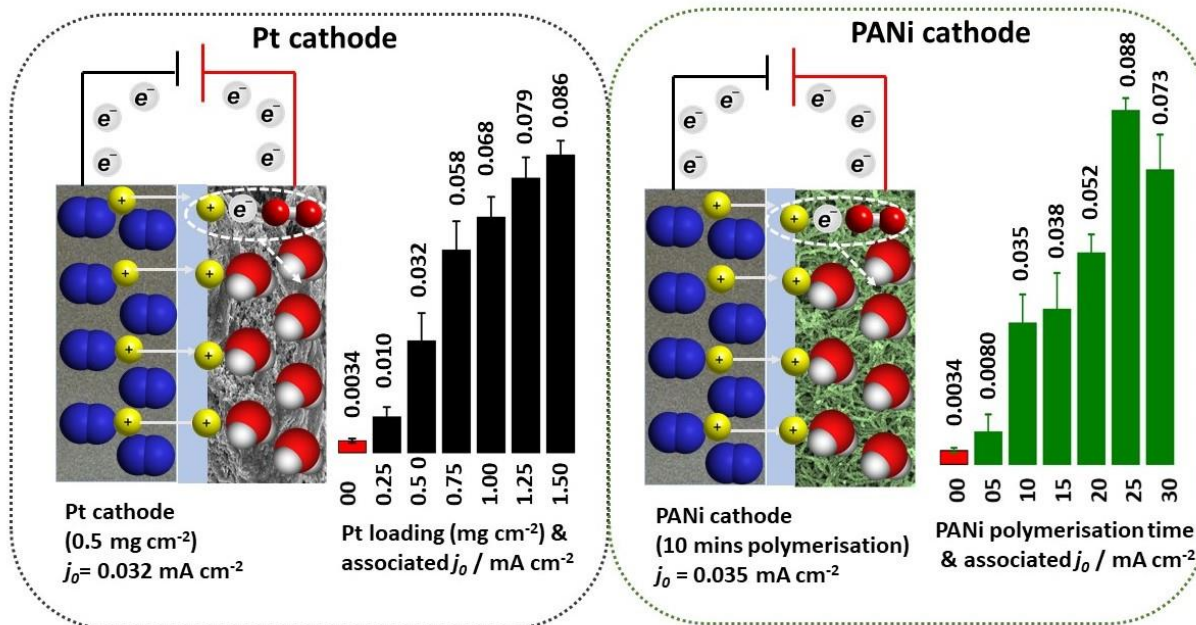
Nomenclature:

F	Faraday's constant [$96,485 \text{ C mol}^{-1}$]
i_0	Exchange current [mA]
j_0	Exchange current density [mA cm^{-2}]
R	Ideal gas constant [$8.31 \text{ J mol}^{-1} \text{ K}^{-1}$]
R	Resistor [Ω]
R_{ct}	Charge transfer resistance [Ω]
T	Absolute temperature [K]
η	Overpotential [mV]

Abbreviations:

Ag/AgCl	Silver/ silver chloride electrode
ATR	Attenuated total reflectance
CNx	N-doped ordered porous carbon
Cu	Copper
Fe-PANi-PAN	Iron-polyaniline/polyacrylonitrile
FTIR	Fourier Transform Infrared Spectroscopy
GDL	Gas diffusion layer
LSV	Linear sweep voltammetry
LTFCs	Low temperature fuel cells
MFCs	Microbial fuel cells
MnFe ₂ O/PANi	Manganese ferrite (/)polyaniline
NPMCs	Non-precious metal catalyst
ORP	Oxidation-reduction potential
ORR	Oxygen reduction reaction
PANi-Co-C	Polyaniline cobalt-carbon
PANi-Fe-C	Polyaniline iron carbon
PANi-Fe-N-C	Polyaniline iron nitrogen-doped carbon
PBS	Phosphate buffer solution
Pt/C	Platinised carbon
SEM	Scanning Electron Microscope
SS	Stainless steel

Graphical abstract



Abstract

Platinum has been used extensively in low-temperature fuel cells (LTFCs), but its possible replacement with low-cost alternatives has been a matter of considerable conjecture for some time. This study explores the use of a carbon paper/polyaniline-Cu composite (CP/PANi-Cu) as a potential low-cost replacement for the conventional Pt cathode. The incorporation of copper, through the addition of CuSO_4 to the monomer and deposition of the metal from this solution, enhanced the catalytic activity of CP/PANi-Cu cathode for oxygen reduction reaction, yielding a 170% higher j_{O_2} of $0.088 \pm 0.003 \text{ mA cm}^{-2}$ than with a conventional Pt cathode ($0.0325 \pm 0.0031 \text{ mA cm}^{-2}$) made up with 0.5 mg cm^{-2} Pt loading. Even with a Pt loading of 1.5 mg cm^{-2} , the j_{O_2} of the Pt cathode ($0.086 \pm 0.004 \text{ mA cm}^{-2}$) was still slightly lower. Also, the optimum CP/PANi-Cu cathode gave a much lower R_{ct} of $1.456 \Omega \text{ cm}^{-2}$ compared to the R_{ct} of $3.95 \Omega \text{ cm}^{-2}$ obtained with the conventional Pt cathode, but the Pt cathode with the higher Pt loading gave a closer R_{ct} of $1.485 \Omega \text{ cm}^{-2}$. Furthermore, the maximum oxygen reduction current of $-6.73 \pm 0.62 \text{ mA cm}^{-2}$ obtained with the CP/PANi-Cu cathode was higher than the $-5.47 \pm 0.60 \text{ mA cm}^{-2}$ obtained with the conventional Pt cathode but was close to the value of $-7.21 \pm 0.79 \text{ mA cm}^{-2}$ obtained with the Pt cathode with higher Pt loading. The presence of Cu in the CP/PANi-Cu composite was confirmed by XPS, and the observed enhancement of the ORR activity by the CP/PANi-Cu composite was not detected in the absence of copper (as CP/PANi composite). The morphology and structure of the CP/PANi-Cu coating and the CP/Pt cathode was also investigated by SEM and 4D X-ray microscopy to gain a better understanding of the performances of the cathodes. A uniform nano-fibrous structure was observed for the CP/PANi-Cu composite, while the CP/Pt revealed a non-uniform agglomeration. The results of this study demonstrate that the proposed CP/PANi-Cu cathode can be adopted as a suitable low-cost replacement for Pt cathode.

6.1 Introduction

Low-temperature fuel cells (LTFCs) have attracted considerable interest due to their unique advantages, such as high power density, low weight, and volume compared to other fuel cells [1]. However, a notable limitation to the wider application of these fuel cells is the cathode [2–4] which depends on the electrokinetics of the chosen catalyst for its established oxidation-reduction potential (ORP). For this reason, platinum (Pt) is often used as the catalyst to achieve maximum LTFC performance, but its rather high cost is a hindrance for commercial-scale application, especially when employed for microbial fuel cells (MFCs) for wastewater treatment [5,6]. Consequently, various attempts have been made in several studies to minimise the Pt content of the cathode, including the use of a wide range of Pt alloys [7,8].

Some of the Pt-based alloys that have been investigated for improving oxygen reduction reaction (ORR) activity in LTFCs include PtAg, PtNi, PtCo, PtPd, PtFe, PtW, PtCu, and PtAu [9–15]. Attempts have also been made to replace conventional Pt catalyst used for LTFCs with Pt-free catalyst based on the development of non-precious metal catalysts (NPMCs) [16–18]. Cheaper metal catalyst, such as silver [19,20], and ruthenium [21,22] based catalyst have also been investigated as an alternative to Pt. Furthermore, several metal-free catalysts for LTFCs have been reported based on the use of various materials [23–26], such as graphene-based nanostructured materials [27–30], carbon nanotubes [27], conductive polymers [31,32] and conductive polymer composites [33].

The use of heterocyclic conjugated polymers, such as polyaniline [34,35] and polypyrrole [36,37], has also gained considerable interest due to their catalytic and electrochemical properties, stability, conductivity, and ease of synthesis. In one case, nitrogen-doped carbon electrocatalyst was used with polyaniline to provide a superior electrocatalytic activity and stability than with Pt/C [38]. It was demonstrated in another study [39] that the incorporation of Pt into a PANi nanotube electrode exhibited improved catalytic activity than with Pt supported on carbon and the conventional electrode. In general, the catalytic activity and morphology of PANi or its composite depend on the adopted synthesis steps, heat treatment temperature and binder [40,41]. Although PANi has high specific capacitance and low synthesis cost, it also has poor stability [42] and a negligible stand-alone ORR catalytic activity. However, its stability and activity can be greatly enhanced by employing synergistic activity with metals and other polymers [42]. The catalytic activity of PANi on its own strongly depends on the carbon and nitrogen sources, as well as the adopted synthesis

conditions [43]. It has been demonstrated that the presence of cupric ions (Cu^{2+}) in the monomer solution accelerates PANi formation and also improves its conductivity [44]. Davis et al. [45] demonstrated that the Cu^{2+} ions enhanced the oxygen reduction kinetics, but the exact role of Cu^{2+} ions on the ORR catalysis remains unknown.

PANi possesses an excellent electrocatalytic activity for ORR due to its involvement in a highly-selective four electron reaction pathway and a positive onset potential [46]. However, the higher exchange current results in lower overpotential barrier. The major issue with a two-electron reaction of associated oxygen reduction is attributed to lower electrode potential [46] which also generates H_2O_2 which may damage the electrode material. Hence, a catalyst with a four-electron reaction is ideal for achieving better cathode performance.

In situ synthesised PANi-Fe-Co complex on the surface of carbon black nanoparticles, followed by heat treatment in the presence of iron and cobalt has been reported [47]. A study of a PANi coating which incorporated iron and carbon (PANi-Fe-C) has shown that heat treatment plays a major role in inducing the catalytic activity of PANi derived catalyst [48]. Another PANi composite which incorporated iron and nitrogen-doped carbon (PANi-Fe-N-C) was synthesised by ultrasonating a mixture containing an iron precursor followed by heat treatment [49]. In another study, PANi cobalt-carbon (PANi-Co-C) composite was synthesised by a reduction method without the need for heat treatment [50]. The use of PANi as a precursor to a carbon-nitrogen template for high-temperature synthesis of catalyst incorporating iron and cobalt has also been reported [51]. The use of one-dimensional nanofibers which contained iron-polyaniline/polyacrylonitrile (Fe-PANi-PAN) composite also gave improved ORR activity than with a Fe-PANi composite which did not contain PAN [52].

The use of PANi has also been explored for preparation of cathodes for MFCs. Most of the studies were based on the formation of composites such as manganese ferrite (MnFe_2O_4)/polyaniline (PANi) cathode for ORR reaction [53]. Also, the use of a PANi-MWCNT cathode for power generation has also been reported [54]. In another study, PANi-Fe₉₀₀ and PANi-Fe₇₀₀ were prepared by treatment at 900 °C and 700 °C, respectively, and subsequently used as cathodes [43]. A PANinf/carbon black composite (PANinf/C) has also been used for MFC cathode [35]. All of these PANi cathodes were prepared by chemical synthesis based on using multi-step cathode ink and then applied by manual coating on the gas diffusion layer (GDL). Their performances were evaluated in a proton exchange membrane or with a rotating disk electrode [47,48]. However, this

is not an ideal approach for producing a PANi cathode. Although both chemical and electrochemical polymerisation of ANi can be used for the formation of PANi and PANi composites [42,55,56], the use of electrochemical polymerisation is more advantageous due to its ease and reproducibility of synthesis. The electropolymerisation can be achieved by either galvanostatic (with a constant applied current density) [57], potentiostatic (with constant applied potential) [58,59] or potentiodynamic (with a variable applied potentials) [60,61] modes. The galvanostatic approach has been recognised as being most useful for producing more uniform and controlled PANi film on working electrodes of different dimensions and shapes [62]. Furthermore, chemically synthesised PANi have the tendency to incorporate additional contact resistance to the cathode [62]. In contrast, electropolymerisation minimises the microscopic contact resistance and allow for compact binding of nanofibers on the surface [62]. For these reasons, it is highly likely that the use of electropolymerised PANi would produce a more superior cathode for achieving a more efficient interfacial electron transfer.

In this study, we investigate the use of CP/PANi-Cu coating deposited galvanostatically on a commercial grade carbon paper as a way of producing a low-cost cathode for LTFCs. The electrochemical evaluation of the resulting PANi cathode will be carried out by using Tafel plots performed in an aqueous proton conductor by using a three-electrode cell arrangement. The PANi cathode will also be compared with Pt cathodes made with varying Pt/C loadings from 0.25 to 1.5 mg cm⁻², on the basis of achievable exchange current density ($j_{0\text{apparent}}$), maximum oxygen reduction current and charge transfer resistance (R_{ct}). Furthermore, detailed microscopic studies will be conducted on the PANi cathode by 4D X-ray microscopy, profilometry, scanning electron microscopy and FTIR to gain a good understanding of the structural composition underlying its performance.

6.2 Materials and methods

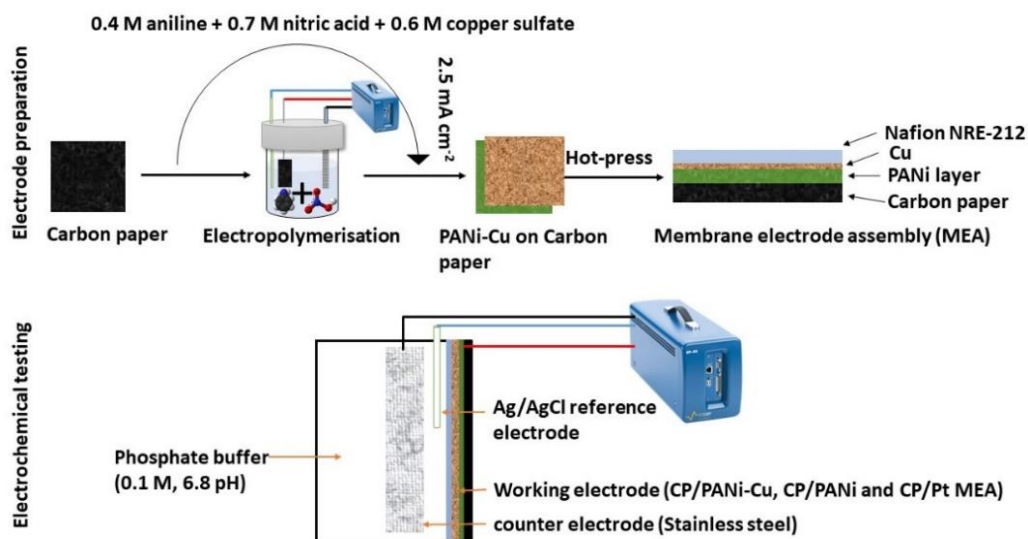
6.2.1 Electrochemical cell setup and PANi synthesis

PANi film was synthesised by galvanostatic electrodeposition using a three-electrode cell assembly. The working electrode was a commercial carbon paper of 210 µm thickness (GDS 210, CeTech, Taichung, Taiwan) of 3 × 2.5 cm (7.5 cm²) in dimensions. The carbon papers were degreased by ultrasonication in acetone before electrodeposition. The counter electrode used for CP/PANi-Cu fabrication was a copper foil (Sigma-Aldrich, Mumbai, India), whereas, for

fabrication of CP/PANi, a titanium mesh (Sigma-Aldrich, Mumbai, India) counter electrode was used. The reference electrode was a miniature Ag/AgCl reference electrode (RRPEAGCL, Pine Research Instrumentation, Durham, USA). All electrochemical experiments were performed with a Biologic SP-150 potentiostat (BioLogic, Claix, France) fitted with EC-Lab V-10.44 software for data processing.

6.2.2 Electropolymerisation of polyaniline (PANi)

Reagent grade aniline (Sigma-Aldrich, Mumbai, India) and nitric acid (Sigma-Aldrich, Mumbai, India) were used for electropolymerisation of aniline on CP. PANi was synthesised by galvanostatic polymerisation with an applied current density of 2.5 mA cm^{-2} (constant current) in a monomer solution which contained 0.4 M aniline, 0.7 M nitric acid and 0.6 M copper (II) sulfate. Copper was then deposited with an applied potential of -0.1 V for 60 secs to form the CP/PANi-Cu. In contrast, CP/PANi was formed by galvanostatic polymerisation with an applied current density of 2.5 mA cm^{-2} in a monomer solution which contained only 0.4 M aniline and 0.7 M nitric acid. The effect of PANi coating thickness on the electrokinetics was investigated by varying the polymerisation times from 5 - 30 mins. The monomer solutions were purged with nitrogen for 10 minutes to remove oxygen before the commencement of electropolymerisation. Scheme 1 outlines the overall process of fabrication of the catalyst and air cathode.



Scheme 6.1 Electropolymerisation of CP/PANi-Cu on carbon paper, preparation of membrane electrode assembly (MEA) and electrochemical testing of the cathodes in an aqueous proton conductor with a three- electrode assembly.

6.2.3 Platinum coating on carbon paper

Vulcan XC-72 platinised carbon powder was coated on carbon paper by using an air spray gun. The platinum loading in the electrodes was varied from 0.25 - 1.0 mg cm⁻² by using perfluorosulphonic acid (Nafion solution, 5%) solution as a binder. All coated electrodes were kept in a hot air oven at 60 °C for 6 hours to complete drying. The electrodes were then hot pressed, as shown in Scheme 1, on one side of a solid polymer electrolyte membrane (50 µm, Nafion NRE-212) under 1-ton pressure at 140 °C for 2 min.

6.2.4 Electrochemical Characterisation

Fabricated air cathodes were tested in an aqueous proton conductor in 0.1 M phosphate buffer solution at pH 6.8. The reference electrode and potentiostat used were the same as previously described in 2.1. Titanium mesh (Sigma-Aldrich, Mumbai, India) was used as the anode.

6.2.4.1 Linear Sweep Voltammetry

The electrokinetics of the PANi coated carbon paper was evaluated by linear sweep voltammetry (LSV) used for plotting Tafel plots and current density versus applied potential plots. Electrochemical measurements were performed with a Biologic SP-150 potentiostat at room temperature (24-27 °C), using a three-electrode system. The working electrodes (cathodes) were fitted in the grid in the three-electrode cell. The LSV was performed at a sweep rate of 1 mVs⁻¹. Each experiment was performed three times, and the standard deviation was calculated.

6.2.4.2 Tafel Plot

Tafel plot, as derived from equation 1 below [63], was employed to measure the reaction kinetics for working electrode (cathode) and an Ag/AgCl (3 M KCl) was used as the reference electrode.

$$\ln\left(\frac{i}{i_0}\right) = \beta\left(\frac{F\eta}{RT}\right) \text{ -----(1)}$$

where i_0 is exchange current density, i is the electrode current density (mA m⁻²), β is the electron transfer coefficient, R is the ideal gas constant (8.31 J mol⁻¹ K⁻¹), F is the Faraday's constant (96,485 C mol⁻¹), T is the absolute temperature, K and η is the activation overpotential. The reference electrode was placed in the cathode chamber (near the working electrode) during the measurements.

The purpose of using a Tafel plot is to calculate the exchange current density i_0 . The i_0 is a fundamental parameter in the rate of electrooxidation or electroreduction of a chemical species at an electrode when in equilibrium. The charge transfer resistance (R_{ct}) was calculated from the following equation [64]:

$$R_{ct} = \frac{RT}{nFi_0}$$

where n is the number of electrons.

Based on the Tafel-type, linear equation obtained from the plots [Fig. 6.3(a) and 6.4(a)], the corresponding slope is F/RT , and the y-axis intercept is the logarithm of the exchange current [63]. For the anodic reaction at 25 °C, the slope of Tafel plot is $b = 0.059 / 1 - a$, while at the same time, the slope for cathodic reaction is $b = 0.059 / a$.

6.2.5 Morphological study of the cathodes

The morphologies of pristine carbon cathode, CP/Pt cathode, and CP/PANi-Cu cathode were obtained with a JSM - 760F FEG scanning electron microscope (SEM) at a 1-micrometer resolution with a 10,000X magnification. Alicona microscope was used to examine the topography of CP/Pt cathode and CP/PANi-Cu cathode with magnifications of 10x, 20x, and 50x. Multiple scans, including triplicates of the carbon, CP/PANi-Cu, and CP/Pt cathode materials were visualised by full three-dimensional scans. Care was taken to avoid surface contamination of electrodes. The quantity of Pt particles embedded in a carbon paper and the growth of CP/PANi-Cu was analysed with a Four-Dimensional X-ray Microscopy, (Versa XRM-520, Xradia, Pleasanton, CA).

6.2.6 X-ray Photoelectron Spectroscopy (XPS)

The XPS spectra of samples were obtained using Thermo Scientific K-Alpha. Survey and core elemental composition were obtained with non-monochromatized Al K α X rays operated at 25.0 eV with 0.100 eV resolution. The scanned area was 400 μm for 1 mins 55.5 secs acquisition time. To recompense surface charging effect, the lowest binding energy of C(1s) of the sample was set at 284.5 eV. The XPS peaks were analysed using a Gaussian line shape with Lorentzian broadening function into different components, and quantitative interpretation was made after baseline

correction. High-resolution scans were obtained in the C(1s), N(1s), O(1s), S(2p), Cu(2p) and Pt(4f) regions of the spectrum. The elemental quantitative determination was based on the integral intensity of signals measured for the different elemental states.

6.2.7 Fourier Transform Infrared Spectroscopy (FTIR)

A Vertex 80 (Bruker Corporation, Massachusetts, United States) FTIR spectrometer was used to record FTIR of CP/Pt, and CP/PANi-Cu. FTIR spectra were obtained by attenuated total reflectance (ATR) method with a resolution of 4 cm^{-1} . The wavenumbers were in the range of $4000\text{--}550\text{ cm}^{-1}$ for both CP/Pt and CP/PANi-Cu cathodes. The baseline corrections were made carefully, and peaks were determined with the aid of an Opus software (Bruker Corporation, Massachusetts, United States).

6.3 Results

6.3.1 Electrochemical deposition of PANi-Cu on CP

Although the use of chemical polymerisation for coating PANi-Cu on carbon paper has been reported in some studies for the development of supercapacitor electrodes [65,66], there is, to our knowledge, no previous report on the use of electropolymerisation of aniline (ANi) for coating PANi-Cu on carbon paper for MFCs or proton exchange membrane fuel cells. A study which considered the use of a PANi-Cu catalyst for a fuel cell [47] also utilised chemical polymerisation and was subsequently deposited on a carbon paper. However, the PANi-Cu coating produced by such an approach was not as robust, conductive and stable as that produced by electropolymerisation in this study.

The deposition of PANi-Cu catalyst on carbon paper by galvanostatic polymerisation was investigated at varying polymerisation times from 5 to 30 mins to determine the influence of coating thickness on the $j_{0\text{apparent}}$ and j_{Red} values of the resulting CP/PANi-Cu cathode. The PANi-Cu coating was formed on one side of the carbon paper. Fig. 6.1 shows a chronopotentiogram obtained for the formation of the PANi-Cu coating on the carbon paper. Evidently, the conductivity of the coating increases with increasing polymerisation time, as reflected by the declining stabilisation potential (E_s) with time.

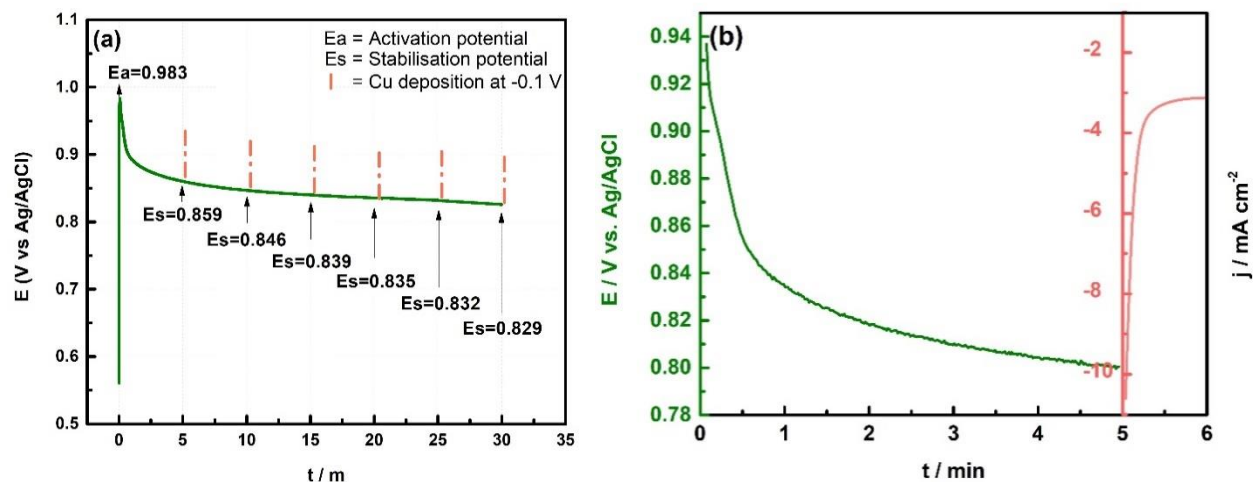


Fig. 6.1 Chronopotentiogram of (a) electrodeposition of CP/PANi-Cu on carbon paper as a function of time and (b) (the representative figure for PANi-Cu deposition) 5 min PANi coating using chronopotentiometry followed by Cu deposition for 1 min using chronoamperometry.

Fig. 6.2(a) shows the morphology of the pristine carbon paper obtained by SEM, where the carbon fibres can be seen without any external particles. In contrast, the micrograph obtained for carbon coated with 0.5 mg cm^{-2} Pt/C and 5% Nafion solution shows in Fig. 6.2(b) that the distribution of Pt is not uniform. Fig. 6.2(c) and 6.2(d) show the morphological changes obtained for CP coated with PANi-Cu at two different magnifications (10,000 X and 50,000 X, respectively). The presence of well-ordered PANi-Cu nanofibers with an average diameter of $112 \pm 11 \text{ nm}$ is clearly obvious. It is important to note that prior acid treatment [65] is normally required when carbon paper is coated with PANi-Cu by chemical polymerisation, but such treatment is not required for the deposition of the composite by electropolymerisation of ANi. Furthermore, after acid treatment of the carbon paper, the average diameter of the PANi-Cu nanofibers was 43 nm, and some PANi-Cu nanofibers aggregated during the chemical polymerisation. In another study of the chemical synthesis of PANi-Cu, the fibres were more variable with diameters ranging between 50 and 120 nm [66]. In contrast, the PANi-Cu nanofibers formed by electropolymerisation without any pre-treatment of the carbon paper in this study were more uniform.

6.3.2 Electrochemical characterisation

Electrochemical measurements, including polarisation behaviour (Tafel plots) of the CP/PANi-Cu and CP/Pt cathodes, were carried out to evaluate the electrochemical performance of the air cathode in phosphate buffer (pH 6.8). The exchange current density, j_0 , was calculated by

extrapolation to $\eta = 0$ of a linear regression ($R^2 > 0.99$) between $\eta = 150$ mV. By applying a 150 mV overpotential, the resulting i_0 values depended on charge limited electrochemical process where mass transfer is limited during the measurement. As the j_0 signifies the rate of electron exchange between the working electrode and the counter electrode at equilibrium, a higher j_0 value is indicative of a faster electron exchange rate. It also demonstrates a lower activation energy barrier for the forward reaction.

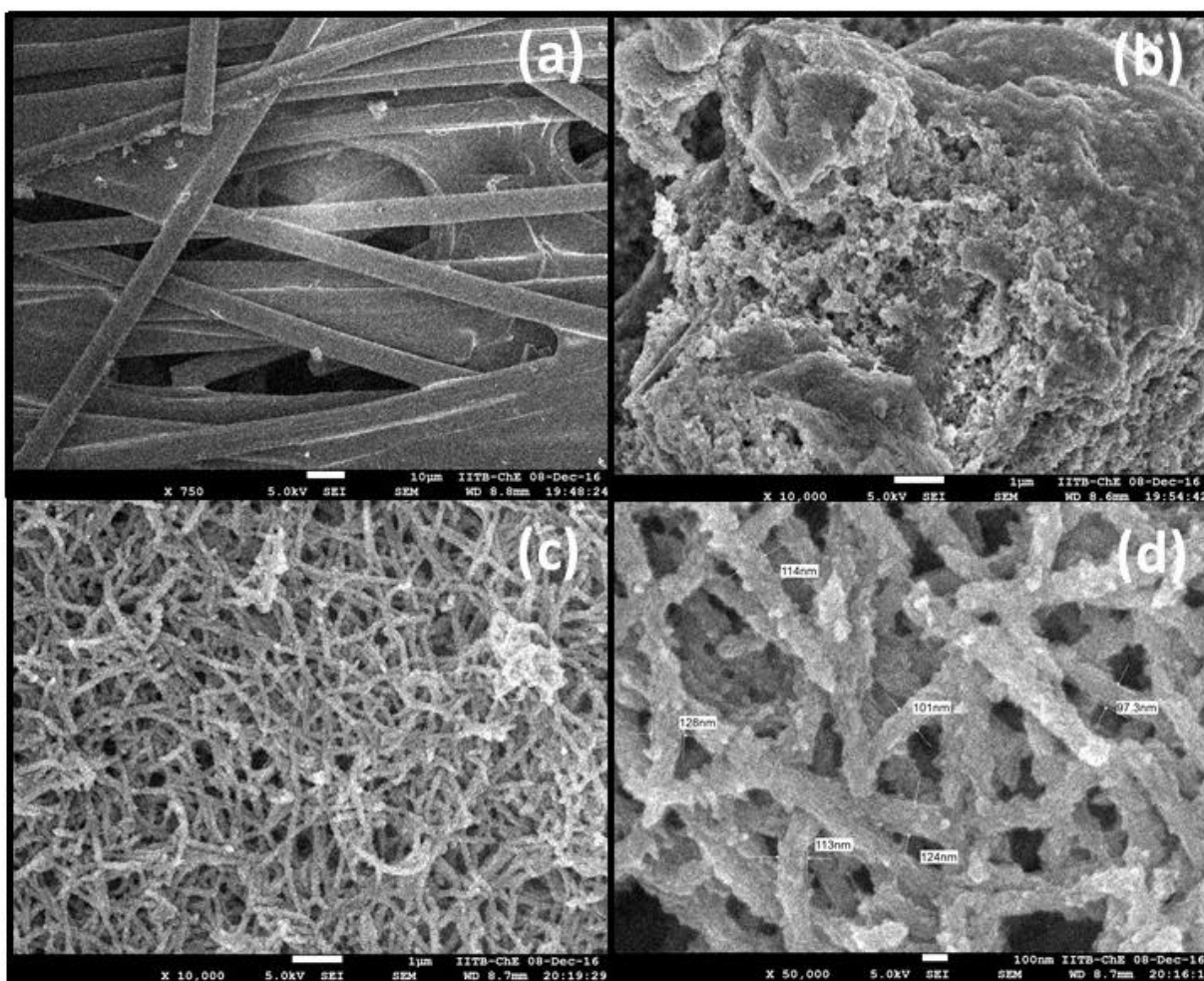


Fig. 6.2 SEM images of (a) Pristine carbon paper, (b) carbon coated with 0.5 mg cm^{-2} Pt, (c) CP/PANi-Cu (20 mins) electrodeposited on carbon paper and (d) measured CP/PANi-Cu nanofibers from SEM image.

6.3.2.1 Electrochemical activity of CP/PANi-Cu and CP/PANi

In the initial experiment, the carbon papers were coated with PANi and PANi-Cu for 20 mins. An air cathode (CP/Pt) with 0.5 mg cm^{-2} Pt loading was employed for the initial comparison. Typically, the platinum loading used in air cathodes for LTFC ranges from $0.5\text{-}0.6 \text{ mg cm}^{-2}$ [67], so the chosen load is within this range.

Tafel plots were recorded for CP/PANi-Cu, CP/PANi and CP/Pt(0.5 mg cm^{-2}) cathodes, and the exchange current densities, $j_{0\text{apparent}}$, were determined by extrapolation to $\eta = 0$ of a linear regression ($R^2 > 0.99$) at $\eta = 150 \text{ mV}$. The Tafel curves are shown in Fig. 6.3(a). As expected and shown in Fig. 6.3(b), the pristine cathode exhibited very low $j_{0\text{apparent}}$ of $0.0032 \pm 0.0012 \text{ mA cm}^{-2}$, whereas the cathode which contained 0.5 mg cm^{-2} CP/Pt gave a $j_{0\text{apparent}}$ of $0.0325 \pm 0.0031 \text{ mA cm}^{-2}$. In contrast, the optimum CP/PANi-Cu cathode exhibited a relatively high $j_{0\text{apparent}}$ of $0.088 \pm 0.003 \text{ mA cm}^{-2}$ which was 170% higher than the $j_{0\text{apparent}}$ obtained with 0.5 mg cm^{-2} CP/Pt cathode. Interestingly CP/PANi gave a negligible exchange current density of $0.006 \pm 0.002 \text{ mA cm}^{-2}$. Even if higher platinum loaded cathode which contained 1.5 mg cm^{-2} Pt was used, the achieved $j_{0\text{apparent}}$ was $0.086 \pm 0.004 \text{ mA cm}^{-2}$ which was still slightly lower than obtained with the optimum CP/PANi-Cu cathode. The considerable improvement observed clearly demonstrates that the CP/PANi-Cu cathode exhibits a faster electron exchange rate than the CP/Pt cathode.

The maximum reduction current obtained with the pristine CP, CP/Pt, CP/PANi-Cu and CP/PANi cathodes were also measured by LSV with an aqueous proton conductor. The pristine cathode (control) only generated a maximum reduction current of $-0.048 \pm 0.006 \text{ mA cm}^{-2}$, but, in contrast, the CP/Pt cathode achieved a maximum reduction current of $-5.36 \pm 0.79 \text{ mA cm}^{-2}$. On the other hand, the CP/PANi-Cu cathode gave a much higher maximum reduction current of $-6.56 \pm 0.34 \text{ mA cm}^{-2}$ which was 22% higher than obtained with the CP/Pt cathode. However, in the absence of Cu, the CP/PANi only gave very low reduction current of $-0.261 \pm 0.064 \text{ mA cm}^{-2}$. Consequently, the CP/PANi-Cu cathode was used for further investigations and for comparison with the CP/Pt cathode.

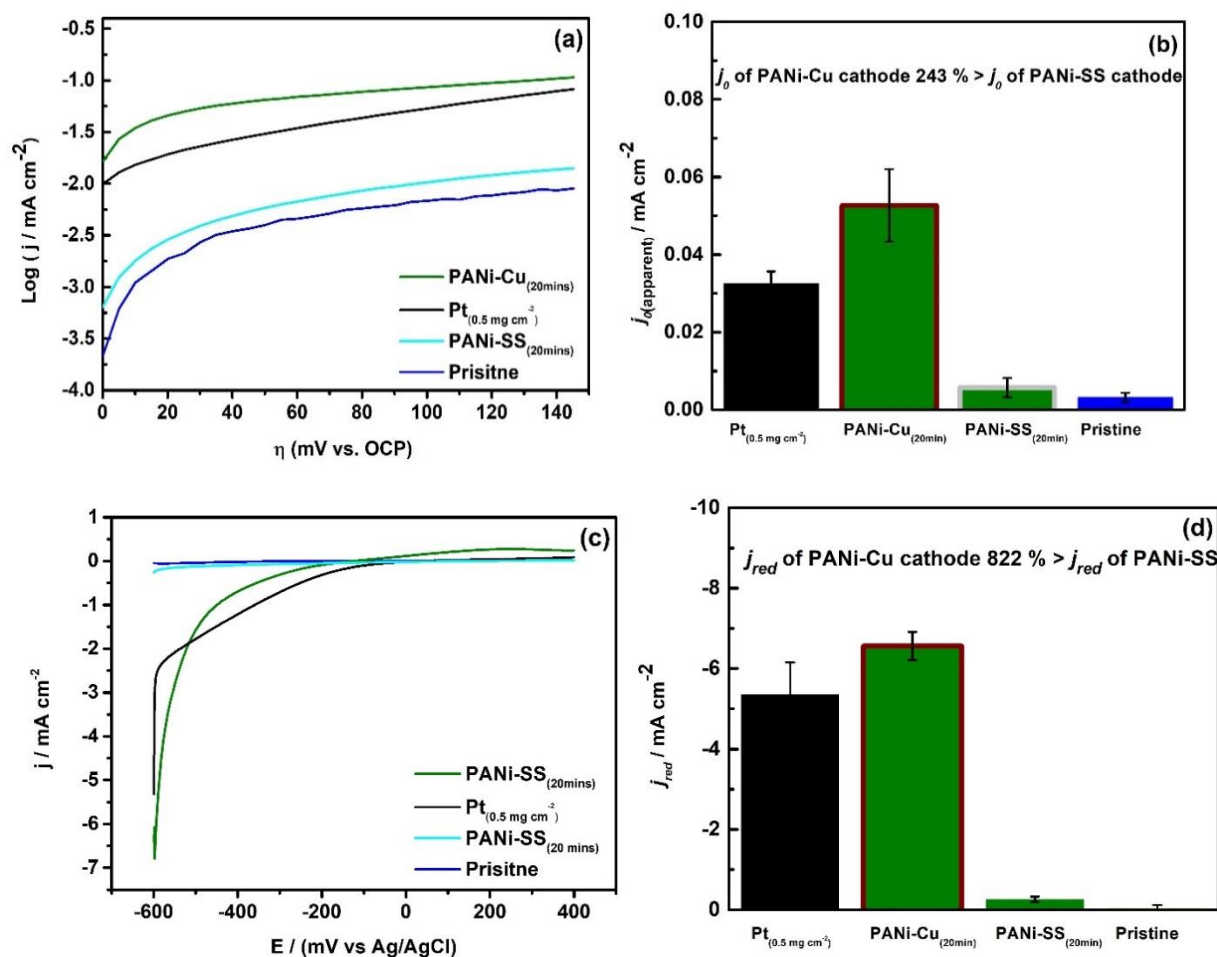


Fig. 6.3 Electrochemical characterisation of the cathodes and effect of PANi electrosynthesis using Cu and SS counter electrode. (a) Tafel plots of pristine CP, CP/PANi-Cu, CP/PANi and CP/Pt cathode, (b) Exchange current densities_(apparent) of the CP, CP/PANi-Cu, CP/PANi and CP/Pt cathode, (c) Cathodic linear sweep polarisation of CP, CP/PANi-Cu, CP/PANi and CP/Pt cathode, (d) Maximum reduction current of CP, CP/PANi-Cu, CP/PANi and CP/Pt cathode.

6.3.2.2 Influence of Pt loading on electrochemical performance

Figure 6.4(a) shows the Tafel plots obtained for the CP/Pt cathode with increasing Pt loading from 0.25 to 1.5 mg cm⁻². The Tafel plots indicate that the $\text{Log}(j / \text{mA cm}^{-2})$ values shifted towards the positive direction with increasing Pt loading due to the presence of an excess catalyst for the ORR reaction. Figure 6.4(b) shows that the reduction current increases with Pt loading and the ORR kinetics were almost equal from 0.5 mg cm⁻² to 1.5 mg cm⁻² Pt loading. The exchange current density was calculated from the Tafel plots and Fig. 6.4(c) illustrates that j_0 values increased

linearly with Pt loading. The maximum j_0 of 0.086 mA cm^{-2} was observed with 1.5 mg cm^{-2} Pt loading. Images obtained by 4D microscopy and SEM revealed an agglomeration structure due to the mixing of Nafion solution with the Pt/C and its spread over the surface of the electrode. The structure allowed oxygen to pass through the surface to reach the reaction centres. Typically, in MFC or PEFC, 0.5 mg cm^{-2} Pt loading is commonly used. The 0.5 mg cm^{-2} loading gave a R_{ct} of $3.953 \Omega \text{ cm}^{-2}$, while the 1.5 mg cm^{-2} loading gave the least R_{ct} of $1.485 \Omega \text{ cm}^{-2}$. Figure 6.4(d) shows the R_{ct} variation as a function of Pt loading. Evidently, the R_{ct} decreased dramatically with increasing Pt loading.

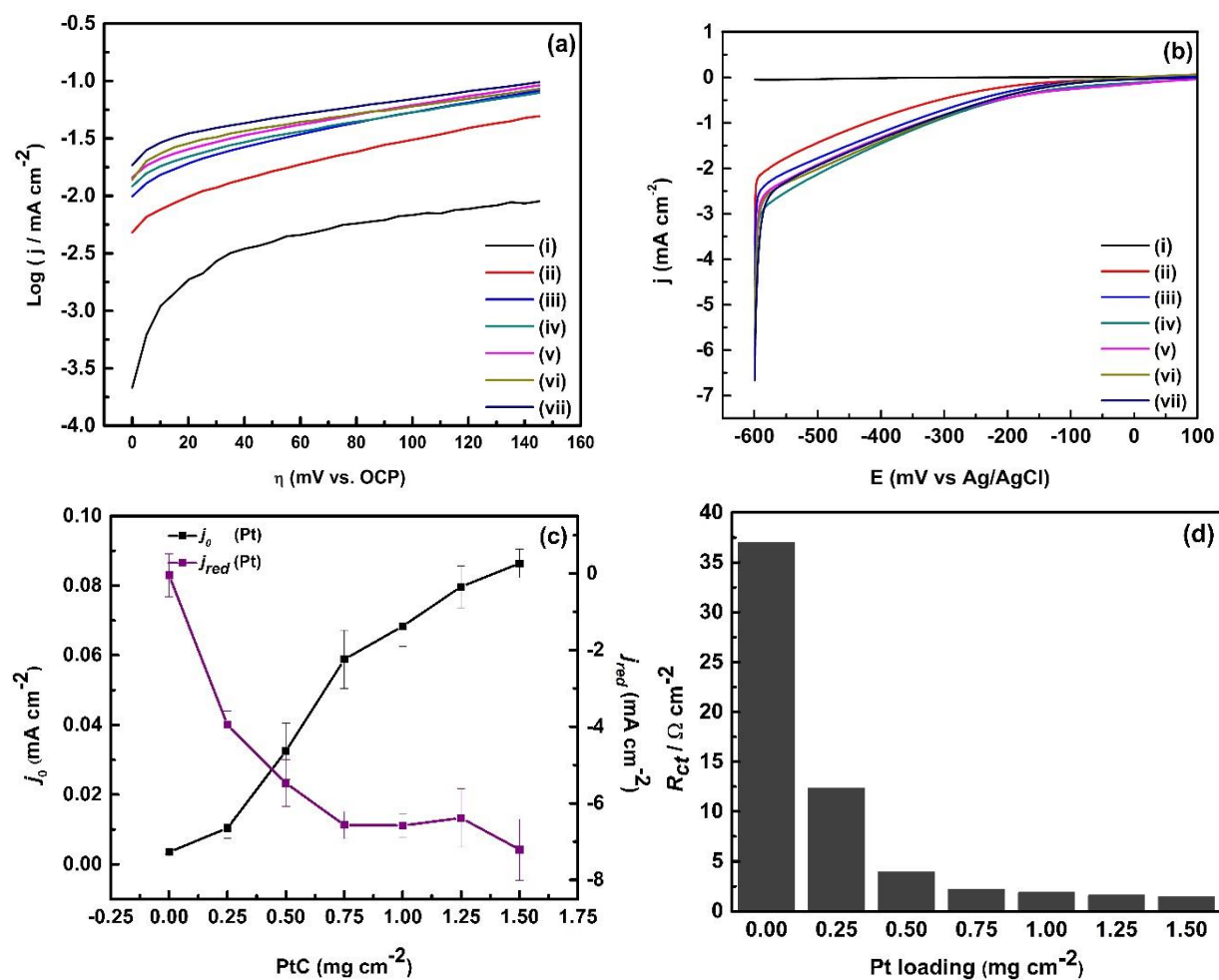


Fig. 6.4 Dependence of electrochemical performance of cathode on Pt loading. (a) Tafel plots, (b) LSVs, (c) exchange current densities and reduction current densities as a function of platinum loading on carbon paper, and (d) Pt on carbon paper and its associated charge transfer resistance (R_{ct}) as a function of loading. Pt loadings: (i) pristine, (ii) 0.25, (iii) 0.5, (iv) 0.75, (v) 1.0, (vi) 1.25 and (vii) 1.5 mg.

6.3.2.3 Electrochemical performance of CP/PANi-Cu coating

Figure 6.5(a) shows the Tafel plots obtained with the CP/PANi-Cu cathode prepared with increasing polymerisation time from 5 to 30 min. A shift in the $\log(j/\text{mA cm}^{-2})$ value towards the positive direction is obvious with increasing polymerisation time, and it is indicative of the increasing conductivity of the coating. Figure 6.5(b) shows the LSV curves obtained for the CP/PANi-Cu cathodes prepared with the different polymerisation times. The exchange current densities (j_0) were calculated from the Tafel slopes, and the maximum oxygen reduction currents are shown in Fig. 6.5(c) as a function of polymerisation time. The j_0 and i_{red} of the CP/PANi-Cu cathode increased linearly with increasing polymerisation time from 5 to 25 min. The exchange current density decreased to 0.073 mA cm^{-2} with the use of a polymerisation time of 30 min. Thus, indicating that the maximum achievable j_0 of 0.088 mA cm^{-2} was obtained with a polymerisation time of 25 min. The decline in j_0 with polymerisation of 30 min is attributed to the increased thickness of the PANi-Cu coating which increased diffusion barrier and limited oxygen diffusion to the electrode. Also, the lowest charge transfer resistance R_{ct} of $1.456 \Omega \text{ cm}^{-2}$ was obtained with the CP/PANi-Cu cathode obtained with a polymerisation time of 25 min. Figure 6.5(d) shows the R_{ct} variation as a function of polymerisation time, with the significant decline observed at polymerisation times longer than 5 min.

The ORR typically follows first-order kinetics with respect to the oxygen concentration at the electrode surface [68]. The exchange current density of an electrode and its efficiency depends on the available oxygen on the surface of the electrode. Thus, the thickness of the dense network of polyaniline nanofibers is a critical parameter influencing the ORR reaction. Consequently, as the coating becomes thicker, it reduces the accessibility of oxygen to the reaction sites due to increased diffusion barrier. Based on the results obtained in this study, the use of a polymerisation time up to 25 min produced PANi-Cu coatings which gave increasing j_0 values. Therefore, it was obvious that the decline in j_0 observed with the use of a polymerisation time of 30 min was due, as previously indicated, to increased PANi-Cu coating thickness and the associated reduction in oxygen reaching the reaction sites.

Also, in terms of thickness, the Pt layer thickness for the CP/Pt cathode produced with 0.5 mg cm^{-2} loading was determined to be $44 \pm 6 \mu\text{m}$, while PANi-Cu coating thickness obtained with 20 mins polymerisation was determined to be $24 \pm 2 \mu\text{m}$. Although the PANi-Cu coating thickness is about half the thickness of Pt in the CP/Pt cathode, it is obviously denser and more compact. As a

result, the CP/PANi-Cu cathode will limit oxygen penetration as it becomes thicker. In contrast, the loaded Pt is more porous and will, thus, enable easier passage for oxygen.

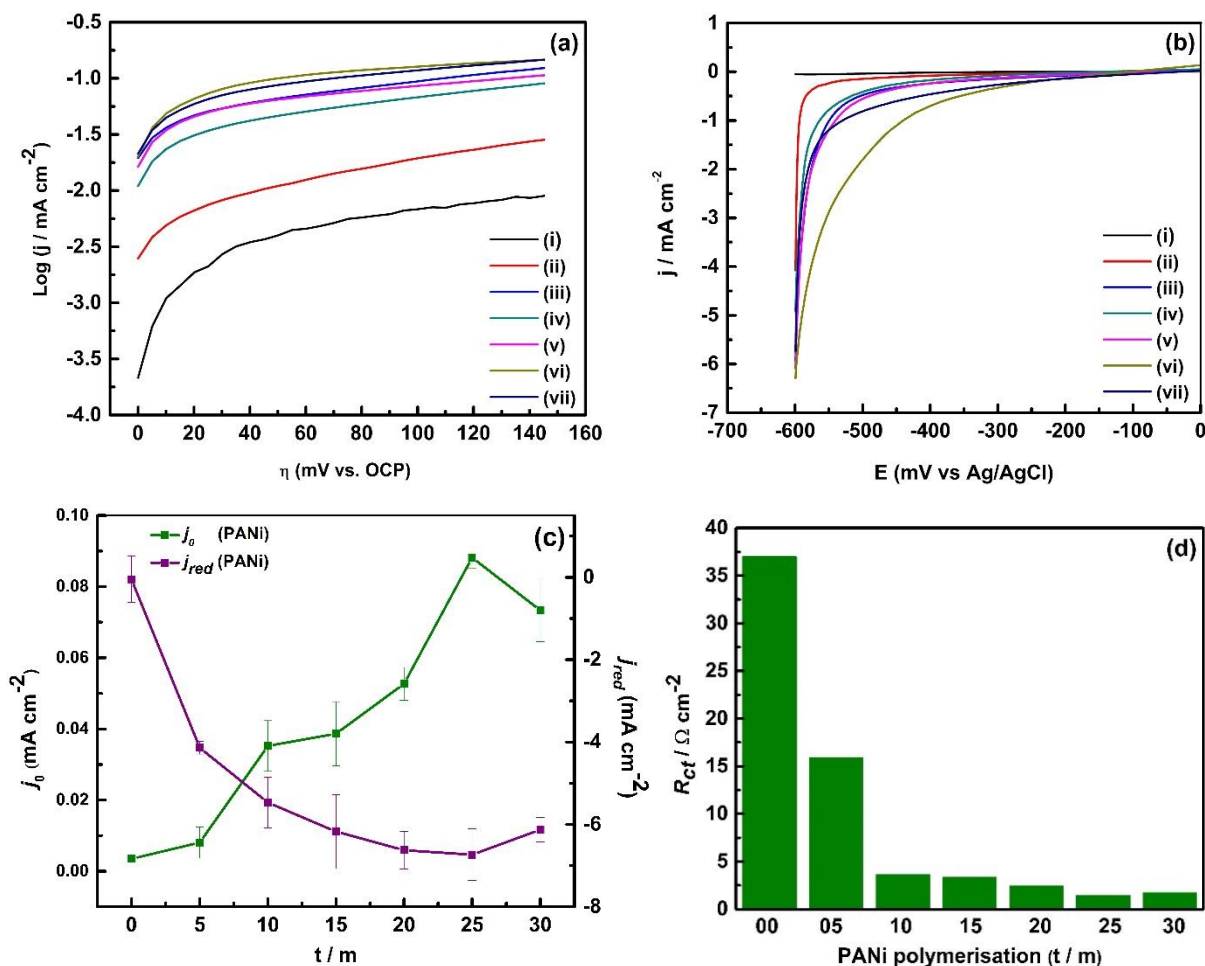
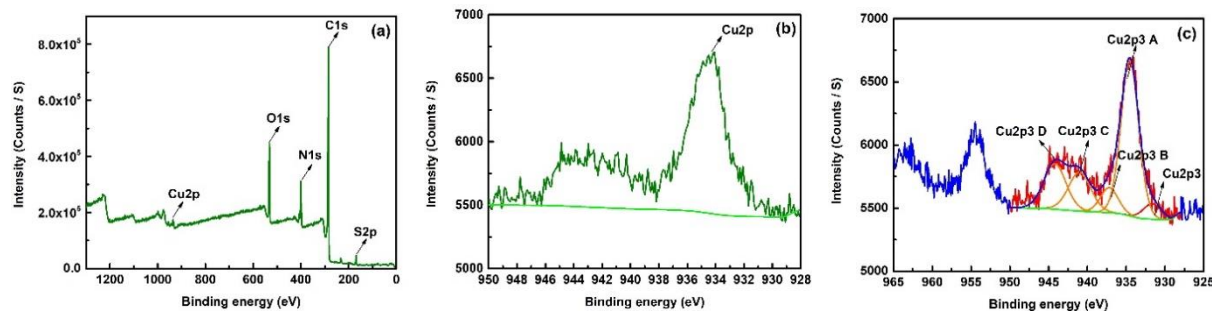


Fig. 6.5 Dependence of electrochemical performance of CP/PANi-Cu cathode with polymerisation time. (a) Tafel plots, (b) LSVs, and (c) exchange current densities and reduction current densities as a function of CP/PANi-Cu. Polymerisation time: (i) - pristine, (ii) 5, (iii) 10, (iv) 15, (v) 20, (vi) 25 and (vii) 30 min. (d) CP/PANi-Cu polymerisation on carbon paper and its associated charge transfer resistance (R_{ct}) as a function of polymerisation time.

6.3.3 X-ray Photoelectron Spectroscopy (XPS)

The analysis of the elemental composition of CP/PANi-Cu and CP-Pt electrodes were carried by XPS. The spectra obtained for CP/PANi-Cu are shown in Fig. 6.6(a) – 6.6(c). The survey of the sample revealed the presence of oxygen O1s - 531.63 eV, sulfur S2p – 168.28 eV, carbon C1s

284.6 eV, and nitrogen N1s 399.30 eV. By using high-resolution XPS analysis, the PANi-Cu coating gave a peak at 934.49 eV, designated as Cu2p3, as shown in Fig. 6.6(a) and 6.6(b). The details element composition is given in supplementary information. The presence of a signal for O1s 531.63 eV indicates that pure Cu metal was not formed during deposition [69]. Also, due to other elements present (S2p) may contribute oxygen adsorption. The spectra in Fig. 6.6(c) shows a clear indication of the presence of monovalent copper. The peaks at 934.52 eV and 944.19 eV were attributed to Cu2p 3/2 (Cu2p3A) and Cu 2p 1/2 (Cu2p3D) which are mainly present as Cu (I) oxide. Also, the Cu2p has a satellite line at 937.18 – 940.99 eV which is attributed to the presence of a minute Cu (II) oxide. The Cu2p3 peak represents 0.52% of the total chemical composition of the CP/PANi-Cu cathode. Table 6.1 presents the elemental identification (ID) and quantification of the CP/PANi-Cu. The XPS spectra of CP/Pt cathode are shown in Fig. 6.6(a')-6.6(c') and the survey of C1s, N1s, O1s, S2p and Pt4f gave binding energies of 284.47, 400.97, 531.95, 168.96 and 72.54 eV, respectively. Fluorine from 5% Nafion is present in the CP-Pt but was not shown in XPS data. Pt4F5 attributed to Pt(0) is from metallic Pt present in Vulcan XC-72. Table 6.2 presents the elemental ID and quantification of the CP/Pt cathode. Interestingly, 0.52% of Cu and 1.16 % of Pt were present in CP/PANi-Cu and CP-Pt cathodes, respectively. The elemental quantification is given in Tables 6.1 and 6.2 for CP/PANi-Cu and CP-Pt cathodes, respectively. Although the Pt catalyst present was more than doubled that of the Cu catalyst, the j_0 values obtained were almost the same for the PANi-Cu coating and CP/Pt cathode with 1.5 gm cm⁻² Pt loading.



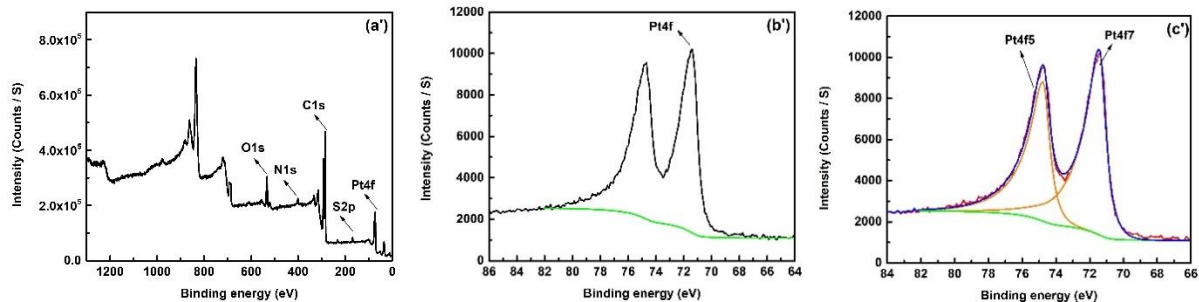


Fig. 6.6 XPS pattern of CP/Cu-PANi cathode and CP/Pt cathode, a, b, c survey, Cu2p presence and various states of the presence of Cu respectively. a', b' and c,' survey, Pt presence and different states of Pt presence respectively.

Table 6.1 Elemental ID and quantification of CP/PANi-Cu

<i>Name</i>	<i>Peak BE</i>	<i>FWHM eV</i>	<i>Atomic %</i>	<i>Name</i>	<i>Peak BE</i>	<i>FWHM eV</i>	<i>Atomic %</i>
S2p	168.28	2.39	1.70	Cu2p3	931.65	2.68	5.11
C1s	284.63	2.20	73.56	Cu2p3 A	934.52	2.68	51.31
N1s	399.30	1.77	12.93	Cu2p3 B	937.18	2.68	8.30
O1s	531.63	2.48	11.28	Cu2p3 C	940.99	3.37	16.26
Cu2p3	934.49	2.73	0.52	Cu2p3 D	944.19	3.37	19.03

Table 6.2 Elemental ID and quantification of CP-Pt

<i>Name</i>	<i>Peak BE</i>	<i>FWHM eV</i>	<i>Atomic %</i>	<i>Name</i>	<i>Peak BE</i>	<i>FWHM eV</i>	<i>Atomic %</i>
C1s	284.47	0.97	91.21	Pt4f7	71.43	1.49	100.00
N1s	400.97	2.52	1.70	Pt4f5	74.76	1.49	0.00
O1s	531.95	2.94	5.07				
S2p	168.96	2.38	0.87				

6.3.4 Fourier Transform Infrared Spectroscopy (FTIR)

FTIR was used to characterise the CP/Pt and CP/PANi-Cu cathodes. The CP/Pt cathode composed of 40% Pt/C and 5% Nafion solution as a binder. The CP/PANi-Cu cathode was synthesised with 0.4 M aniline in 0.7 M nitric acid for 25 min with an applied current density of 2.5 mA cm⁻², followed by deposition of copper from 0.6 M copper sulfate solution. The respective spectral obtained for each of the cathode are discussed below.

6.3.4.1 FTIR of CP/Pt cathode

Figure 6.7(a) shows the FTIR spectra obtained for Pt/C on the carbon paper. The carbonyl acid C=O stretch and the N-H deformation are evident at 1695 and 1549 cm⁻¹, respectively. The absorption bands at 1148 and 1210 cm⁻¹ correspond to the symmetric and asymmetric vibrations

of $-\text{CF}_2$ groups in the hydrophobic fluorocarbon backbone. Symmetric stretching of the sulfonate group is observed at 1059 cm^{-1} . The twin peak at 972 cm^{-1} is due to the presence of two ether linkages ($-\text{C}-\text{O}-\text{C}-$) in Nafion solution side chain [70]. The peaks at 846 cm^{-1} and 702 cm^{-1} are associated with SO_3^- group from the Nafion solution [71].

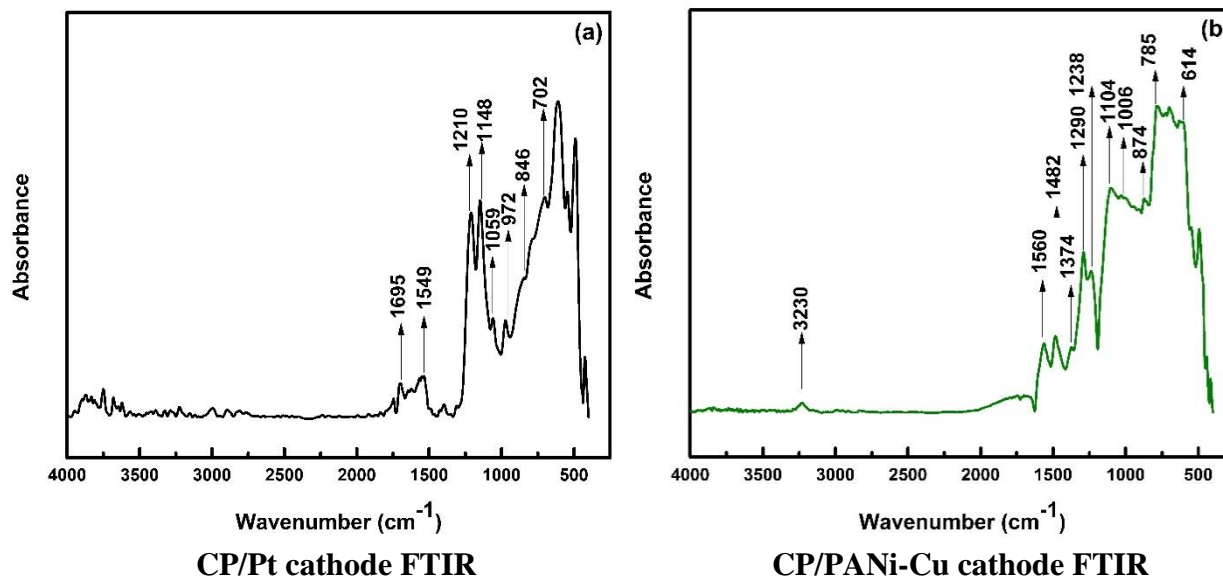


Fig. 6.7 Fourier transform infrared (FTIR) spectra of (a) CP/Pt cathode with 0.5 Pt loading on carbon paper and (b) CP/PANi-Cu cathode electrodeposited for 20 min.

6.3.4.2 FTIR of CP/PANi-Cu cathode

Figure 6.7(b) shows the FTIR spectra obtained for the CP/PANi-Cu-coated carbon paper cathode with the obvious characteristic bands of the secondary amine (N–H) at 3230 cm^{-1} [72], and the C=C stretching deformation of the quinoid at 1560 and 1374 cm^{-1} . The band at 1482 cm^{-1} is attributed to a benzenoid ring system in polyaniline [73]. The band at 1289 cm^{-1} is characteristic of the C–N stretching of the secondary aromatic amine and the one at 1238 cm^{-1} is due to C–H bending of the benzenoid. The absorption peak at 1104 cm^{-1} is assigned to the N=Q=N. All of these peaks are characteristics of the formation of the emeraldine form of PANi. The bands at 614 cm^{-1} are assigned to the symmetric and antisymmetric stretching of the sulfonate groups [74]. A small peak at 1006 cm^{-1} is due to the sulphonic group from Nafion solution [71]. Out-of-plane bends of C–H on substituted aromatic rings are evident at 874 cm^{-1} .

The FTIR measurements adequately distinguished between the CP/Pt and CP/PANi-Cu cathodes based on the identification of the principal functional groups that are distinctly reflective of the composition of the different cathodes.

6.3.5 3D Profilometry and 4D X-ray microscopy

The 3D profilometric images obtained for the pristine and coated carbon papers are shown in Fig. 6.8. The image obtained from the pristine carbon clearly shows the interlinked carbon fibres. The average roughness was $8.39\ \mu\text{m}$, $0.70\ \mu\text{m}$ and $4.35\ \mu\text{m}$ for pristine CP, CP/PANi-Cu and CP/Pt cathodes, respectively. From the profilometry data, it was obvious that the CP/PANi-Cu cathode displayed very high surface uniformity compared to CP and CP/Pt. The cracks observed in CP/PANi-Cu, as shown in Fig. 6.8(c) were due to the drying out of the Nafion solution during the drying process in a hot air oven.

The four-dimensional (4D) X-ray microscopy revealed that the Pt/C and PANi-Cu were deposited on the surface and inside the carbon paper. Fig. 6.9(a) shows Pt/C coating with granular deposition of Pt and carbon particles. At 4X magnification, the thickness of the coating was determined to be $44 \pm 6\ \mu\text{m}$ with non-uniform deposition. The Pt/C was deposited with an air gun and, due to its pressure, the Pt/C particles also reached the slight core of the carbon paper. In the core, the compact layer can be seen. In contrast, Fig. 6.9(b) shows that the CP/PANi-Cu deposition was very uniformly grown on the surface. The average thickness of the CP/PANi-Cu coating was determined to be $24 \pm 2\ \mu\text{m}$. Its thickness can be tuned by varying the applied current density and electropolymerisation time.

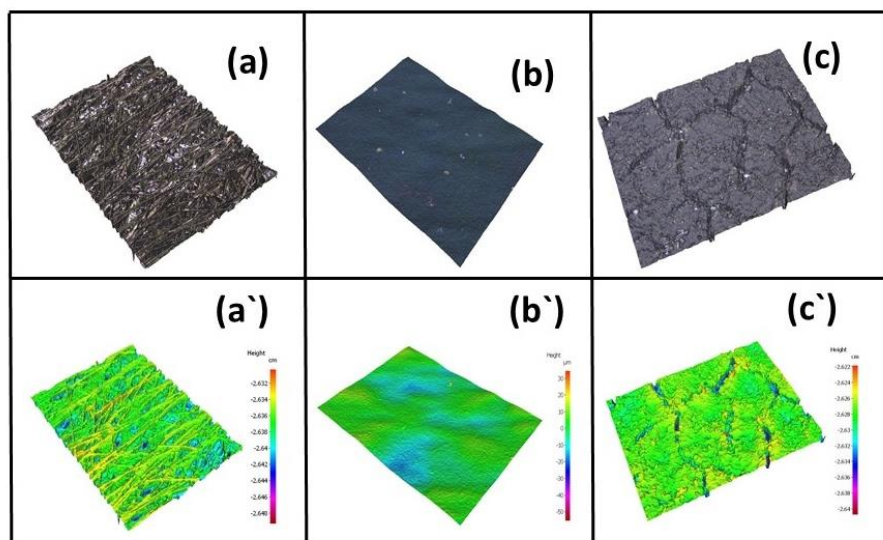


Fig. 6.8 3D profilometry of (a) pristine carbon paper, (b) carbon paper coated with 0.5 mg cm^{-2} CP/Pt/C, and (c) CP/PANi-Cu. CP/PANi-Cu coating was obtained by electrodeposition for 20 mins.

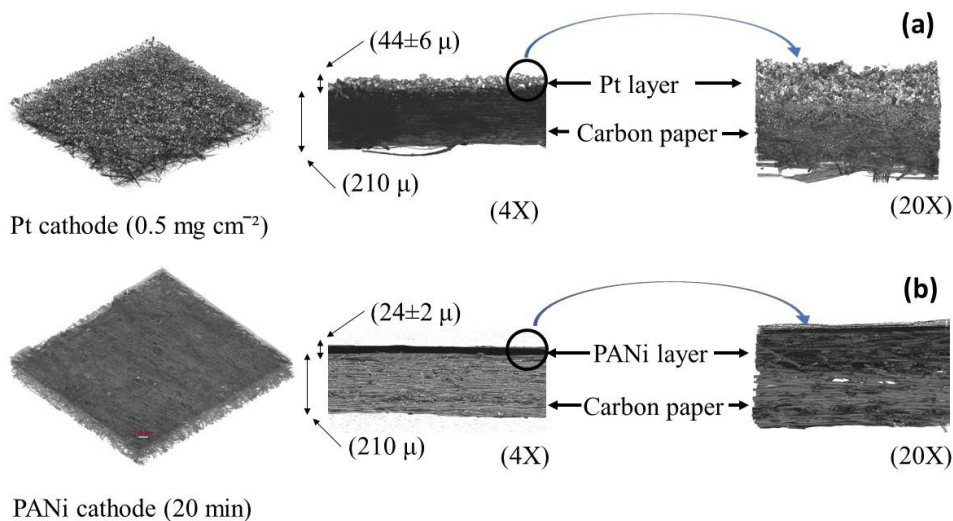


Fig. 6.9 4D X-ray microscopy of (a) carbon coated with 0.5 mg cm^{-2} and (b) CP/PANi-Cu (20 mins) electrodeposited on carbon paper.

6.4. Conclusion

This study has successfully demonstrated the feasibility, effectiveness, and usefulness of fabricating and utilising a low-cost CP/PANi-Cu cathode for potential replacement of Pt cathode in MFCs and LTFCs. Uniform PANi-Cu coating was obtained on the CP and, due to its nanofibrous structure, it performed effectively as a cathode. The incorporation of copper, through the addition of CuSO_4 to the monomer and deposition of the metal from this solution, resulted in enhanced ORR activity. The optimum PANi cathode gave a much higher $j_{0\text{apparent}}$ of $0.088 \pm 0.003 \text{ mA cm}^{-2}$ which was 170% higher than the $j_{0\text{apparent}}$ obtained with 0.5 mg cm^{-2} CP/Pt cathode and was still slightly higher even when a platinum loading of 1.5 mg cm^{-2} Pt was used. The R_{ct} of $1.456 \Omega \text{ cm}^{-2}$ obtained for the optimum CP/PANi-Cu cathode was much lower than the $3.95 \Omega \text{ cm}^{-2}$ obtained for the CP/Pt cathode with $0.5 \text{ mg Pt cm}^{-2}$ loading but close to the R_{ct} of $1.485 \Omega \text{ cm}^{-2}$ obtained with a platinum loading of 1.5 mg cm^{-2} CP/Pt. Both of these results demonstrate that the Pt cathode needed 3 times the Pt loading (1.5 mg cm^{-2} Pt) of the commonly used cathode to perform as good as the optimum CP-PANi-Cu cathode. The SEM revealed that unlike the nanofiber mat

formed by the PANi-Cu coating on the CP, the Pt formed agglomeration on CP when deposited with an air gun. The 4D X-ray microscopy also revealed that a uniform PANi-Cu coating was formed over the surface of the carbon paper (thickness) and also on the core of the carbon paper matrix. In contrast, the deposited Pt/C particles on the carbon paper were not uniform, with some particles getting into the core of the matrix possibly due to the pressure of the airgun. Further studies are still required to gain a good understanding of the longevity of the CP/PANi-Cu coated cathode in aqueous proton conductor and measure its real performances in PEM fuel cells and MFCs. We are conducting further studies into these two important aspects.

At present, the cost of 1 g Pt/C (40%) is \$334 (₹ 22402) [75]. In contrast, based on a rough estimate, the cost of 1 g PANi deposition is approximate \$3.5. Evidently, if the CP-PANi-Cu cathode can demonstrate good longevity and performance in fuel cells, it will enable a substantial reduction in the current cost of Pt-based cathodes for MFCs and LTFCs. This is highly important as the use of Pt/C catalyst currently contributes almost half of the current construction costs of MFC reactors, which has hindered the wider commercial applications of MFC technology to date [43].

References

- [1] D. Feroldi, M. Basualdo, Description of PEM Fuel Cells System, *Green Energy Technol.* 87 (2012) 49–72. doi:10.1007/978-1-84996-184-4_2.
- [2] J.M. Sonawane, A. Gupta, P.C. Ghosh, Multi-electrode microbial fuel cell (MEMFC): A close analysis towards large scale system architecture, *Int. J. Hydrogen Energy.* 38 (2013) 5106–5114. doi:10.1016/j.ijhydene.2013.02.030.
- [3] J.M. Sonawane, E. Marsili, P. Chandra Ghosh, Treatment of domestic and distillery wastewater in high surface microbial fuel cells, *Int. J. Hydrogen Energy.* 39 (2014) 21819–21827. doi:10.1016/j.ijhydene.2014.07.085.
- [4] S.B. Pasupuleti, S. Srikanth, S. Venkata Mohan, D. Pant, Development of exoelectrogenic bioanode and study on feasibility of hydrogen production using abiotic VITO-CoRETM and VITO-CASETM electrodes in a single chamber microbial electrolysis cell (MEC) at low current densities, *Bioresour. Technol.* 195 (2015) 131–138. doi:10.1016/j.biortech.2015.06.145.
- [5] S.B. Pasupuleti, S. Srikanth, S. Venkata Mohan, D. Pant, Continuous mode operation of microbial fuel cell (MFC) stack with dual gas diffusion cathode design for the treatment of dark fermentation effluent, *Int. J. Hydrogen Energy.* 40 (2015) 12424–12435. doi:10.1016/j.ijhydene.2015.07.049.
- [6] Y. Nie, L. Li, Z. Wei, Recent advancements in Pt and Pt-free catalysts for oxygen reduction reaction, *Chem. Soc. Rev.* 44 (2015) 2168–2201. doi:10.1039/c4cs00484a.
- [7] M.K. Debe, Electrocatalyst approaches and challenges for automotive fuel cells, *Nature.* 486 (2012) 43–51. doi:10.1038/nature11115.
- [8] Y.-J. Wang, D.P. Wilkinson, J. Zhang, Noncarbon Support Materials for Polymer Electrolyte Membrane Fuel Cell Electrocatalysts, *Chem. Rev.* 111 (2011) 7625–7651. doi:10.1021/cr100060r.
- [9] Y. Bing, H. Liu, L. Zhang, D. Ghosh, J. Zhang, Nanostructured Pt-alloy electrocatalysts for PEM fuel cell oxygen reduction reaction, (2010). doi:10.1039/b912552c.
- [10] B.T.X. Lam, M. Chiku, E. Higuchi, H. Inoue, PtAg Nanoparticle Electrocatalysts for the Glycerol Oxidation Reaction in Alkaline Medium, *Adv. Nanoparticles.* 05 (2016) 167–175. doi:10.4236/anp.2016.53018.
- [11] N. Chaisubanan, K. Pruksathorn, H. Vergnes, F. Senocq, M. Hunsom, Stability of TiO₂

- Promoted PtCo/C Catalyst for Oxygen Reduction Reaction, *Int. J. Electrochem. Sci.* 11 (2016) 1012–1028. www.electrochemsci.org (accessed January 16, 2017).
- [12] F. Kadirgan, A.M. Kannan, T. Atilan, S. Beyhan, S.S. Ozenler, S. Suzer, A. Yörür, Carbon supported nano-sized Pt–Pd and Pt–Co electrocatalysts for proton exchange membrane fuel cells, *Int. J. Hydrogen Energy*. 34 (2009) 9450–9460. doi:10.1016/j.ijhydene.2009.09.028.
- [13] L.G.S. Pereira, V.A. Paganin, E.A. Ticianelli, Investigation of the CO tolerance mechanism at several Pt-based bimetallic anode electrocatalysts in a PEM fuel cell, *Electrochim. Acta*. 54 (2009) 1992–1998. doi:10.1016/j.electacta.2008.07.003.
- [14] Y. Liao, G. Yu, Y. Zhang, T. Guo, F. Chang, C.-J. Zhong, Composition-Tunable PtCu Alloy Nanowires and Electrocatalytic Synergy for Methanol Oxidation Reaction, *J. Phys. Chem. C*. 120 (2016) 10476–10484. doi:10.1021/acs.jpcc.6b02630.
- [15] M. Wang, W. Zhang, J. Wang, A. Minett, V. Lo, H. Liu, J. Chen, Mesoporous hollow PtCu nanoparticles for electrocatalytic oxygen reduction reaction, *J. Mater. Chem. A*. 1 (2013) 2391. doi:10.1039/c2ta01470j.
- [16] R. Bashyam, P. Zelenay, A class of non-precious metal composite catalysts for fuel cells, *Nature*. 443 (2006) 63–66. doi:10.1038/nature05118.
- [17] G. Liu, X. Li, P. Ganesan, B.N. Popov, Development of non-precious metal oxygen-reduction catalysts for PEM fuel cells based on N-doped ordered porous carbon, *Appl. Catal. B Environ.* 93 (2009) 156–165. doi:10.1016/j.apcatb.2009.09.025.
- [18] F. Jaouen, E. Proietti, M. Lefèvre, R. Chenitz, J.-P. Dodelet, G. Wu, H.T. Chung, C.M. Johnston, P. Zelenay, Recent advances in non-precious metal catalysis for oxygen-reduction reaction in polymer electrolyte fuelcells, *Energy Environ. Sci.* 4 (2011) 114–130. doi:10.1039/C0EE00011F.
- [19] H. Bunazawa, Y. Yamazaki, Influence of anion ionomer content and silver cathode catalyst on the performance of alkaline membrane electrode assemblies (MEAs) for direct methanol fuel cells (DMFCs), *J. Power Sources*. 182 (2008) 48–51. doi:10.1016/j.jpowsour.2008.03.068.
- [20] L. Zeng, T.S. Zhao, L. An, A high-performance supportless silver nanowire catalyst for anion exchange membrane fuel cells, *J. Mater. Chem. A*. 3 (2015) 1410–1416. doi:10.1039/C4TA05005C.
- [21] Y. Zheng, Y. Jiao, Y. Zhu, L.H. Li, Y. Han, Y. Chen, M. Jaroniec, S.Z. Qiao, High

- Electrocatalytic Hydrogen Evolution Activity of an Anomalous Ruthenium Catalyst, *J. Am. Chem. Soc.* 138 (2016) jacs.6b11291. doi:10.1021/jacs.6b11291.
- [22] S. Mukerjee, Systematic Investigation of Carbon Supported Ru Based Chalcogenides As ORR Catalysts and Their Application in Safc, (2016).
- [23] Z. Yang, Z. Yao, G. Li, G. Fang, H. Nie, Z. Liu, X. Zhou, X. Chen, S. Huang, Sulfur-Doped Graphene as an Efficient Metal-free Cathode Catalyst for Oxygen Reduction, *ACS Nano.* 6 (2012) 205–211. doi:10.1021/nn203393d.
- [24] M. Zhang, L. Dai, Carbon nanomaterials as metal-free catalysts in next generation fuel cells, 2012. doi:10.1016/j.nanoen.2012.02.008.
- [25] O.-H. Kim, Y.-H. Cho, D.Y. Chung, M.J. Kim, J.M. Yoo, J.E. Park, H. Choe, Y.-E. Sung, Facile and gram-scale synthesis of metal-free catalysts: toward realistic applications for fuel cells., *Sci. Rep.* 5 (2015) 8376. doi:10.1038/srep08376.
- [26] L. Qu, Y. Liu, J.-B. Baek, L. Dai, Nitrogen-Doped Graphene as Efficient Metal-Free Electrocatalyst for Oxygen Reduction in Fuel Cells, *ACS Nano.* 4 (2010) 1321–1326. doi:10.1021/nn901850u.
- [27] J.M. Sonawane, A. Yadav, P.C. Ghosh, S.B. Adeloju, Recent advances in the development and utilization of modern anode materials for high performance microbial fuel cells, *Biosens. Bioelectron.* 90 (2017) 558–576. doi:10.1016/j.bios.2016.10.014.
- [28] A.A. Elzatahry, A.M. Abdullah, T.A. Salah El-Din, A.M. Al-Enizi, A.A. Maarouf, A. Galal, H.K. Hassan, E.H. El-Ads, S.S. Al-Theyab, A.A. Al-Ghamdi, Nanocomposite Graphene-Based Material for Fuel Cell Applications, *Int. J. Electrochem. Sci.* 7 (2012) 3115–3126. www.electrochemsci.org (accessed January 16, 2017).
- [29] H. Yuan, Z. He, Graphene-modified electrodes for enhancing the performance of microbial fuel cells, *Nanoscale.* 7 (2015) 7022–7029. doi:10.1039/c4nr05637j.
- [30] A. ElMekawy, H.M. Hegab, D. Losic, C.P. Saint, D. Pant, Applications of Graphene in Microbial Fuel Cells: The Gap between Promise and Reality, *Renew. Sustain. Energy Rev.* (2016) 0–1. doi:10.1016/j.rser.2016.10.044.
- [31] G. Gnana, C.J. Kirubaharan, S. Udhayakumar, C. Karthikeyan, K.S. Nahm, Conductive Polymer / Graphene Supported Platinum Nanoparticles as Anode Catalysts for the Extended Power Generation of Microbial Fuel Cells, (2014).
- [32] J. Peron, Z. Shi, S. Holdcroft, Hydrocarbon proton conducting polymers for fuel cell catalyst

- layers, *Energy Environ. Sci.* 4 (2011) 1575. doi:10.1039/c0ee00638f.
- [33] Y. Qiao, C.M. Li, S.-J. Bao, Q.-L. Bao, Carbon nanotube/polyaniline composite as anode material for microbial fuel cells, *J. Power Sources.* 170 (2007) 79–84. doi:10.1016/j.jpowsour.2007.03.048.
- [34] Y. Yuan, J. Ahmed, S. Kim, Polyaniline/carbon black composite-supported iron phthalocyanine as an oxygen reduction catalyst for microbial fuel cells, *J. Power Sources.* 196 (2011) 1103–1106. doi:10.1016/j.jpowsour.2010.08.112.
- [35] J. Ahmed, H.J. Kim, S. Kim, Polyaniline Nanofiber/Carbon Black Composite as Oxygen Reduction Catalyst for Air Cathode Microbial Fuel Cells, *J. Electrochem. Soc.* 159159 (2012) 497–501. doi:10.1149/2.049205jes.
- [36] H. Zhao, L. Li, J. Yang, Y. Zhang, Nanostructured polypyrrole/carbon composite as Pt catalyst support for fuel cell applications, in: *J. Power Sources*, 2008: pp. 375–380. doi:10.1016/j.jpowsour.2008.03.024.
- [37] X. Yuan, X.-L. Ding, C.-Y. Wang, Z.-F. Ma, Use of polypyrrole in catalysts for low temperature fuel cells, *Energy Environ. Sci.* 6 (2013) 1105. doi:10.1039/C3EE23520C.
- [38] L.-M. Zhang, Z.-B. Wang, X.-L. Sui, C.-Z. Li, L. Zhao, D.-M. Gu, Nitrogen-doped carbon with mesoporous structure as high surface area catalyst support for methanol oxidation reaction, *RSC Adv.* 6 (2016) 39310–39316. doi:10.1039/C6RA06104D.
- [39] B. Rajesh, K.R. Thampi, J.M. Bonard, H.J. Mathieu, N. Xanthopoulos, B. Viswanathan, Nanostructured Conducting Polyaniline Tubules as Catalyst Support for Pt Particles for Possible Fuel Cell Applications, *Electrochem. Solid-State Lett.* 7 (2004) A404. doi:10.1149/1.1799955.
- [40] G. Wu, C.M. Johnston, N.H. Mack, K. Artyushkova, M. Ferrandon, M. Nelson, J.S. Lezama-Pacheco, S.D. Conradson, K.L. More, D.J. Myers, P. Zelenay, Synthesis-structure-performance correlation for polyaniline-Me-C non-precious metal cathode catalysts for oxygen reduction in fuel cells, *J. Mater. Chem.* 21 (2011) 11392–11405. doi:10.1039/c0jm03613g.
- [41] G. Wu, P. Zelenay, Nanostructured nonprecious metal catalysts for oxygen reduction reaction, *Acc. Chem. Res.* 46 (2013) 1878–1889. doi:10.1021/ar400011z.
- [42] H. Wang, J. Lin, Z.X. Shen, Polyaniline (PANi) based electrode materials for energy storage and conversion, *J. Sci. Adv. Mater. Devices.* 1 (2016) 225–255.

- doi:10.1016/j.jsamd.2016.08.001.
- [43] X. Tang, H. Li, Z. Du, H.Y. Ng, Polyaniline and iron based catalysts as air cathodes for enhanced oxygen reduction in microbial fuel cells, *RSC Adv.* 5 (2015) 79348–79354. doi:10.1039/C5RA16148G.
- [44] N. Pekmez, A. Yildiz, Electropreparation of polyaniline in the presence of anhydrous cuprous ions in acetonitrile, *J. Electroanal. Chem.* 386 (1995) 121–126. doi:10.1016/0022-0728(94)03815-K.
- [45] D.J. Davis, T.N. Lambert, J.A. Vigil, M.A. Rodriguez, M.T. Brumbach, E.N. Coker, S.J. Limmer, Role of Cu-Ion doping in Cu- α -MnO₂ nanowire electrocatalysts for the oxygen reduction reaction, *J. Phys. Chem. C.* 118 (2014) 17342–17350. doi:10.1021/jp5039865.
- [46] J.B. Gerken, S.S. Stahl, High-Potential Electrocatalytic O₂ Reduction with Nitroxyl/NO_x Mediators: Implications for Fuel Cells and Aerobic Oxidation Catalysis, *ACS Cent. Sci.* 1 (2015) 234–243. doi:10.1021/acscentsci.5b00163.
- [47] G. Wu, Z. Chen, K. Artyushkova, F.H. Garzon, P. Zelenay, Polyaniline-derived Non-Precious Catalyst for the Polymer Electrolyte Fuel Cell Cathode, *ECS Trans.* 16 (2008) 159–170. doi:10.1149/1.2981852.
- [48] M. Ferrandon, X. Wang, A.J. Kropf, D.J. Myers, G. Wu, C.M. Johnston, P. Zelenay, Stability of iron species in heat-treated polyaniline-iron-carbon polymer electrolyte fuel cell cathode catalysts, *Electrochim. Acta.* 110 (2013) 282–291. doi:10.1016/j.electacta.2013.03.183.
- [49] H. Lee, M.J. Kim, T. Lim, Y.-E. Sung, H.-J. Kim, H.-N. Lee, O.J. Kwon, Y.-H. Cho, A facile synthetic strategy for iron, aniline-based non-precious metal catalysts for polymer electrolyte membrane fuel cells, *Sci. Rep.* 7 (2017) 5396. doi:10.1038/s41598-017-05830-y.
- [50] J.-H. Choi, Synthesis and Characterization of Non-precious Metal Co-PANI-C Catalysts for Polymer Electrolyte Membrane Fuel Cell Cathodes, *J. Korean Electrochem. Soc.* 16 (2013) 52–58. doi:10.5229/JKES.2013.16.1.52.
- [51] G. Wu, K.L. More, C.M. Johnston, P. Zelenay, High-Performance Electrocatalysts for Oxygen Reduction Derived from Polyaniline, Iron, and Cobalt, *Science* (80-.). 332 (2011) 443–447. doi:10.1126/science.1200832.
- [52] P. Zamani, D. Higgins, F. Hassan, G. Jiang, J. Wu, S. Abureden, Z. Chen, Electrospun Iron–

- Polyaniline–Polyacrylonitrile Derived Nanofibers as Non–Precious Oxygen Reduction Reaction Catalysts for PEM Fuel Cells, *Electrochim. Acta.* 139 (2014) 111–116. doi:10.1016/j.electacta.2014.07.007.
- [53] S. Khilari, S. Pandit, J.L. Varanasi, D. Das, D. Pradhan, Bifunctional Manganese Ferrite/Polyaniline Hybrid as Electrode Material for Enhanced Energy Recovery in Microbial Fuel Cell, *ACS Appl. Mater. Interfaces.* 7 (2015) 20657–20666. doi:10.1021/acsami.5b05273.
- [54] Y. Jiang, Y. Xu, Q. Yang, Y. Chen, S. Zhu, S. Shen, Power generation using polyaniline/multi-walled carbon nanotubes as an alternative cathode catalyst in microbial fuel cells, *Int. J. Energy Res.* 38 (2014) 1416–1423. doi:10.1002/er.3155.
- [55] J.M. Kinyanjui, J. Hanks, D.W. Hatchett, A. Smith, M. Josowicz, Chemical and Electrochemical Synthesis of Polyaniline Õ Gold Composites, *J. Electrochem. Soc.* 151 (2004) 275–280. doi:10.1149/1.1808593.
- [56] S.H. Hosseini, M. Malekdar, S. Naghdi, Chemical and electrochemical synthesis of crosslinked aniline sulfide resin, *Polym. J.* 42 (2010) 640–647. doi:10.1038/pj.2010.56.
- [57] H.H. Zhou, S.Q. Jiao, J.H. Chen, W.Z. Wei, Y.F. Kuang, Relationship between preparation conditions, morphology and electrochemical properties of polyaniline prepared by pulse galvanostatic method (PGM), *Thin Solid Films.* 450 (2004) 233–239. doi:10.1016/j.tsf.2003.10.017.
- [58] H. Zhou, J. Wen, X. Ning, C. Fu, J. Chen, Y. Kuang, Electrosynthesis of polyaniline films on titanium by pulse potentiostatic method, *Synth. Met.* 157 (2007) 98–103. doi:10.1016/j.synthmet.2006.12.013.
- [59] V. Gupta, N. Miura, Large-area network of polyaniline nanowires prepared by potentiostatic deposition process, 2005. doi:10.1016/j.elecom.2005.07.008.
- [60] P. Wang, H. Li, Z. Du, Polyaniline synthesis by cyclic voltammetry for anodic modification in microbial fuel cells, *Int. J. Electrochem. Sci.* 9 (2014) 2038–2046.
- [61] A.Y. Obaid, E.H. El-Mossalamy, S.A. Al-Thabaiti, I.S. El-Hallag, A.A. Hermas, A.M. Asiri, Electrodeposition and Characterization of Polyaniline on Stainless Steel Surface via Cyclic, Convulsive Voltammetry and SEM in Aqueous Acidic Solutions, *Int. J. Electrochem. Sci.* 9 (2014) 1003–1015.
- [62] S.S. Mahapatra, S. Shekhar, B.K. Thakur, H. Priyadarshi, Synthesis and Characterization

- of Electrodeposited C-PANI-Pd-Ni Composite Electrocatalyst for Methanol Oxidation, *Int. J. Electrochem.* 2014 (2014) 1–8. doi:10.1155/2014/383892.
- [63] A.J. Bard, L.R. Faulkner, *Electrochemical Methods: Fundamentals and Applications*, Wiley, 2001. doi:10.1016/j.aca.2010.06.020.
- [64] L. Hui, *Proton Exchange Membrane Fuel Cells: Contamination and Mitigation Strategies*, CRC Press, 2010.
- [65] D.J. Choi, A. Boscá, J. Pedrós, J. Martínez, V. Barranco, J.M. Rojo, J.J. Yoo, Y.-H. Kim, F. Calle, Improvement of the adhesion between polyaniline and commercial carbon paper by acid treatment and its application in supercapacitor electrodes, *Compos. Interfaces.* 6440 (2015) 1–11. doi:10.1080/09276440.2016.1112221.
- [66] X. Yan, Z. Tai, J. Chen, Q. Xue, Fabrication of carbon nanofiber–polyaniline composite flexible paper for supercapacitor, *Nanoscale.* 3 (2011) 212–216. doi:10.1039/C0NR00470G.
- [67] J. Boudreau, E. Choi, R. Datta, O. Rezhdo, K. Saeed, Platinum Supply and the Growth of Fuel Cell Vehicles, *Proc. 27th Int. Conf. Syst. Dyn. Soc.* (2009). <https://www.systemdynamics.org/conferences/2009/proceed/papers/P1256.pdf> (accessed April 22, 2017).
- [68] K. Shimizu, L. Sepunaru, R.G. Compton, Innovative catalyst design for the oxygen reduction reaction for fuel cells, *Chem. Sci.* 7 (2016) 3364–3369. doi:10.1039/C6SC00139D.
- [69] S. Mondal, S.R. Bhattacharyya, Oxidation behaviour of copper nanofractals produced by soft-landing of size-selected nanoclusters, *RSC Adv.* 5 (2015) 99425–99430. doi:10.1039/C5RA20694D.
- [70] N. Ramaswamy, T.M. Arruda, W. Wen, N. Hakim, M. Saha, A. Gullá, S. Mukerjee, Enhanced activity and interfacial durability study of ultra low Pt based electrocatalysts prepared by ion beam assisted deposition (IBAD) method, *Electrochim. Acta.* 54 (2009) 6756–6766. doi:10.1016/j.electacta.2009.06.040.
- [71] O. Nibel, T.J. Schmidt, L. Gubler, Bifunctional Ion-Conducting Polymer Electrolyte for the Vanadium Redox Flow Battery with High Selectivity, *J. Electrochem. Soc.* 163 (2016) A2563–A2570. doi:10.1149/2.0441613jes.
- [72] F. Beshkar, S. Zinatloo-Ajabshir, S. Bagheri, M. Salavati-Niasari, Novel preparation of

- highly photocatalytically active copper chromite nanostructured material via a simple hydrothermal route, *PLoS One*. 12 (2017) e0158549. doi:10.1371/journal.pone.0158549.
- [73] R. Khan, P. Khare, B.P. Baruah, A.K. Hazarika, N.C. Dey, Spectroscopic, Kinetic Studies of Polyaniline-Flyash Composite, *Adv. Chem. Eng. Sci.* 1 (2011) 37–44. doi:10.4236/aces.2011.12007.
- [74] M. Zhou, W. Li, T. tian Gu, K. Wang, S. Cheng, K. Jiang, A sulfonated polyaniline with high density and high rate Na-storage performances as a flexible organic cathode for sodium ion batteries, *Chem. Commun.* 51 (2015) 14354–14356. doi:10.1039/C5CC05654C.
- [75] Vulcan | Sigma-Aldrich, Vulcan | Sigma-Aldrich, [Http://Www.Sigmaaldrich.Com/Catalog/Search?Term=Vulcan&interface=All&N=0&mode=match](http://www.sigmaaldrich.com/catalog/search?Term=Vulcan&interface=All&N=0&mode=match) Partial. (n.d.). [http://www.sigmaaldrich.com/catalog/search?term=Vulcan&interface=All&N=0&mode=match partialmax&lang=en®ion=IN&focus=product](http://www.sigmaaldrich.com/catalog/search?term=Vulcan&interface=All&N=0&mode=matchpartialmax&lang=en®ion=IN&focus=product) (accessed February 22, 2017).

Chapter 7

Exploration of a carbon paper/polyaniline-copper hybrid as an air cathode
for microbial fuel cells

[To be submitted as, JM Sonawane, D Pant, PC Ghosh, SB Adeloju, T Exploration of a carbon paper/copper-polyaniline hybrid as an air cathode for microbial fuel cells, Applied Materials and Interfaces, ACS]

Nomenclature:

F	Faraday's constant [$96,485 \text{ C mol}^{-1}$]
I	Current [mA]
i_0	Exchange current [mA]
j_0	Exchange current density [mA cm^{-2}]
R	Ideal gas constant [$8.31 \text{ J mol}^{-1} \text{ K}^{-1}$]
R_{ext}	External Resistor [Ω]
T	Absolute temperature, [298.15 K]
V	Voltage [mV]
η	Overpotential [mV]

Abbreviations:

EPS	Exopolysaccharide
FePc	Iron phthalocyanine
GDL	Gas diffusion layer
LSV	Linear sweep voltammetry
MEAs	Membrane electrode assemblies
MFC	Microbial fuel cells
MnFe_2O_4	Manganese ferrite
MWNT	Multi-walled carbon nanotube
OCV	Open circuit voltage
ORR	Oxygen reduction reaction
PANi	Polyaniline
PANi/C	Polyaniline/carbon black
PB/PANi	Prussian Blue/polyaniline
PtC	Platinum cathode
SPG	Spectrographic pure graphite

Abstract

In search of a cheaper alternative to the expensive platinum-copper (Pt-Cu) catalysts used in air cathode for microbial fuel cells (MFCs), this study explores the use of a carbon paper/copper-polyaniline (CP/PANi-Cu) hybrid as a cheap and efficient air cathode. The resulting CP/PANi-Cu cathode is characterised by a uniform layer and relatively strong adhesion of PANi-Cu which enabled a significant oxygen reduction reaction (ORR). The maximum current generated by the CP/PANi-Cu cathode was $0.50 \pm 0.02 \text{ mA cm}^{-2}$ which was significantly higher than $0.35 \pm 0.03 \text{ mA cm}^{-2}$ obtained with a traditional Pt cathode. The power densities obtained for MFCs with these cathodes were $2.44 \pm 0.14 \text{ mW cm}^{-2}$ under a current density of $0.85 \pm 0.08 \text{ mA cm}^{-2}$ for Pt cathode, and $1.01 \pm 0.01 \text{ mW cm}^{-2}$ at $0.37 \pm 0.04 \text{ mA cm}^{-2}$ for CP/PANi-Cu cathode. Despite showing a loss of cathodic activity of 33%, the CP/PANi-Cu cathode experienced much less biofouling of the associated Nafion membrane than with the membrane used with the Pt cathode, and, thus, indicated that on the basis of overall performance, usage and stability, the CP/PANi-Cu cathode was better than the Pt cathode. Furthermore, a detailed characterisation of the Nafion membranes by Fourier transforms infrared spectroscopy, and 3D profilometry revealed a more complex and thicker biofouling of the membrane attached to the Pt cathode than with the CP/PANi-Cu cathode.

7.1. Introduction

A typical microbial fuel cell (MFC) comprises of a cathode, an anode, and a proton exchange membrane (PEM). It is now well recognised that the cathode is the limiting electrode which defines MFC performance and this has led in recent years to an increasing interest in developing new cathodes [1-5]. Air cathodes have proven in this regard to be the most efficient cathode to date [1]. Often, platinum (Pt) is used for the construction of air cathodes, with loadings ranging from 0.3 – 0.7 mg Pt cm⁻² on carbon papers [2–4]. Thus, the use of Pt in these cathodes contributes significantly to the cost of MFCs and has often limited their wider adoption.

In looking for cheaper alternatives, several different types of cathode catalyst (non-precious metal) have been explored on carbon paper or cloth for various MFCs. These include the use of non-activated and activated biochars prepared from banana [5], iron aminoantipyrine (Fe-AAPyr) [6], cobalt-aminoantipyrine (Co-AAPyr) [6], nickel aminoantipyrine (Ni-AAPyr) [6], manganese-aminoantipyrine (Mn-AAPyr) [6], manganese oxides with a cryptomelane-type octahedral molecular sieve [7], flower-like cobalt(II,III) oxide (Co₃O₄) [8]; iron-based catalysts [9] and platinum-iron-titanium dioxide (Pt–Fe/TiO₂) [10]. Each of these materials has its own merits and demerits.

The methods for depositing catalyst on a gas diffusion layer (GDL) include brush coating [11], inkjet printing [12], ultrasonic spray coating [13], doctor blade coating [14], and sputtering [15]. There has been no direct method for binding the catalyst onto GDL. However, the aforementioned methods have their own merits and demerits. A major demerit of these coating methods is the often inadequate and ineffective adhesion of the substrate catalyst to the carbon supports which are more commonly employed for this purpose [16].

The use of conductive polymers as composites, including with graphene as catalysts in MFC cathodes for ORR reaction has been widely reported [17–19]. One of these air cathodes used iron-containing polyaniline prepared by heat treatment and coated with graphite felt [20]. Polyaniline/carbon black (PANi/C) composite-supported iron phthalocyanine (FePc), collectively termed PANi/C/FePc, was also coated on carbon cloth [21]. A Prussian Blue/polyaniline (PB/PANi)-modified electrode was developed by using a three-step method involving both electropolymerisation and chemical polymerisation on spectrographic pure graphite (SPG) rod [22]. In another study, fibrous PANi–MnO₂ nanocomposites were prepared by using a chemical oxidative polymerisation method on carbon paper [23]. Polyaniline (PANI)/multi-walled carbon

nanotube (MWCNT) composites synthesised chemically were also explored as a catalyst in air cathodes [24]. A manganese ferrite (MnFe_2O_4)/polyaniline (PANI)-based cathode catalyst has also been developed by electropolymerisation [25]. In addition, a polyaniline nanofiber/carbon black composite has also been synthesised by interfacial polymerisation [17].

To date, most of the PANi cathodes that have been explored for MFCs are based on PANi composites, such as manganese ferrite (MnFe_2O_4)/polyaniline (PANi) cathode [25]. In one study, heat treated PANi- Fe_{900} and PANi- Fe_{700} were synthesised at 900 °C and 700 °C, respectively, and subsequently used as MFC cathodes [20]. A PANi/carbon black composite was also explored for MFCs [17]. These PANi based cathodes were mostly prepared by chemical polymerisation which involves various steps. Furthermore, the resulting catalyst inks are often applied manually or mechanically onto the cathode surface. These often lead to uneven catalyst distribution and surface poor adhesion.

The use of electrochemical polymerisation for the formation of PANi is advantageous in its ability to be grown directly on any substrate of different size and dimension, and thus effective for minimising contact resistance. The lower contact resistance is also attributed to the in-situ synthesis of compact PANi nanofibers on the chosen substrate. It is therefore anticipated that the adoption of electrochemical synthesis of PANi or PANi composites would produce a more superior cathode capable of accomplishing a more efficient interfacial electron transfer on the triple phase boundary of the membrane electrode assembly (MEA) than those reported by other approaches to date. It has been reported that the interfacial contact resistance between the membrane and the electrodes can influence the performance of MFCs [26]. The microscopic contact resistance of the deposited catalyst and sublayers of the catalyst on carbon paper/ cloth has also been reported to influence the MEA performance [11].

In this study, we explore the use of a PANi-Copper composite coated directly on carbon paper by galvanostatic polymerisation of aniline (ANi) as a direct method for binding the catalyst onto the GDL and overcoming inadequate adhesion and interfacial contact resistance. The deliberate use of a copper counter electrode in the monomer which contained nitric acid is explored as a means of introducing copper ions. The presence of cupric ions (Cu(II)) during the electropolymerisation of ANi on the carbon paper is intended to produce a Cu doped PANi which may be useful in further enhancing the oxygen reduction kinetics. The presence of Cu in the resulting CP/PANi-Cu composite will be verified by time-of-flight secondary ion mass spectrometry (ToF-SIMS). The

resulting carbon paper/polyaniline-copper (CP/PANi-Cu) hybrid will be subsequently hot-pressed with a Nafion membrane to form the half MEA and subsequently explored for use in MFCs to compare its electrochemical performance with that of a Pt cathode. Also, the biofouling of the Nafion membrane and the loss of catalytic activity of both types of cathodes will be evaluated by using 4D X-ray Microscopy and 3D profilometry. Time-dependent Tafel plots (linear sweep voltammetry) will also be used to assess the dependent loss of cathodic activity. Furthermore, FTIR analysis of Nafion will be used to evaluate the nature and composition of the deposited macromolecules on the fouled membrane.

7.2 Materials and method

7.2.1 Electrode preparation

7.2.1.1 Anode fabrication

The stainless-steel wool (Scotch-Brite, India) with polyaniline anode fabricated by previously described in the report [27,28]. In brief, SS/PANi-W was explored as an anode material with an apparent surface area of 50 cm^2 . Before coating with PANi, the SS wool (SS-W) was degreased by ultrasonication for 15 mins in 100% acetone. Reagent grade aniline (Sigma-Aldrich, Mumbai, India) and nitric acid (Sigma-Aldrich, Mumbai, India) were used for electropolymerisation of aniline on SS-W. The polymerisation of ANi was carried in 0.4 M aniline in 0.7 M nitric acid with an applied current density of 2.5 mA cm^{-2} for 15 mins in a 3-electrode cell. The monomer solution was purged with nitrogen for 10 mins to remove oxygen before the beginning of polymerisation. The coated electrodes were rinsed with distilled water several times to ensure complete removal of untreated aniline and nitric acid.

7.2.1.2 Preparation of CP/PANi-Cu cathode

The deposition of PANi on carbon paper was achieved in a three-electrode cell assembly by galvanostatic polymerisation of ANi. The electrodeposition was performed with a Biologic SP-150 potentiostat (BioLogic, Claix, France) equipped with an EC-Lab V-10.44 software for data processing. Reagent grade aniline (Sigma-Aldrich, Mumbai, India) and nitric acid (Sigma-Aldrich, Mumbai, India) were used for this purpose. The monomer solution consists of 0.4 M aniline in 0.7 M nitric acid and copper (II) sulfate. The PANi was synthesised by applying a constant current density of 2.5 mA cm^{-2} for 25 mins. The solution was purged with nitrogen gas to remove oxygen

before the commencement of electropolymerisation. The working electrode was a commercial carbon paper of 210 μm thickness (GDS 210, CeTech, Taichung, Taiwan) with a dimension of $3 \times 2.5 \text{ cm}$ (7.5 cm^2). The carbon paper was degreased in an ultrasonication bath, as described for the SS-W. Copper felt was used as a counter electrode. The copper electrode also acts as a source of copper ions during PANi electrodeposition in the acid medium to form a PANi-Cu composite. The presence of a PANi-Cu composite was verified by time-of-flight secondary ion mass spectrometry (ToF-SIMS).

7.2.1.3 Fabrication of Pt cathode

Pt air cathodes with 0.5 mg cm^{-2} loading were fabricated by following the previously described method [29]. Briefly, Vulcan XC-72 (Sigma-Aldrich, Australia), 20 % w/w Pt content was coated onto $12 \times 10 \text{ cm}$ commercial carbon paper (GDS 210, CeTech, Taichung, Taiwan). PtC ink was prepared in 5% Nafion solution as a binder in isopropyl alcohol (Sigma-Aldrich, Australia) and was coated with a spray paint gun.

7.2.1.4 Hotpressing of Pt and PANi-Cu electrodes

All fabricated electrodes were dried at $60 \text{ }^\circ\text{C}$ for 6 hrs to confirm complete drying. Resulted electrodes were again coated with 5% Nafion solution subsequently placed for drying for 30 mins. Coated electrode hot pressed on one side using Nafion NRE-212 (Sigma-Aldrich, Australia) under 10 kg cm^{-2} at $140 \text{ }^\circ\text{C}$ for 3 mins using a Carver hot press (Carver, Inc, Indiana, USA). The fabricated CP/Pt and CP/PANi-Cu MEAs were cut into a size of $3 \times 2.5 \text{ cm}$ (apparent surface area 7.5 cm^2).

7.2.2 Configuration of MFC reactor

The MFC reactors were made of a transparent acrylic sheet of 5 mm thickness. The sheets were cut using a laser to ensure identical sizes in all reactors. Three sheets with a dimension of $6.8 \times 6.8 \text{ cm}$ were fixed together to form the base of the MFC reactor. The dimension of the top and bottom sheets were $3 \times 2.5 \text{ cm}$. The inner dimension of $3 \times 3 \times 3 \text{ cm}$ was formed as an anode compartment. The empty bed volume of the anode was 27 cm^3 . The resulting one-sided MEAs were sandwiched in an acrylic mesh, with an aluminum mesh of similar dimension acting as a current collector in the MFC reactors. This was kept in place with nuts and bolts to ensure leakproof assembly. A miniature Ag/AgCl (sat. KCl) electrode was used (RRPEAGCL, Pine Research Instrumentation,

Durham, USA) as a reference electrode for the electrochemical measurements. The SS-W anode modified with PANi was connected with tantalum wire which acted as an anode connection.

7.2.3 Characterisation of Pt and PANi-Cu cathodes

7.2.3.1 Microscopy

The membranes were carefully harvested after the completion of the experiments to identify the extent of fouling experienced during the study. Extreme care was taken to evade surface contamination of membranes. The topography of both Nafion membranes attached to the CP/PANi-Cu and CP/Pt cathodes were examined in triplicates with the Alicona microscope with magnifications of 10x, 20x, and 50x, visualised by full 3D scans. Some samples were further subjected to the phase contrast tomography using a Four-Dimensional X-ray Microscopy, (Versa XRM-520, Xradia, Pleasanton, CA).

7.2.3.2 Time-of-Flight Secondary Ion Mass Spectrometry (ToF-SIMS)

The atomic and molecular species concentration of CP/Pt and CP/Cu-PANi cathodes were investigated using TRIFT V NANO TOF, (Physical Electronics, Inc. (Phi), Chanhassen, Minnesota, USA). The data were recorded by a focused ion beam. The primary ions were 30 KV Ga⁺ by 10 min Spectra acquisition using liquid metal ion gun (LMIG) in 500 μ x 500 μ sq. area. The subsequent secondary ions were augmented into the mass spectrometer, and the ions were then separated by determining time-of-flight. A 2D image was made by focussed ion beam on the specimen surface.

7.2.3.3 Attenuated Total Reflectance -Fourier Transform Infrared Spectroscopy

A Vertex 80 FTIR spectrometer (Bruker Corporation, Massachusetts, United States) was used to analyse the FTIR properties of the biofouled Nafion membranes attached to the cathodes at the completion of the experiments. FTIR bands were obtained with the attenuated total reflectance (ATR) method with a resolution of 4 cm⁻¹. The wavenumbers were in the range of 4000–550 cm⁻¹ for Nafion attached to the CP/Pt and CP/PANi-Cu cathodes. The baseline rectifications were thru carefully, and the peaks were resolute with an Opus software (Bruker Corporation, Massachusetts, United States).

7.2.4 Operation of the MFCs

MFCs were fed in triplicate with M9 media to which 4% landfill leachate was added as a bacterial inoculum. We have previously proposed the use of landfill leachate as a promising substrate for MFCs[30] and, thus, serve as our basis for selecting it as a bacterial source in this study. The ingredients of the M9 media per L of deionised water is as follows - NH_4Cl : 0.31 g, KCl : 0.13 g, $\text{NaH}_2\text{PO}_4 \cdot \text{H}_2\text{O}$: 2.69 g, Na_2HPO_4 : 4.33 g, and 12.5 mL of each trace metal and vitamin solutions [31,32]. Additionally, 2% sodium acetate was added as the sole carbon source in the M9 media. The landfill leachate was sampled from a landfill site in Turbhe, Mumbai. The feed and reactor was sparged with nitrogen gas to remove oxygen and minimise aerobic oxidation during electrogenesis. All experimentations were carried at an ambient temperature of 27 ± 3 °C. The experiments were conducted in a fed-batch mode. First two cycles at open circuit voltage (OCV) mode for 6 days per batch and subsequently with an applied constant external resistor for 5 days per batch. After each successive batch, 90% of the spent medium was replaced with fresh medium. In the first phase, the MFCs ran initially in an OCV mode for two cycles to enrich biofilm on the anode. In the second phase, a 100 Ω external resistor was applied to evaluate the magnitude of the current generation and continued until a stable performance was achieved. The control set of each cathode materials were run only in sterile M9 media.

7.2.5 Analytics and calculations

MFCs equipped separately with CP/Pt cathode, and CP/ PANi-Cu cathode were run initially in an OCV mode to establish biofilm formation without any external load. After two succeeding cycles, a 100 Ω resistor was coupled to each MFC set-up to evaluate current generation. Each reading was taken at 30 min intervals using a data logger (Graphtec GL820, Graphtec corporation, Shinanocho, Japan). From the recorded voltage (V), the corresponding current (I) was calculated by Ohm's law: $I=V/R$; where R represents R_{ext} and V is the voltage between the electrodes. The electrochemical performance and data were standardised with the apparent surface area (7.5 cm^2) of the cathode. All electrochemical experiments and Tafel plot analysis were conducted with a Biologic SP-150 potentiostat (BioLogic, Claix, France) equipped with EC-Lab V 11.10 software. The polarisation curves were obtained using linear sweep voltammetry (LSV) recorded at a scan rate of 1 mV s^{-1} in a potential window from OCV to 0 V. These were carried out during the 6th batch cycle running

across constant resistance mode when the observed current was at stationary phase. The cathodic Tafel plots were carried out in both systems in the middle of every batch cycles using LSV (scanning from OCV to 150 mV, at a scan rate of 1 mV s⁻¹)

After the application of overpotential (η), positive deviation from OCV to 150 mV shows an initial log of η and further Tafel lines become linear. With the Tafel equation, the X-axis intercept gives us the log of the current exchange densities ($\ln j_0$). Cathodic Tafel plot, as derived from the equation below, was employed to measure the reaction kinetics.

$$\ln\left(\frac{i}{i_0}\right) = \beta\left(\frac{F\eta}{RT}\right)$$

where i_0 is exchanged current, i is the electrode current density (mA cm⁻²), β is the electron transfer coefficient, R is the ideal gas constant (8.31 J mol⁻¹ K⁻¹), F is the Faraday's constant (96485 C mol⁻¹), T is the absolute temperature, K (298.15 K) and η is the activation overpotential. The purpose of using the Tafel plot is to calculate the i_0 value, an essential parameter in the rate of electro-oxidation or electro-reduction of a chemical species at an electrode in equilibrium.

7.3 Results and discussion

7.3.1 Morphology of Pt and CP/PANi-Cu cathodes

The topographies of the uncoated, PANi-Cu coated, and Pt_(0.5 mg cm⁻²) coated carbon papers were obtained with an Alicona profilometer, as shown in Figure 7.1. The pictures show the variance in the surface profiles of the cathode materials at mm/ μ m scale. The mean roughness of pristine CP, CP/ PANi-Cu, and Pt-coated carbon papers were 8.4, 1.2, and 6.0 μ m, respectively. The surface of the CP/Pt cathode was obviously the roughest due to the variation of coating layers (than CP/ PANi-Cu cathode) caused by pressure from spray coating. In comparison, the CP/ PANi-Cu cathode showed a more uniform surface with electrodeposition on the CP. Also, the electrodeposition was much better controlled and uniform than with spray coating. During the electropolymerisation, the growth of PANi-Cu starts on the core of the GDL and results in the formation of PANi-Cu nanofibers of 40.8 \pm 7.2 nm diameter [(Figure 7.1(d)]. Due to the in-situ polymerisation, the bonding of PANi-Cu nanofiber network to the surface of the carbon paper lowers the interfacial contact resistance through strong adhesion.

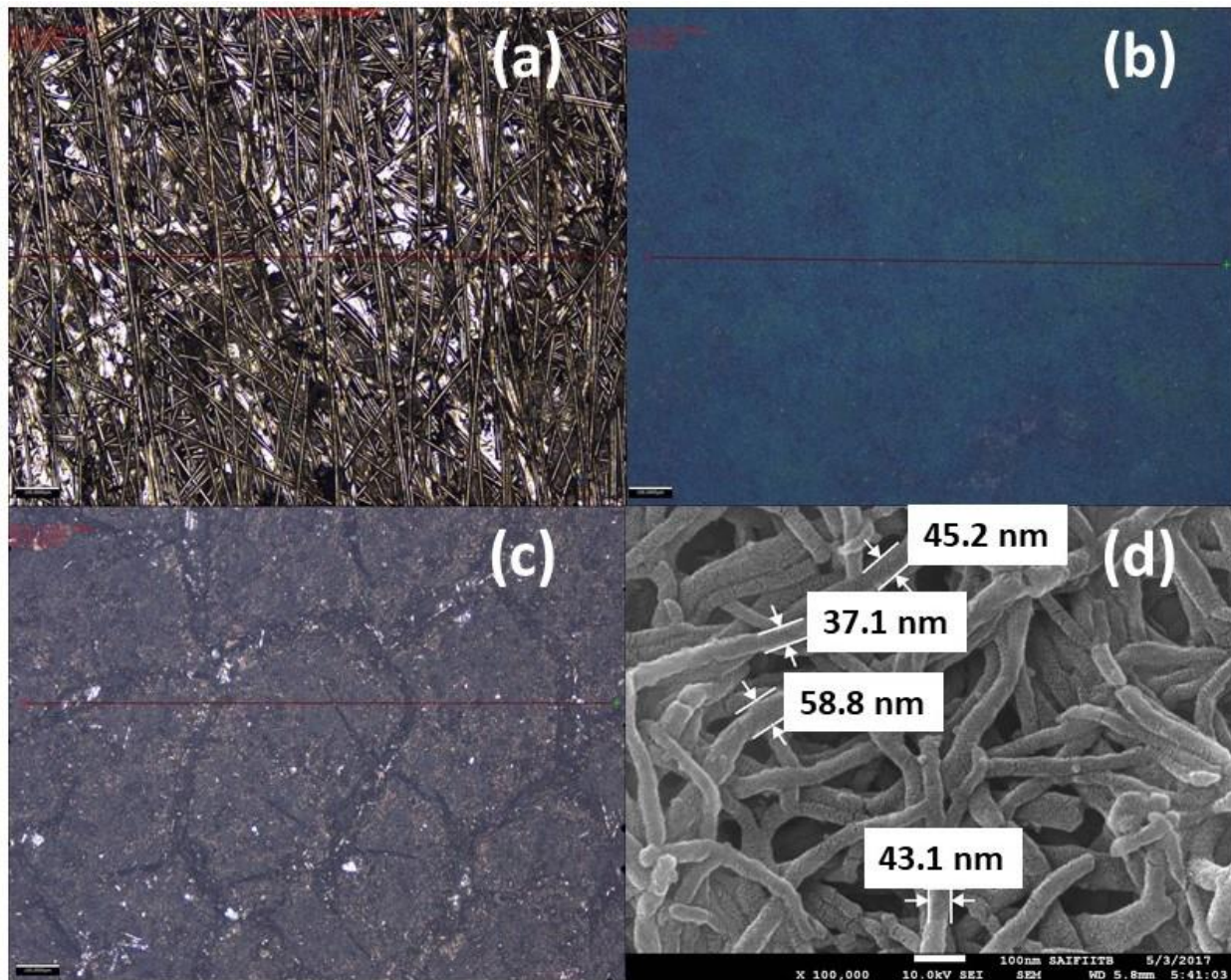


Fig. 7.1 Micrographs of the different cathodes explored in the study. Profilometer image of (a) pristine CP, (b) CP/ PANi-Cu cathode and (c) CP/Pt cathode; and (d) scanning electron micrograph of the CP/ PANi-Cu cathode (magnification 100,000X).

7.3.2 Time-of-Flight Secondary Ion Mass Spectrometry (ToF-SIMS)

The composition of atoms in the coating was evaluated by ToF-SIMS. The 2D images in Fig. 7.2 show the total ion counts and densities of CP/Pt and CP/ PANi-Cu cathodes, respectively. The carbon ion count obtained for the CP/Pt cathode was almost four times greater than obtained for the CP/ PANi-Cu cathode. This was due to the pure carbon content relative to the minuscule amount of Pt nanoparticles present. The images obtained for the CP/PANi-Cu cathode revealed the presence Cu in the sample. The distribution of Cu ions in $500 \mu \times 500 \mu$ sq. area is shown in Fig. 7.2(b). Interestingly, the counts for hydrogen and nitrogen ions are significantly higher in the

PANi cathode than in Pt cathode. The high oxygen and nitrogen contents in the PANi coating are known to be responsible for the excellent electrocatalytic effect with Cu on ORR [33].

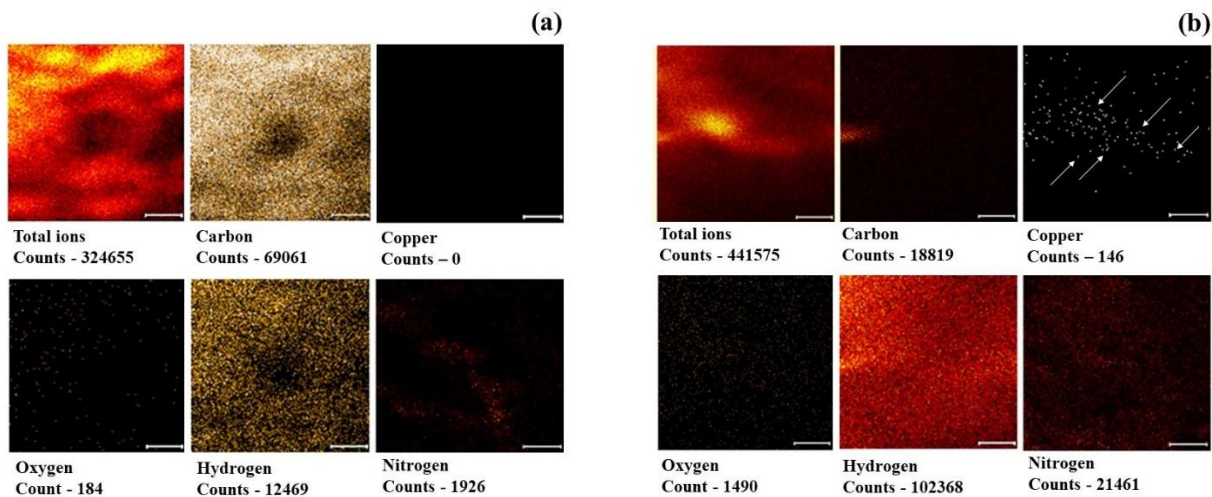


Fig. 7.2 2D image of ion counts obtained by ToF SIMS. (a) CP/Pt cathode and (b) CP/PANi-Cu cathode.

7.3.3 Bioelectrocatalytic performance of Pt and CP/PANi-Cu cathodes

The reactors were operated in batch modes; the first cycle was OCV mode operation without any external load. The high OCVs recorded for MFCs with CP/Pt, and CP/PANi-Cu cathodes may be due to aerobic degradation of the organic substrate. Figure 7.3(a) shows the initial OCVs observed for both CP/Pt and CP/PANi-Cu based MFC systems. In the first cycle of both cathodes, the OCV declined slightly over time. This phenomenon is attributed to a log phase due to the adjustment of the bacterial consortia at the electrode surface. After the first cycle and with the incorporation of 25 mM acetate, the OCVs obtained for both cathodes increased exponentially with time. This represents the lag phase of both MFCs, and the highest OCV was observed on the 6th day and 4th day of the second cycle of the operation of CP/PANi-Cu cathode and CP/Pt cathode, respectively. The MFC with the CP/PANi-Cu cathode gave stable readings from the 4th to 6th day of operation, followed by a decline in the OCV. The average OCV obtained for the CP/Pt cathode system increased from 137 ± 22 mV to 477 ± 43 mV in the second cycle. Likewise, the OCV recorded for the CP/PANi-Cu cathode rose from 107 ± 18 mV to 290 ± 29 mV. In both cases, the MFC with the CP/Pt cathode gave a high OCV than that with the CP/PANi-Cu cathode. However, the MFC with CP/PANi-Cu cathode gave a maximum OCV on the 9th day of the operation and remained stable for the next three days, followed by a decline in OCV. In contrast, the MFC with Pt cathode

was still in the exponential phase up to the 12th day of operation. These results indicate that the fall in the OCVs in both systems may be due to their high start-up times in the M9 media.

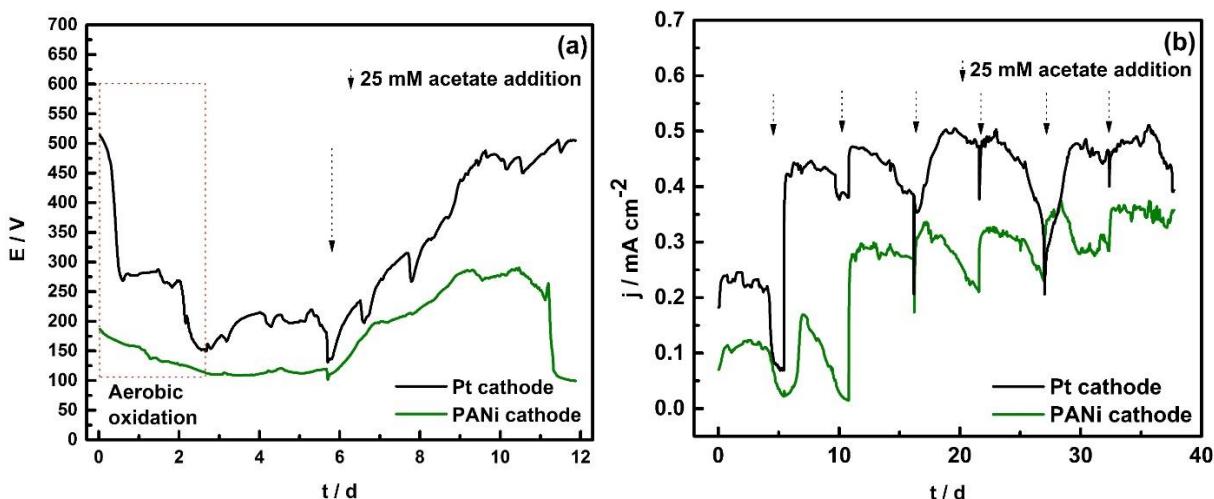


Fig. 7.3 Performance of CP/Pt and CP/PANi-Cu cathodes in MFCs. (a) Open circuit voltage as a function of time, and (b) current generation as a function of time.

Both MFCs subsequently ran in a constant resistance (CR) with a R_{ext} of 100 Ω for seven batch cycles, each cycle with around 5 days [(Fig. 7.3(b)]. Overall, the MFC with the Pt cathode gave higher current density than with the CP/PANi-Cu cathode. Also, the startup time for the current generation was quick with the CP/Pt cathode than with the CP/PANi-Cu cathode. Both CP/Pt and CP/PANi-Cu cathodes produced j_{max} during the 8th and 9th batch cycles (based on the two OCV cycles). The j_{max} were 0.50 ± 0.02 and 0.35 ± 0.03 mA cm^{-2} for the CP/Pt and CP/PANi-Cu cathodes, respectively. The difference in the achieved j_{max} may be accredited to the higher oxygen reduction kinetics of the CP/Pt cathode than that with the CP/PANi-Cu cathode. Both systems showed immediate current generation from the 3rd cycle, signifying that there was no delay in the startup of the bioelectrocatalyst due to the operation of the two prior OCV cycles to establish the growth of electroactive biofilm on the anode. This phenomenon can be ascribed to their 3D available areas that offer more surface area to the anode respiring bacterial communities.

7.3.4 Current-voltage characteristics

The polarisation behaviour was studied by using linear sweep voltammetry, as shown in Fig. 7.4. The scan rate was kept at 1 mV s^{-1} . The area-specific power densities for the CP/Pt and CP/PANi-Cu cathodes were 2.44 ± 0.14 mW cm^{-2} under a current density of 0.85 ± 0.08 mA cm^{-2} , and 1.01

$\pm 0.01 \text{ mW cm}^{-2}$ at $0.37 \pm 0.04 \text{ mA cm}^{-2}$, respectively. It has been described that the Pt loading on the Pt cathode significantly affects the power generation [34]. In comparison, the air cathode reportedly generated a maximum power density (P_{max}) of 0.054 mW cm^{-2} in a MFC [24]. It has also been observed that the P_{max} obtained for unlike cathodes are proportional to the voltage output of the system. Similarly, the attainment of higher OCVs has been related to the achievement of higher P_{max} [24].

Apart from being conductive, the CP/PANi-Cu composite has also been shown to serve as a catalyst with high redox activity [35]. The catalytic activity of the CP/PANi-Cu cathode was enhanced by the presence of the cupric ions generated from the exposure of the copper counter electrode to nitric acid during CP/PANi-Cu deposition. The cupric ions formed in the acidic aniline monomer were reduced to form a CP/PANi-Cu composite. Also, the synergistic ORR activity from oxygen transport from the cathode interphase to the triple phase boundary was facilitated by the resulting CP/PANi-Cu nanofiber network [$40.8 \pm 7.2 \text{ nm}$, Fig. 7.1(d)].

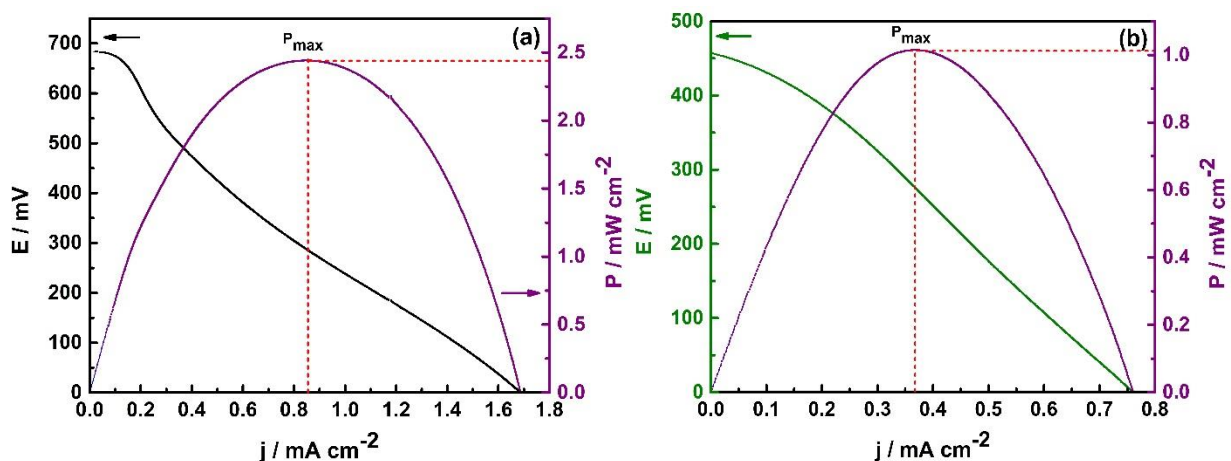


Fig. 7.4 Polarisation curves of the MFCs operated with CP/Pt and CP/PANi-Cu. (a) CP/Pt cathode, and (b) CP/PANi-Cu cathode.

7.3.5 Longevity of cathodic activity

After completion of the experiment, both cathodes were removed from the aluminium current collectors. Interestingly, deposition of aluminum oxide (Al_2O_3) was found on the interface of the cathodes, but, notably, more Al_2O_3 deposition was observed on the CP/Pt cathode current collector than on that of the CP/PANi-Cu cathode, as shown in Figure 7.5. This observation indicates that the CP/Pt cathode current collector corroded more significantly with the passage of current through it. This may be due to the much higher potential difference between the CP/Pt cathode and the Al

current collector. It suggests that the use of a more stable current collector is preferred when running the MFCs for extended periods.

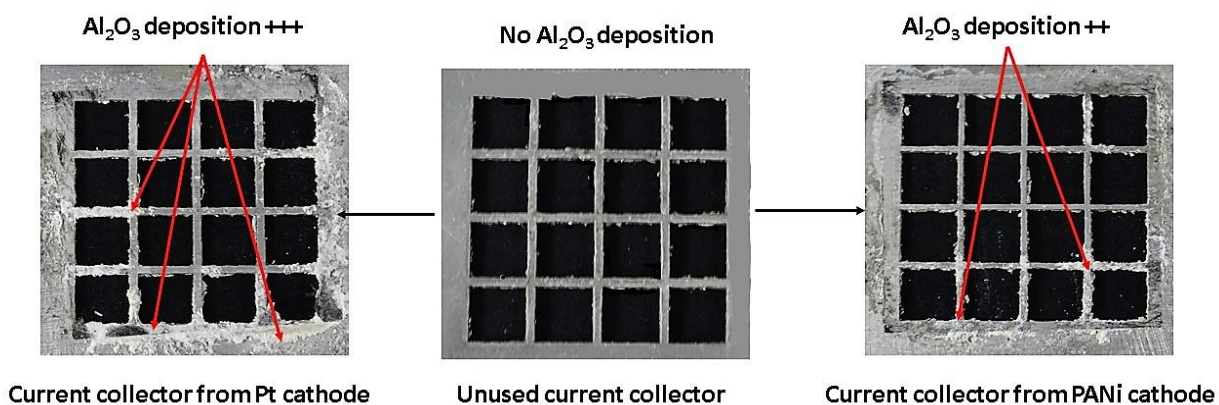


Fig. 7.5 Evidence of the formation of Al_2O_3 on current collectors used with the CP/Pt and CP/PANi-Cu cathodes after exposure to the M9 media.

The longevity of the cathodic activity of the cathodes was evaluated electrochemically by linear sweep voltammetry (LSV) after each successful batch cycle. The Tafel plots were derived from the LSV to gain an understanding of the kinetics of the cathodes. From the Tafel-type linear equation obtained from the LSV plots, the corresponding slope is F/RT , and the y-axis intercept is the logarithm of the exchange current. For both MFCs, the Tafel plots were recorded at the beginning of the experiments. The exchange current density (j_0) was calculated by extrapolation to $\eta = 0$ with a linear regression ($R^2 > 0.99$) between $\eta = 150$ mV. By application of 150 mV overpotential, the j_0 values depend on the charge limited electrochemical process where mass transfer is limited during the measurements. The j_0 value signifies the rate of electron exchange from the anodic biofilm to the cathode at equilibrium. The average j_0 values based on triplicate measurements were used to plot the Tafel curves. The Tafel plots obtained for CP/Pt and CP/PANi-Cu cathodes are shown in Fig. 7.6(a,b). Also, the $j_{0(\text{apparent})}$ values obtained for these cathodes (calculated from the Tafel plots) are shown in Fig. 7.6(c,d).

The initial $j_{0(\text{apparent})}$ values obtained for CP/Pt and CP/PANi-Cu cathodes were 0.0199 ± 0.0019 and 0.0193 ± 0.0004 mA cm^{-2} , respectively. Although slightly lower, the values obtained with the CP/PANi-Cu cathodes were more reproducible. The $j_{0(\text{apparent})}$ values obtained after the first OCV cycle for both MFCs decreased to 0.0181 ± 0.0013 , and 0.0154 ± 0.0005 mA cm^{-2} , respectively. The changes in the $j_{0(\text{apparent})}$ were 2.6 % and 20.2 % for the CP/Pt and CP/PANi-Cu cathodes, respectively. When operated under a constant current mode, the $j_{0(\text{apparent})}$ at the end of the first

current cycle were $0.0164 \pm 0.0007 \text{ mA cm}^{-2}$ and $0.0114 \pm 0.0006 \text{ mA cm}^{-2}$ for the CP/Pt and CP/PANi-Cu cathodes, respectively. In this case, the cathodic loss observed in both MFCs were 11.8% and 41% for CP/Pt and CP/PANi-Cu cathodes, respectively. The cathodic loss is the sum of the catalyst deterioration and the current collector corrosion which ultimately increases contact resistant of the MFC. The $j_{0(\text{apparent})}$ of the CP/Pt and CP/PANi-Cu cathodes at the end of the experiment were $0.0100 \pm 0.0001 \text{ mA cm}^{-2}$ and $0.0056 \pm 0.0003 \text{ mA cm}^{-2}$, respectively.

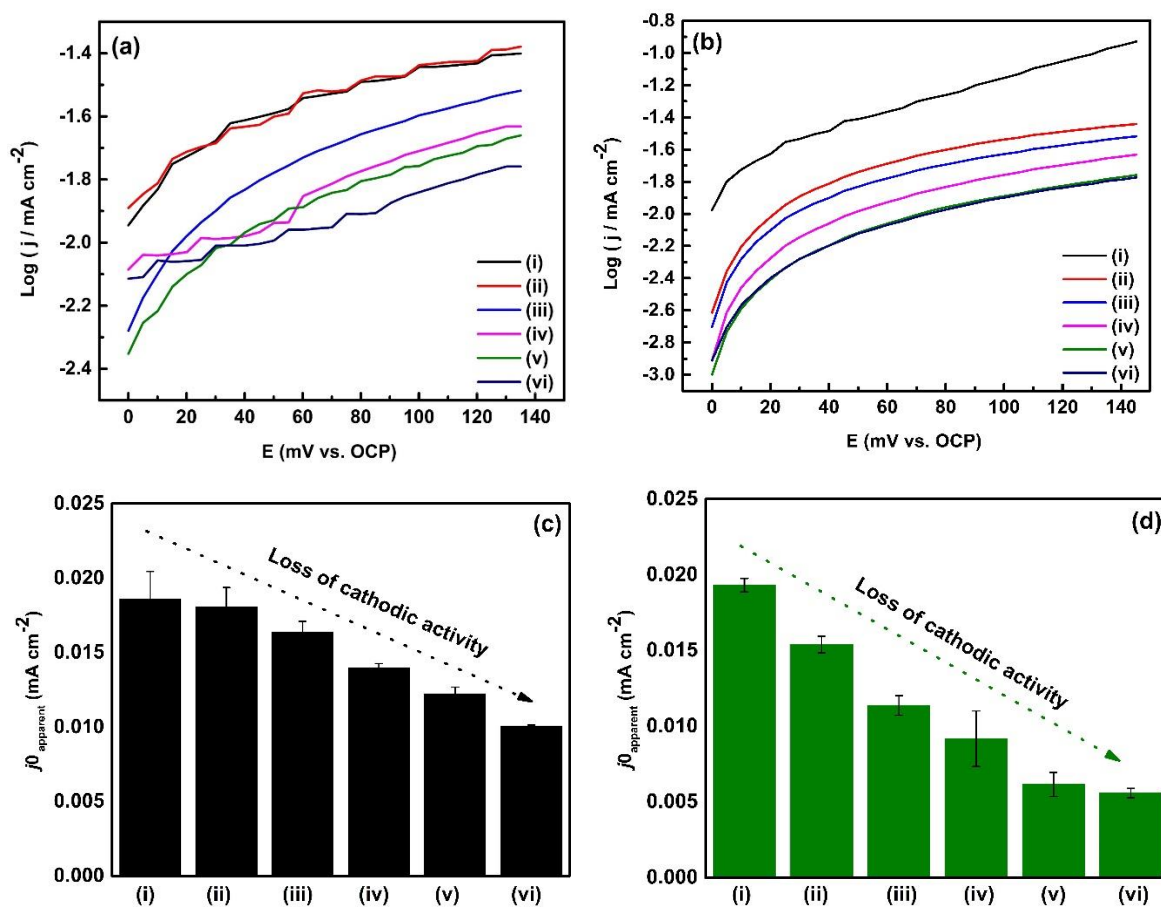


Fig. 7.6 Electrochemical analysis of the longevity of the cathodes. (a) Tafel plots of CP/Pt cathode, (b) Tafel plots of CP/PANi-Cu cathode. (c) $j_{0(\text{apparent})}$ of CP/Pt cathode after every successive cycle. (i) is for the initial cycle, (ii) for cycle 2, (iii) for cycle 3, and so on to cycle 6 (vi) for cycle 6 and (d) $j_{0(\text{apparent})}$ of CP/PANi-Cu cathode after every successive cycle. (i) is for the initial cycle, (ii) for cycle 2, (iii) for cycle 3, and so on to cycle 6.

The percent change of electrokinetics in both MFCs from the initial to the end of the experiment was 46% for the CP/Pt cathode and 71% for CP/PANi-Cu cathode. The large change in the electrokinetics of the cathodes suggests that the CP/PANi-Cu cathode deteriorated faster compared to the CP/Pt cathode. However, the deposition of aluminum oxide was more pronounced on the Pt cathode which may have contributed significantly to the cathodic activity loss because aluminum oxide is a poor conductor of electricity and, thus, directly increases the contact resistance of the cathode. The deterioration of the aluminium current collector in this study was due to the M9 media permeation from the Nafion membrane[36–38] through the carbon paper. However, it is also possible to protect the aluminium current collector by coating with CP/PANi, as previously reported [39].

7.3.6 Biofouling of Nafion membrane

Bacterial communities tend to grow on hydrophilic surfaces [40]. The biofilm slowly forms on the membrane surface when one of its sides is exposed to the liquid organic material on the anode side. It has been reported that the biofouling of membranes leads to an unwanted distortion of its function and structure [41,42]. It is recognised as a major obstacle to the long-term operation of MFCs [41,42]. It has also been observed that the formation of slime on Nafion leads to resistance to mass transfer from the anode chamber to Nafion [43]. The electrogenic bacterial communities produced extrapolymeric substance consisting of proteins, nucleic acids, lipids, and polysaccharides. These macromolecules promote mechanical adhesion to the Nafion surface to form a three-dimensional polymeric network which immobilises the biofilm communities [43]. The changes due to biofilm formation on the Nafion membrane exposed to M9 media for nine batch cycles was examined. The membrane was carefully harvested and detached from the carbon paper. The photographs were taken before and after the experiment. As obvious in Fig. 7.7(a), the Nafion membrane before the experiment was black from the platinised carbon coated on the carbon paper, whereas, after the exposure to the M9 media, the membrane revealed a significant deposition of bacterial debris and exopolysaccharides (EPS) and a biofouled wrinkled surface. In Fig. 7.7(b), the Nafion membrane before the experiment was slightly green from the PANi-Cu deposition, but after the experiment, evidence of slight bacterial debris and EPS deposition was obvious. Table – 7.1 gives surface profile measurement of CP/Pt and CP/PANi-Cu cathodes

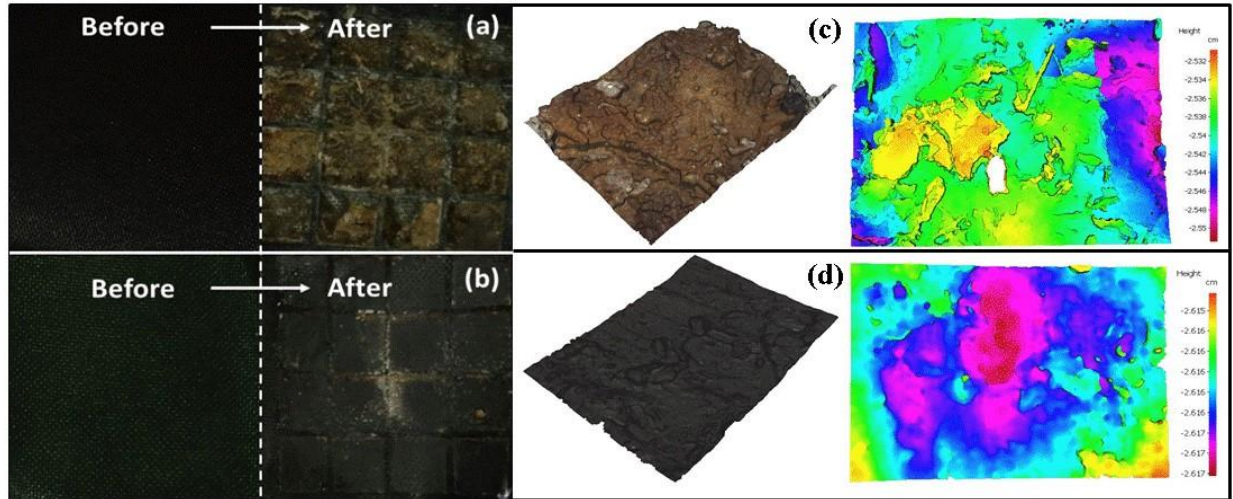


Fig. 7.7 Observed changes in Nafion membranes before and after exposure to M9 media. (a) membrane attached to the CP/Pt cathode before and after the experiment, and (b) membrane attached to the CP/PANi-Cu cathode before and after the experiments. 3D-profilogram of the used Nafion membrane attached to (c) CP/Pt and (d) CP/PANi-Cu cathodes (50X).

Table 7.1 Surface profile of CP/Pt and CP/PANi-Cu cathodes

Name	Unit	Pt cathode	Cu-PANi cathode	Description
Ra	μm	5.9955	1.2306	Average roughness of profile
Rq	μm	8.1917	1.6416	Root-Mean-Square roughness of profile
Rt	μm	53.7711	12.6996	Maximum peak to valley height of roughness profile
Rz	μm	29.0302	7.3990	Mean peak to valley height of roughness profile
Rmax	μm	44.4310	11.6705	Maximum peak to valley height of roughness profile within a sampling length
Rp	μm	24.7106	4.1984	Maximum peak height of roughness profile
Rv	μm	29.0605	8.5012	Maximum valley height of roughness profile
Rc	μm	28.9865	7.0898	Mean height of profile irregularities of roughness profile
Rsm	μm	197.9616	187.2283	Mean spacing of profile irregularities of roughness profile

7.3.7 Four-dimensional X-ray microscopy

The 4D X-ray microscopy was performed by scanning both fouled membranes at 360 degrees. Triplicate scans were carried out at 4x and 20x magnifications. Fig. 7.8(a) shows the membrane attached to the CP/Pt cathode and, from the lateral view, the presence of bacterial debris along with macromolecule deposition can be seen. The front view shows the uneven deposition of bacterial debris and EPS. The clear black embossed impressions are from current collector material that did not encounter M9 media. Fig. 7.8(b) shows the Nafion membrane attached to the CP/PANi-Cu cathode and, in this case, the lateral view shows a smoother deposition in comparison to the Nafion attached to the CP/Pt cathode. The smooth deposition was also observed in the front view. In the auxiliary view, the EPS deposition was denser than observed for the Nafion membrane of the CP/Pt cathode. These observations clearly demonstrate that membrane fouling is more pronounced in the MFC which employed the CP/Pt cathode than the one with CP/PANi-Cu cathode. However, the current generation was higher with the CP/Pt cathode and, thus, suggests that the proton transfer across the membrane is not the rate limiting process in the energy conversion.

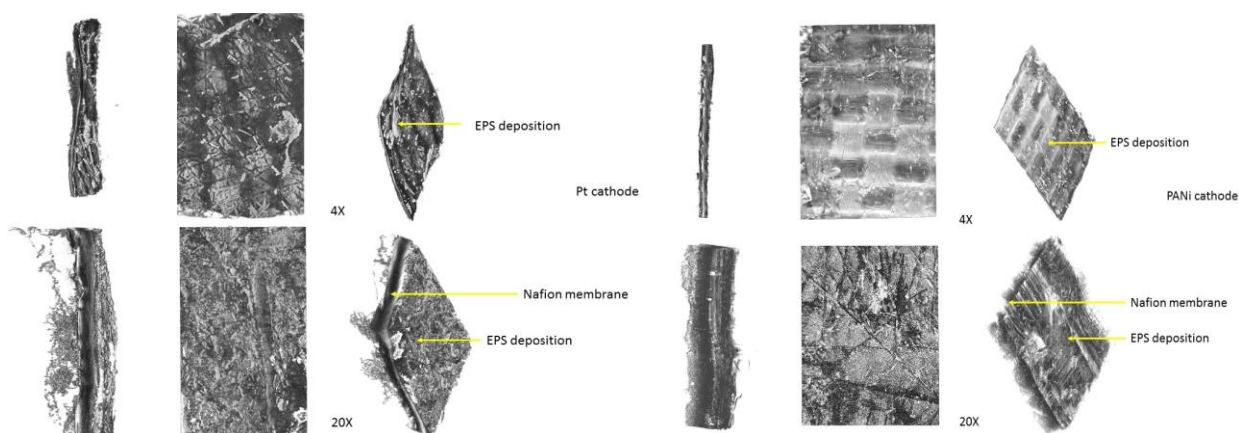


Fig. 7.8 4D X-Ray micrograph of Nafion membrane attached to CP/Pt and CP/Cu-PANi cathodes.

7.3.8 Attenuated Total Reflectance Fourier Transformed Infrared Spectroscopy

Attenuated total reflectance Fourier transformed infrared spectroscopy (ATR-FITR) is a non-destructive tool for analysis of biofilm formation based on the fingerprints of biomolecules, such as proteins, nucleic acids, and polysaccharides. The FTIR spectra for CP/Pt and CP/PANi-Cu cathodes are shown in Fig. 7.9(a) and (b), respectively. This approach is therefore useful for the detection of accumulated biomass [44–46]. The FTIR spectra of both membranes from the CP/Pt

and CP/PANi-Cu cathodes revealed the presence of polysaccharides. The peaks at 2961 cm^{-1} assigned to CH_3 , 2925 cm^{-1} to CH_2 , 2897 cm^{-1} to CH tertiary, 2874 cm^{-1} to CH_3 , and 2854 cm^{-1} to CH_2 are all principal compounds of cell membranes' fatty chains [45]. The peak at 1631 cm^{-1} in the spectrum for the Pt membrane and 1638 cm^{-1} for the PANi-Cu membrane are assigned to Amide I ($\nu\text{C}=\text{O}$ coupled with $\delta\text{N-H}$), $\delta\text{H}_2\text{O}$. These are markers of proteins and water molecules which is the major component of the membrane, flagella, pili, and cytoplasm [45]. The peak at 1545 cm^{-1} for the Pt membrane and at 1535 cm^{-1} for the PANi-Cu membrane are assigned to Amide II ($\delta\text{N-H}$ coupled with $\nu\text{C-N}$) which is a principal compound of proteins. The peak at 1401 cm^{-1} for both membranes are assigned to $\nu_s\text{COO}^-$ which is a signature of Amino acids, fatty acid chains and mostly composed of peptidoglycan. The peaks at 1232 and 1260 cm^{-1} are assigned to phosphodiester, phospholipids, lipopolysaccharides (LPS), and nucleic acids which are the major component of membranes and nucleoid [45].

FTIR spectra of the membranes attached to CP/Pt and CP/PANi-Cu cathodes revealed the presence of polysaccharides and nucleic acids ($1,600$ to 900 cm^{-1}), as well as the presence of proteins, lipids, and polysaccharides (3700 to 3000 cm^{-1}). The spectra have variances both in shape and in absorbance intensity, indicating that there was variation in the composition and quantity of each component. The peaks obtained for both protein and polysaccharides are substantially higher for membranes attached to the CP/Pt cathode than with the CP/PANi-Cu cathode. These were deposited from the organic substrate as well as the bacterial biomass. Interestingly, a low level of lipids was also observed in the CP/Pt cathode Nafion membrane, whereas the lipid peaks were slightly intense in the CP/PANi-Cu cathode membrane. Water permeation and water intake in the Nafion membrane have been reported in previous studies [36–38].

It has been elucidated that the Nafion NRE - 212 has water membrane permeabilities (k_w) of 4.09 at room temperature ($23\text{ }^\circ\text{C}$ used in the experiment) [47]. Moreover, the water flux was higher in the NRE - 212 than, N - 1035, N - 115, and N - 1110 [47]. However, another study suggested that the permeation coefficients may not be dependent on membrane thickness as long as the feed side is in contact with liquid water [38]. In MFCs where proton transfer from the anode to cathode is facilitated via PEM (Nafion), it was observed that the interfacial proton transport enhances the water permeation through the hydrophilic phase of the Nafion membrane [38]. The M9 media interacted readily with the interface of the Nafion membrane, and PtC nanoparticles from the Pt cathode since one side of the GDL is exposed to the anode. In contrast, the MFC with the CP/Cu-

CP/PANi-Cu cathode does not react with a metal catalyst. It is clear from the 3D profilometric images, and FTIR of the Nafion attached to both cathodes that they show variable biofouling. The CP/Pt cathode exhibited higher biofouling than the CP/PANi-Cu cathode. Reith et al. [48] elucidated that a biofilm which contained abundant platinum group elements nanoparticles was mostly dominated by Proteobacteria. Intestinal electrogenic bacterial communities predominantly belong to α -, β -, γ - or δ -proteobacteria [49]. From the FTIR data, it was clear that the CP/Pt cathode displayed higher and more complex macromolecule signatures than the CP/PANi-Cu cathode. The lower degree of biofouling on the CP/PANi-Cu cathode suggests that the use of the Pt air cathode enhances the membrane biofouling. Ultimately, biofouling deteriorates the performance of the MFC by increasing the mass transfer resistance to the system over time [50,51]. Therefore, our study suggests that the Pt catalyst may not be suitable for long-term and practical MFC operation if used with an Al current collector. It is possible that the use of a more robust, but cheap current collector may give a different outcome, and this will be considered in future studies.

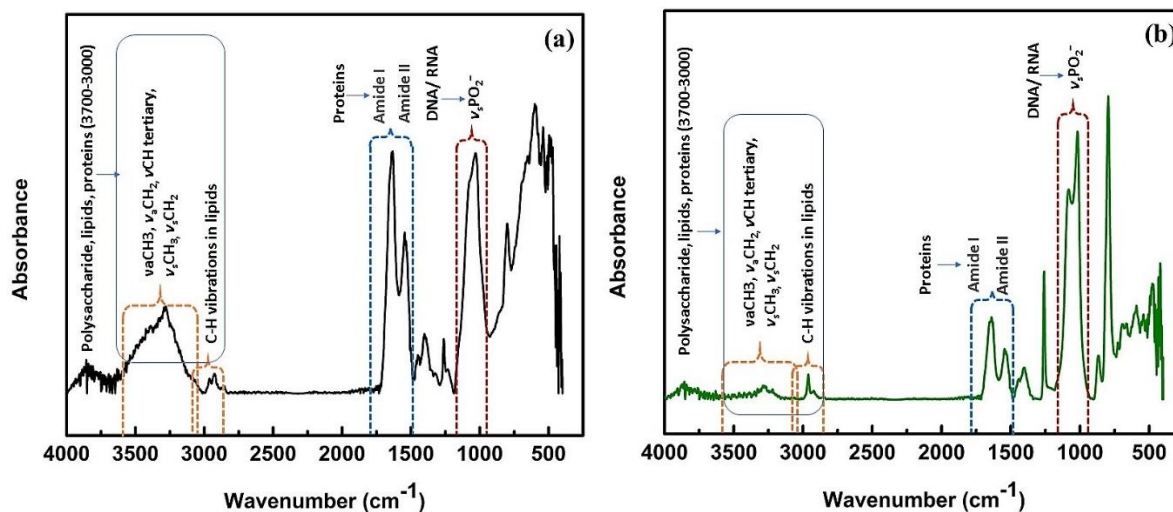


Fig. 7.9 ATR-FTIR spectra of Nafion membrane attached to CP/Pt and CP/PANi-Cu cathodes.

7.4 Conclusion

The use of an electro synthesised PANi-Cu composite on a carbon paper has demonstrated to be a cost-effective substitute for the use of expensive Pt-based cathodes for MFCs. The CP/PANi-Cu cathode is relatively cheap and easy to prepare for about 1 % of the cost of a Pt catalyst. The loss of cathodic activity with both cathodes after nine cycles of the MFC operation by 46 % and 71 % for CP/Pt and CP/PANi-Cu cathode, respectively. Most of the cathodic performance loss is contributed by an aluminum oxide layer on the aluminum current collector which hinders the interfacial charge transfer from the cathode to an external circuit. The loss of cathodic activity can be suppressed by a coating of PANi-Cu on the current collector. The CP/Pt cathode was surprisingly found to be more prone to the biofouling of the Nafion membrane and may lead to the deterioration of performance in long-term MFC operations. The FTIR analysis of fouled membranes revealed that there are more complex macromolecules on the membrane attached to the CP/Pt cathodes supporting the biofouling of the Nafion membrane over a period. Biofouling may hinder the proton transfer from the anode compartment to the triple phase boundary of MEA for the cathodic reaction. Further studies are vital to improve the efficacy of the CP/PANi-Cu cathode and gain a solid understanding of the membrane biofouling. We are conducting additional investigations into these two critical aspects.

References

- [1] S. Bajracharya, K. Vanbroekhoven, C.J.N. Buisman, D. Pant, D.P.B.T.B. Strik, Application of gas diffusion biocathode in microbial electrosynthesis from carbon dioxide, *Environ. Sci. Pollut. Res.* 23 (2016) 22292–22308. doi:10.1007/s11356-016-7196-x.
- [2] M. Ma, S. You, J. Qu, N. Ren, Natural eggshell membrane as separator for improved coulombic efficiency in air-cathode microbial fuel cells, *RSC Adv.* 6 (2016) 66147–66151. doi:10.1039/C6RA13052F.
- [3] S. Cheng, H. Liu, B.E. Logan, Power densities using different cathode catalysts (Pt and CoTMPP) and polymer binders (Nafion and PTFE) in single chamber microbial fuel cells, *Environ. Sci. Technol.* 40 (2006) 364–369. doi:10.1021/es0512071.
- [4] S. Mateo, F.J. Fernandez-Morales, P. Cañizares, M.A. Rodrigo, Influence of the Cathode Platinum Loading and of the Implementation of Membranes on the Performance of Air-Breathing Microbial Fuel Cells, *Electrocatalysis.* 8 (2017) 442–449. doi:10.1007/s12678-017-0393-7.
- [5] H. Yuan, L. Deng, Y. Qi, N. Kobayashi, J. Tang, Nonactivated and Activated Biochar Derived from Bananas as Alternative Cathode Catalyst in Microbial Fuel Cells, *Sci. World J.* 2014 (2014) 832850. doi:10.1155/2014/832850.
- [6] M. Kodali, C. Santoro, A. Serov, S. Kabir, K. Artyushkova, I. Matanovic, P. Atanassov, Air Breathing Cathodes for Microbial Fuel Cell using Mn-, Fe-, Co- and Ni-containing Platinum Group Metal-free Catalysts, *Electrochim. Acta.* 231 (2017) 115–124. doi:10.1016/j.electacta.2017.02.033.
- [7] X. Li, B. Hu, S. Suib, Y. Lei, B. Li, Manganese dioxide as a new cathode catalyst in microbial fuel cells, *J. Power Sources.* 195 (2010) 2586–2591. doi:10.1016/j.jpowsour.2009.10.084.
- [8] R. Kumar, L. Singh, A.W. Zularisam, Enhanced oxygen reduction reaction in air-cathode microbial fuel cells using flower-like Co₃O₄ as an efficient cathode catalyst, *Int. J. Hydrogen Energy.* 42 (2017) 19287–19295. doi:10.1016/j.ijhydene.2017.06.065.
- [9] M. Kodali, R. Gokhale, C. Santoro, A. Serov, K. Artyushkova, P. Atanassov, High Performance Platinum Group Metal-Free Cathode Catalysts for Microbial Fuel Cell (MFC), *J. Electrochem. Soc.* 164 (2017) H3041–H3046. doi:10.1149/2.0061703jes.

- [10] P.N. Venkatesan, S. Dharmalingam, Synthesis and characterization of Pt, Pt_{1-x}Fe_x/TiO₂ cathode catalysts and its evaluation in microbial fuel cell, *Mater. Renew. Sustain. Energy*. 5 (2016) 11. doi:10.1007/s40243-016-0074-0.
- [11] B. Bladergroen, H. Su, S. Pasupathi, V. Linkov, Overview of Membrane Electrode Assembly Preparation Methods for Solid Polymer Electrolyte Electrolyzer, in: *Electrolysis*, 2012. doi:10.5772/52947.
- [12] M. Klingele, M. Breitwieser, R. Zengerle, S. Thiele, Direct deposition of proton exchange membranes enabling high performance hydrogen fuel cells, *J. Mater. Chem. A*. 3 (2015) 11239–11245. doi:10.1039/C5TA01341K.
- [13] S. Erkan, I. Eroglu, Ultrasonic Spray Coating Technique for High-Performance PEM Fuel Cell Electrode Manufacturing, in: *Prog. Clean Energy, Vol. 2 Nov. Syst. Appl.*, Springer International Publishing, Cham, 2015: pp. 481–492. doi:10.1007/978-3-319-17031-2_34.
- [14] S.B. Park, Y. il Park, Fabrication of gas diffusion layer (GDL) containing microporous layer using fluorinated ethylene propylene (FEP) for proton exchange membrane fuel cell (PEMFC), *Int. J. Precis. Eng. Manuf.* 13 (2012) 1145–1151. doi:10.1007/s12541-012-0152-x.
- [15] M.D. Gasda, R. Teki, T.-M. Lu, N. Koratkar, G.A. Eisman, D. Gall, Sputter-Deposited Pt PEM Fuel Cell Electrodes: Particles vs Layers, *J. Electrochem. Soc.* 156 (2009) B614. doi:10.1149/1.3097188.
- [16] Y. Show, Y. Ueno, Formation of Platinum Catalyst on Carbon Black Using an In-Liquid Plasma Method for Fuel Cells, *Nanomaterials*. 7 (2017) 31. doi:10.3390/nano7020031.
- [17] J. Ahmed, H.J. Kim, S. Kim, Polyaniline Nanofiber/Carbon Black Composite as Oxygen Reduction Catalyst for Air Cathode Microbial Fuel Cells, *J. Electrochem. Soc.* 159 (2012) 497–501. doi:10.1149/2.049205jes.
- [18] Y. Ren, D. Pan, X. Li, F. Fu, Y. Zhao, X. Wang, Effect of polyaniline-graphene nanosheets modified cathode on the performance of sediment microbial fuel cell, *J. Chem. Technol. Biotechnol.* 88 (2013) 1946–1950. doi:10.1002/jctb.4146.
- [19] C. Cao, L. Wei, G. Wang, J. Liu, Q. Zhai, J. Shen, A polyaniline-derived iron–nitrogen–carbon nanorod network anchored on graphene as a cost-effective air-cathode electrocatalyst for microbial fuel cells, *Inorg. Chem. Front.* (2017). doi:10.1039/C7QI00452D.

- [20] X. Tang, H. Li, Z. Du, H.Y. Ng, Polyaniline and iron based catalysts as air cathodes for enhanced oxygen reduction in microbial fuel cells, *RSC Adv.* 5 (2015) 79348–79354. doi:10.1039/C5RA16148G.
- [21] Y. Yuan, J. Ahmed, S. Kim, Polyaniline/carbon black composite-supported iron phthalocyanine as an oxygen reduction catalyst for microbial fuel cells, *J. Power Sources.* 196 (2011) 1103–1106. doi:10.1016/j.jpowsour.2010.08.112.
- [22] L. Fu, S.-J. You, G.-Q. Zhang, F.-L. Yang, X.-H. Fang, Z. Gong, Biosensors and Bioelectronics PB / PANI-modified electrode used as a novel oxygen reduction cathode in microbial fuel cell, *Biosens. Bioelectron.* 26 (2011) 1975–1979. doi:10.1016/j.bios.2010.08.061.
- [23] S.A. Ansari, N. Parveen, H. Han, O. Ansari, Fibrous polyaniline @ manganese oxide nanocomposites as supercapacitor electrode materials and cathode catalysts for improved, *Phys. Chem. Chem. Phys.* 18 (2016) 9053–9060. doi:10.1039/C6CP00159A.
- [24] Y. Jiang, Y. Xu, Q. Yang, Y. Chen, S. Zhu, S. Shen, Power generation using polyaniline/multi-walled carbon nanotubes as an alternative cathode catalyst in microbial fuel cells, *Int. J. Energy Res.* 38 (2014) 1416–1423. doi:10.1002/er.3155.
- [25] S. Khilari, S. Pandit, J.L. Varanasi, D. Das, D. Pradhan, Bifunctional Manganese Ferrite/Polyaniline Hybrid as Electrode Material for Enhanced Energy Recovery in Microbial Fuel Cell, *ACS Appl. Mater. Interfaces.* 7 (2015) 20657–20666. doi:10.1021/acsami.5b05273.
- [26] G.H. Kim, K.S. Eom, M.J. Kim, S.J. Yoo, J.H. Jang, H.J. Kim, E.A. Cho, Design of an Advanced Membrane Electrode Assembly Employing a Double-Layered Cathode for a PEM Fuel Cell, *ACS Appl. Mater. Interfaces.* 7 (2015) 27581–27585. doi:10.1021/acsami.5b07346.
- [27] J.M. Sonawane, S. Al-Saadi, R.K. Singh, P.C. Ghosh, S.B. Adeloju, Exploring the use of polyaniline-modified stainless steel plates as low-cost, high-performance anodes for microbial fuel cells, *Electrochim. Acta.* (2018). doi:10.1016/j.electacta.2018.01.163.
- [28] J.M. Sonawane, S.A. Patil, P.C. Ghosh, S.B. Adeloju, Low-cost stainless-steel wool anodes modified with polyaniline and polypyrrole for high-performance microbial fuel cells, *J. Power Sources.* 379 (2018) 103–114. doi:10.1016/j.jpowsour.2018.01.001.
- [29] J.M. Sonawane, E. Marsili, P. Chandra Ghosh, Treatment of domestic and distillery

- wastewater in high surface microbial fuel cells, *Int. J. Hydrogen Energy*. 39 (2014) 21819–21827. doi:10.1016/j.ijhydene.2014.07.085.
- [30] J.M. Sonawane, S.B. Adeloju, P.C. Ghosh, Landfill leachate: A promising substrate for microbial fuel cells, *Int. J. Hydrogen Energy*. (2017). doi:10.1016/j.ijhydene.2017.03.137.
- [31] F. Harnisch, C. Koch, S.A. Patil, T. Hübschmann, S. Müller, U. Schröder, Revealing the electrochemically driven selection in natural community derived microbial biofilms using flow-cytometry, *Energy Environ. Sci.* 4 (2011) 1265. doi:10.1039/c0ee00605j.
- [32] Y. Liu, F. Harnisch, K. Fricke, R. Sietmann, U. Schröder, Improvement of the anodic bioelectrocatalytic activity of mixed culture biofilms by a simple consecutive electrochemical selection procedure, *Biosens. Bioelectron.* 24 (2008) 1006–1011. doi:10.1016/j.bios.2008.08.001.
- [33] R. Silva, D. Voiry, M. Chhowalla, T. Asefa, Efficient metal-free electrocatalysts for oxygen reduction: Polyaniline-derived N- and O-doped mesoporous carbons, *J. Am. Chem. Soc.* 135 (2013) 7823–7826. doi:10.1021/ja402450a.
- [34] C. Santoro, B. Li, P. Cristiani, G. Squadrito, Power generation of microbial fuel cells (MFCs) with low cathodic platinum loading, *Int. J. Hydrogen Energy*. 38 (2013) 692–700. doi:10.1016/j.ijhydene.2012.05.104.
- [35] N. Gospodinova, L. Terlemezyan, Conducting polymers prepared by oxidative polymerization: polyaniline, *Prog. Polym. Sci.* 23 (1998) 1443–1484. doi:10.1016/S0079-6700(98)00008-2.
- [36] A. Narębska, S. Koter, W. Kujawski, Ions and water transport across charged nafion membranes. Irreversible thermodynamics approach, *Desalination*. 51 (1984) 3–17. doi:10.1016/0011-9164(84)85048-1.
- [37] F. Volino, M. Pineri, A.J. Dianoux, A. De Geyer, Water mobility in a water-soaked nafion® membrane: A high-resolution neutron quasielastic study, *J. Polym. Sci. Polym. Phys. Ed.* 20 (1982) 481–496. doi:10.1002/pol.1982.180200310.
- [38] P. Majsztik, A. Bocarsly, J. Benziger, Water permeation through nafion membranes: the role of water activity, *J. Phys. Chem. B.* 112 (2008) 16280–16289. doi:10.1021/jp804197x.
- [39] R. Racicot, R. Brown, S.C. Yang, Corrosion protection of aluminum alloys by double-strand polyaniline, *Synth. Met.* 85 (1997) 1263–1264. doi:10.1016/S0379-6779(97)80232-9.
- [40] M. Pontié, S. Ben Rejeb, J. Legrand, Anti-microbial approach onto cationic-exchange

- membranes, *Sep. Purif. Technol.* 101 (2012) 91–97. doi:10.1016/j.seppur.2012.09.022.
- [41] M. Miskan, M. Ismail, M. Ghasemi, J. Md Jahim, D. Nordin, M.H. Abu Bakar, Characterization of membrane biofouling and its effect on the performance of microbial fuel cell, *Int. J. Hydrogen Energy.* 41 (2016) 543–552. doi:10.1016/j.ijhydene.2015.09.037.
- [42] G. Pasternak, J. Greenman, I. Ieropoulos, Regeneration of the power performance of cathodes affected by biofouling, *Appl. Energy.* 173 (2016) 431–437. doi:10.1016/j.apenergy.2016.04.009.
- [43] J.M. Sonawane, A. Gupta, P.C. Ghosh, Multi-electrode microbial fuel cell (MEMFC): A close analysis towards large scale system architecture, *Int. J. Hydrogen Energy.* 38 (2013) 5106–5114. doi:10.1016/j.ijhydene.2013.02.030.
- [44] F. Humbert, F. Quilès, In-situ study of early stages of biofilm formation under different environmental stresses by ATR-FTIR spectroscopy, in: *Sci. against Microb. Pathog. Commun. Curr. Res. Technol. Adv.*, 2011: pp. 889–895. <http://www.formatex.info/microbiology3/book/889-895.pdf> (accessed September 20, 2017).
- [45] F. Quilès, F. Humbert, A. Delille, Analysis of changes in attenuated total reflection FTIR fingerprints of *Pseudomonas fluorescens* from planktonic state to nascent biofilm state, *Spectrochim. Acta - Part A Mol. Biomol. Spectrosc.* 75 (2010) 610–616. doi:10.1016/j.saa.2009.11.026.
- [46] J.J. Ojeda, M. Dittrich, Fourier transform infrared spectroscopy for molecular analysis of microbial cells, *Methods Mol. Biol.* 881 (2012) 187–211. doi:10.1007/978-1-61779-827-6_8.
- [47] Q. Duan, H. Wang, J. Benziger, Transport of liquid water through Nafion membranes, *J. Memb. Sci.* 392–393 (2012) 88–94. doi:10.1016/j.memsci.2011.12.004.
- [48] F. Reith, C.M. Zammit, S.S. Shar, B. Etschmann, R. Bottrill, G. Southam, C. Ta, M. Kilburn, T. Oberthür, A.S. Ball, J. Brugger, Biological role in the transformation of platinum-group mineral grains, *Nat. Geosci.* 9 (2016) 294–298. doi:10.1038/ngeo2679.
- [49] B.E. Logan, J.M. Regan, Electricity-producing bacterial communities in microbial fuel cells, *Trends Microbiol.* 14 (2006) 512–518. doi:10.1016/j.tim.2006.10.003.
- [50] S. Kondaveeti, R. Kakarla, H.S. Kim, B. goon Kim, B. Min, The performance and long-term stability of low-cost separators in single-chamber bottle-type microbial fuel cells,

- Environ. Technol. (United Kingdom). (2017) 1–10. doi:10.1080/09593330.2017.1299223.
- [51] J. Xu, G.-P. Sheng, H.-W. Luo, W.-W. Li, L.-F. Wang, H.-Q. Yu, Fouling of proton exchange membrane (PEM) deteriorates the performance of microbial fuel cell, *Water Res.* 46 (2012) 1817–1824. doi:10.1016/j.watres.2011.12.060.

Chapter 8

A highly efficient microbial fuel cell stack for enhanced power generation and treatment of a landfill leachate

[To be submitted as, JM Sonawane, R Goenka, PC Ghosh, SB Adeloju, A highly efficient microbial fuel cell stack for enhanced power generation and treatment of a landfill leachate, Materials Today, Elsevier]

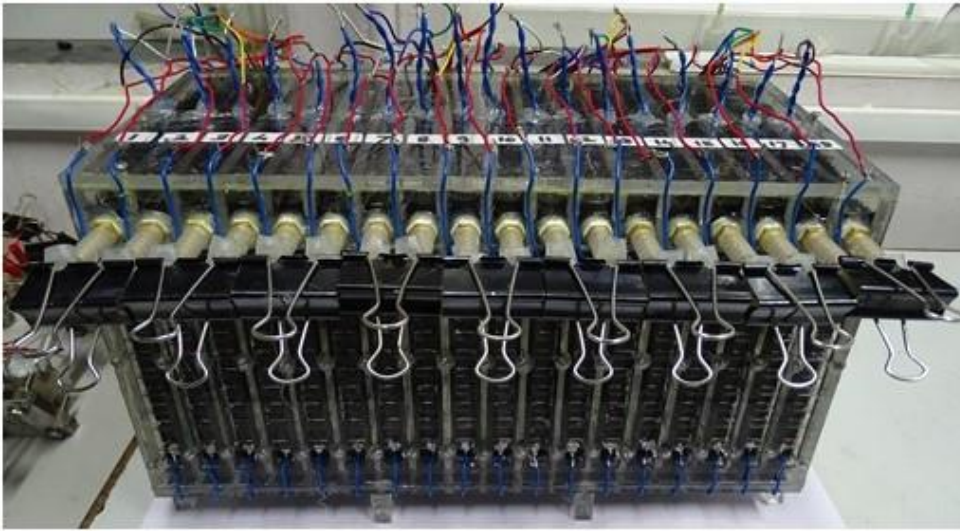
Nomenclature:

μ	Biomass yield
b	Constant [$\text{gm A}^{-1}\text{d}^{-1}\%$]
$\text{COD}(0)$	Initial COD [mg L^{-1}]
$\text{COD}(t)$	COD at the time t [mg L^{-1}]
F	Faraday's constant [C mol^{-1}]
i_{av}	Average current during period t [mA]
M	Molecular weight of oxygen [gm]
n	Number of electrons exchanged per mole of oxygen reduction
η_{col}	Coulombic efficiency
q_s	Maximum specific substrate consumption
R	Resistor [Ω]
V	Volume of the anode chamber (Litre)
y	Maximum specific growth rate
$\Delta\text{COD}(t)$	Total COD removal in t days [mg]
$\Delta\text{COD}_{\text{cu}\%}(t)$	Cumulative COD removal efficiency (%) after time t
$\Delta\text{COD}_{\text{cu}}(t)$	Cumulative COD removal after time t [mg L^{-1}]
η	Coulombic efficiency [%]

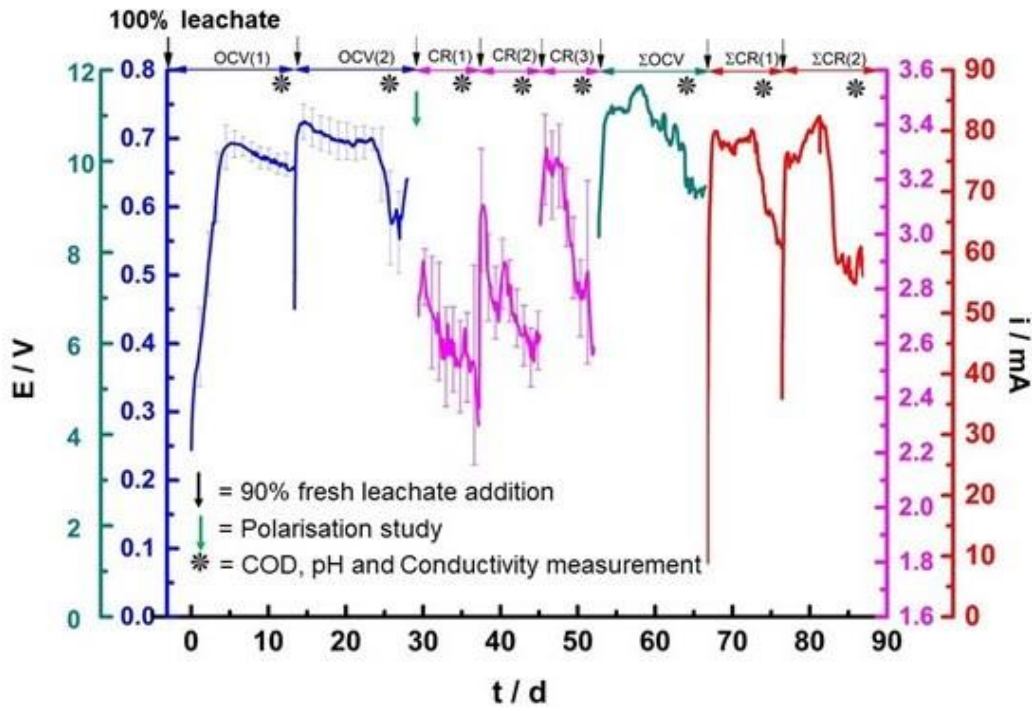
Abbreviations:

Ag/AgCl	Silver Silver chloride
ANi	Aniline
CE	Coulombic efficiency
COD	Chemical oxygen demand
LSV	Linear sweep voltammetry
MEA	Membrane electrode assemblies
MFCs	Microbial fuel cells
OCV	Open circuit voltage
PANi	Polyaniline
SS/PANi-W	Stainless coated polyaniline wool

Graphical abstract



↑
Microbial fuel cell stack



↑
85 days Performance

Abstract

One of the major challenges in achieving large-scale energy generation from microbial fuel cells (MFCs) is the need to develop suitable high-performance anode materials and implementable system architecture. In this study, we have demonstrated that this can be accomplished by designing a modified system architecture to improve the performance of a MFC based on the use of stainless steel wool coated with polyaniline (SS/PANi-W) and a half membrane electrode assembly air cathode. The stack composed of eighteen separate cells, each supported by three air-cathodes to reduce the internal resistance of the system. The stack was tested with landfill leachate for 85 days by operation in four phases at ambient condition. The first two batch cycles involved the operation of the reactor in an open circuit voltage mode (OCV) and, thus, permit measurement of the OCV of an individual cell. The starting average OCV ranged from 210 ± 30 mV to 695 ± 25 mV with a significant lag phase. Transient lag, log phase was observed in the OCV cycle, and an average of 665 ± 5 mV stable voltage was obtained for each cell, lasting for ten days followed by a decline phase. In the second phase of the investigation, a 10-ohm resistor was applied to each cell and then operated for three cycles. The average current obtained for the first, second and third cycle were 2.6 ± 0.4 , 3.1 ± 0.5 , 3.2 ± 0.5 mA cm⁻², respectively. In third and fourth phases, all cells were connected in series and tested for overall OCV and current generation. The achieved maximum OCV was 12.8 V, and the total current generated were 78 and 83 mA for the first and second parallel current cycles, respectively. Furthermore, a chemical oxygen demand (COD) removal from the leachate during the OCV mode was 79.7%, whereas COD removal of 87.0% and 86.3% were accomplished in the current generation mode from the first and second cycle, respectively. An average Coulombic efficiency (η) of 28.9 ± 1.8 , 23.4 ± 0.9 and 22.7 ± 0.4 from the first, second and third cycles, respectively. Furthermore, 35.3 and 36.9% operated in series connection from the first and second cycle, respectively. This study demonstrates that the developed stack can be deployed in wastewater treatment train for real-time energy production from wastewater treatment.

8.1 Introduction

With the growing global population, a massive volume of wastewater is being generated by industries and households. The cost of treating the wastewaters are increasing, while at the same time more and more areas are experiencing a shortage of water. Furthermore, the treatment of wastewaters is often cost-intensive due to the energy requirements [1]. A solution to the emerging problems with the growing volumes of wastewaters and the energy requirements for wastewater treatment can be realised by deployment of effective microbial fuel cell (MFC) technology [2–4]. Although this technology has been under consideration for wastewater treatment for about two decades, its wider use and commercialisation has been hindered by high material costs [5,6] and low efficiencies [7,8]. To be more acceptable, necessary improvements must be made to enable MFCs to produce sufficient electricity to cater for the power requirements of the wastewater treatment facility itself to make the process self-sustainable [9,10]. Unless such self-sustainability is possible, it is difficult to attract more extensive use and commercial interest in MFCs. Some researchers have recently reported improvements in the power generation by MFCs and their capabilities for accomplishing wastewater treatment, but there is still a rather large gap between these laboratory scale demonstrations and the expectations to achieve commercial viability [11,12].

To bridge this gap, different system architecture and MFC configurations have been explored, including single chamber MFC [13], dual chamber MFC [14], benthic MFC [15], tubular type MFC [16,17], upflow MFC [18,19], flat-plate MFC [20] and stack MFC [21–23]. However, to generate adequate power, the development of efficient MFC stack by multiple connections of MFCs in series or parallel is highly desirable for achieving a high voltage and high current. To achieve this goal, various MFC stacks have recently been developed to treat wastewaters and generate improved power [22,24–28]. Two of these studies [22,24] employed synthetic wastewaters with MFC stacks to develop strategies for improving power generation. In one study [24], a 45 L MFC stack system was developed to achieve continuous production of energy from a glass fiber-reinforced plastic and ceramic separator with a multielectrode assembly. The maximum power generated was 14.28 mW, while also removing 84% COD from the synthetic wastewater and using sucrose as a carbon source [24]. In the other study, a four-cell MFC stack was employed with pure glucose as carbon source and *Saccharomyces cerevisiae* as a biocatalyst. The current and power densities generated were 6447 mA m⁻² and 2003 mW m⁻², respectively, with a 22%

Coulombic efficiency (CE) [22]. Only a few MFC [25] stacks have been explored with real wastewater, such as distillery wastewater [21], ethanolamine wastewater [25], domestic wastewater [20,29], kitchen wastewater [23], and swine wastewater [30]. Among these, a multi-electrode microbial fuel cell (MEMFC) was developed, based on the anaerobic baffled reactor, to treat distillery wastewater, achieving a power density of 0.059 mW cm^{-2} with 43% COD removal, and 23% CE [21]. In another study [25], a dual anode/cathode MFC stack was developed to treat ethanolamine wastewater and continuously generate electricity. In a stack of eight MFCs in series, the maximum power density produced was 0.086 mW cm^{-2} and 96.05% COD removal was achieved. Another MFC stack design based on the use of an ionic liquid-type membrane-cathode assembly achieved a maximum power density of 12.3 W m^{-2} and 60% COD removal, with a lower feed flow rate [26]. It was noted that the parallel electrode connection provides a stable ORP. The highest power density of 420 mW m^{-2} (12.8 W m^{-3}) was accomplished in series flow and parallel connection mode at an organic loading rate of $25.6 \text{ g COD L}^{-1} \text{ d}^{-1}$ (HRT of 0.33 h), with a COD removal efficiency of 44% [27].

Among the various MFC designs, one was crafted with a dual gas diffusion cathode design for the treatment of dark fermentation effluent [28]. The stack achieved 2.12 V and 3.16 W m^{-3} with a CE of 9.85% and about 82% COD removal [28]. In another study [23], five chambers MFCs were hydraulically connected for integration into a sink drainage-pipe for kitchen wastewater treatment. An average OCV of 3.44 V and a maximum power density of 809 mW m^{-2} was achieved with a CE of 78.2%. A tubular air-cathode MFC stack was also used for the treatment of swine wastewater [30]. The reactor was tested with 1.2 kg and 4.9 kg COD/ m^3d loading. This stack design produced a maximum power density of 17.5 mW cm^{-2} and achieved 83 % COD removal with a CE of 0.3%. [30].

In an effort to achieve a considerable improvement in performance, we propose, in this study, the use of an MFC stack with eighteen independent cells stacked together to a volume of $\sim 7.5 \text{ L}$ in a batch mode operation. The anode employed in the is polyaniline modified stainless steel wool which we recently reported [31,32] and the half-cell membrane electrode assembly is an air cathode. Landfill leachate will be used to investigate the electrochemical performance of the MFC stack system by recording current generation, COD removal, and Coulombic efficiency.

8.2 Materials and Methods

8.2.1 Construction of MFC stack

The stacked MFC system considered in this study consisted of 18 individual MFCs stacked in series. The MFCs are fabricated by using transparent acrylic sheets of 6 mm thickness. The inner dimensions of the individual cell are 16 cm x 1.5 cm x 17 cm. Each cell is fitted with a pair of nozzles on opposite walls to allow inlet and outlet of the batch. The three adjacent walls of the cell (excluding the top) are accompanied by slits with dimensions of 13.3 cm x 1 cm x 3 sides (39.9 cm²). These slots are provided to allow the Nafion coated carbon cathode to be in contact with air. The cavity of the cell is filled with polyaniline coated stainless steel wool, acting as the anode. The free bed volume of the stacked MFC is 408 mL. Total empty bed volume of the cell is 7.34 L. The outer dimensions of the assembly was 38 cm x 17.4 cm x 18.5 cm. After making electrical connections, the three adjacent walls were sandwiched by acrylic sheets with similar slots to provide support for the structure and was secured with screws. 3 cm acrylic legs were placed to raise the base by offering aid to ensure air contact with the base air-cathode. Experimental setup of the 18 unit MFC stack is shown in Fig. 8.1.

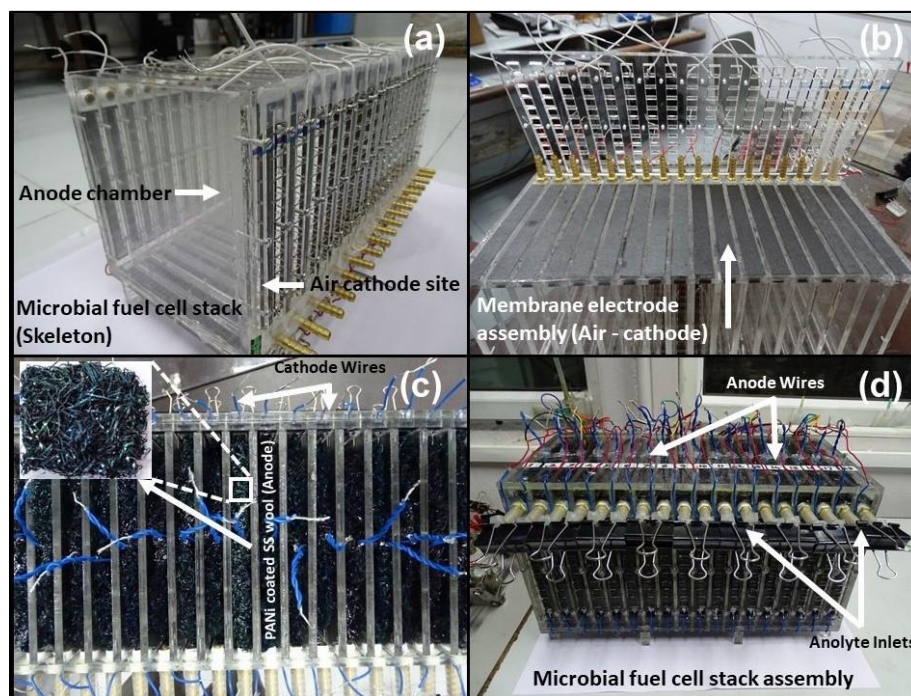


Fig. 8.1 Experimental setup of the 18 unit MFC stack. (a) top view of air cathode, (b) air cathode sandwiched in PANi-coated wool, (c) top view of anode wool in each cell, and (d) complete assembly of MFC stack.

8.2.2 Polyaniline (PANi) anode preparation

SS wool (domestic grade, Scotch-Brite, India) was used as base anode material (projected surface area of 700 cm^2). The measured thickness of SS wool (SS-W) was $26.66 \pm 3.34 \text{ }\mu\text{m}$, and the density was 2.39 gm cm^{-3} . The SS-W was subjected to ultrasonication for 15 minutes in acetone to degrease before electropolymerisation. A miniature saturated Ag/AgCl (sat. KCl) was used as the reference electrode (RRPEAGCL, Pine Research Instrumentation, USA). The counter electrode used for electrochemical experiments was a titanium mesh (Amac, Australia). The electropolymerisation was performed as previously described [31,32] with a potentiostat (SP150, BioLogic, France) equipped with an EC-Lab 10.44 software. For electropolymerisation of aniline on SS wool, reagent grade aniline and nitric acid (Sigma-Aldrich, India) were used. PANi was synthesised by application of a constant current of 2.5 mA cm^{-2} in 0.4 M ANi in 0.7 M nitric acid for 15 min. All solutions were purged with nitrogen for 15 min to remove oxygen before the commencement of polymerisation.

8.2.3 Cathode fabrication

The air cathodes were prepared by following a previously reported method [33]. Briefly, fine platinised (Vulcan XC-72) carbon powder, Pt content of 20% w/w (Sigma-Aldrich, Australia), was coated on a $15 \text{ cm} \times 10 \text{ cm}$ commercial carbon paper (GDS 210, CeTech, Taiwan). The Pt loading was kept at 0.5 mg cm^{-2} by using 5% Nafion solution as a binder (Sigma-Aldrich, Australia). All coated electrodes were dried in a hot air oven at $60 \text{ }^\circ\text{C}$ for 6 h to ensure complete dryness. Subsequently, the dry cathodes were hot pressed on one side using Nafion NRE-212 (Sigma-Aldrich, Australia) under 10 kg cm^{-2} at $140 \text{ }^\circ\text{C}$ for 3 min using a hot press (Model no., Carver Inc., USA). Prepared membrane electrode assemblies (MEA) were cut into $15 \text{ cm} \times 1 \text{ cm}$ (projected surface area 15 cm^2 , but the actual exposed surface was 13 cm^2). The cathode was connected with a wire by using a silver paste, which forms the cathodic connection.

8.2.4 Operation

MFCs were fed with landfill leachate, collected from the landfill site at Turbhe (Navi Mumbai, India) and the initial pH, conductivity and COD were 7.6, 11.36 mS, 2273 mg L^{-1} , respectively. All experiments were conducted at ambient temperature: $26 \pm 3 \text{ }^\circ\text{C}$. The landfill leachate was purged with N_2 for 30 min before inoculation, and the individual cells were purged with N_2 for 10

min after inoculation to promote the growth of the primary activity of obligate anaerobes and minimise aerobic degradation of organic matter. The present MFC were operated for 85 days in a fed-batch mode (by refilling 90 % of the spent landfill leachate with fresh after every batch cycle) in four distinct stages. In the first stage, each of the 18 cells were operated under open circuit conditions for two batch cycles of 13 days each [OCV(1) & OCV(2)], i.e., a total of 26 days. This was done to establish a biofilm on the anodes without any external load [33]. In the second stage, from the 27th day, a 10 Ω external resistor was connected to each of the cells, individually and operated in three batch cycles of 7 days each [CR(1), CR(2) & CR(3)], i.e., a total of 21 days. The individual current generation from each of the cells was thus determined. In the third stage, from the 49th day, all the cells were connected in series and operated under open circuit conditions for 16 days [Σ OCV] to ascertain the maximum voltage generation capability of the MFC stack. In the fourth stage, from the 65th day, a 10 Ω external resistor was connected to all the cells connected in series to investigate the total current generation from the system, for two batch cycles of 10 days each [Σ CR(1) & Σ CR(2)], i.e., a total of 20 days.

8.2.5 Analytics and Calculations

Open circuit voltage (OCV) measurements were done at 30-minute intervals using a data logger (GL820, Graphtec Instruments, USA) in the OCV(1), OCV(2) and Σ OCV batch cycles. In the CR(1), CR(2), CR(3), Σ CR(1) & Σ CR(2) batch cycles, the voltage was recorded across the 10 Ω external resistor by the same data logger. The current was calculated by Ohm's law, and the current and power generation data were normalised by the projected surface area of the cathode (39.9 cm²).

All electrochemical experiments and further data processing were conducted using the same potentiostat (SP150, BioLogic, France) fitted with EC-Lab V 10.44 software. Current and power density curves were obtained using linear sweep voltammetry (LSV) recorded at a scan rate of 1 mV s⁻¹ in a potential window from OCV to short circuit. These were measured after completion of the OCV(2) batch cycle when a stable voltage was observed. For quality control of MFC stack, the cell resistances were calculated using current interrupt resistance to ensure each has similar cathodic resistance.

8.2.6 Physicochemical characterisation of leachate

The pH and conductivity of the leachate before and after being fed into the MFC were measured using a pH meter (111, PCI Analytics, India) and a conductivity meter (EQ660A, Equip-Tronics, India), respectively. Chemical Oxygen Demand (COD) measurement was carried out as per the standard closed reflux titrimetric method – 5220C [34], using a COD Incubator (DRB200, Hach, India). The elemental composition of the leachate was measured using Inductively Coupled Plasma - Atomic Emission Spectrometry (ICP- AES) The pH and conductivity of the leachate before and after being fed into the MFC were measured using a pH meter (111, PCI Analytics, India) and a conductivity meter (EQ660A, Equip-Tronics, India), respectively. Chemical Oxygen Demand (COD) measurement was carried out as per the standard closed reflux titrimetric method – 5220C [34], using a COD Incubator (DRB200, Hach, India). The elemental composition of the leachate was measured using Inductively Coupled Plasma - Atomic Emission Spectrometry (ICP- AES) (ARCOS, Simultaneous ICP Spectrometer, SPECTRO Analytical Instruments GmbH, Germany). The measurements were done before and after being fed into the MFC.

(ARCOS, Simultaneous ICP Spectrometer, SPECTRO Analytical Instruments GmbH, Germany). The measurements were done before and after being fed into the MFC.

8.2.6.1 Chemical Oxygen Demand & Coulombic Efficiency

Chemical Oxygen Demand (COD) was carried out as per the standard closed titrimetric reflux method – 5220C [34], using a COD Incubator (DRB200, Hach, India). The subsequent equations, 2.1 and 2.2 [21,33], are used to calculate collective COD removal efficiency in percentage and the Coulombic efficiency (η_{col}) respectively:

$$\Delta COD_{cu\%}(t) = \frac{COD(0) - COD(t)}{COD(0)} \times 100 \quad [2.1]$$

where,

$\Delta COD_{cu\%}(t)$ is cumulative COD removal efficiency (%) after time t

$COD(0)$ is initial COD ($mg L^{-1}$) at the time of feeding the reactor

and, $COD(t)$ is the COD ($mg L^{-1}$) at the time of sampling.

$$\eta_{col} = \frac{M \int_0^t i \cdot dt}{F \cdot n \cdot V \cdot \Delta COD_{cu}(t)} \times 100 \quad [2.2]$$

where,

η_{col} is the Coulombic efficiency

M is the molecular weight (gm) of oxygen

F is Faraday's constant

n represents the number of electrons exchanged per mole of oxygen

V is the volume of the anode chamber (L)

$\Delta\text{COD}_{\text{cu}}(t)$ is the cumulative COD removal in time t

8.3 Results and Discussions

8.3.1 Bioelectrocatalytic performance

The first two OCV cycles ensure the formation of electrogenic biofilm on the anode [35]. It has been suggested that the biofilm formed under OCV condition, increased COD removal [35]. It is well known that the transfer of enriched electroactive culture to the new MFC shorten start-up time (less than ten days) and accelerate power generation [36]. Nevertheless, start-up time can be decreased polyaniline based anode materials, and high bacterial load fed [37,38].

The proposed MFC stack in this study was operated under ambient condition. Throughout the duration of the investigation, the temperature fluctuated between 23 and 29°C. In this mesophilic temperature range, the bacteria are most active and will often result in an excellent MFC performance [39]. Therefore, the proposed MFC stack can be used in the tropical and subtropical region where there is insignificant temperature fluctuation.

8.3.1.1 Individual cell operation

During the first stage of operation [Figure 8.2 (a)], OCV(1) and OCV(2) batch cycles, an OCV of 0.18 – 0.34 V was obtained, but this rose to 0.672 – 0.714 V on the 4th day of operation and then declined slowly. On the 13th day of operation, the voltage declined to between 0.635 – 0.687 V for all the cells. At this stage, 90% of all cells from stack were emptied to leave 10% acclimatised bacterial communities on the anode surface, and then fresh leachate was added to start the next cycle. The initial OCV obtained with the addition of the fresh leachate was between 0.331 – 0.502 V and, thus, indicative the development of a biofilm in the anode chambers, as planned. The peak OCV of 0.664 – 0.742 V was observed on the 15th day of operation and remained stable for up to the 23rd day. The slow decline during the first OCV cycle is indicative of a lower depletion rate of organic matter. In contrast, the fast deterioration of OCV in the second cycle in each cell from the 24th day is indicative of a rapid reduction of organic material in the leachate, as illustrated in Fig.

8.2(a).

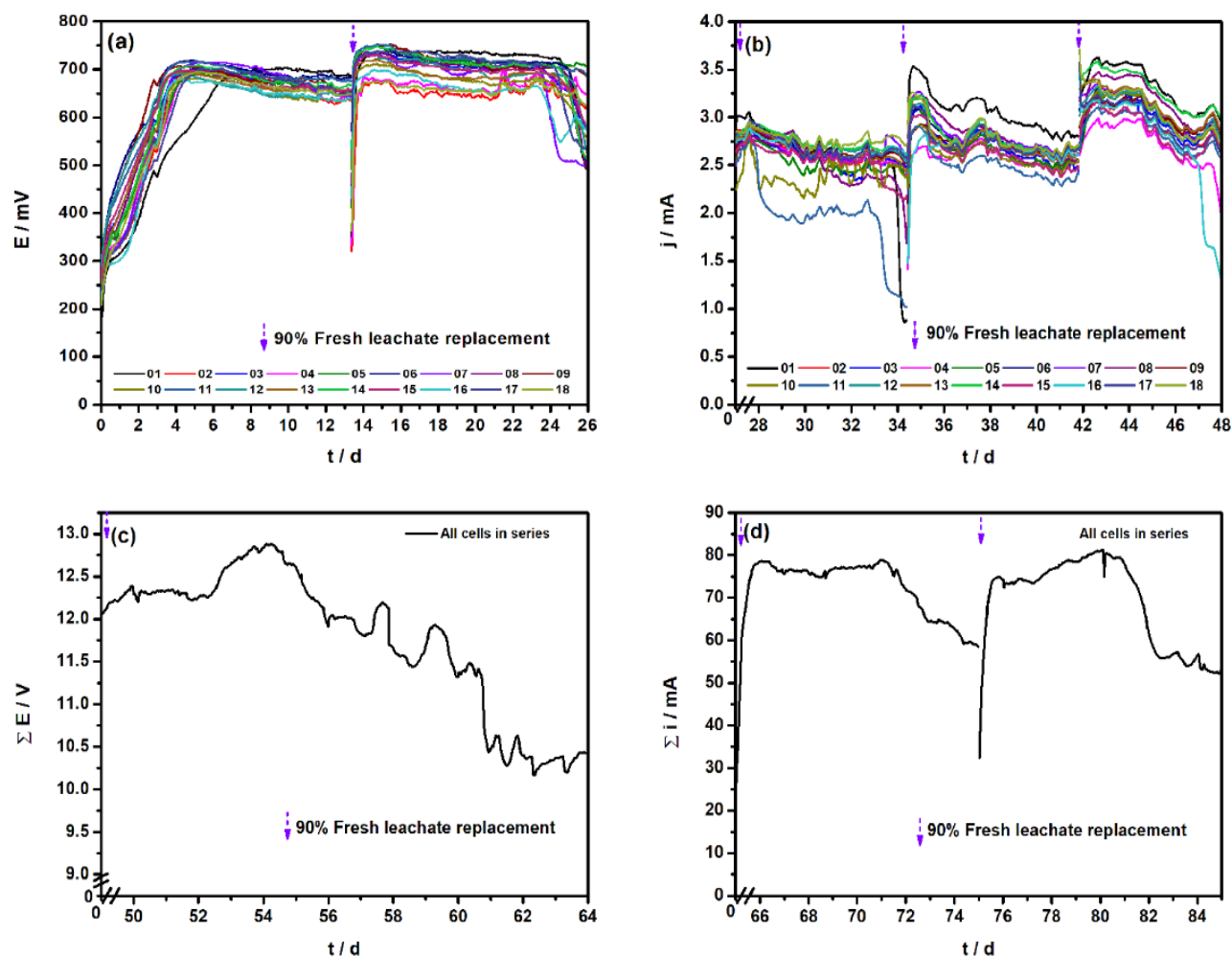


Fig. 8.2 Variation in the bioelectrocatalytic performance of the cells in a) the first stage with two open circuit voltage cycles, b) the second stage with three constant resistance cycles, c) the third stage with one open circuit voltage cycle of the stack, and d) the fourth stage with two constant resistance cycles of the stack.

In the first cycle (CR(1)) of the second stage [Figure 8.2 (b)], the observed current from each cell was in between 0.055 to 0.072 mA cm⁻². However, an immediate decline was observed. In the second cycle (CR(2)), observed currents were between 0.067 to 0.085 mA cm⁻², and they remained stable for a short duration. Better stability in the peak currents (for ~3 days) was observed in the third cycle (CR(3)), where initially the currents were in between 0.072 to 0.090 mA cm⁻². This

indicates that in the CR(1) & CR(2) cycles, the microbes in the MFCs get better acclimatized and deliver better performance (current) in the subsequent CR(3) cycle.

8.3.1.2 Stacked cell operation

In the third stage of the study, (Σ OCV cycle), a maximum OCV of 12.8 V was obtained for the stacked cell on the 6th day of operation, but it gradually decreased after that. Similar to the first stage, the Σ OCV cycle was also followed by two closed-circuit operation cycles (Σ CR(1) & Σ CR(2)) with a R_{ext} of 10 Ω .

A substantially lower start-up time of a few hours [Figure 8.2 (d)], was observed in these Σ CR(1) & Σ CR(2) cycles which may be attributed to the fact that the biofilm development on the anode was significant. A maximum total current observed was 78 mA, and it remained stable for another six days of the operation followed by a gradual decline. The performance in the Σ CR(2) cycle was very much similar to the Σ CR(1) cycle with high and stable currents.

8.3.1.3 Polarisation behaviour

The power output from each cell was determined from the polarisation curves [Figure 8.3]. The short circuit current densities and the maximum power density for the individual cells ranged from 1.77 to 3.34 mA cm⁻² and 0.22 to 0.45 mW cm⁻², respectively. A comparison of these cell performances with those reported in previous studies is provided in Table 8.1. Evidently, the polyaniline (PANi) modified stainless steel wool demonstrated improved MFC performance on the basis of achieved power density than most other stacked anode cells. The performance of the PANi-modified stack was affected by many kinetic losses. The low electrolyte conductivity of the leachate contributed to significant losses in the performance. The dominance of activation, ohmic loss, and mass transfer was manifested in the entire range of operation. The internal resistance of the cells (from the slope of polarisation curve) ranged between 7.11 and 8.55 Ω , with an overall average of $7.83 \pm 0.72 \Omega$ for all cells.

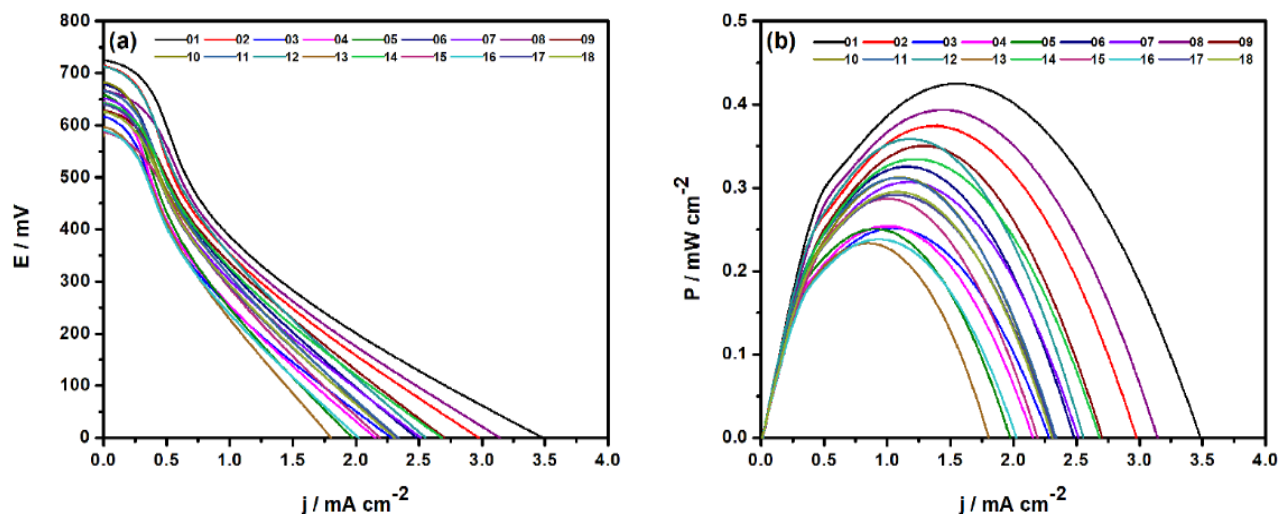


Fig. 8.3 Polarisation behaviour of the individual cell in a stack a) current density b) power density.

8.3.2 Physicochemical analysis

8.3.2.1 Chemical oxygen demand and Coulombic Efficiency

The reduction of chemical oxygen demand (COD) during the operation of the stack in the OCV mode was found to be 79.74%, but with treatment in the successive Σ CR(1) & Σ CR(2) cycles a better COD removals of 87.04 % and 86.27 % were obtained, as illustrated in Fig. 8.4. However, the achieved COD removal is less than the 94.76% achieved by aerobic treatment of the landfill leachate Nevertheless, the COD removal achieved in this study is still considerable and it is much higher than achieved with the individual cell [Fig. 8.4(a)]. Also, when compared to previous studies, the achieved COD removal is reasonable [Table 8.1].

Successive operation cycles in the OCV and the constant resistance modes improved the COD removal efficiency of the cell operation, and this is indicative of the role of biofilm formation on the anode in the active removal of COD [35]. It is also worth noting that the operation of the entire cells as a stack was performed after the cells were operated individually, which gave better performance in terms of current and voltage [Fig. 8.3], as well as COD removal [Fig. 8.4]. The improvement in COD removal by successive current cycle over OCV mode may be attributed to the high metabolic activity of electrogenic bacteria. It was obvious that the COD removal rate is low when the reactor operates under OCV mode.

The Coulombic efficiency (η_{col}) was found to be 35.30 and 36.93 % [Fig. 8.5(b)] operated in the $\Sigma CR(1)$ and $\Sigma CR(2)$ cycles respectively. An average Coulombic efficiency (η_{col}) of 28.86 ± 1.82 %, 23.38 ± 0.88 % and 22.71 ± 0.42 % was obtained in the CR(1), CR(2) & CR(3) cycles respectively. The achieved CE is better than obtained in previous studies, as demonstrated by the data in Table 8.1. The progressive increase in η from CR(1) cycle to CR(3) cycle is indicative of the adaptation of the electrogenic bacterial consortia on the anodes.

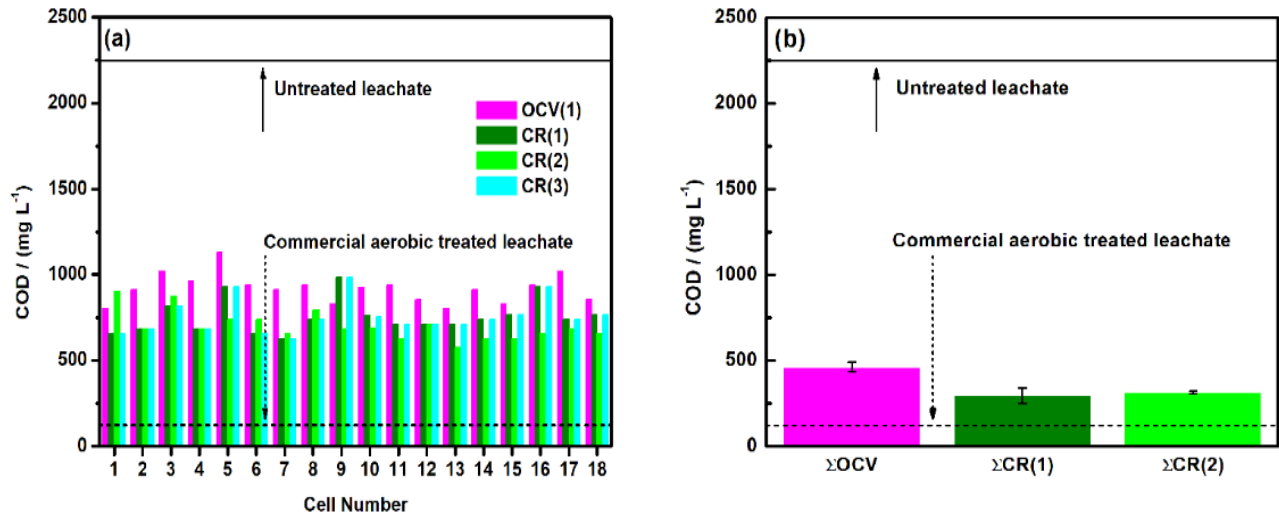


Fig. 8.4 COD removal from landfill leachate a) COD removal from individual cells b) COD of initial landfill leachate, treated from the landfill leachate treatment plant, COD removal from OCV cycle, current cycle one and current cycle two.

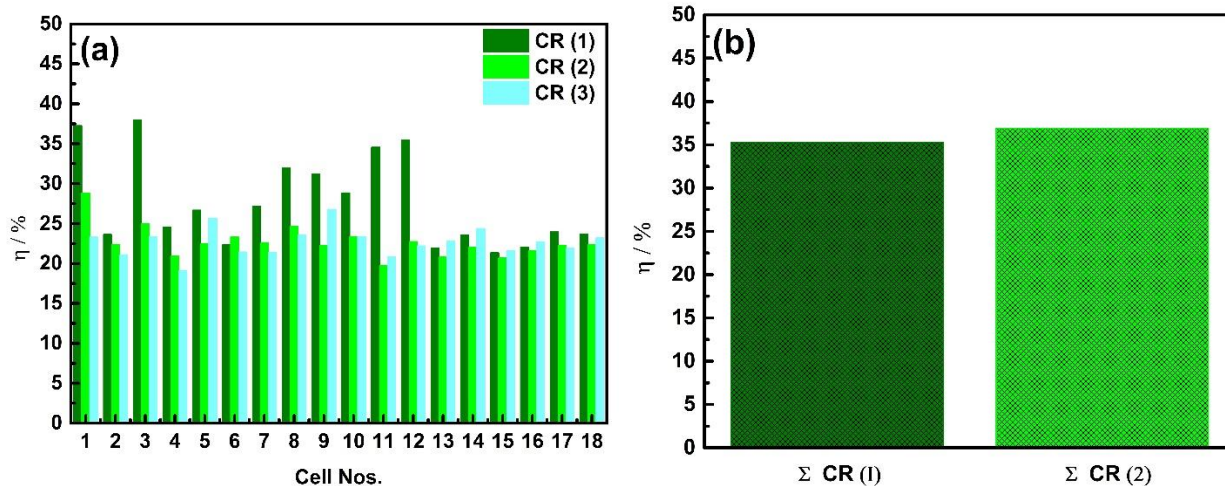


Fig. 8.5 Coulombic efficiency of the MFC stack a) individual cells for cycle 1, 2, and 3 for each cells b) all the cells operated as a stack after the various cycles of operation.

8.3.2.2 pH, conductivity and elemental composition

The pH and conductivity of the leachate did not vary much over successive cycles when the cells were operated individually, as illustrated in Fig. 8.6(a) to (e) and no significant difference was observed among the individual cells. The pH remained close to neutral for all the individual cells, as well as when operated as a stack. However, the conductivity decreased when the cell was operated as a stack in the constant resistance mode (Σ CR(1) & Σ CR(2) cycles), as illustrated in Figure 8.6(f). This may be due to the much larger current flowing into the cell which resulted in a change in the chemical composition of the leachate, such as in the concentration of metals. The commercial aerobically treated leachate is found to have a minimum concentration of metals [Fig. 8.7] and also the lowest conductivity [Fig. 8.6(f)]. A similar trend is observed with the leachate treated in the (Σ CR(1) & Σ CR(2) cycles with a stack. The metal concentration is lower than that of the untreated leachate and the leachate used in the Σ OCV cycle operation with a stack [Fig. 8.7], and the conductivity was also low [Fig.8.6(f)].

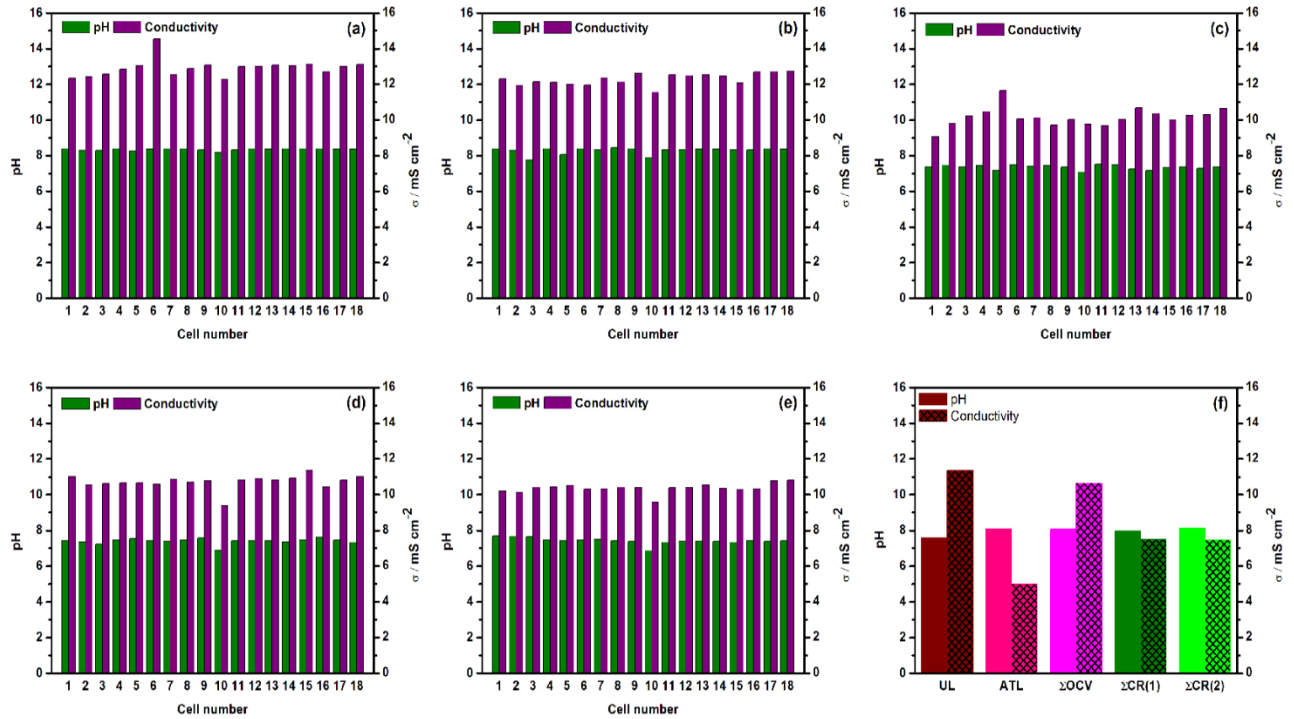


Fig. 8.6 Variation in pH and conductivity of individual cells after (a) OCV(1) cycle, (b) OCV(2) cycle, (c) CR(1) cycle, (d) CR(2) cycle, $\Sigma\text{CR}(3)$ cycle, and (f) various cycles of operation as a stack [UL-Untreated leachate, ATL-Commercial aerobic treated leachate].

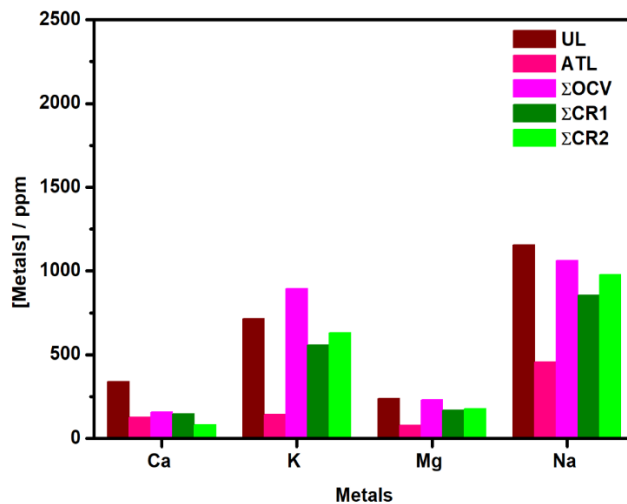


Fig. 8.7 Elemental composition of leachate; UL-untreated leachate, ATL-aerobic treated leachate, OCV-leachate from open circuit voltage, CR (1) – leachate from constant resistor cycle1 and CR (2) – leachate from constant resistor cycle 2.

8.3.3 Comparison with previous work

Several MFC stacks have been made by several research groups for treatment of various real and synthetic wastewaters [40,41]. The reported performances are summarised in Table 8.1 for comparison with the 18-cell MFC stack with SS/PANi-W and air cathode used in our study. The reactors are compared on the basis of reactor volume, type of wastewater, power generation, COD removal, and CE. The cell volume ranges from 0.112 to 72 L. The proposed 18-cell reactor achieved a power density of 0.43 mW cm^{-2} . In contrast, a tubular MFC and a 8 anode/cathode MFC achieved power densities of 17.5 mW cm^{-2} and 17.63 mW cm^{-2} , with swine wastewater [30] and sucrose [24], respectively. However, the COD removal was comparable to that achieved with the proposed 18-cell stack.

Table 8.1 Comparison with previous works

Reactor type/ Identification	No. of cells	Total volume (L)	Type of wastewater	Anode	Cathode	Power density (mW cm ⁻²)	COD removal (%)	CE (%)	Reference
Multielectrode MFC	6	3.270	Distillery wastewater	Flexible graphite sheets	Air cathode	0.059	43	23	[21]
Dual anode/cathode MFC	9	1.000	Ethanolamine wastewater	Carbon cloth	Carbon cloth	0.086	96	NA	[25]
Air cathode MFC	4	0.112	primary sediment effluent	Graphite fibre brush	Carbon cloth	0.042	44	13	[27]
Stacked MFC	3	72.00	Synthetic wastewater	Granular activated carbon	Granular activated carbon	5.09*	97	NA	[42]
VITO-CoRE™ MFC	3	0.550	Dark fermentation effluent	Carbon cloth	VITO- CoRE™	0.002	60	9	[28]
Paper based MFC stack	4	NA	Luria Bertani medium	screen- printed carbon	screen- printed carbon	0.0012	NA	NA	[43]
Pluggable MFC	3	3**	Synthetic wastewater	Activated carbon cloth	Air cathode	0.0142	94	35	[44]
Self-sustainable MFC	40	0.020	Activated sewage sludge	Plain carbon veil	Plain carbon veil	0.127*	NA	0.018	[45]

Cubic stack MFC	4	0.350	Glucose	Graphite plates	Graphite plates	0.2003	NA	22	[22]
Tubular MFC	5	0.295	Swine wastewater	Graphite felt	Air cathode	17.5	83	0.3	[30]
Two chamber MFC	5	1.765	Synthetic wastewater	Carbon cloth	Carbon cloth	0.080	NA	78	[23]
8 Anode/cathode	8	45	Sucrose	Carbon felt + SS [‡]	Carbon felt	17.63 [§]	69	NA	[24]
Polyaniline wool anode MFC	18	7.344	Landfill leachate	Polyaniline modified stainless steel wool	Air cathode	0.43	85	37	Present work

* Volumetric power density (mW cm⁻³)

** Stack is placed in the container

[‡]SS = Stainless steel

[§] Total power

8.4 Conclusion

We have successfully fabricated and tested an 18-cell stacked MFC with PANi-modified stainless steel anode and an air cathode. The investigation of the stacked cell with landfill leachate achieved maximum OCPs from each cell ranging from 0.67 to 0.71 V. However, a total open circuit voltage of 12.8 V (average 0.711 V from the individual cell) was achieved with the stacked cells. It is clear that the three side Pt air cathodes adjacent to PANi wool anode design provide an efficient proton transfer from the anode to the membrane. The proposed MFC stack achieved COD removals ranging from 86.27 to 87.04% when operated in the CR mode. The CEs of 35.30 and 36.93% obtained with the MFC stack from cycles 1 and 2, respectively, are better/comparable to those obtained in previous studies illustrated in Table 8.1. The efficient operation under ambient condition confirms that the architecture suitable for operation in the tropical regions. The achieved performances of reactor demonstrate that the stacked MFCs can be deployed in landfill leachate site for power generation and effective COD treatment.

References

- [1] M.P. Shah, Industrial Wastewater Treatment: A Challenging Task in the Industrial Waste Management, *Adv. Recycl. Waste Manag.* 01 (2017) 1–11. doi:10.4172/2475-7675.1000115.
- [2] J.M. Sonawane, A. Yadav, P.C. Ghosh, S.B. Adeloju, Recent advances in the development and utilization of modern anode materials for high performance microbial fuel cells, *Biosens. Bioelectron.* 90 (2017) 558–576. doi:10.1016/j.bios.2016.10.014.
- [3] C. Feng, C.C. Tsai, C.Y. Ma, C.P. Yu, C.H. Hou, Integrating cost-effective microbial fuel cells and energy-efficient capacitive deionization for advanced domestic wastewater treatment, *Chem. Eng. J.* 330 (2017) 1–10. doi:10.1016/j.cej.2017.07.122.
- [4] S. Wu, W. He, W. Yang, Y. Ye, X. Huang, B.E. Logan, Combined carbon mesh and small graphite fiber brush anodes to enhance and stabilize power generation in microbial fuel cells treating domestic wastewater, *J. Power Sources.* 356 (2017) 348–355. doi:10.1016/j.jpowsour.2017.01.041.
- [5] M. Rahimnejad, A. Adhami, S. Darvari, A. Zirepour, S.E. Oh, Microbial fuel cell as new technology for bioelectricity generation: A review, *Alexandria Eng. J.* 54 (2015) 745–756. doi:10.1016/j.aej.2015.03.031.
- [6] M. Zhou, M. Chi, J. Luo, H. He, T. Jin, An overview of electrode materials in microbial fuel cells, *J. Power Sources.* 196 (2011) 4427–4435. doi:10.1016/j.jpowsour.2011.01.012.
- [7] M. Kherat, M. Hariti, N. Mameri, A.H. Badi, E. Harrach, A. Algiers, Comparison of the chemical removal rates of a low cost microbial fuel cell and an aerated activated sludge bioreactor, and evaluation of its performances, *Rev. Des Energies Renouvelables.* 17 (2014) 2–279. http://www.cder.dz/download/Art17-2_9.pdf (accessed October 3, 2017).
- [8] H. Yang, M. Zhou, M. Liu, W. Yang, T. Gu, Microbial fuel cells for biosensor applications, *Biotechnol. Lett.* 37 (2015) 2357–2364. doi:10.1007/s10529-015-1929-7.
- [9] W.-W. Li, H.-Q. Yu, Z. He, Towards sustainable wastewater treatment by using microbial fuel cells-centered technologies, *Energy Environ. Sci.* 7 (2014) 911–924. doi:10.1039/c3ee43106a.
- [10] Y. Dong, Y. Feng, Y. Qu, Y. Du, X. Zhou, J. Liu, A combined system of microbial fuel cell and intermittently aerated biological filter for energy self-sufficient wastewater treatment, *Sci. Rep.* 5 (2016) 18070. doi:10.1038/srep18070.

- [11] B.E. Logan, M.J. Wallack, K.Y. Kim, W. He, Y. Feng, P.E. Saikaly, Assessment of Microbial Fuel Cell Configurations and Power Densities, *Environ. Sci. Technol. Lett.* 2 (2015) 206–214. doi:10.1021/acs.estlett.5b00180.
- [12] F. Zhang, Z. Ge, J. Grimaud, J. Hurst, Z. He, Long-term performance of liter-scale microbial fuel cells treating primary effluent installed in a municipal wastewater treatment facility, *Environ. Sci. Technol.* 47 (2013) 4941–4948. doi:10.1021/es400631r.
- [13] S. Cheng, W. Liu, J. Guo, D. Sun, B. Pan, Y. Ye, W. Ding, H. Huang, F. Li, Effects of hydraulic pressure on the performance of single chamber air-cathode microbial fuel cells, *Biosens. Bioelectron.* 56 (2014) 264–270. doi:10.1016/j.bios.2014.01.036.
- [14] H.F. Cui, L. Du, P.B. Guo, B. Zhu, J.H.T. Luong, Controlled modification of carbon nanotubes and polyaniline on macroporous graphite felt for high-performance microbial fuel cell anode, *J. Power Sources.* 283 (2015) 46–53. doi:10.1016/j.jpowsour.2015.02.088.
- [15] J.J. Guzman, K.G. Cooke, M.O. Gay, S.E. Radachowsky, P.R. Girguis, M.A. Chiu, Benthic Microbial Fuel Cells: Long-Term Power Sources for Wireless Marine Sensor Networks, *Proc. SPIE Defense, Secur. Sens.* (2010) 76662M–76662M–12. doi:10.1117/12.854896.
- [16] J. Li, C. Liu, Q. Liao, X. Zhu, D. Ye, Improved performance of a tubular microbial fuel cell with a composite anode of graphite fiber brush and graphite granules, *Int. J. Hydrogen Energy.* 38 (2013) 15723–15729. doi:10.1016/j.ijhydene.2013.05.067.
- [17] Q. Liao, J. Zhang, J. Li, D. Ye, X. Zhu, B. Zhang, Increased performance of a tubular microbial fuel cell with a rotating carbon-brush anode, *Biosens. Bioelectron.* 63 (2015) 558–561. doi:10.1016/j.bios.2014.08.014.
- [18] Z. He, S.D. Minter, L.T. Angenent, Electricity generation from artificial wastewater using an upflow microbial fuel cell, *Environ. Sci. Technol.* 39 (2005) 5262–5267. doi:10.1021/es0502876.
- [19] Z.Z. Ismail, A.J. Jaeeel, Sustainable power generation in continuous flow microbial fuel cell treating actual wastewater: Influence of biocatalyst type on electricity production, *Sci. World J.* 2013 (2013) 713515. doi:10.1155/2013/713515.
- [20] B. Min, B.E. Logan, Continuous electricity generation from domestic wastewater and organic substrates in a flat plate microbial fuel cell., *Environ. Sci. Technol.* 38 (2004) 5809–5814. doi:10.1021/Es0491026.
- [21] J.M. Sonawane, A. Gupta, P.C. Ghosh, Multi-electrode microbial fuel cell (MEMFC): A

- close analysis towards large scale system architecture, *Int. J. Hydrogen Energy*. 38 (2013) 5106–5114. doi:10.1016/j.ijhydene.2013.02.030.
- [22] M. Rahimnejad, A.A. Ghoreyshi, G.D. Najafpour, H. Younesi, M. Shakeri, A novel microbial fuel cell stack for continuous production of clean energy, *Int. J. Hydrogen Energy*. 37 (2012) 5992–6000. doi:10.1016/j.ijhydene.2011.12.154.
- [23] D. Ye, B. Deng, J. Li, W. Zou, C. Ke, Z. Yuan, X. Zhu, Q. Liao, Electricity production of a microbial fuel cell stack integrated into a sink drain pipe, *Res. Chem. Intermed.* 42 (2016) 7689–7700. doi:10.1007/s11164-016-2654-0.
- [24] A.N. Ghadge, D.A. Jadhav, M.M. Ghangrekar, Wastewater treatment in pilot-scale microbial fuel cell using multielectrode assembly with ceramic separator suitable for field applications, *Environ. Prog. Sustain. Energy*. 35 (2016) 1809–1817. doi:10.1002/ep.12403.
- [25] B.M. An, Y. Heo, H.A. Maitlo, J.Y. Park, Scaled-up dual anode/cathode microbial fuel cell stack for actual ethanalamine wastewater treatment, *Bioresour. Technol.* 210 (2016) 68–73. doi:10.1016/j.biortech.2016.01.108.
- [26] M.J. Salar-García, V.M. Ortiz-Martínez, Z. Baicha, A.P. de los Ríos, F.J. Hernández-Fernández, Scaled-up continuous up-flow microbial fuel cell based on novel embedded ionic liquid-type membrane-cathode assembly, *Energy*. 101 (2016) 113–120. doi:10.1016/j.energy.2016.01.078.
- [27] J. Choi, Y. Ahn, Continuous electricity generation in stacked air cathode microbial fuel cell treating domestic wastewater, *J. Environ. Manage.* 130 (2013) 146–152. doi:10.1016/j.jenvman.2013.08.065.
- [28] S.B. Pasupuleti, S. Srikanth, S. Venkata Mohan, D. Pant, Continuous mode operation of microbial fuel cell (MFC) stack with dual gas diffusion cathode design for the treatment of dark fermentation effluent, *Int. J. Hydrogen Energy*. 40 (2015) 12424–12435. doi:10.1016/j.ijhydene.2015.07.049.
- [29] Y. Ahn, B.E. Logan, Effectiveness of domestic wastewater treatment using microbial fuel cells at ambient and mesophilic temperatures, *Bioresour. Technol.* 101 (2010) 469–475. doi:10.1016/j.biortech.2009.07.039.
- [30] L. Zhuang, Y. Zheng, S. Zhou, Y. Yuan, H. Yuan, Y. Chen, Scalable microbial fuel cell (MFC) stack for continuous real wastewater treatment, *Bioresour. Technol.* 106 (2012) 82–88. doi:10.1016/j.biortech.2011.11.019.

- [31] J.M. Sonawane, S.A. Patil, P.C. Ghosh, S.B. Adeloju, Low-cost stainless-steel wool anodes modified with polyaniline and polypyrrole for high-performance microbial fuel cells, *J. Power Sources*. 379 (2018) 103–114. doi:10.1016/j.jpowsour.2018.01.001.
- [32] J.M. Sonawane, S. Al-Saadi, R.K. Singh, P.C. Ghosh, S.B. Adeloju, Exploring the use of polyaniline-modified stainless steel plates as low-cost, high-performance anodes for microbial fuel cells, *Electrochim. Acta*. (2018). doi:10.1016/j.electacta.2018.01.163.
- [33] J.M. Sonawane, E. Marsili, P. Chandra Ghosh, Treatment of domestic and distillery wastewater in high surface microbial fuel cells, *Int. J. Hydrogen Energy*. 39 (2014) 21819–21827. doi:10.1016/j.ijhydene.2014.07.085.
- [34] A.D. Eaton, L.S. Clesceri, A.E. Greenberg, M.A.H. Franson, W.E.F. American Public Health Association., American Water Works Association., Standard Methods for the Examination of Water and Wastewater, Washington, DC, American Public Health Association, 1998.
- [35] A. Larrosa-Guerrero, K. Scott, K.P. Katuri, C. Godinez, I.M. Head, T. Curtis, Open circuit versus closed circuit enrichment of anodic biofilms in MFC: Effect on performance and anodic communities, *Appl. Microbiol. Biotechnol.* 87 (2010) 1699–1713. doi:10.1007/s00253-010-2624-1.
- [36] D. Aaron, C. Tsouris, C.Y. Hamilton, A.P. Borole, Assessment of the effects of flow rate and ionic strength on the performance of an air-cathode microbial fuel cell using electrochemical impedance spectroscopy, *Energies*. 3 (2010) 592–606. doi:10.3390/en3040592.
- [37] B. Lai, X. Tang, H. Li, Z. Du, X. Liu, Q. Zhang, Power production enhancement with a polyaniline modified anode in microbial fuel cells, *Biosens. Bioelectron.* 28 (2011) 373–377. doi:10.1016/j.bios.2011.07.050.
- [38] Y. Yuan, S. Zhou, Y. Liu, J. Tang, Nanostructured macroporous bioanode based on polyaniline-modified natural loofah sponge for high-performance microbial fuel cells, *Environ. Sci. Technol.* 47 (2013) 14525–14532. doi:10.1021/es404163g.
- [39] A. Larrosa-Guerrero, K. Scott, I.M. Head, F. Mateo, A. Ginesta, C. Godinez, Effect of temperature on the performance of microbial fuel cells, *Fuel*. 89 (2010) 3985–3994. doi:10.1016/j.fuel.2010.06.025.
- [40] J. Luo, M. Chi, H. Wang, H. He, M. Zhou, Electrochemical surface modification of carbon

- mesh anode to improve the performance of air-cathode microbial fuel cells, *Bioprocess Biosyst. Eng.* 36 (2013) 1889–1896. doi:10.1007/s00449-013-0963-x.
- [41] M. Mahmoud, T.A. Gad-Allah, K.M. El-Khatib, F. El-Gohary, Power generation using spinel manganese-cobalt oxide as a cathode catalyst for microbial fuel cell applications, *Bioresour. Technol.* 102 (2011) 10459–10464. doi:10.1016/j.biortech.2011.08.123.
- [42] S. Wu, H. Li, X. Zhou, P. Liang, X. Zhang, Y. Jiang, X. Huang, A novel pilot-scale stacked microbial fuel cell for efficient electricity generation and wastewater treatment, *Water Res.* 98 (2016) 396–403. doi:10.1016/j.watres.2016.04.043.
- [43] A. Fraiwan, S. Choi, A stackable, two-chambered, paper-based microbial fuel cell, *Biosens. Bioelectron.* 83 (2016) 27–32. doi:10.1016/j.bios.2016.04.025.
- [44] H. Yazdi, L. Alzate-Gaviria, Z.J. Ren, Pluggable microbial fuel cell stacks for septic wastewater treatment and electricity production, *Bioresour. Technol.* 180 (2015) 258–263. doi:10.1016/j.biortech.2014.12.100.
- [45] P. Ledezma, A. Stinchcombe, J. Greenman, I. Ieropoulos, The first self-sustainable microbial fuel cell stack, *Phys. Chem. Chem. Phys.* 15 (2013) 2278. doi:10.1039/c2cp44548d.

Chapter 9

Conclusions and Future Directions

9.1 Conclusions

In principle, microbial fuel cells (MFCs) are promising biotechnological innovations enabling wastewater treatment with simultaneous electricity production from a range of organic substrates. However, to construct the large-scale MFC reactors commercially, several factors influence the MFC performance and need to be explored and addressed. Amongst several other parameters, the most important is electrodes, since anode and cathode play a crucial role in the overall performance. In this regard, my PhD thesis defines the development and investigation of low-cost conductive polymers coated stainless steel (SS) wool anode, and polyaniline coated cathode, which is of high importance for both the meticulous selection and development of electrode materials. It helps in the fundamental understanding as well as the incorporation in MFC stacks.

The research work is concluded in the following sections:

The growing MFC research emphasises the importance of the choice of an anode (*CHAPTER 1*), and the material from which it is made, as it a limiting factor for the effective operation of an MFC. This chapter comprehensively reviews recent advances in the construction and utilization of novel anodes for MFCs. In particular, it highlights some of the critical roles and functions of anodes in MFCs, strategies available for improving surface areas of anodes, dominant performance of stainless-steel based anode materials, and the emerging benefits of inclusion of nanomaterials. The review also demonstrates that some of the very promising materials for the large-scale MFC applications and are likely to replace conventional anodes for the development of next-generation MFC systems. Here, the hurdles to the development of commercial MFC technology are also discussed. Furthermore, the future directions in the design and selection of materials for construction and utilisation of anodes used for MFCs are also highlighted.

The microbial kinetics employed with MFCs are much sluggish than those achievable with a cathode material or cathode catalyst. The use of 3D anodes has increased power generation by several orders of magnitude compared with the use of 2D plane anodes. There is still need to improve efficiency before the large-scale power generation from wastewater can be realised. Power generation is not only based on the choice of anode material but also requires consideration of intrinsic parameters such as kinetics, internal resistance, surface anatomy and interaction of surface with biofilm. Further studies are required to address the development of cost-effective and efficient material for new renewable and sustainable MFCs, which can be deployed in wastewater

treatment plants. For five years of review of anodes materials, it was clear that the metal-based anodes are less explored. However, it was demonstrated that the stainless steel is the promising anode material for MFCs.

The chapter two demonstrates the development of highly conductive and stable polyaniline (PANi) coated stainless (SS) plates (**CHAPTER 2**) that have been successfully prepared by galvanostatic polymerisation of ANi (0.4 ANi and 0.7 M nitric acid). In this chapter, we explored the use of polyaniline (PANi) modified stainless steel plates (SS-Ps) as potential low-cost anodes for MFCs, with capability for effective promotion of microbial growth and retention of long-term stability. Careful and selective choice of acid and aniline concentrations for galvanostatic polymerisation produced highly uniform, and adherent conductive PANi coating on SS-P which is desirable for use as anodes in MFC FTIR and CV measurements confirmed the formation of emeraldine structure on the PANi coated SS-P. Electrochemical impedance spectroscopy was useful in understanding the mechanism of coating deterioration over time. The preliminary test of the SS-P/PANi anode in an MFC gave a P_{\max} of 0.078 ± 0.011 mW cm⁻², whereas SS-P anode produced a P_{\max} of 0.010 ± 0.008 mW cm⁻². Investigations are in progress to determine long-term performance to achieve maximum current from the SS-P/PANi anode and consideration of using SS wool modified with PANi to achieve a higher surface anode for more improved microbial fuel cells.

Similar to PANi, in this chapter (**CHAPTER 3**), we explored the use of polypyrrole coating on stainless steel as a basis for producing low-cost anode for MFC, with the ability to effectively promote microbial growth and retain long-term stability. To achieve this goal, we initially established the best conditions for producing a more uniform coating of stainless steel with polypyrrole by galvanostatic polymerisation of aniline by careful consideration of the use of L-(+)-Tartaric acid, as suitable electrolytes. For this, the optimum Ppy coating was formed on SS-P with 0.4 M pyrrole in 0.7 M L-(+)-Tartaric acid. The coated PPy/SS-P after immersed in 0.1 M NaCl solution and the time-dependent EIS_(TD) performed after every 24 hours' time for seven days to study the change in coating resistance. The FTIR measurements confirm the formation of PPy on SS plate. Thus, suggesting a significant difference in the longevity of the coating in both dopant media. Therefore, PPy prepared in 0.4 M Py in 0.7 M L-(+)-Tartaric acid is qualified for long-term protection to corrosive media and could be useful for MFCs anode. 3D profilometry and Bode plots revealed the mechanism of coating deterioration over the time.

The contact angle measurement with SS/PPy-P was hydrophobic and only became hydrophilic when immersed in water for few mins. The PPy coated SS-P (SS/PPy-P) was evaluated as a potential low-cost anode for MFCs in a M9media which contained 4% landfill leachate. Comparison of the SS/PPy-P anode with a pristine (uncoated) SS-P anode revealed much higher OCV_{max} of 664 ± 27 mV, j_{max} of 0.027 ± 0.002 mA cm⁻² and a P_{max} of 0.012 ± 0.009 mW cm⁻² compared with an OCV_{max} of 624 ± 47 mV, j_{max} of 0.070 ± 0.028 mA cm⁻² and P_{max} of 0.020 ± 0.023 mW cm⁻² obtained in the absence of PANi coating. Notably, during the startup phase, a 3-fold increase in current generation was achieved with SS/PPy-P over the SS-P anode. Undoubtedly, the coating of the SS-P with PPy (as SS/PPy-P) substantially improved its performance and its potential utilisation as a low-cost anode for MFCs.

Although SS material is the best anode materials for MFC but still possess several issues such as poor biocompatibility, high charge transfer resistance and high activation overpotential (**CHAPTER 4**). The electrochemical kinetic behaviour of stainless steel (SS), SS coated PANi and, SS coated PPy anodes during the enrichment of MFCs have been significantly enhanced by application of a carefully selected external resistance (R_{ext}). Pristine and modified anode system was enriched without R_{ext} ($\neq R_{ext}$), with $R_{ext}=R_{int}$ and very low R_{ext} . The effect of external resistance on their electrokinetic activities as a function of time was studied for seven days to evaluate the startup time of the system. The j_0 achieved with the use of the SS/PANi-W anode was 121% higher than with pristine SS-W anode on the fourth day of operation under Ohmic region ($R_{ext}=R_{int}$) incubation mode. Pristine SS-W and SS/PANi-W anodes exhibited similar activity upon application of external resistance. The lower R_{ct} obtained for SS/PANi-P and SS/PANi-W anodes compared with SS-P, SS-W, SS/PPy-P and SS/PPy-W anodes are indicative of higher electron transfer kinetics.

The study demonstrated that defined R_{ext} could, in fact, lower the start-up time. However, the application of very low resistance increases the start-up time of the same anode material. FTIR results elucidated the signature of biomolecules and complexity of MFCs anode order for biofilm formation on PANi>SS>PPy. The FTIR bands of heteropolysaccharide, proteins, nucleic acids and polysaccharides are the signature of growing biofilm on the anode surfaces. The development of air cathode MFC with tested anode materials can give better insights of long-term operation of MFCs for power production. However, it is necessary to start the reactor with tuned R_{ext} to

minimise start-up time and ensure high electricity generation. PANi on stainless steel proved to be a more efficient and cheaper anode material for MFCs and has the potential to be a very promising anode for microbial fuel cell development. Further experiments are required to elucidate the actual performance of MFC with the proposed anode.

In this chapter (*CHAPTER 5*), under optimum conditions, PANi and PPy were developed, and for the first time, the potential use of low-cost SS-W scrubber as a cheap and efficient anode in air-cathode MFCs was shown. A conducting polymer coated stainless-steel wool (SS-W) is proposed for use as a low-cost anode for microbial fuel cells (MFCs).

When coated with polyaniline (PANi) and polypyrrole (PPy), the pristine SS-W, SS/PANi-W and SS/PPy-W anodes produced maximum current densities of 0.30 ± 0.04 , 0.67 ± 0.05 , 0.56 ± 0.07 mA cm⁻², respectively, in air-cathode MFCs. Also, based on achieving power density, both SS/PANi-W and SS/PPy-W achieved 0.288 ± 0.036 mW cm⁻² and 0.187 ± 0.017 mW cm⁻², respectively, which were superior to 0.127 ± 0.011 mW cm⁻² obtained with the pristine SS-W. Further, in comparison with SS plate-based anodes, all SS wool-based anodes considered gave improved power densities under similar experimental conditions by at least 70%.

It was observed that the performance of the SS-W anode was far superior to that of the most commonly used SS-P anode on as the basis of achieved current density, power density, charge transfer resistance and electrokinetic behaviour. The PANi and PPy coatings of the SS-W improved their performances as anodes for MFCs considerably. In particular, the SS-W coated with PANi gave the best performance with 54% more power density than achieved with the SS/PPy-W anode. Considering the many advantages, such as tunable shape, size, design, high surface area and mechanical properties along with the commercial availability of SS-W, it is a most suited material for relatively cheap MFC anodes. As the SS/PANi-W anode exhibited the highest power generation in this study, further study of its long-term stability is necessary before its adoption for the construction of a pilot scale MFC stack in an endeavour to achieve a high-performance MFC system with the potential capability for treating landfill leachate.

Considering the wide applications of PANi and its nanofibrous nature upon electrochemical synthesis, it gives a good replacement for the carbon-based catalyst. This chapter explains the use of polyaniline (PANi) coated carbon paper as a low-cost replacement for Pt cathode (*CHAPTER*

6). The PANi-Cu deposition enhanced the catalytic activity for oxygen reduction reaction. Our study has successfully demonstrated the feasibility and effectiveness of fabricating and utilising a low-cost CP/PANi-Cu cathode for the replacement of Pt cathode in MFCs and LTFCs applications. Uniform PANi coating was obtained on the carbon paper, and it performed effectively as a cathode due to its nano-fibrous structure. The introduction of cupric ions by the copper counter electrode resulted in the incorporation of copper in the PANi film and consequently resulted in enhanced ORR activity. The optimum PANi-Cu_(25 min) cathode gave a much higher $j_{0\text{apparent}}$ of 0.0881 ± 0.003 mA cm⁻² which was 170% higher than the $j_{0\text{apparent}}$ obtained with 0.5 mg cm⁻² Pt cathode and was still slightly higher when a higher platinum loaded cathode which contained 1.5 mg cm⁻² Pt was used. The R_{ct} obtained for the optimum CP/PANi-Cu cathode was 1.456 Ω cm⁻² which was much lower than 3.95 Ω cm⁻² obtained for a Pt cathode with 0.5 mg Pt cm⁻² loading, but close to a R_{ct} of 1.485 Ω cm⁻² obtained with a higher platinum loaded cathode which contained 1.5 mg cm⁻² Pt. Both these results demonstrate that the Pt cathode needed 3 times the Pt loading (1.5 mg cm⁻² Pt) of the commonly used cathode to perform as well as the optimum CP/PANi-Cu cathode.

The SEM revealed that PANi formed nanofiber mat on the carbon paper, whereas the Pt formed agglomeration when deposited with an air gun. The 4D X-ray microscopy also revealed that a uniform PANi coating was formed over the surface of the carbon paper (thickness) and also at the core of carbon paper matrix. The PANi coating revealed uniform nano-fibrous structure, while the Pt loading showed non-uniform agglomeration. The results indicate that PANi cathode is a suitable low-cost replacement to Pt cathode.

The carefully developed PANi and electrochemical evaluation of electropolymerisation time gave an optimum condition for PANi synthesis on carbon paper. The use of electropolymerised PANi-Cu_(20 mins) on carbon paper cathode in MFCs resulted in a 40% drop in performance compared with the Pt_(0.5 mg cm⁻²) cathode (**CHAPTER 7**). Although it has a lower performance, the PANi catalyst is relatively cheap and easy to prepare for 1 % of the cost of Pt catalyst. Importantly, the durability and efficiency of PANi catalysts can be improved by making metal composites with PANi. The loss of cathodic activity in both the cathodes after nine cycles of the MFC operation obtained low by 46 % and 71 % for CP/PANi-Cu and CP/Pt cathodes, respectively. The loss of cathodic activity can be suppressed by a coating of PANi on the current collector; even it would lead high interfacial electron transfer from external resistance to the cathode, ultimately increase the overall

performance of the system. It is surprising that the Pt cathode was found to be more prone to the biofouling of the Nafion membrane and may lead to the deterioration of performance in long-term MFC operations.

The FTIR analysis of fouled membranes revealed that there are more complex macromolecules on the membrane attached to the Pt cathodes supporting the biofouling of the Nafion membrane over a period. Biofouling may hinder the proton transfer from the anode chamber to the triple phase boundary of MEA for the cathodic reaction. Further studies are required to improve the efficacy of the CP/PANi-Cu cathode and gain a solid understanding of the membrane biofouling. We are conducting additional investigations into these two critical aspects.

Finally, in this chapter, low-cost, readily synthesising, the high-performance anode and air cathode were developed. Also, the modified system architecture is designed to improve the performance of the MFC by using stainless steel wool coated with polyaniline (SS/PANi-W) as an anode and a free air-breathing cathode. The 18-cell stack was successfully fabricated and tested with SS/PANi-W anode (*CHAPTER 8*). Landfill leachate was used to test the stack for 85 days operated in four phases under ambient condition. The stack was investigated for the current generation, and COD removal efficiency. The maximum open circuit potential developed from each cell ranged from 0.672 V to 0.714 V. Whereas; a total open circuit voltage of 12.8 V was obtained from when all cells were connected in series. It is clear that the three side Pt air cathodes adjacent to the PANi wool anode design provide an efficient proton transfer from the anode to the membrane. The developed MFC stacks architecture offers a COD removal in the range of 86.27 % to 87.04 % when running in series connection in CR mode together with a CE in 35.30 and 36.93% from cycles 1 and 2, respectively.

The efficient operation under ambient condition confirms that the architecture suitable for operation in the tropical regions. The reactor can be deployed in a landfill leachate site for power generation and effective treatment. In summary, the thesis work has expressively contributed to the development low-cost SS wool modified with highly conductive polyaniline. Also, PANi coating was explored for air cathode for MFCs. The second phase basically designed and developed the practical engineering of microbial fuel cells stacks.

9.2 Future prospective

For application of the MFC stack in real time wastewater treatment trains, a greater focus on cathode developments using conducting polymers is required. The stability of CP/PANi-Cu composite one of the key parameters for cathode catalyst for low-temperature fuel cells. Despite successful fabrication and testing of CP/PANi-Cu cathode in aqueous proton conductor and MFCs. The results reveal that more effort is needed to improve the stability of developed ORR cathode. Since the PANi-Cu cathode is relatively less stable than Pt cathode due to the very low amount of Cu deposition during electropolymerisation. Further stability can be increased by depositing higher amount of Cu on in the PANi matrix.

Another major challenge is the engineering of the system architecture. The proton transfer from anode site to cathode site is sluggish due to the distance and configuration between the anode, proton exchange membrane and cathode. It is obvious that the more the distance, the higher will the mass transfer loss will be. Therefore, membrane electrode assembly with surface modification of anode and cathodes using suitable conductive polymers can be the best solution towards the power enhancement in MFCs. Much advancement in the last few years has been observed which enhance the ability to reduce cathodic limitations using biocathodes. However, there is a great scope of biocathode development using microalgae or green bacteria. Synergistic hydrogen production at cathode site can be possible.

Fabricated PANi based anode was successfully applied in the laboratory and pre-pilot MFC stack (7.5 L) for power generation and landfill leachate treatment. The use of computational fluid dynamics can also be employed to further investigate the developed MFC stack to gain an understanding of the charge transfer and mixing phenomena. Apart from this, engineering of the reactors, the role of recombinant DNA technology would help to construct specific strain such as *Geobacter metallireducens* in *Escherichia coli* using high expression vector and *E coli* strain to make particular enhancement in the MFC applications. It is expected that the developed strain can produce pili on the membrane, which could attribute higher electrons transfer from bacteria to the electrode. Recent advances in new and efficient electrode materials enable a better understanding of charge transfer from bio-anodes, electrogenic bacterial communities and efficient cathodes. By developed materials, and results from several MFC stacks and configuration tests are good indicators for the conceivable commercialisation of MFC technology shortly.
